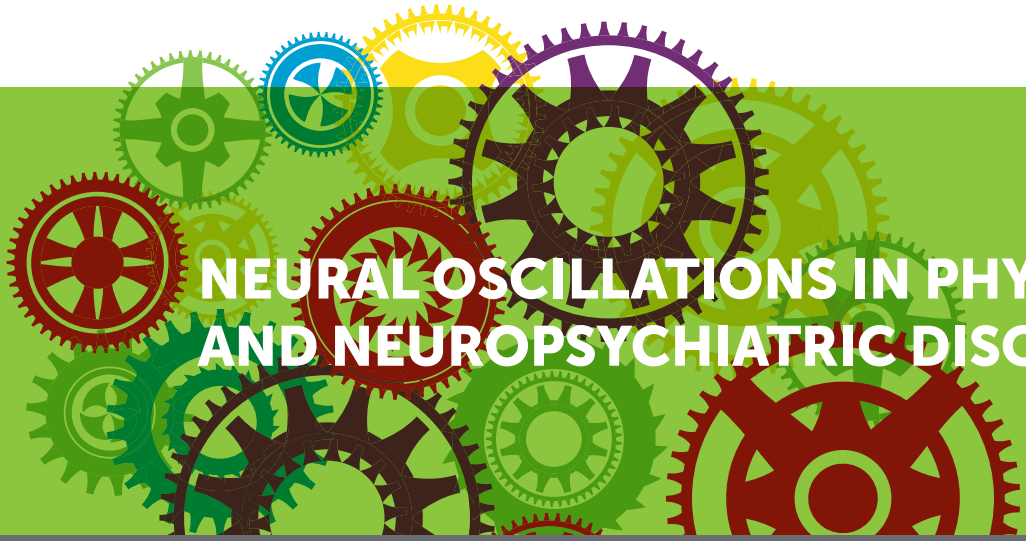

NEURAL OSCILLATIONS IN PHYSIOLOGY AND NEUROPSYCHIATRIC DISORDERS

EDITED BY: Shozo Tobimatsu and Atsushi Nambu

PUBLISHED IN: Frontiers in Human Neuroscience and Frontiers in Behavioral Neuroscience

frontiers Research Topics

frontiers

ISSN 1664-8714
ISBN 978-2-83250-198-6
DOI 10.3389/978-2-83250-198-6

About Frontiers

Frontiers is more than just an open-access publisher of scholarly articles: it is a pioneering approach to the world of academia, radically improving the way scholarly research is managed. The grand vision of Frontiers is a world where all people have an equal opportunity to seek, share and generate knowledge. Frontiers provides immediate and permanent online open access to all its publications, but this alone is not enough to realize our grand goals.

Frontiers Journal Series

The Frontiers Journal Series is a multi-tier and interdisciplinary set of open-access, online journals, promising a paradigm shift from the current review, selection and dissemination processes in academic publishing. All Frontiers journals are driven by researchers for researchers; therefore, they constitute a service to the scholarly community. At the same time, the Frontiers Journal Series operates on a revolutionary invention, the tiered publishing system, initially addressing specific communities of scholars, and gradually climbing up to broader public understanding, thus serving the interests of the lay society, too.

Dedication to Quality

Each Frontiers article is a landmark of the highest quality, thanks to genuinely collaborative interactions between authors and review editors, who include some of the world's best academicians. Research must be certified by peers before entering a stream of knowledge that may eventually reach the public - and shape society; therefore, Frontiers only applies the most rigorous and unbiased reviews.
Frontiers revolutionizes research publishing by freely delivering the most outstanding research, evaluated with no bias from both the academic and social point of view. By applying the most advanced information technologies, Frontiers is catapulting scholarly publishing into a new generation.

What are Frontiers Research Topics?

Frontiers Research Topics are very popular trademarks of the Frontiers Journals Series: they are collections of at least ten articles, all centered on a particular subject. With their unique mix of varied contributions from Original Research to Review Articles, Frontiers Research Topics unify the most influential researchers, the latest key findings and historical advances in a hot research area! Find out more on how to host your own Frontiers Research Topic or contribute to one as an author by contacting the Frontiers Editorial Office: frontiersin.org/about/contact

NEURAL OSCILLATIONS IN PHYSIOLOGY AND NEUROPSYCHIATRIC DISORDERS

Topic Editors:
Shozo Tobimatsu, Kyushu University, Japan
Atsushi Nambu, National Institute for Physiological Sciences (NIPS), Japan

Citation: Tobimatsu, S., Nambu, A., eds. (2022). Neural Oscillations in Physiology and Neuropsychiatric Disorders. Lausanne: Frontiers Media SA.
doi: 10.3389/978-2-83250-198-6

Table of Contents

frontiers | Frontiers in Human Neuroscience

TYPE Editorial
PUBLISHED 31 August 2022
DOI 10.3389/fnhum.2022.1016481

OPEN ACCESS

EDITED AND REVIEWED BY
Mingzhou Ding,
University of Florida, United States

*CORRESPONDENCE
Shozo Tobimatsu
tobimatsu.shozo.592@m.kyushu-u.ac.jp

SPECIALTY SECTION
This article was submitted to Brain Imaging and Stimulation, a section of the journal Frontiers in Human Neuroscience

RECEIVED 11 August 2022
ACCEPTED 17 August 2022
PUBLISHED 31 August 2022

CITATION
Tobimatsu S (2022) Editorial: Neural oscillations in physiology and neuropsychiatric disorders. *Front. Hum. Neurosci.* 16:1016481. doi: 10.3389/fnhum.2022.1016481

Editorial: Neural oscillations in physiology and neuropsychiatric disorders

Shozo Tobimatsu*

Department of Orthoptics, Faculty of Medicine, Fukuoka International University of Health and Welfare, Fukuoka, Japan

KEYWORDS

neural oscillations, neuropsychiatric disorders, EEG, magnetoencephalography (MEG), non-invasive brain stimulation (NIBS), time-frequency (TF) analysis

Editorial on the Research Topic
Neural oscillations in physiology and neuropsychiatric disorders

Oscillatory neuronal (electrical) activity in defined frequency ranges supports synchronous interactions between anatomically distinct regions of the human brain during cognitive tasks (Singer, 1999, 2018). From our previous studies (Tobimatsu, 2020a,b), altered neural synchronization plays an important role in distributed cortico-cortical processing. Thus, some neuropsychiatric disorders can be conceptualized as network diseases. Interestingly, the development of non-invasive brain stimulation techniques such as repetitive transcranial magnetic stimulation (rTMS) and transcranial alternating current stimulation (tACS) enables us to manipulate the brain oscillations and brain function in human (Vosskuhl et al., 2018).

Taken together, the goal of this Research Topic is to conceptualize the brain as a self-organizing complex system in which numerous, densely interconnected, but functionally specialized areas cooperate in context- and task-dependent constellations. In the following, a total of nine articles focusing on cognitive abnormalities and underlying oscillatory dysfunctions in animals and humans were published.

Kajita et al. reported "*Heterogeneous GAD65 Expression in Subtypes of GABAergic Neurons Across Layers of the Cerebral Cortex and Hippocampus.*" Neuronal oscillations are modulated by the excitatory-inhibitory balance among the neurons. They found that each GABAergic subtype exhibited a distinct GAD65 expression pattern across layers of the cerebral cortex and hippocampus in colchicine-treated rats. These findings suggest that exploration of the distinct profiles of GAD65 expression among GABAergic subtypes could clarify the roles that GABAergic subtypes play in maintaining the excitatory-inhibitory balance.

Sakamoto et al. reported "*Shape and Rule Information Is Reflected in Different Local Field Potential Frequencies and Different Areas of the Primate Lateral Prefrontal Cortex.*" They analyzed how local field potentials (LFPs) recorded from the monkey lateral prefrontal cortex (LFPC) were modulated by the crucial factors of a shape manipulation task. The transformed shape in the sample period strongly affected the

theta and delta waves in the delay period on the ventral side, while the arm-manipulation assignment influenced the gamma components on the dorsal side. Thus, area- and frequency-selective LFP modulations are involved in dynamically recruiting different behavior-relevant information in the LFPC.

Saito et al. reported "*D1 Receptor Mediated Dopaminergic Neurotransmission Facilitates Remote Memory of Contextual Fear Conditioning*." They studied the role of dopaminergic neurotransmission *via* dopamine D1 receptors (D1Rs) in aversive memory formation in contextual and auditory cued fear conditioning tests using D1R knockdown (KD) mice, in which the expression of D1Rs could be conditionally and reversibly controlled with doxycycline (Dox) treatment. When D1R expression was suppressed using Dox, behavioral experiments revealed impaired contextual fear learning in remote aversion memory following footshock stimulation. Thus, deficiency in D1R-mediated dopaminergic neurotransmission is an important factor in impairing contextual fear memory formation for remote memory.

Okazaki et al. published "*Frequency- and Area-Specific Phase Entrainment of Intrinsic Cortical Oscillations by Repetitive Transcranial Magnetic Stimulation*." They tested whether spontaneous neural oscillations in different local cortical areas and large-scale networks can be phase-entrained by direct perturbation with distinct frequencies of rTMS in humans. rTMS at 23 Hz over the motor cortex and 11 Hz over the visual cortex induced a prominent and progressive increase in phase-locking factor (PLF) that lasted for a few cycles after the termination of rTMS. Moreover, the local increase in PLF propagated to other cortical areas. These results suggest that distinct cortical areas have area-specific oscillatory frequencies, and the manipulation of oscillations in local areas impacts other areas through the large-scale oscillatory network with the corresponding frequency specificity.

Gordon et al. reported "*Prefrontal Theta-Phase Synchronized Brain Stimulation With Real-Time EEG-Triggered TMS*." They investigated individual source-space beamforming-based estimation of the prefrontal theta oscillation as a method to target specific phases of the ongoing theta oscillations in the human dorsomedial prefrontal cortex (DMPFC) with real-time EEG-triggered TMS. Using optimized parameters, prefrontal theta-phase synchronized TMS of DMPFC was achieved with an accuracy of $\pm 55^{\circ}$. This method is relevant for brain state-dependent stimulation in human studies of cognition. It will also enable new personalized therapeutic repetitive TMS protocols for more effective treatment of neuropsychiatric disorders.

Ogata et al. published "*After-Effects of Intermittent Theta-Burst Stimulation Are Differentially and Phase-Dependently Suppressed by α- and β-Frequency Transcranial Alternating Current Stimulation*." Intermittent theta-burst stimulation (iTBS) using TMS is known to produce excitatory after-effects over the primary motor cortex (M1). They tested their hypothesis that tACS would modulate the after-effects of iTBS depending on the stimulation frequency and phase using motor evoked potentials (MEPs). α-tACS suppressed iTBS effects at the peak phase but not at the trough phase, while β-tACS suppressed the effects at both phases. Thus, although both types of tACS inhibited the facilitatory effects of iTBS, only α-tACS did so in a phase- dependent manner. In conclusion, the action of iTBS is differentially modulated by neuronal oscillations depending on whether α- or β-tACS is applied.

Kobayashi et al. reported "*Exclusion of the Possibility of "False Ripples" From Ripple Band High-Frequency Oscillations Recorded From Scalp Electroencephalogram in Children With Epilepsy*." Ripple-band epileptic high-frequency oscillations (HFOs) can be recorded by scalp EEG in association with epileptic spikes. But the filtration of steep waveforms such as spikes may cause spurious oscillations or "false ripples." They have demonstrated that the numerical differentiation of EEG data provides convincing evidence that HFOs were detected in terms of the presence of such unusually fast oscillations over the scalp and the importance of this electrophysiological phenomenon.

Sultana et al. reported "*A Long Time Constant May Endorse Sharp Waves and Spikes Over Sharp Transients in Scalp Electroencephalography: A Comparison of After-Slow Among Different Time Constants Concordant With High-Frequency Activity Analysis*." They examined whether long time constant (TC) is useful for detecting the after-slow activity of epileptiform discharges (EDs): sharp waves and spikes and for differentiating EDs from sharp transients (Sts). Compared to Sts, high-frequency activity (HFA) was found significantly more with the apical component of EDs. Thus, long TC could be useful for selectively endorsing after-slow of EDs and differentiating EDs from Sts.

Roberts et al. published "*Magnetoencephalography Studies of the Envelope Following Response During Amplitude-Modulated Sweeps: Diminished Phase Synchrony in Autism Spectrum Disorder*." Auditory steady-state responses (ASSR, driven at 40 Hz) can elicit coherent electrophysiological responses from intact circuitry in adults. Thus, the authors applied amplitude-modulated (AM) sweep stimuli (500 Hz carrier; sweep 10–100 Hz up and down) bilaterally to 40 typically developing and 80 children with autism spectrum disorder (ASD). They found an imbalance of excitatory and inhibitory neurotransmission in MEG and concluded that (1) the AM sweep stimulus provides a mechanism for probing ASSR in an unbiased fashion, during developmental maturation of peak response frequency, (2) peak frequencies vary, in part due to developmental age, and importantly, (3) intra-trial coherence (ITC) at this peak frequency is diminished in ASD, with the degree of ITC disturbance related to clinically assessed language impairment.

In conclusion, we hope that these papers will shed light on the nature of brain oscillations in animals and humans.

Author contributions

The author confirms being the sole contributor of this work and has approved it for publication.

Funding

This work was supported in part by Grant-in-Aid for Scientific Research on Innovative Areas MEXT KAKENHI 15H05875.

Conflict of interest

The author declares that the research was conducted in the absence of any commercial or financial relationships that could be construed as a potential conflict of interest.

Publisher's note

All claims expressed in this article are solely those of the authors and do not necessarily represent those of their affiliated organizations, or those of the publisher, the editors and the reviewers. Any product that may be evaluated in this article, or claim that may be made by its manufacturer, is not guaranteed or endorsed by the publisher.

References

Singer, W. (1999). Neuronal synchrony: a versatile code for the definition of relations? *Neuron* 24, 49–65. doi: 10.1016/S0896-6273(00)80821-1

Singer, W. (2018). Neuronal oscillations: unavoidable and useful? *Euro J. Neurosci.* 48, 2389–2398. doi: 10.1111/ejn.13796

Tobimatsu, S. (2020a). Neuromagnetic oscillations in the human sensory systems: a mini review of our series and literature. *Neurosci. Res.* 156, 117–129. doi: 10.1016/j.neures.2019.12.007

Tobimatsu, S. (2020b). Neural oscillations and network diseases of the human brain. *Brain Nerve* 72, 1183–1194 (in Japanese). doi: 10.11477/mf.1416201671

Vosskuhl, J., Strüber, D., and Herrmann, C. S. (2018). Non-invasive brain stimulation: a paradigm shift in understanding brain oscillations. *Front Hum Neurosci.* 12, 211. doi: 10.3389/fnhum.2018.00211

frontiers in Human Neuroscience

ORIGINAL RESEARCH
published: 12 March 2021
doi: 10.3389/fnhum.2021.608947

Frequency- and Area-Specific Phase Entrainment of Intrinsic Cortical Oscillations by Repetitive Transcranial Magnetic Stimulation

Yuka O. Okazaki[1,2,3], *Yumi Nakagawa*[1], *Yuji Mizuno*[1,4], *Takashi Hanakawa*[1,4,5] *and Keiichi Kitajo*[1,2,3*]

[1] RIKEN CBS-TOYOTA Collaboration Center, RIKEN Center for Brain Science, Wako, Japan, [2] Division of Neural Dynamics, Department of System Neuroscience, National Institute for Physiological Sciences, National Institutes of Natural Sciences, Okazaki, Japan, [3] Department of Physiological Sciences, School of Life Science, The Graduate University for Advanced Studies (SOKENDAI), Okazaki, Japan, [4] Integrative Brain Imaging Center, National Center of Neurology and Psychiatry, Kodaira, Japan, [5] Department of Integrated Neuroanatomy and Neuroimaging, Graduate School of Medicine, Kyoto University, Kyoto, Japan

OPEN ACCESS

Edited by:
Shozo Tobimatsu,
Kyushu University, Japan

Reviewed by:
Domenica Veniero,
University of Nottingham,
United Kingdom
Reza Kazemi,
Atieh Clinical Neuroscience Center, Iran
Yasuo Terao,
Kyorin University, Japan
Keiji Iramina,
Kyushu University, Japan

***Correspondence:**
Keiichi Kitajo
kkitajo@nips.ac.jp

Specialty section:
This article was submitted to Brain Imaging and Stimulation, a section of the journal Frontiers in Human Neuroscience

Received: 22 September 2020
Accepted: 19 February 2021
Published: 12 March 2021

Citation:
Okazaki YO, Nakagawa Y, Mizuno Y, Hanakawa T and Kitajo K (2021) Frequency- and Area-Specific Phase Entrainment of Intrinsic Cortical Oscillations by Repetitive Transcranial Magnetic Stimulation. Front. Hum. Neurosci. 15:608947. doi: 10.3389/fnhum.2021.608947

Synchronous oscillations are ubiquitous throughout the cortex, but the frequency of oscillations differs from area to area. To elucidate the mechanistic architectures underlying various rhythmic activities, we tested whether spontaneous neural oscillations in different local cortical areas and large-scale networks can be phase-entrained by direct perturbation with distinct frequencies of repetitive transcranial magnetic stimulation (rTMS). While recording the electroencephalogram (EEG), we applied single-pulse TMS (sp-TMS) and rTMS at 5, 11, and 23 Hz over the motor or visual cortex. We assessed local and global modulation of phase dynamics using the phase-locking factor (PLF). sp-TMS to the motor and the visual cortex triggered a transient increase in PLF in distinct frequencies that peaked at 21 and 8 Hz, respectively. rTMS at 23 Hz over the motor cortex and 11 Hz over the visual cortex induced a prominent and progressive increase in PLF that lasted for a few cycles after the termination of rTMS. Moreover, the local increase in PLF propagated to other cortical areas. These results suggest that distinct cortical areas have area-specific oscillatory frequencies, and the manipulation of oscillations in local areas impacts other areas through the large-scale oscillatory network with the corresponding frequency specificity. We speculate that rTMS that is close to area-specific frequencies (natural frequencies) enables direct manipulation of brain dynamics and is thus useful for investigating the causal roles of synchronous neural oscillations. Moreover, this technique could be used to treat clinical symptoms associated with impaired oscillations and synchrony.

Keywords: rTMS-EEG, phase entrainment, natural frequency, visual cortex, motor cortex, phase locking

INTRODUCTION

Large-scale phase synchronization of neural oscillations plays a role in linking task-relevant brain regions associated with information processing (Varela et al., 2001; Fries, 2005). Although phase synchronization of neural oscillations is ubiquitous in the brain, the frequency of synchronous oscillations varies across distinct brain regions and networks (Siegel et al., 2012), and is presumably associated with segregated and integrated networks that mediate various functions, such as face perception (Rodriguez et al., 1999), selective attention (Doesburg et al., 2008), and working memory (Kawasaki et al., 2010).

Frequency-specific network structures characterized by phase synchronization also exist in the resting state (Hillebrand et al., 2012; Hipp et al., 2012) and are spatially consistent with the task-driven networks, as demonstrated by fMRI studies (Smith et al., 2009; Deco and Corbetta, 2011). Moreover, research in animals has shown that sensory-evoked population firing patterns are geometrically confined to subregions of the neuronal state space delineated by spontaneous activity (Luczak et al., 2009). These studies suggest that the spatiotemporal patterns of spontaneous neural activity reflect a wide repertoire of neural dynamics, and may constrain the task-related neural dynamics. However, few mechanistic details are known about the various sets of rhythmic activity in different cortical areas.

Non-invasive brain stimulation techniques such as transcranial magnetic and electrical stimulation (TMS and TES) have emerged as promising manipulative tools, enabling direct perturbation of local brain areas. TMS, in particular, can be used to target spatially confined regions involved in generating oscillations. The use of TMS in combination with EEG allows us to study the mechanisms underlying changes in response measures (excitability and connectivity) to perturbations within brain networks. In a previous TMS-EEG study, we showed that the phase synchronization of the intercortical networks changes dynamically according to the attentional state (Okazaki et al., 2020). In addition, single-pulse TMS has been shown to directly interfere with the phase dynamics of oscillations and trigger a transient phase reset of intrinsic oscillations in visual areas (Kawasaki et al., 2014). It is noteworthy that when single-pulse TMS was applied to different cortical regions that constitute specific corticothalamic networks, oscillations induced in occipital, parietal, and frontal cortices fell into distinct frequency bands (Rosanova et al., 2009). This indicates that each corticothalamic network has its own characteristic intrinsic frequency, or "natural frequency." Given the results of single pulse-induced brain oscillations, entrainment of the oscillatory phase can be predicted when further TMS pulses are applied in phase with the induced oscillations (Lakatos et al., 2019). Consequently, the amplitude of oscillations gradually increases as more and more intrinsic neural oscillators are entrained to the repetitive TMS pulses (Thut et al., 2011a). In line with this hypothesis, Thut et al. demonstrated local enhancement of alpha oscillations by applying alpha-frequency train of TMS pulses to the parietal cortex (Thut et al., 2011b).

To our knowledge, no previous study has applied rhythmic stimulation at multiple frequencies to distinct cortical regions. However, based on the above-mentioned evidence (Rosanova et al., 2009; Thut et al., 2011b), it seems probable that distinct cortical regions have their own optimal frequencies for the phase entrainment of intrinsic neural oscillations. We, therefore, hypothesized that there exist region-specific differences in the frequency characteristics of phase entrainment of intrinsic oscillations by external stimulation. Moreover, it is not clear how locally entrained oscillations impact oscillations in other cortical regions *via* large-scale functional networks. Given that local brain areas that are targeted by periodic stimulation are globally coupled to oscillatory modules in other brain regions, we also hypothesized that locally entrained oscillations propagate to other connected areas with specific frequency characteristics. To address these hypotheses, we measured phase dynamics using scalp electroencephalography (EEG) while applying rTMS to either the motor or visual cortex at theta- (5 Hz), alpha- (11 Hz), or beta- (23 Hz) band frequencies.

MATERIALS AND METHODS

Participants

Fourteen healthy right-handed participants (two females and 12 males aged 30.8 ± 5.5 years, mean ± SD) provided informed, written consent to participate in the study. This study was conducted in accordance with the declaration of Helsinki, and was approved by the RIKEN Ethics Committee.

TMS-EEG Experiments

TMS was applied in a biphasic pulse configuration by a Magstim Rapid unit with a figure-of-eight coil (Double 70 mm Alpha coil; Magstim, UK). Stimulation was applied over either the visual or motor regions, or a sham control location (**Figure 1A**). For the sham stimulation, the coil was positioned 10 cm above the vertex with the coil handle oriented in a posterior direction. Thus, sham stimulation produced a TMS "click" sound that occurred at the same frequency as that of the real TMS session, but without cortical stimulation; in all conditions, the click sound was attenuated by earplugs. For stimulation of visual regions, the coil was located centrally between the Oz and O2 electrodes with the coil handle pointing rightward. For stimulation of motor regions, the coil position was determined individually at the "hotspot" that activated the right first dorsal interosseous (FDI) (approximately at the C3 electrode, with the handle perpendicular to the central sulcus). Posterior-anterior current flow for the second half-wave of the biphasic pulse induces an effective current flow for axon depolarization (Kammer et al., 2001). In terms of noise reduction (Komssi et al., 2004; Litvak et al., 2007) and induction of recordable phase reset (Kawasaki et al., 2014), a stimulation intensity of 90% of the FDI active motor threshold was used in all conditions. To reduce the noise induced in the electrode lead wire, the lead wire and the TMS coil handle are arranged orthogonally.

EEG Recordings

During stimulation, EEG (left earlobe reference; ground AFz was continuously recorded at a 5 kHz sampling rate (filtering: DC to 1,000 Hz) from 63 scalp sites *via* Ag/AgCl

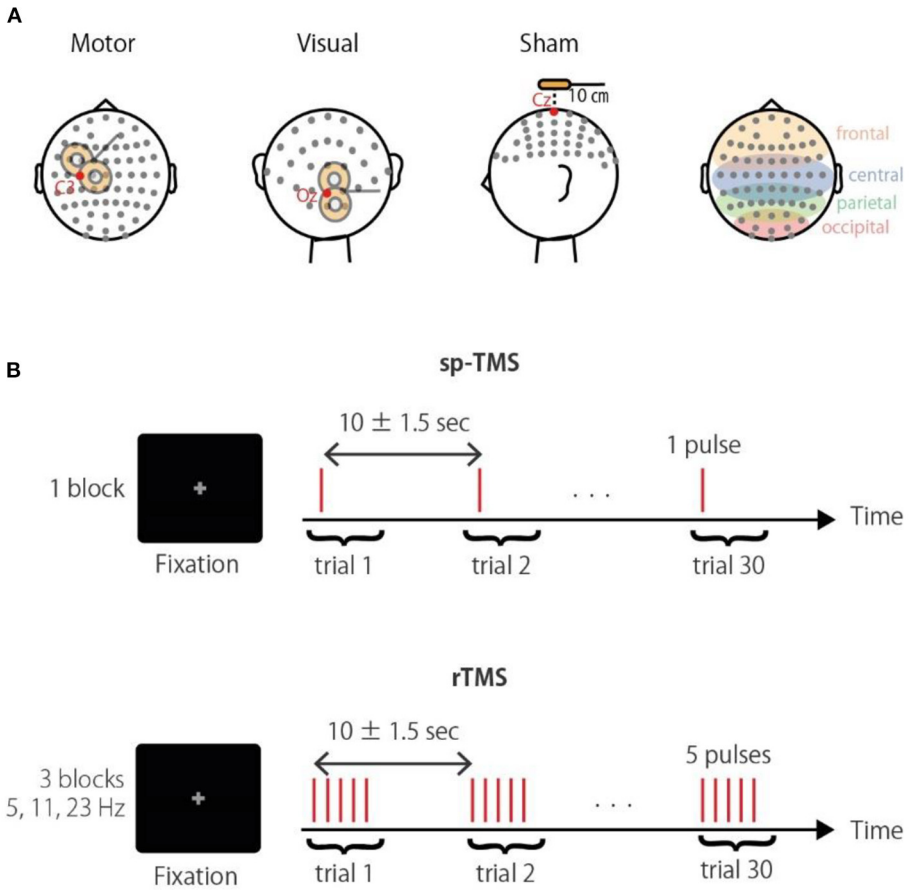

FIGURE 1 | Experimental paradigm. **(A)** Schematic illustration of the stimulation sites. Corresponding electrodes to the occipital, parietal, central, and frontal areas are highlighted in the right panel. **(B)** The TMS conditions were a single pulse (sp-TMS), and five pulses at 5, 11, or 23 Hz (rTMS). The TMS conditions were provided in blocks with 30 repetitions. Participants had to fixate a central cross during trials.

TMS-compatible electrodes mounted on a 10/10 system EasyCap (EASYCAP GmbH, Germany). Horizontal and vertical electrooculography (EOG; ground electrode, left mastoid) signals were simultaneously recorded. Electrode impedance was maintained below 10 kΩ. The EEG and EOG signals were amplified using a BrainAmp MR plus system (Brain Products GmbH, Germany).

Experimental Procedure

Three TMS-EEG sessions with different stimulation sites (visual, motor, and sham) were conducted in a semi-random order that was counterbalanced across participants. Each session consisted of the four following blocks: a single pulse (sp-TMS), and a 5-pulse train at 5 Hz (θ-rTMS), 11 Hz (α-rTMS), and 23 Hz (β-rTMS). Thus, the duration from the first to the last pulse of rTMS was 800, ∼364, and ∼174 ms, respectively. These frequencies were chosen to differentiate the entrained frequencies, including their harmonics. The block order was also counterbalanced. Each block comprised 30 trains with an inter-train interval of 10 ± 1.5 s. Participants were fixated on a centrally presented gray cross on a black background during each block (**Figure 1B**). Stimulus delivery was controlled using Psychtoolbox-3 (Brainard, 1997; Pelli, 1997; Kleiner et al., 2007).

Preprocessing

EEG data were analyzed using MATLAB (Mathworks, USA) scripts that were developed in-house with FieldTrip (Oostenveld et al., 2011) and EEGLAB (Delorme and Makeig, 2004). For segmented (from 2 s before the first pulse to 3 s after the last pulse) and re-referenced (the average of the left and right earlobe electrode signals) EEG data, TMS artifacts and noisy epochs were removed by performing the following steps according to Herring et al. (2015) (see also http://www.fieldtriptoolbox.org/tutorial/tms-eeg for the detailed procedure). First, we linearly interpolated the 40 samples (8 ms) after TMS onset, which is the period that usually shows excessive TMS artifacts. In the case of artifacts occurring after 8 ms, we used interpolation of 60 samples (12 ms). Second, we attenuated the exponentially decaying TMS artifacts using independent component analysis (ICA) (Korhonen et al., 2011). Independent components with extremely large amplitudes, i.e., those with maximum z-score values >1.65 between 0 and 100 ms, were removed. Third, we

discarded epochs within 1 s pre- or post-stimulation in which the EEG amplitude exceeded 200 μV; on average, 24.8 ± 2.5 [SD] trials remained in each condition. Then, we applied current source density (CSD) transformation to the EEG voltage map using the spherical-spline surface Laplacian algorithm to attenuate the effects of volume conduction using the CSD Toolbox (Perrin et al., 1989; Kayser and Tenke, 2006). Finally, the data were downsampled to 1,000 Hz. The artifact-corrected TMS-EEG data were also analyzed in our previous study, which had a different purpose (i.e., probing phase-amplitude coupling) (Glim et al., 2019). Data and code are available upon reasonable request to the corresponding author.

Time-Frequency Analysis

The time–frequency representations (TFRs) of the instantaneous amplitude and phase were obtained using a wavelet transform at a center frequency f and time t, with standard deviations $\sigma_f = 4f/m$ and $\sigma_t = m/2\pi f$ (Lachaux et al., 2000). The constant m was set to 3. In general, the phase entrainment of oscillations is achieved through the gradual phase alignment of the oscillations by periodic external inputs. We expected that the phase of EEG oscillations would be gradually aligned *via* successive pulses of rTMS, and the degree of phase alignment would be assessed as the phase consistency of EEG signals across trials. We also expected that the phase-aligned oscillations would persist for a short time even after rTMS was terminated (Thut et al., 2011a). Here, the phase entrainment was defined as the phase-locking factor (PLF) (Tallon-Baudry et al., 1996), which evaluates phase consistency across trials. If the phase shifts toward a particular phase due to the TMS pulses, the phase will be consistent across trials and the PLF will increase.

$$PLF_m = \left| \frac{1}{N} \sum_{n=1}^{N} \exp(i(\varphi_{m,\,n}\ (f,t)) \right|,$$

where $\varphi_{m,n}$ is the instantaneous phase of the nth trial at electrode m and N denotes the total number of trials. Based on the circular statistics, Rayleigh's Z transform is used to test for circular uniformity, which takes into account the critical value bias according to the sample size. We applied it to PLF to compare between conditions with different numbers of trials due to the artifact removal procedure:

$$ZPLF = N \times PLF^2$$

(Fisher, 1993; Mazaheri and Jensen, 2006; Bonnefond and Jensen, 2012). The biased PLF and unbiased ZPLF according to the number of trials, which was limited due to the total duration of the experiment in the current study, were confirmed using our empirical EEG data (**Supplementary Figure 1**).

Statistical Analysis

Significant differences in the ZPLF between TMS (sp-TMS and rTMS) and sham-TMS were determined by performing cluster-based permutation tests (Maris and Oostenveld, 2007), which evaluate comparisons between cluster-level statistics of the observed data matrices and those of the null distribution. First, ZPLF matrices (i.e., 63 electrodes, 3–45 Hz, −0.5 to 1.5 s) for the TMS and sham-TMS conditions were compared using a two-tailed paired t-test with a threshold uncorrected p-value < 0.05 to locate contiguous negative and positive clusters in the matrices. Cluster-level statistics were determined as the sum of the t-values within the cluster. Second, to generate a null distribution for the cluster-level statistics, the highest cluster-level statistic was identified from matrices in which two condition labels were randomly permuted within participants and iterated 500 times. Finally, a significant cluster level was defined in the observed data as the 97.5th percentile of the null distribution.

Next, we tested whether modulation of the ZPLF was more globally distributed at frequencies matching the stimulation frequency than at other frequencies. The number of significant electrodes, identified by the above cluster-permutation test, at each frequency and time was counted. Then, the numbers of significant electrodes at the stimulation frequency and at other frequencies were compared using the binomial test. All statistical results are summarized in **Table 1**.

RESULTS

Phase Entrainment of Intrinsic Local Oscillations by Periodic Stimulation

To assess the phase entrainment of neural oscillations by TMS, we first examined the TFR of the ZPLF for each stimulated area. The cluster-based permutation test revealed significant increases in phase locking by sp-TMS and rTMS (θ-rTMS, α-rTMS, β-rTMS) compared with the corresponding sham condition ($p < 0.05$, cluster-based permutation test). **Figure 2** shows the significant t-values derived from cluster statistics (non-significant values are masked by zero). For stimulation over motor areas, sp-TMS induced a transient increase in the ZPLF at a broad frequency band, peaking at 21 Hz (**Figure 2A**). rTMS induced a prolonged increase in the ZPLF at the stimulation frequency (horizontal dashed line) during α-rTMS (**Figure 2C**) and β-rTMS (**Figure 2D**), but this effect was non-significant for the theta-band ZPLF during θ-rTMS (**Figure 2B**). For stimulation over visual areas, the peak response frequency to sp-TMS was 8 Hz (**Figure 2E**). In all rTMS conditions, a continuous increase in phase entrainment around the stimulation frequency was observed (**Figures 2F–H**).

Next, we examined whether the effects of phase locking across trials lasted, even after the rTMS train had terminated. If intrinsic oscillations are generated by self-sustaining systems without external input (Komssi et al., 2004), the phase locking should persist for a short time after the end of the stimulation train (Klimesch et al., 2004). We observed that the increase in the ZPLF lasted for more than two cycles after the last pulse of β-rTMS to the motor cortex (**Figure 2D**, magnified view) and 1.5 cycles after the last pulse of α-rTMS to the visual cortex (**Figure 2G**, magnified view). This lasting effect was not due to a signal processing limitation, i.e., spectral leakage in the time domain of the wavelet convolution, because its effect is theoretically <5% after one cycle and must be observed under all conditions. We also noted that these sustained frequencies

(i.e., 23 Hz for the motor cortex and 11 Hz for the visual cortex) were slightly different from the frequencies of oscillations evoked by sp-TMS (i.e., peaks at 21 Hz for the motor cortex and 8 Hz for the visual cortex). Furthermore, we investigated whether the neural oscillations of participants with individual alpha frequencies (IAF) close to the α-rTMS frequency, i.e., 11 Hz, were more entrained. Participants who showed a prominent power peak were separated into low-IAF and high-IAF groups, as shown in **Supplementary Figure 2A** (four participants were excluded because they did not show a prominent power peak). Standardized by the mean and SD of the ZPLF over time points in the entire epoch interval, the ZPLFs were averaged for each group for α-rTMS over the visual cortex (**Supplementary Figure 2B**). Compared with the low-IAF group and the high-IAF group, the group whose intrinsic alpha frequency was closer to the stimulation frequency showed a longer phase entrainment effect. These results suggest that α-rTMS, which has a frequency sufficiently close (but not necessarily the same) to that of the natural frequency, was most effective for entraining intrinsic brain oscillations.

TABLE 1 | A summary of statistics for each figure.

Figure #	Statistics	Comparison	Statistical representation
2	Cluster-based permutation test	Real vs. Sham TMS	The sum of *t*-values within significant clusters
3	Dunnett's test	Baseline vs. Each pulse	The mean of ZPLFnorm
4	Cluster-based permutation test	Real vs. Sham TMS	The sum of *t*-values within significant clusters
5 A, C	Cluster-based permutation test	Real vs. Sham TMS	The number of electrodes in significant clusters
5 B, D	Binomial test	Real vs. Real TMS	
6	Cluster-based permutation test	Real vs. Real TMS	The sum of *t*-values within significant clusters

Gradual Modulation of Phase-Locked Frequency Over TMS Pulses

If entrainment is achieved through a phase alignment of ongoing oscillations to periodic force, successive phase alignment should result in gradual increases in the ZPLF (Thut et al., 2011a). As

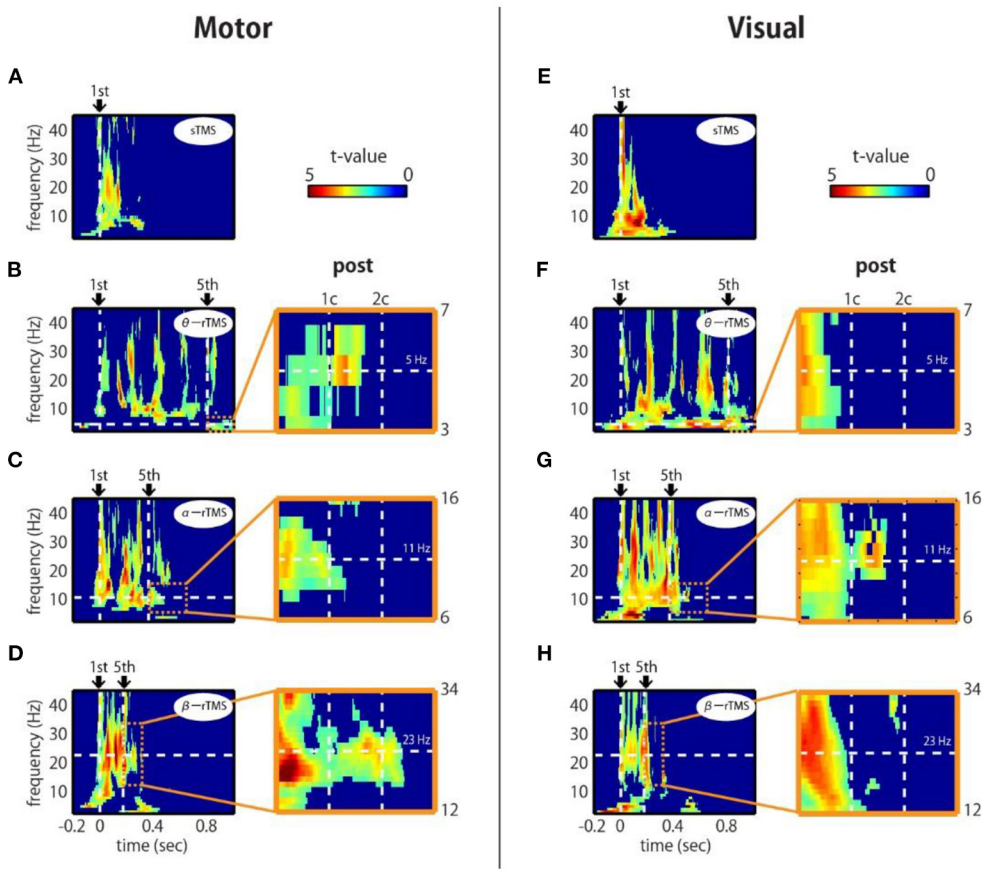

FIGURE 2 | Time-frequency representations of ZPLF at the stimulated areas. Each map with *t*-values indicates significantly larger ZPLF for motor (C3) stimulation **(A–D)** and for visual (Oz) stimulation **(E–H)** than under the sham condition. The vertical lines in the left panels correspond to the first and last stimulation pulses. The horizontal lines indicate the stimulation frequency. Right panels are magnified views of three cycles after the end of rTMS. Vertical lines indicate the post-one cycle (1c) and post-two cycles (2c) for each stimulation frequency.

shown in **Figure 2**, increases in the ZPLF occurred not only around the stimulation frequency but also at a broad range of frequencies. Intriguingly, however, the most prominent phase-locked frequency varied over the course of the stimulation train. To measure which frequency showed the most prominent increase at each TMS pulse, we standardized the ZPLF using the mean and SD of the ZPLF over all frequencies ($ZPLF_{norm}$). **Figure 3** shows the $ZPLF_{norm}$ averaged over ±0.5 cycles of each frequency for each TMS pulse. For example, for α-rTMS over the visual cortex, the dominant frequency was 5 Hz at the first pulse (brown line), but 11 Hz for the last three pulses (**Figure 3E**). The charts inset in each panel quantify, for each pulse in the train, whether the $ZPLF_{norm}$ at the stimulation frequency was significantly larger than the ZPLF at baseline control (ctrl). Here, the $ZPLF_{norm}$ at ctrl indicates the mean value of $ZPLF_{norm}$ during the baseline period from −5 to −2 stimulation-frequency cycles. We applied a one-way ANOVA with the factor pulse (ctrl, 1st, 2nd, 3rd, 4th, 5th) to assess the effect of the pulse on phase locking. The one-way ANOVA revealed a significant main effect of the pulse on the $ZPLF_{norm}$ in β-rTMS over the motor cortex [$F_{(5, 78)} = 3.40$, $p = 0.008$], but not in stimulation over the visual cortex [$F_{(5, 78)} = 1.65$, $p = 0.156$]. On the other hand, stimulation over the visual cortex showed a significant main effect of the pulse on the $ZPLF_{norm}$ in α-rTMS [$F_{(5, 78)} = 2.81$, $p = 0.022$] and θ-rTMS [$F_{(5, 78)} = 3.11$, $p = 0.013$]. The Dunnett's *post-hoc* tests comparing each pulse with ctrl confirmed a significantly stronger ($p < 0.05$) phase locking than ctrl after the 3rd pulse of β-rTMS over the motor cortex (**Figure 3C**) and α-rTMS over the visual cortex (**Figure 3E**), although 5th pulse did not induce a maximum $ZPLF_{norm}$. In addition, we confirmed the linearly increasing trend of the ZPLF as a function of the number of pulses using Pearson's correlation analysis (β-rTMS: $r = 0.30$, $p = 0.005$; α-rTMS: $r = 0.39$, $p = 0.0002$). Although there was a significant difference between pulses and ctrl in θ-rTMS over the visual cortex (**Figure 3D**), the phase locking to the stimulation frequency was more dominant than other frequencies for every TMS pulse in the train, i.e., it is not gradually increasing.

Global Propagation of Phase Entrainment

Next, we addressed the question of whether local phase locking to rTMS propagates to other cortical areas. We first examined the spatial extent of the significant increases in the ZPLF by performing cluster-based permutation tests between TMS and sham conditions. Increases in the ZPLF with rTMS to the motor cortex were distributed to the ipsilateral hemisphere and partially extended to the contralateral hemisphere (**Figure 4A**). For stimulation over the visual cortex, rTMS resulted in widespread increases in the ZPLF reaching frontal areas (**Figure 4B**). The extensive phase locking during stimulation of the motor and visual cortices appears to be more localized for later pulses. Moreover, in several areas, phase locking persisted even after the end of the stimulation. In particular, phase locking of frontoparietal areas with θ-rTMS, the left occipitoparietal area with α-rTMS, and the right motor area with β-rTMS were maintained in both the visual and motor area TMS-target conditions (see magnified topography at post 1.5 cycles in **Figures 4A,B**).

We further examined the time–frequency profile of the spatial extent of phase locking from the number of electrodes with significant phase locking. For motor stimulation, phase locking at alpha-band frequencies was induced in many electrodes by α-rTMS (**Figures 5A,B**, middle panels). On the other hand, β-rTMS induced oscillations at both the alpha- and beta-band frequencies (**Figures 5A,B**, bottom panels). For α-rTMS or β-rTMS over the visual cortex, the induced oscillations were prominent at the stimulation frequency (**Figures 5C,D**, middle and bottom panels). To quantify this frequency specificity, we averaged the number of significant electrodes over four cycles at each frequency (indicated by the red lines in **Figures 5A,C**). We used the binomial test to assess whether more electrodes were phase locked at the stimulation frequency than at the other frequencies; for example, for θ-rTMS, we assessed whether there were significantly more phase-locked electrodes at 5 Hz (the theta band) than at 11 or 23 Hz (see **Figures 5B,D**). The mean number of electrodes with significant phase locking was greater around the stimulation frequency than at the other frequencies. Namely, for α-rTMS to the motor cortex (**Figure 5B**, middle panel) and visual cortex (**Figure 5D**, middle panel), alpha-band neural oscillations were more globally entrained than oscillations in other frequency bands. Similarly, for β-rTMS to the motor cortex (**Figure 5B**, bottom panel) and visual cortex (**Figure 5D**, bottom panel), beta-band oscillations were more globally entrained than those in other frequency bands. We also noted that there were significantly more electrodes with significant phase locking for visual cortex stimulation than for motor cortex stimulation (θ-rTMS: $p = 0.1727$; α-rTMS: $p = 0.0008$; β-rTMS: $p = 0.0019$; binomial test). The fact that phase locking beyond the stimulation site was most prominent around the stimulation frequency suggests that globally coupled frequency-specific neural oscillators in brain networks were phase-entrained by rTMS. While sp-TMS also resulted in global phase locking, this was non-frequency-specific (**Supplementary Figure 3**).

Elimination of Common Components Induced by Stimulation

Finally, to investigate the frequency-specific spatial distribution of phase locking, we determined the regions in which non-common phase locking occurred under distinct stimulation conditions. Specifically, we compared the topographies of the ZPLF for each stimulation pulse across θ-rTMS, α-rTMS, and β-rTMS conditions using the cluster-based permutation test. Under motor cortical stimulation conditions (**Figure 6A**), the β-band ZPLF in β-rTMS was significantly stronger than the beta-band ZPLF in θ-rTMS (**Figure 6A**, upper panel), and α-rTMS (**Figure 6A**, lower panel). Interestingly, there was no significant difference in the ZPLF for the first pulse; however, a stronger ZPLF was observed outside the stimulation area after the second pulse and even after stimulation terminated. Under visual cortical stimulation conditions (**Figure 6B**), α-rTMS resulted in a significantly larger α-band ZPLF than θ-rTMS in widely distributed areas (**Figure 6B**, upper panel), while it was negligible under the β-rTMS condition (**Figure 6B**, lower panel). Direct comparisons between rTMS frequency conditions not only revealed frequency-specific responses but also removed non-specific noise and evoked components, which were common

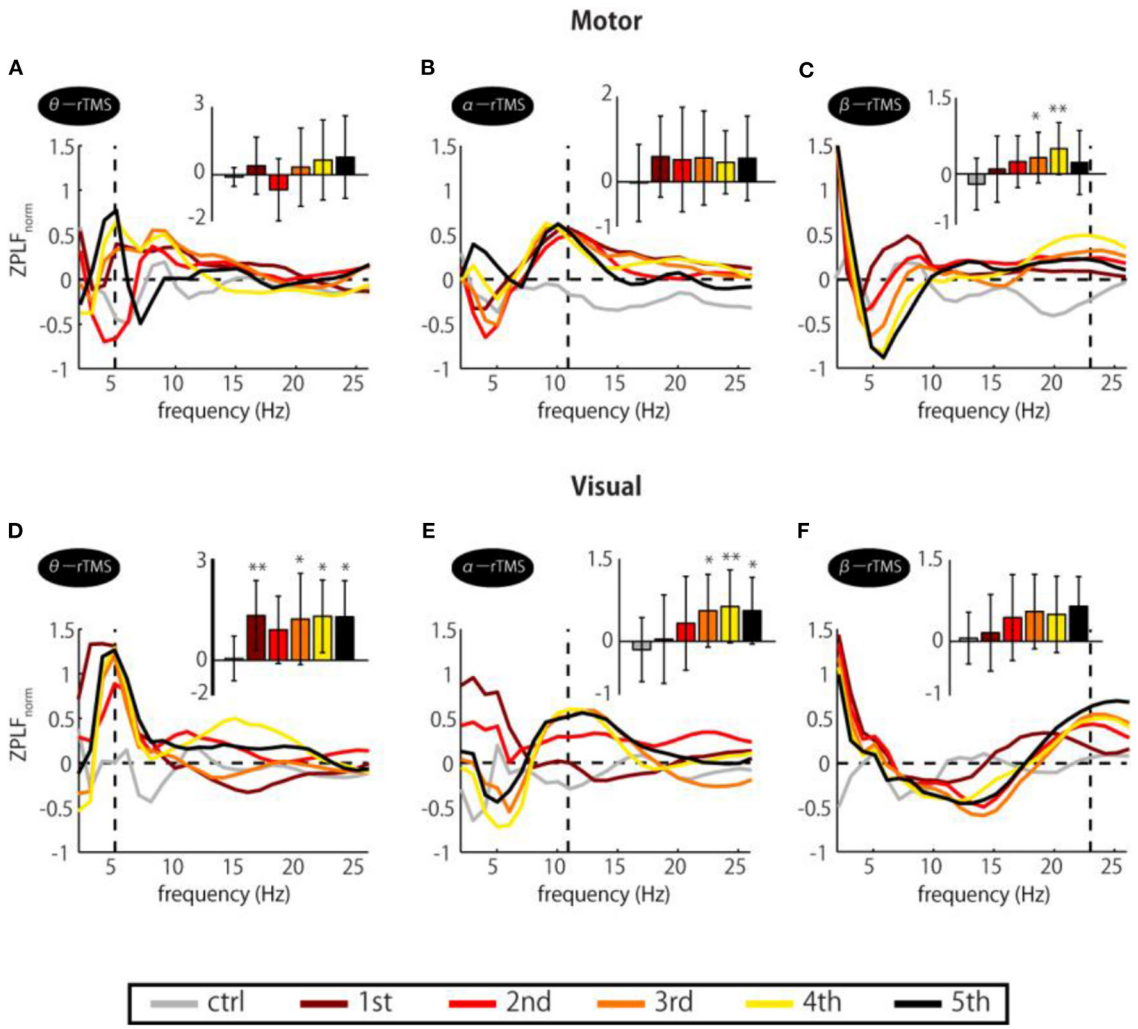

FIGURE 3 | Changes in $ZPLF_{norm}$ over TMS train. Each colored line corresponds to $ZPLF_{norm}$ for each TMS pulse to the motor **(A–C)** and the visual cortex **(D–F)**. Together, they indicate which frequency was the most prominent during the train and how it varied with pulse repetition. The charts inset in each panel indicate the $ZPLF_{norm}$ at the frequency corresponding to the rTMS stimulation frequency, i.e., the values of $ZPLF_{norm}$ at the vertical dashed line. Significant changes from the baseline control period (ctrl) were assessed by Dunnett's test (*$p < 0.05$, **$p < 0.01$). The baseline was the mean value during the period from −5 to −2 stimulation-frequency cycles. Error bars: SD.

across all stimulation conditions. Thus, these topographical representations indicate that rhythmic stimulation induces the spatial spread of frequency-specific phase locking.

DISCUSSION

Efficient Stimulation Frequencies for the Phase Entrainment of Intrinsic Oscillations

It has been reported that rhythmic stimulation at a frequency that matches physiological rhythms is the most efficient in modulating behaviors *via* the entrainment of task-related oscillations (Klimesch et al., 2003; Sauseng et al., 2009; Romei et al., 2011). In particular, Klimesch et al. demonstrated that rTMS at the stimulation frequency of IAF +1 Hz was beneficial for cognitive performance, whereas it was ineffective at the stimulation frequency of IAF +3 Hz (Klimesch et al., 2003). More recently, an rTMS-EEG study by Thut et al. showed that intrinsic alpha oscillations were entrained by rTMS at the IAF applied to the alpha source (Thut et al., 2011b). From the perspective of non-linear dynamical systems theory, the degree of entrainment of an oscillatory system to the rhythmic stimulation changes as a function of stimulation frequency and amplitude; this is known as the "synchronization region," or the "Arnold tongue" (Pikovsky et al., 2003). If the stimulation amplitude is low, only rhythms close to the natural frequency can entrain the system, but as the stimulation amplitude increases, the system is entrained to a wider range of stimulation frequencies. In a model evaluating the degree of entrainment by transcranial alternating current stimulation (tACS) under a comprehensive array of stimulation conditions (amplitude: 1–13 pA; frequency: 0–6 Hz;), tACS matched to the natural frequency was the most efficient in

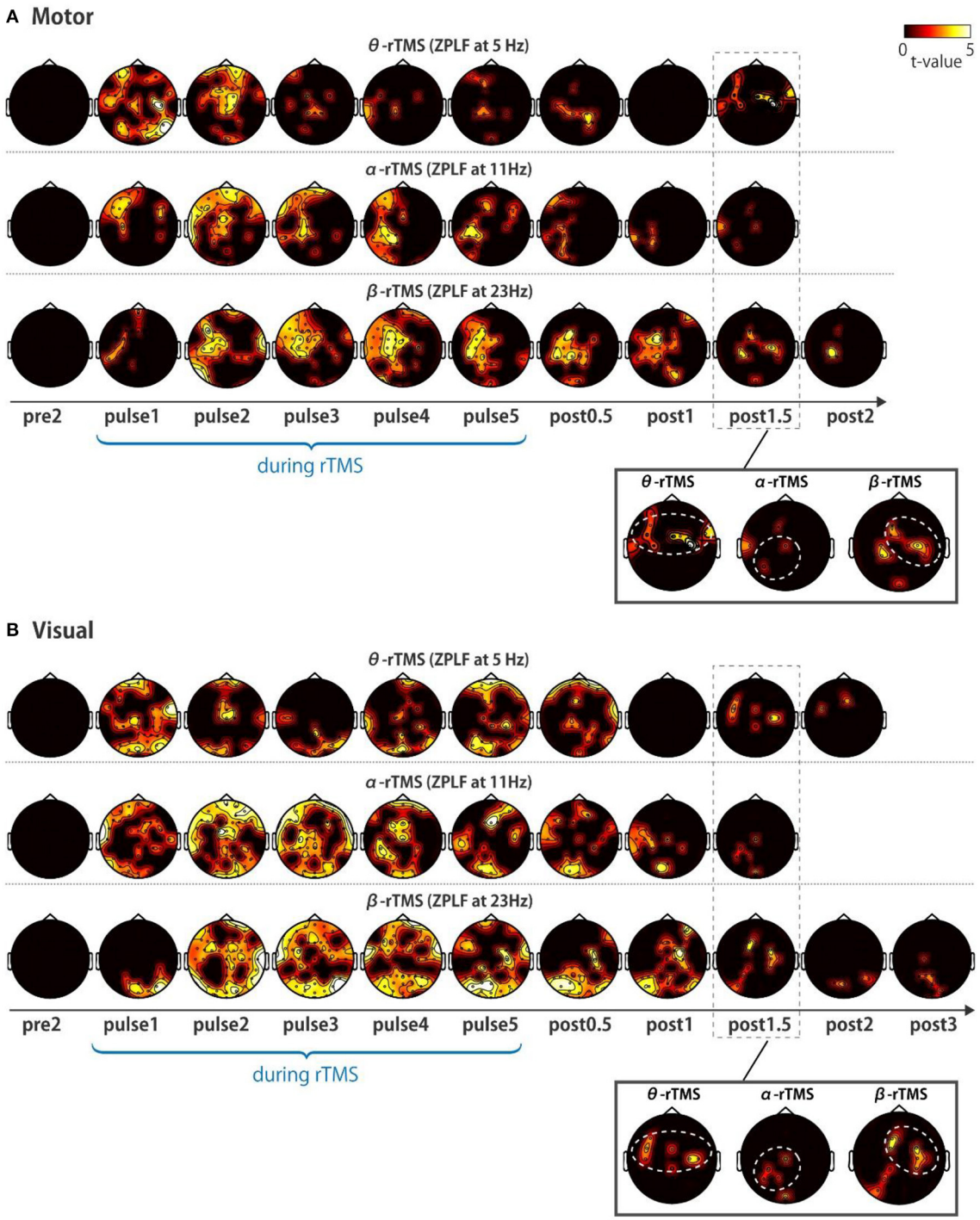

FIGURE 4 | Topographic representation of ZPLF. Each map with *t*-values from two cycles pre-stimulation (pre2) to post-stimulation (post2) indicates significantly larger ZPLF for the motor **(A)**, and for visual stimulation **(B)** than under the sham condition ($p < 0.05$). The phase-locking of theta frequency oscillations in the frontoparietal, alpha frequency in the left occipitoparietal and beta frequency in the right motor areas are highlighted with white dotted circles in the magnified view of post 1.5 cycles.

entraining network activity at the lowest amplitude (Ali et al., 2013).

To our knowledge, the present study is the first to demonstrate frequency-specific phase entrainment of ongoing oscillations that correspond to the natural frequency characteristic of each local area; phase entrainment was observed at specific frequencies depending on the stimulation site. Specifically, local activity during α-rTMS over the visual cortex and β-rTMS over the motor cortex exhibited some signatures of phase entrainment, such as a continuous and gradual increase in phase locking and

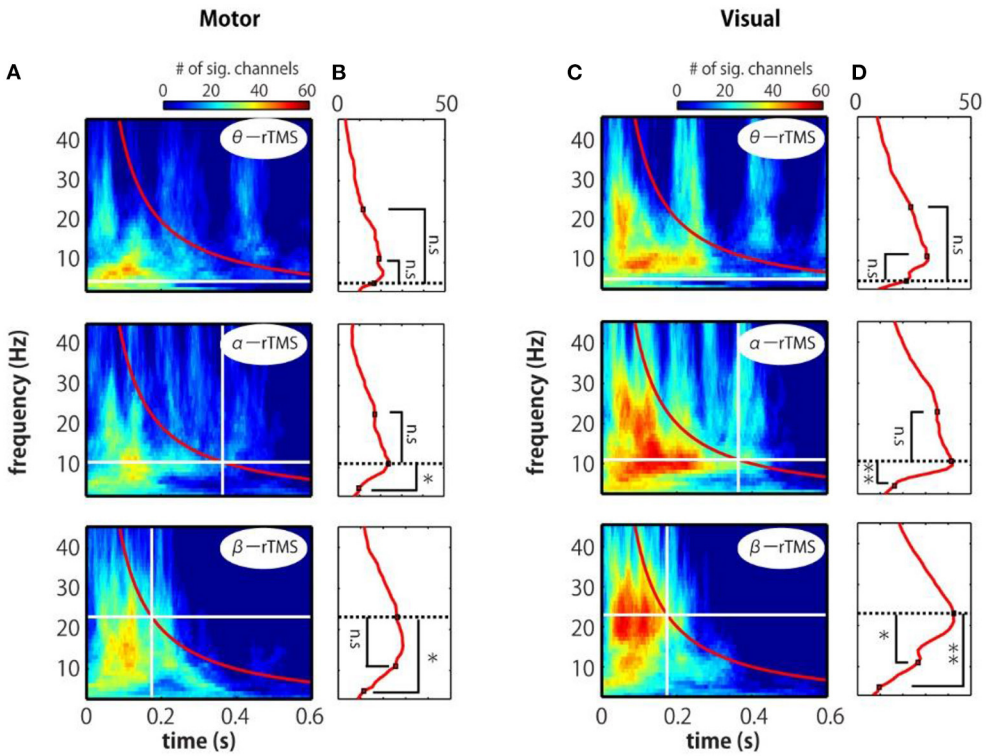

FIGURE 5 | Time-frequency representations of the number of significant electrodes. **(A,C)** Each map indicates the number of significant electrodes, determined by comparing the real and sham conditions. **(B,D)** Mean number of significant electrodes over four cycles at each frequency (red line in panels **A** and **C**). The vertical and horizontal lines indicate the timing of the last pulse and the stimulation frequency. The number of significant electrodes was compared between the stimulation frequency and other frequencies (binomial test; $^{*}p < 0.005$, $^{**}p < 0.001$).

its persistence after the stimulation had ended. The reason why responses to periodic stimulation differed between regions may be because the natural frequency of each region is different, and only stimulation within the synchronization region was effective for entrainment.

Local Entrainment Signatures

Phase entrainment is established by a sequential phase shift (Lakatos et al., 2019) when there is an effective relationship between the rhythm of the oscillating system and the external force, i.e., within the synchronization region. Thus, it is expected that the phase shift induced by a periodic external force of an appropriate intensity (i.e., not too strong and not too weak) and an appropriate frequency (i.e., near-natural frequency) will result in a gradual increase in phase locking across trials (Thut et al., 2011a). In other words, it takes some time for the oscillatory system and the external rhythm to synchronize completely, and as the frequency of the two differs, the time for synchronization may be prolonged or synchronization might not even occur. Furthermore, when the external force is terminated, the entrained oscillations slowly revert to their natural frequencies (Lakatos et al., 2019). However, the stronger the entrainment to the external rhythm was, the more the phase locking at that frequency sustained. Given the progressive increase in the ZPLF in the alpha and beta bands and the sustainability of the effect at these frequencies, α-rTMS and β-rTMS likely match the natural frequencies of the visual and motor cortices, respectively. However, phase locking did not last under other TMS conditions, probably because the stimulation rhythm and the natural frequencies of the motor and visual cortices were significantly different. In this case, it is likely that they will hardly synchronize, or if they do, the oscillations of the cortical system will return to their natural frequencies more rapidly.

Such lasting effects were consistently apparent, even in the individual natural frequencies of alpha-band oscillations. Specifically, participants with an IAF closer to (not equal to) the stimulation frequency (i.e., closer to 11 Hz; see **Supplementary Figure 2**) had longer phase locking after the end of stimulation. Conversely, if the stimulation frequency and intensity are within the appropriate range, i.e., within the synchronization region, it is possible to cause entrainment even if the stimulation frequency and the natural frequency are different.

One might ask why phase locking after sp-TMS lasted longer than that after rTMS; for instance, significant phase locking of motor and visual cortex after sp-TMS lasted for about 150 ms (ca. 3 cycles) or about 200 ms (ca. 2 cycles), peaking at 21 and 8 Hz, respectively (see **Figures 2A,E**). On the other hand, phase locking after β-rTMS and α-rTMS lasted for about 2.5 cycles and about 1.5 cycles, respectively (see **Figures 2D,G**). The effect of sp-TMS is obviously not phase entrainment. Under the sp-TMS condition, neural oscillations

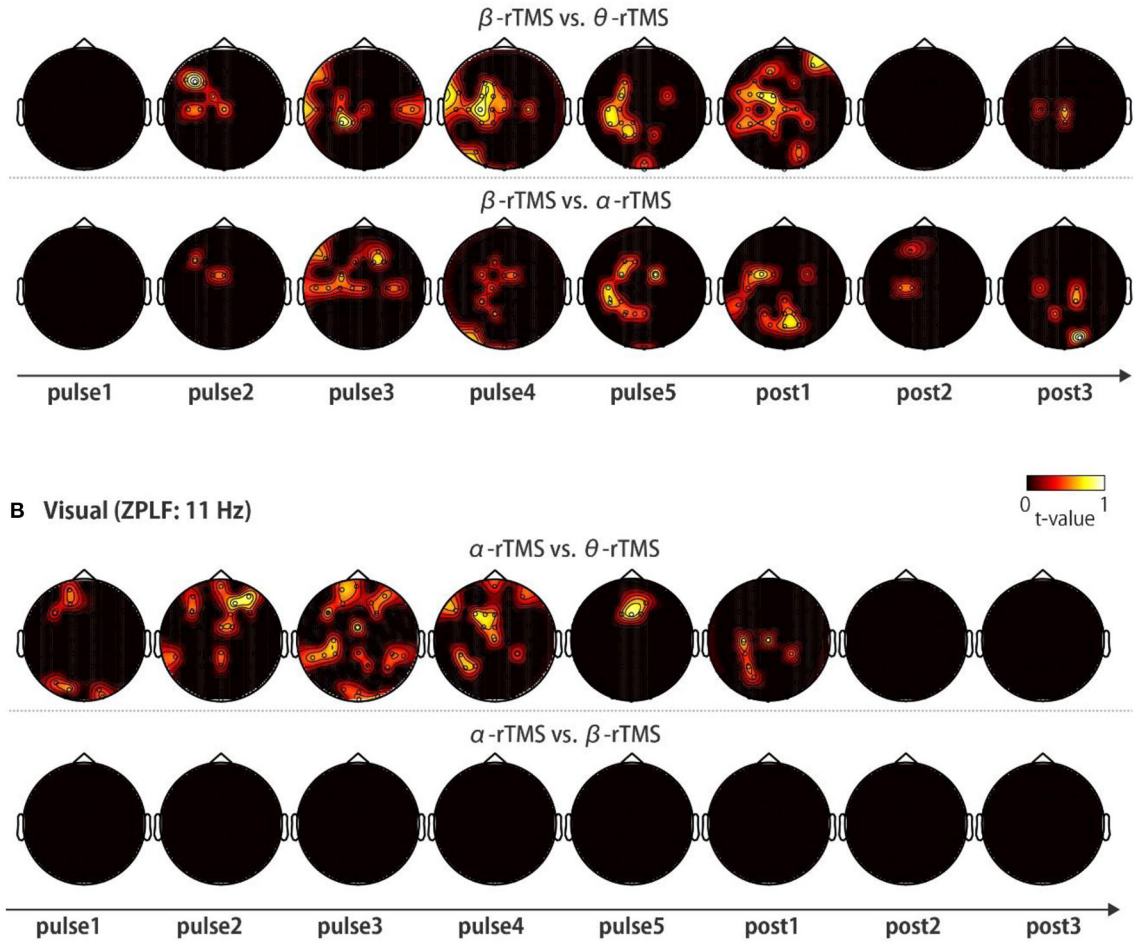

FIGURE 6 | Topographic representation of the ZPLF. Each map with *t*-values was obtained from comparisons of the ZPLF between β-rTMS and the other stimulation frequency, i.e., θ-rTMS (upper panels) and α-rTMS (lower panels) for motor cortex stimulation **(A)**, and between α-rTMS and the other frequency, i.e., θ-rTMS (upper panels) and β-rTMS (lower panels) for visual cortex stimulation **(B)** ($p < 0.05$).

are phase reset once, but they continue to oscillate at the natural frequency (Rosanova et al., 2009; Herring et al., 2015; Lakatos et al., 2019). On the other hand, under the rTMS condition, the ongoing oscillations synchronized with a cycle that was slightly different from the natural frequency. Thus, the prominent frequencies of sp-TMS are different from those of rTMS, and the phase-entrained oscillations return to the intrinsic oscillations a few cycles after rTMS has been terminated. Additionally, we found that phase locking to the theta stimulation frequency was prominent and significant for every TMS pulse (see **Figure 3D**). This may be attributed to either phase reset by every pulse, as observed in sp-TMS, or by repeated evoked neural components (discussed in section Limitations), or both. Taken together, our results suggest that different local areas have their own natural frequency and that rTMS tuned to frequencies close to the natural frequency of those areas can most efficiently modulate their oscillatory dynamics.

Local Entrainment Propagates to Other Areas in a Frequency-Specific Manner

We showed that rhythmic stimulation initially causes phase locking over a wide spatial area and a broad range of frequencies, but that phase locking around the stimulation frequency is predominantly propagated as the pulse train continues. Furthermore, the areas to which phase locking eventually propagated differed for each stimulation frequency. These results suggest that local phase entrainment may lead to global phase entrainment of neural oscillators with the same natural frequency in functionally coupled regions.

Prior MEG/EEG studies have demonstrated that functionally relevant networks are spatially organized through a frequency-specific synchronous oscillating activity (Laufs et al., 2003; Hillebrand et al., 2012; Hipp et al., 2012). Thus, frequency-tuned stimulation to the frequency-specific network node may drive chained phase entrainment of coupled neural oscillators from local to distant brain regions. We anticipated that β-rTMS

over the motor cortex would be particularly effective because the functional connectivity between the motor area and other cortical areas is largely achieved *via* beta-band oscillations (Hillebrand et al., 2012). However, β-rTMS over the motor cortex increased ZPLF in the alpha band as well as that in the beta band (**Figure 5B**, bottom panel). The stimulation frequency used in our study (23 Hz) may have been suboptimal for entraining intrinsic oscillations because the intrinsic Rolandic beta frequency over the sensory-motor strip varies among individuals in a broad range from 14 to 30 Hz. Alternatively, the functional connectivity between the motor cortex and other cortices might be lower than that between the visual cortex and other cortices (Hillebrand et al., 2012). This hypothesis is plausible because the primary motor cortex is the final cortical stage for executing a motor output and hence mainly receives inputs from other brain areas, whereas the primary visual cortex is the first cortical stage to receive visual inputs, and it then sends these signals to functionally connected areas.

Limitations

The number of survived trials (24.8 ± 2.5 trials) per block was relatively small and might have been insufficient to yield significant differences in PLF across conditions. This limitation was due to the already long total length of experiments (4–5 h) and involved a tradeoff with finishing the experiment within a single day to avoid daily variation. Thus, we acknowledge that the small number of trials may have resulted in a statistical type II error; additional trials or samples for conditions or time ranges that were not statistically significant would have overcome this. Furthermore, there were differences in the number of trials that were caused by the removal of artifact-contaminated trials. However, we assessed an unbiased estimator of PLF (i.e., the ZPLF), which corrects for the differences in the number of trials and gives a robust measure for phase locking using even <30 trials, both theoretically and empirically (see **Supplementary Figure 1**). As the mean and variance in the PLF were corrected across stimulation conditions (areas and frequencies), the number of trials used in the current study should not have biased the ZPLF results.

TMS-induced EEG potentials are composed of transcranial- and non-transcranial-neural activity, i.e., those derived from auditory and somatosensory cortices, and various artifacts, including those caused by signal processing limitations such as the wavelet time window and interpolation. Findings on the increases in the ZPLF during stimulation may be partially due to contamination with repeated evoked neural components and repeated artifacts. If an evoked component with a constant latency and polarity is superimposed on ongoing oscillations, the intertrial phase variability of the EEG signals will decrease as if the ongoing oscillation is aligned to a specific phase (Sauseng et al., 2007). Such spurious phase locking can partially be produced by repeated TMS-related artifacts, as well as by repeated TMS-evoked neural activity.

While it is challenging to distinguish phenomena caused by neural phase entrainment, recurring evoked activities, or repetition of artifacts produced by TMS, phase entrainment signatures such as cumulative phase locking and sustained effects after the end of stimulation cannot be explained by the linear sum of single evoked components (Thut et al., 2011a). Moreover, each cortical system has a specific frequency that is particularly effective for entraining the system. Stimulation with such area-specific frequencies resulted in significantly stronger phase locking than other periodic stimulations; these results are thus unlikely to be the result of TMS artifacts and evoked activity. Furthermore, the significant differences in topographic maps revealed by comparing the ZPLF between stimulus conditions imply the existence of frequency-specific oscillatory networks that are not common components, such as auditory responses, somatosensory responses, or various artifacts caused by each TMS pulse.

Nevertheless, non-transcranial periodic sensory inputs derived from somatosensory and auditory systems *via* bone conduction can indirectly entrain the phase of ongoing oscillations of the motor and visual cortex, much like steady-state somatosensory/auditory evoked potentials). Auditory components were partially attenuated by earplugs and compensated for by including a sham control. However, compared with the direct cortical effects, phase entrainment caused by indirect interactions is unlikely or marginal in terms of temporal accuracy of periodicity. In other words, neural responses to sensory inputs were not identical every time, as observed in many event-related studies. Further studies are needed to clarify whether phase entrainment occurs remotely *via* non-transcranial stimulation to different modalities from the stimulation area. It is also an open question as to how much the direct impacts of cortical stimulation can be maximized in the presence of noise by optimizing experimental and analytic methods, including the inclusion of realistic sham control (Ruohonen et al., 2000; Rossi et al., 2007; Hoeft et al., 2008; Conde et al., 2019) and reference methods (Belardinelli et al., 2019). Although contamination by TMS-related artifacts remains a possibility, we believe that the neural phase entrainment observed in this study is more likely to have been caused by the phase entrainment of ongoing oscillations rather than by repetitive evoked and/or artifact components.

Potential Applications

It should be noted that it is impossible to dissociate real and spurious connectivity of two cortical regions through conventional phase synchronization analyses if the two regions are driven by a common source (Kitajo and Okazaki, 2016). However, effective connectivity that is indicative of directional causality between two regions can be probed by local perturbations. We, therefore, propose that rhythmic stimulation can be used to probe causal communication between cortical regions that are fueled by oscillatory activity with a specific frequency.

In addition, the present results suggest that rTMS can be used as an efficient tool to manipulate and measure frequency-specific brain dynamics. This application could provide insights into the causal roles of rhythmic activity in brain networks by looking at the functional outcomes of modulating synchronous neural oscillations that mediate specific cognitive functions.

Several brain disorders show impaired neural oscillations and synchrony within brain networks, including schizophrenia (Lee et al., 2006; Uhlhaas et al., 2006) and stroke (Wu et al.,

2011; Kawano et al., 2017, 2020). Therefore, this rTMS-EEG technique has clinical potential for the treatment of impaired oscillations and synchrony in such brain disorders. For instance, it has been reported that resting-state interhemispheric alpha-band and beta-band phase synchrony networks are impaired in stroke patients (Kawano et al., 2017). The degree of impairment of the interhemispheric phase synchrony networks was highly correlated with the functional independence measure (FIM), which assesses activities of daily living (ADL) in stroke patients. We, therefore, speculate that alpha- or beta-band rTMS targeting interhemispheric synchrony networks can be a potential neurorehabilitation treatment for ADL-related functional brain networks in stroke.

DATA AVAILABILITY STATEMENT

The datasets presented in this article are not readily available because the data that support the findings of this study are available from the corresponding author upon reasonable request. Requests to access the datasets should be directed to kkitajo@nips.ac.jp.

ETHICS STATEMENT

The studies involving human participants were reviewed and approved by the RIKEN Ethics Committee. The patients/participants provided their written informed consent to participate in this study.

AUTHOR CONTRIBUTIONS

KK and TH conceived and designed the experiments. YN and YM prepared the experiments. YO, YN, KK, and TH collected the data. YO and YN analyzed the data. YO, KK, and TH wrote the manuscript. All authors reviewed the manuscript.

FUNDING

This study was supported by JST PRESTO, MEXT Grants-in-Aid for Scientific Research 26282169, 15H05877, and a research grant from TOYOTA Motor Corporation for KK. The funder was not involved in the study design, collection, analysis, interpretation of data, the writing of this article or the decision to submit it for publication.

ACKNOWLEDGMENTS

We are grateful to Shun Sato, Atsushi Negishi, and Hiroyuki Okura for help with data analysis.

SUPPLEMENTARY MATERIAL

The Supplementary Material for this article can be found online at: https://www.frontiersin.org/articles/10.3389/fnhum.2021.608947/full#supplementary-material

REFERENCES

Ali, M. M., Sellers, K. K., and Frohlich, F. (2013). Transcranial alternating current stimulation modulates large-scale cortical network activity by network resonance. *J. Neurosci.* 33, 11262–11275. doi: 10.1523/JNEUROSCI.5867-12.2013

Belardinelli, P., Biabani, M., Blumberger, D. M., Bortoletto, M., Casarotto, S., David, O., et al. (2019). Reproducibility in TMS-EEG studies: a call for data sharing, standard procedures and effective experimental control. *Brain Stimul.* 12, 787–790. doi: 10.1016/j.brs.2019.01.010

Bonnefond, M., and Jensen, O. (2012). Alpha oscillations serve to protect working memory maintenance against anticipated distracters. *Curr. Biol.* 22, 1969–1974. doi: 10.1016/j.cub.2012.08.029

Brainard, D. H. (1997). The psychophysics toolbox. *Spat. Vis.* 10, 433–436. doi: 10.1163/156856897X00357

Conde, V., Tomasevic, L., Akopian, I., Stanek, K., Saturnino, G. B., Thielscher, A., et al. (2019). The non-transcranial TMS-evoked potential is an inherent source of ambiguity in TMS-EEG studies. *Neuroimage* 185, 300–312. doi: 10.1016/j.neuroimage.2018.10.052

Deco, G., and Corbetta, M. (2011). The dynamical balance of the brain at rest. *Neuroscientist* 17, 107–123. doi: 10.1177/1073858409354384

Delorme, A., and Makeig, S. (2004). EEGLAB: an open source toolbox for analysis of single-trial EEG dynamics including independent component analysis. *J. Neurosci. Methods* 134, 9–21. doi: 10.1016/j.jneumeth.2003.10.009

Doesburg, S. M., Roggeveen, A. B., Kitajo, K., and Ward, L. M. (2008). Large-scale gamma-band phase synchronization and selective attention. *Cereb. Cortex* 18, 386–396. doi: 10.1093/cercor/bhm073

Fisher, N. I. (1993). *Statistical Analysis of Circular Data*. New York, NY: Cambridge University Press. doi: 10.1017/CBO9780511564345

Fries, P. (2005). A mechanism for cognitive dynamics: neuronal communication through neuronal coherence. *Trends Cogn. Sci.* 9, 474–480. doi: 10.1016/j.tics.2005.08.011

Glim, S., Okazaki, Y. O., Nakagawa, Y., Mizuno, Y., Hanakawa, T., and Kitajo, K. (2019). Phase-amplitude coupling of neural oscillations can be effectively probed with concurrent TMS-EEG. *Neural Plast.* 2019:6263907. doi: 10.1155/2019/6263907

Herring, J. D., Thut, G., Jensen, O., and Bergmann, T. O. (2015). Attention modulates TMS-locked alpha oscillations in the visual cortex. *J. Neurosci.* 35, 14435–14447. doi: 10.1523/JNEUROSCI.1833-15.2015

Hillebrand, A., Barnes, G. R., Bosboom, J. L., Berendse, H. W., and Stam, C. J. (2012). Frequency-dependent functional connectivity within resting-state networks: an atlas-based MEG beamformer solution. *Neuroimage* 59, 3909–3921. doi: 10.1016/j.neuroimage.2011.11.005

Hipp, J. F., Hawellek, D. J., Corbetta, M., Siegel, M., and Engel, A. K. (2012). Large-scale cortical correlation structure of spontaneous oscillatory activity. *Nat. Neurosci.* 15, 884–890. doi: 10.1038/nn.3101

Hoeft, F., Wu, D. A., Hernandez, A., Glover, G. H., and Shimojo, S. (2008). Electronically switchable sham transcranial magnetic stimulation (TMS) system. *PLoS ONE* 3:e1923. doi: 10.1371/journal.pone.0001923

Kammer, T., Beck, S., Thielscher, A., Laubis-Herrmann, U., and Topka, H. (2001). Motor thresholds in humans: a transcranial magnetic stimulation study comparing different pulse waveforms, current directions and stimulator types. *Clin. Neurophysiol.* 112, 250–258. doi: 10.1016/S1388-2457(00)00513-7

Kawano, T., Hattori, N., Uno, Y., Hatakenaka, M., Yagura, H., Fujimoto, H., et al. (2020). Electroencephalographic phase synchrony index as a biomarker of poststroke motor impairment and recovery. *Neurorehabil. Neural Repair* 34, 711–722. doi: 10.1177/1545968320935820

Kawano, T., Hattori, N., Uno, Y., Kitajo, K., Hatakenaka, M., Yagura, H., et al. (2017). Large-scale phase synchrony reflects clinical status after stroke: an EEG study. *Neurorehabil. Neural Repair* 31, 561–570. doi: 10.1177/1545968317697031

Kawasaki, M., Kitajo, K., and Yamaguchi, Y. (2010). Dynamic links between theta executive functions and alpha storage buffers in

auditory and visual working memory. *Eur. J. Neurosci.* 31, 1683–1689. doi: 10.1111/j.1460-9568.2010.07217.x

Kawasaki, M., Uno, Y., Mori, J., Kobata, K., and Kitajo, K. (2014). Transcranial magnetic stimulation-induced global propagation of transient phase resetting associated with directional information flow. *Front. Hum. Neurosci.* 8:173. doi: 10.3389/fnhum.2014.00173

Kayser, J., and Tenke, C. E. (2006). Principal components analysis of Laplacian waveforms as a generic method for identifying ERP generator patterns: II. Adequacy of low-density estimates. *Clin. Neurophysiol.* 117, 369–380. doi: 10.1016/j.clinph.2005.08.033

Kitajo, K., and Okazaki, Y. O. (2016). TMS-EEG for probing distinct modes of neural dynamics in the human brain. *Adv. Cogn. Neurodyn.* 5, 211–216. doi: 10.1007/978-981-10-0207-6_30

Kleiner, M., Brainard, D., Pelli, D., Ingling, A., Murray, R., and Broussard, C. (2007). What's new in psychtoolbox-3. *Perception* 36, 1–16. doi: 10.1177/03010066070360S101

Klimesch, W., Sauseng, P., and Gerloff, C. (2003). Enhancing cognitive performance with repetitive transcranial magnetic stimulation at human individual alpha frequency. *Eur. J. Neurosci.* 17, 1129–1133. doi: 10.1046/j.1460-9568.2003.02517.x

Klimesch, W., Schack, B., Schabus, M., Doppelmayr, M., Gruber, W., and Sauseng, P. (2004). Phase-locked alpha and theta oscillations generate the P1-N1 complex and are related to memory performance. *Brain Res. Cogn. Brain Res.* 19, 302–316. doi: 10.1016/j.cogbrainres.2003.11.016

Komssi, S., Kahkonen, S., and Ilmoniemi, R. J. (2004). The effect of stimulus intensity on brain responses evoked by transcranial magnetic stimulation. *Hum. Brain Mapp.* 21, 154–164. doi: 10.1002/hbm.10159

Korhonen, R. J., Hernandez-Pavon, J. C., Metsomaa, J., Maki, H., Ilmoniemi, R. J., and Sarvas, J. (2011). Removal of large muscle artifacts from transcranial magnetic stimulation-evoked EEG by independent component analysis. *Med. Biol. Eng. Comput.* 49, 397–407. doi: 10.1007/s11517-011-0748-9

Lachaux, J. P., Rodriguez, E., Van Quyen, M. L., Lutz, A., Martinerie, J., and Varela, F. J. (2000). Studying single-trials of phase synchronous activity in the brain. *Int. J. Bifurcat. Chaos* 10, 2429–2439. doi: 10.1142/S0218127400001560

Lakatos, P., Gross, J., and Thut, G. (2019). A new unifying account of the roles of neuronal entrainment. *Curr. Biol.* 29, R890–R905. doi: 10.1016/j.cub.2019.07.075

Laufs, H., Krakow, K., Sterzer, P., Eger, E., Beyerle, A., Salek-Haddadi, A., et al. (2003). Electroencephalographic signatures of attentional and cognitive default modes in spontaneous brain activity fluctuations at rest. *Proc. Natl. Acad. Sci. U. S. A.* 100, 11053–11058. doi: 10.1073/pnas.1831638100

Lee, S. H., Wynn, J. K., Green, M. F., Kim, H., Lee, K. J., Nam, M., et al. (2006). Quantitative EEG and low resolution electromagnetic tomography (LORETA) imaging of patients with persistent auditory hallucinations. *Schizophr. Res.* 83, 111–119. doi: 10.1016/j.schres.2005.11.025

Litvak, V., Komssi, S., Scherg, M., Hoechstetter, K., Classen, J., Zaaroor, M., et al. (2007). Artifact correction and source analysis of early electroencephalographic responses evoked by transcranial magnetic stimulation over primary motor cortex. *Neuroimage* 37, 56–70. doi: 10.1016/j.neuroimage.2007.05.015

Luczak, A., Bartho, P., and Harris, K. D. (2009). Spontaneous events outline the realm of possible sensory responses in neocortical populations. *Neuron* 62, 413–425. doi: 10.1016/j.neuron.2009.03.014

Maris, E., and Oostenveld, R. (2007). Nonparametric statistical testing of EEG- and MEG-data. *J. Neurosci. Methods* 164, 177–190. doi: 10.1016/j.jneumeth.2007.03.024

Mazaheri, A., and Jensen, O. (2006). Posterior alpha activity is not phase-reset by visual stimuli. *Proc. Natl. Acad. Sci. U. S. A.* 103, 2948–2952. doi: 10.1073/pnas.0505785103

Okazaki, Y. O., Mizuno, Y., and Kitajo, K. (2020). Probing dynamical cortical gating of attention with concurrent TMS-EEG. *Sci. Rep.* 10:4959. doi: 10.1038/s41598-020-61590-2

Oostenveld, R., Fries, P., Maris, E., and Schoffelen, J. M. (2011). FieldTrip: open source software for advanced analysis of MEG, EEG, and invasive electrophysiological data. *Comput. Intell. Neurosci.* 2011:156869. doi: 10.1155/2011/156869

Pelli, D. G. (1997). The VideoToolbox software for visual psychophysics: transforming numbers into movies. *Spat. Vis.* 10, 437–442. doi: 10.1163/156856897X00366

Perrin, F., Pernier, J., Bertrand, O., and Echallier, J. F. (1989). Spherical splines for scalp potential and current density mapping. *Electroencephalogr. Clin. Neurophysiol.* 72, 184–187. doi: 10.1016/0013-4694(89)90180-6

Pikovsky, A., Rosenblum, M., and Kurths, J. (2003). *Synchronization - A Universal Concept in Nonlinear Sciences*. Cambidge: Cambidge University Press.

Rodriguez, E., George, N., Lachaux, J. P., Martinerie, J., Renault, B., and Varela, F. J. (1999). Perception's shadow: long-distance synchronization of human brain activity. *Nature* 397, 430–433. doi: 10.1038/17120

Romei, V., Driver, J., Schyns, P. G., and Thut, G. (2011). Rhythmic TMS over parietal cortex links distinct brain frequencies to global versus local visual processing. *Curr. Biol.* 21, 334–337. doi: 10.1016/j.cub.2011.01.035

Rosanova, M., Casali, A., Bellina, V., Resta, F., Mariotti, M., and Massimini, M. (2009). Natural frequencies of human corticothalamic circuits. *J. Neurosci.* 29, 7679–7685. doi: 10.1523/JNEUROSCI.0445-09.2009

Rossi, S., Ferro, M., Cincotta, M., Ulivelli, M., Bartalini, S., Miniussi, C., et al. (2007). A real electro-magnetic placebo (REMP) device for sham transcranial magnetic stimulation (TMS). *Clin. Neurophysiol.* 118, 709–716. doi: 10.1016/j.clinph.2006.11.005

Ruohonen, J., Ollikainen, M., Nikouline, V., Virtanen, J., and Ilmoniemi, R. J. (2000). Coil design for real and sham transcranial magnetic stimulation. *IEEE Trans. Biomed. Eng.* 47, 145–148. doi: 10.1109/10.821731

Sauseng, P., Klimesch, W., Gruber, W. R., Hanslmayr, S., Freunberger, R., and Doppelmayr, M. (2007). Are event-related potential components generated by phase resetting of brain oscillations? A critical discussion. *Neuroscience* 146, 1435–1444. doi: 10.1016/j.neuroscience.2007.03.014

Sauseng, P., Klimesch, W., Heise, K. F., Gruber, W. R., Holz, E., Karim, A. A., et al. (2009). Brain oscillatory substrates of visual short-term memory capacity. *Curr. Biol.* 19, 1846–1852. doi: 10.1016/j.cub.2009.08.062

Siegel, M., Donner, T. H., and Engel, A. K. (2012). Spectral fingerprints of large-scale neuronal interactions. *Nat. Rev. Neurosci.* 13, 121–134. doi: 10.1038/nrn3137

Smith, S. M., Fox, P. T., Miller, K. L., Glahn, D. C., Fox, P. M., Mackay, C. E., et al. (2009). Correspondence of the brain's functional architecture during activation and rest. *Proc. Natl. Acad. Sci. U. S. A.* 106, 13040–13045. doi: 10.1073/pnas.0905267106

Tallon-Baudry, C., Bertrand, O., Delpuech, C., and Pernier, J. (1996). Stimulus specificity of phase-locked and non-phase-locked 40 Hz visual responses in human. *J. Neurosci.* 16, 4240–4249. doi: 10.1523/JNEUROSCI.16-13-04240.1996

Thut, G., Schyns, P. G., and Gross, J. (2011a). Entrainment of perceptually relevant brain oscillations by non-invasive rhythmic stimulation of the human brain. *Front. Psychol.* 2:170. doi: 10.3389/fpsyg.2011.00170

Thut, G., Veniero, D., Romei, V., Miniussi, C., Schyns, P., and Gross, J. (2011b). Rhythmic TMS causes local entrainment of natural oscillatory signatures. *Curr. Biol.* 21, 1176–1185. doi: 10.1016/j.cub.2011.05.049

Uhlhaas, P. J., Linden, D. E., Singer, W., Haenschel, C., Lindner, M., Maurer, K., et al. (2006). Dysfunctional long-range coordination of neural activity during Gestalt perception in schizophrenia. *J. Neurosci.* 26, 8168–8175. doi: 10.1523/JNEUROSCI.2002-06.2006

Varela, F., Lachaux, J. P., Rodriguez, E., and Martinerie, J. (2001). The brainweb: phase synchronization and large-scale integration. *Nat. Rev. Neurosci.* 2, 229–239. doi: 10.1038/35067550

Wu, W., Sun, J., Jin, Z., Guo, X., Qiu, Y., Zhu, Y., et al. (2011). Impaired neuronal synchrony after focal ischemic stroke in elderly patients. *Clin. Neurophysiol.* 122, 21–26. doi: 10.1016/j.clinph.2010.06.003

Conflict of Interest: The authors declare that the research was conducted in the absence of any commercial or financial relationships that could be construed as a potential conflict of interest.

frontiers in Human Neuroscience

ORIGINAL RESEARCH
published: 15 June 2021
doi: 10.3389/fnhum.2021.696882

Exclusion of the Possibility of "False Ripples" From Ripple Band High-Frequency Oscillations Recorded From Scalp Electroencephalogram in Children With Epilepsy

Katsuhiro Kobayashi, Takashi Shibata, Hiroki Tsuchiya and Tomoyuki Akiyama*

Department of Child Neurology, Okayama University Graduate School of Medicine, Dentistry and Pharmaceutical Sciences and Okayama University Hospital, Okayama, Japan

OPEN ACCESS

Edited by:
Shozo Tobimatsu, Kyushu University, Japan

Reviewed by:
Georgia Ramantani, University Children's Hospital Zurich, Switzerland
Michel Le Van Quyen, INSERM U1127 Institut du Cerveau et de la Moelle épinière (ICM), France

***Correspondence:**
Katsuhiro Kobayashi
k_koba@md.okayama-u.ac.jp

Specialty section:
This article was submitted to Brain Imaging and Stimulation, a section of the journal Frontiers in Human Neuroscience

Received: *18 April 2021*
Accepted: *24 May 2021*
Published: *15 June 2021*

Citation:
Kobayashi K, Shibata T, Tsuchiya H and Akiyama T (2021) Exclusion of the Possibility of "False Ripples" From Ripple Band High-Frequency Oscillations Recorded From Scalp Electroencephalogram in Children With Epilepsy. Front. Hum. Neurosci. 15:696882. doi: 10.3389/fnhum.2021.696882

Aim: Ripple-band epileptic high-frequency oscillations (HFOs) can be recorded by scalp electroencephalography (EEG), and tend to be associated with epileptic spikes. However, there is a concern that the filtration of steep waveforms such as spikes may cause spurious oscillations or "false ripples." We excluded such possibility from at least some ripples by EEG differentiation, which, in theory, enhances high-frequency signals and does not generate spurious oscillations or ringing.

Methods: The subjects were 50 pediatric patients, and ten consecutive spikes during sleep were selected for each patient. Five hundred spike data segments were initially reviewed by two experienced electroencephalographers using consensus to identify the presence or absence of ripples in the ordinary filtered EEG and an associated spectral blob in time-frequency analysis (Session A). These EEG data were subjected to numerical differentiation (the second derivative was denoted as EEG″). The EEG″ trace of each spike data segment was shown to two other electroencephalographers who judged independently whether there were clear ripple oscillations or uncertain ripple oscillations or an absence of oscillations (Session B).

Results: In Session A, ripples were identified in 57 spike data segments (Group A-R), but not in the other 443 data segments (Group A-N). In Session B, both reviewers identified clear ripples (strict criterion) in 11 spike data segments, all of which were in Group A-R ($p < 0.0001$ by Fisher's exact test). When the extended criterion that included clear and/or uncertain ripples was used in Session B, both reviewers identified 25 spike data segments that fulfilled the criterion: 24 of these were in Group A-R ($p < 0.0001$).

Discussion: We have demonstrated that real ripples over scalp spikes exist in a certain proportion of patients. Ripples that were visualized consistently using both ordinary filters

and the EEG″ method should be true, but failure to clarify ripples using the EEG″ method does not mean that true ripples are absent.

Conclusion: The numerical differentiation of EEG data provides convincing evidence that HFOs were detected in terms of the presence of such unusually fast oscillations over the scalp and the importance of this electrophysiological phenomenon.

Keywords: epilepsy, child, scalp EEG, false ripple, high-frequency oscillation (HFO), fast oscillation (FO)

INTRODUCTION

High-frequency oscillations (HFOs) have attracted attention due to their close relationship with epileptogenicity (Jacobs et al., 2010; Akiyama et al., 2011; Frauscher et al., 2017; Thomschewski et al., 2019). Ripple band epileptic HFOs can be recorded from a scalp electroencephalogram (EEG; Kobayashi et al., 2010; Andrade-Valenca et al., 2011; Zelmann et al., 2014; von Ellenrieder et al., 2014; Shibata et al., 2016; Bernardo et al., 2018), and they are suggested to indicate disease severity particularly in children with developmental and epileptic encephalopathy, such as West syndrome (Kobayashi et al., 2011; Kobayashi et al., 2015; van Klink et al., 2016; Nariai et al., 2020). Epileptic ripples, however, tend to be associated with epileptic discharges or spikes, and there is a concern that filtration of steep waveforms such as spikes may cause spurious oscillations or "false ripples" (Bénar et al., 2010). Although time–frequency analysis (TFA) supplements HFO detection, TFA is not a perfect solution because the spectra are based on frequency analysis, and occasionally, noisy and high-frequency spectral blobs may be buried in lower-frequency activities.

We aimed to exclude the possibility of such false ripples from at least some ripples that were observed in association with scalp spikes using numerical differentiation processing of EEG data, which relatively enhances high-frequency signals and does not generate spurious oscillations or ringing, in theory. There are several methods to reduce slow frequency activity (i.e., whitening) to improve HFO detectability, but avoiding the generation of spurious oscillations has not received much attention (Roehri et al., 2016). In the present study, we intended to show that ripples really exist in association with spikes using a straightforward method.

MATERIALS AND METHODS

Background

The derivative of sine waves with a certain frequency yields sine waves that have the identical frequency and a phase shift. Let x denote a sine function of time (t) in the original data:

$$x = A \cdot \sin(2\pi ft)$$

where A and f denote amplitude and frequency, respectively.

Its first derivative is indicated as:

$$x' = 2\pi fA \cdot \cos\left(2\pi ft\right) = 2\pi fA \cdot \sin\left(2\pi ft + \frac{\pi}{2}\right).$$

It indicates the degree of temporal EEG change (denoted herein as EEG' according to the prime notation of derivative). Let $X(t)$ denote EEG potential data at time point t, the numerical approximation of EEG' is defined simply as the potential difference between two adjacent time points divided by the sampling interval (Δt), which was 2 ms in the present study with the sampling rate at 500 Hz, as follows:

$$X'(t) = \{X(t + \Delta t) - X(t)\} / \Delta t.$$

The second derivative is denoted as EEG″, and it is obtained by differentiation of the first derivative, as follows:

$$x'' = -4\pi^2 f^2 A \cdot \sin\left(2\pi ft\right) = 4\pi^2 f^2 A \cdot \sin\left(2\pi ft + \pi\right).$$

Its numerical approximation is indicated as follows:

$$X''(t) = \frac{\left\{X'(t+\Delta t) - X'(t)\right\}}{\Delta t} =$$
$$\{X(t + 2\Delta t) - 2X(t + \Delta t) + X(t)\} / \Delta t^2.$$

This equation denotes a type of finite impulse response (FIR) filter that has only three coefficients, which limit the responses within the duration of these samples ($3\Delta t$ = 6 ms) and, therefore, do not allow ringing or the generation of spurious oscillations with ≥4 cycles. This is because the duration of four oscillations with a frequency of 200 Hz (wavelength 5 ms) is 20 ms.

Figure 1 shows a representative example of ringing at the arrows that is caused by a type of FIR filter based on application of the discrete Fourier transform, zeroing parameter values below 80 Hz, and the subsequent inverse Fourier transform. Note that the EEG' and EEG″ traces do not cause ringing. Conversely, **Figure 2** shows a spike that was recorded from a representative pediatric patient with focal epilepsy and was processed similarly, as follows: ripple oscillations are clearly observed in the FIR filtered trace and the EEG″ trace. Therefore, it is evident that ripples can be found in at least some EEG″ traces without concerns about the possibility of false ripples. However, it is still unknown how efficient it is to detect ripples particularly from routine, possibly noisy, pediatric EEG records. The present study was designed to clarify this issue.

Subjects

Fifty pediatric patients who visited Okayama University Hospital from January 2017 to August 2019 and who were 3–13 years old at the time of the scalp EEG recording that showed frequent spikes with a presumed focal origin during sleep were enrolled into the study. The participants were limited to those who had

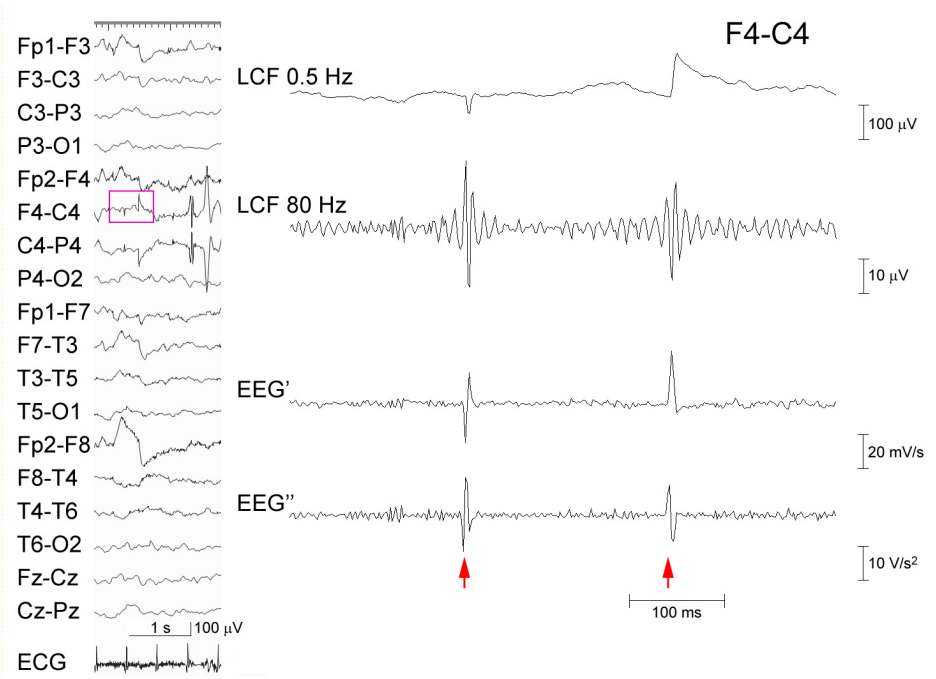

FIGURE 1 | Processing of EEG artifacts. Two artifacts that were caused by poor electrode contact at C4 (left panel). The EEG data at F4–C4 (pink rectangle) that were recorded from a 5-year-old boy is temporally expanded (right panel) (abrupt potential jumps at arrows). From the top: EEG processed with an FIR low-cut frequency (LCF) filter at 0.5 Hz; EEG LCF filtered at 80 Hz showing spurious oscillations; EEG'; and EEG″ showing no ringing. The corresponding time–frequency analysis is shown in **Supplementary Figure 1A**.

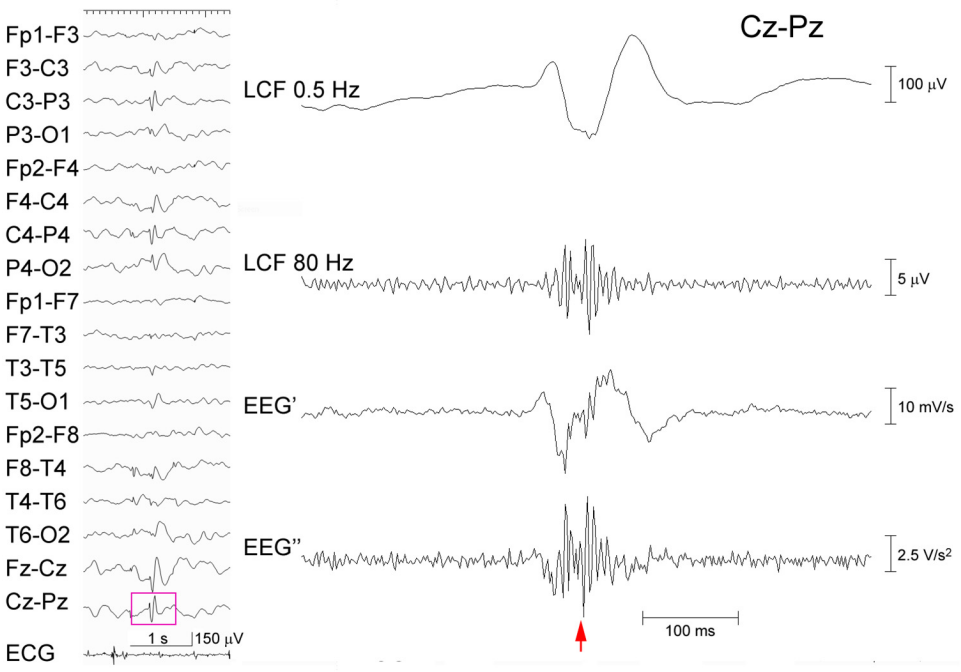

FIGURE 2 | Processing of an EEG epileptic discharge. A spike-wave recorded from a 5-year-old boy (left panel). The EEG data (pink rectangle) at Cz–Pz including the spike (arrow) is temporally expanded and processed (right panel) as in **Figure 1**. Ripple oscillations can be seen in both the trace LCF filtered at 80 Hz and the EEG″ trace. The corresponding time–frequency analysis is shown in **Supplementary Figure 1B**.

not yet undergone an EEG analysis. Children with such an EEG abnormality pattern were selected because they tend to show ripples in association with spikes (Ohuchi et al., 2019). The demographic data of these patients are shown in **Table 1**.

This study was approved by the Okayama University Ethics Committee (approval No. 1911-024).

Methods of Analysis

Electroencephalography data were recorded with a sampling rate at 500 Hz using a Nihon-Kohden (Tokyo, Japan) Neurofax system, which used a low-cut frequency filter at 0.08 Hz before digital sampling. The international 10–20 electrode system was used. Computation was performed using a program written in-house for MATLAB (version 7.5.0; MathWorks Inc., Natick, MA, United States).

For each participant, ten consecutive spikes were selected with a minimal interval of 1.5 s. Five hundred data segments with a duration of 1.4 s, among which each segment including a spike at the mid-point, were initially analyzed in a single bipolar channel that showed clear spike morphology; these spike-data were processed using a combination of TFA and an FIR low-cut filter at 80 Hz. In each spike-data segment, after discarding the beginning and ending 400-ms part, the middle 600-ms part was reviewed by two experienced electroencephalographers using consensus to identify the presence or absence of ripples that had $\geq$4 oscillations and an amplitude that was clearly above the background signal according to Andrade-Valenca et al. (2011). In this study, the ripple-associated spectral blobs should have peak power $\geq$0.05 μV^2 in TFA (Session A).

These EEG data segments were subjected to numerical differentiation as explained above. The EEG″ trace of the middle part of each spike-data segment was presented to two other electroencephalographers without information about the results in Session A. The order of presentation was randomized. The latter electroencephalographers reviewed each EEG″ trace independently to judge for the presence of clear ripple oscillations, uncertain oscillations, or the absence of oscillations (Session B).

Statistical Analysis

In the judgments in Session B, the strict criterion for ripples was defined to include only clear ripples, and the extended criterion included clear and/or uncertain ripples. The judgments in Session B were compared to the initial categorization in Session A using Fisher's exact test.

RESULTS

In Session A, ripples were identified in 57 spike-data segments (Group A-R) that were recorded from 14 children and not in the other 443 segments (Group A-N), as shown in **Table 1**. Ripples were predominantly observed in patients with focal epilepsy that evolved to epileptic encephalopathy with continuous spike-and-wave during sleep or related disorders. Conversely, ripples were rare and variable in focal epilepsies, and lacking in patients with spikes with no clinical seizures.

In Session B, as indicated in **Table 2**, both reviewers consistently found clear ripples (strict criterion) in the 11 spike-data segments, which were all included in Group A-R and not in Group A-N ($p < 0.0001$; sensitivity 19.3%, specificity 100%). For the inter-rater agreement between the two reviewers in Session B, the Kappa coefficient was 0.331.

When the extended criterion of ripples was used in Session B, there were 25 spike-data segments, which fulfilled the criterion and was agreed-upon by the two reviewers; 24 of these were in Group A-R and the remaining one was in the Group A-N ($p < 0.0001$; sensitivity 42.1%, specificity 99.8%; Kappa coefficient of the inter-rater agreement 0.391). There was only one spike-segment that was categorized as Group A-N for Session A and fulfilled the extended criterion in Session B (judged to show clear ripples by one reviewer and to show uncertain ripples by the other reviewer). In this segment, there were considerable background oscillations in the initial FIR filtered EEG in Session A, and the background activity looked irregular and noise-like on the EEG″ trace, showing discernible ripples in Session B (**Figure 3**). Spike-data surrounded by heavy background noise signals tended to result in failure of ripple identification in Session B (**Figure 4**).

DISCUSSION

We have demonstrated that real ripples over scalp spikes exist in some patients, and that these real ripples can be distinguished from false ripples using numerical differentiation of EEG data. The possibility of false ripples might make researchers uneasy, but the present findings will form the basis to study scalp HFOs particularly in children with developmental and epileptic encephalopathy. There should be true ripples that have a relatively low amplitude in a noisy background, and thus, cannot be clearly depicted in the EEG″ traces. Ripples that are visualized consistently using both ordinary filters and the EEG″ method should be true, but failure to clarify the ripples using the EEG″ method does not mean that the true ripples are not present.

Although the combination of TFA and EEG filtering that was used in Session A is a standard method to identify HFOs, true HFOs that are buried in slower potentials may not always build isolated peaks, and filtration may generate redundant oscillations at spikes and in the background. As illustrated in **Figure 3**, the spike that showed ripples based on the extended criterion in Session B and no ripples in Session A may include some sort of true oscillations that were not easily discernible from the noisy background in the ordinary-filtered EEG. The EEG″ traces that were shown to have a high specificity may supplement these methods to recognize true ripples. The modest sensitivity of the EEG″ technique may be due to the effects of confounding background noise, as shown in **Figure 4**. There is no single perfect analysis method, and we do not have the ground truth or ideal baseline data to assess the true performance of each available method. We hope that future studies using simulated data will help to solve these issues.

The 500 spikes that were used in the present study were not intentionally selected using previous information on ripples and the background noise level. Spikes in epileptic encephalopathy

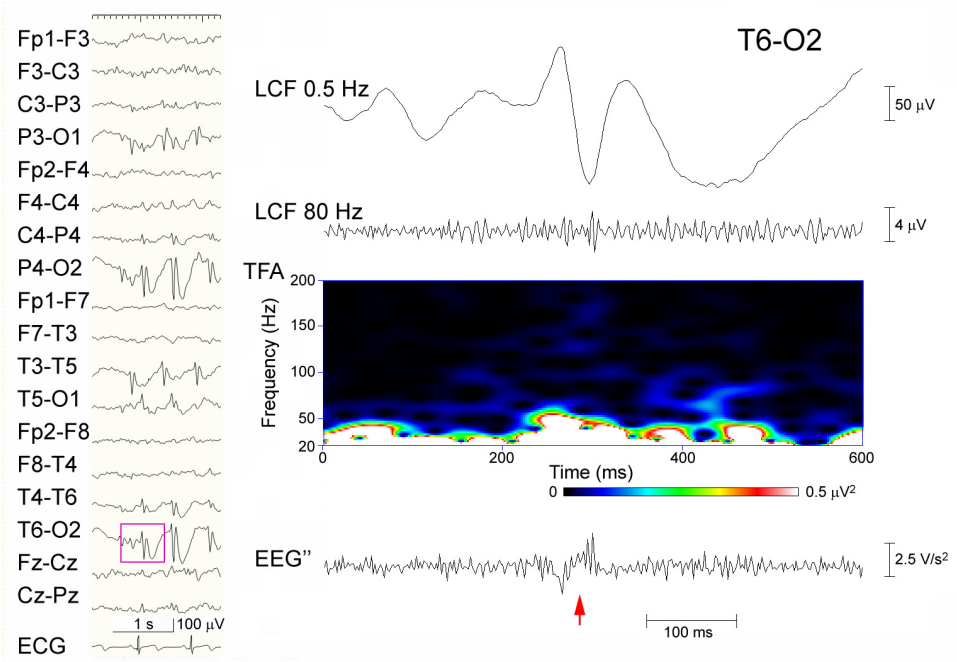

FIGURE 3 | Discordant judgment in an epileptic discharge (possible ripples that were not identified in Session A but identified using the extended criterion in Session B). Spike-waves are dominant over the right occipital region that was recorded from an 8-year-old girl (left panel), and the part of EEG data (pink rectangle) at T6–O2 including the spike (arrow) is temporally expanded and processed (right panel). From the top: filtered at 0.5 Hz; filtered at 80 Hz with background oscillations; time–frequency analysis (TFA) lacking clear spectral blobs; and the EEG″ trace showing spike-associated oscillations surrounded by noise-like background activity. In Session A, this spike was categorized as devoid of ripples, whereas in Session B, it was judged to include clear ripple oscillations by one reviewer and to include uncertain oscillations by the other.

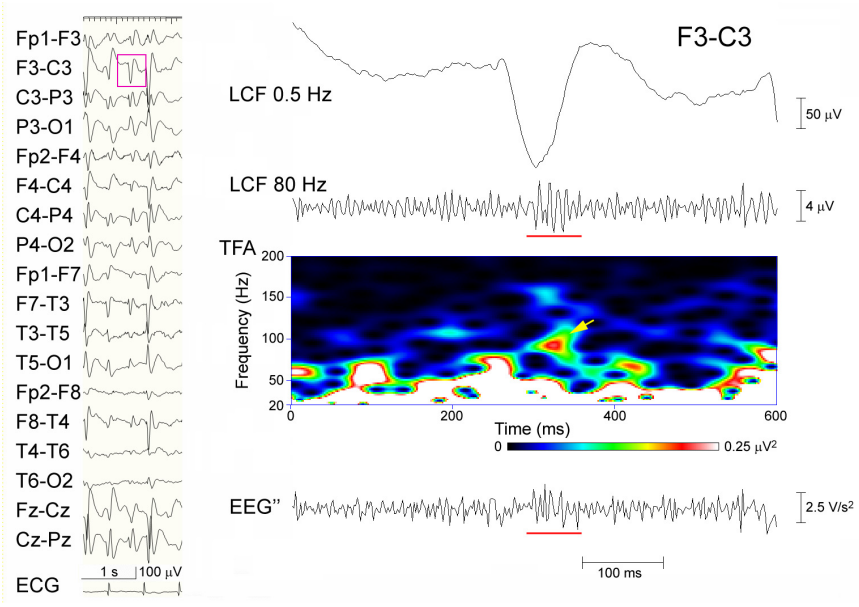

FIGURE 4 | A representative failure to detect ripples in Session B. Spike-waves are almost generalized in a sleep EEG that was recorded from an 8-year-old girl (left panel), and the EEG data (pink rectangle) at F3–C3 including the spike is temporally expanded and processed (right panel). From the top: filtered at 0.5 Hz; filtered at 80 Hz with ripple oscillations (underline) and background noise; TFA showing a clear spectral blob (arrow); and the EEG″ trace showing some spike-associated oscillations (underline) buried in noise-like background activity. In Session A, this spike was categorized as having ripples, whereas in Session B, neither of the reviewers judged it to include ripple oscillations.

TABLE 1 | Demographic data of the patients.

Age		**7.93 ± 2.53 years**				
		Number of pts.	**Number of spikes with ripples**	**Mean peak frequency of ripple-blobs (Hz)**	**Mean peak power of ripple-blobs (μV^2)**	**Mean duration of ripples (ms)**
Total		50 [14]	57 (1.14)	114.4 ± 18.6 {80.1–160.2}	0.46 ± 0.62 {0.05–3.77}	98.8 ± 28.6 {52–186}
Sex						
	Male	32 [7]	22 (0.69)	110.2 ± 17.1 {82.0–140.6}	0.29 ± 0.21 {0.10–0.78}	97.8 ± 34.5 {52–186}
	Female	18 [7]	35 (1.94)	117.1 ± 19.2 {80.1–160.2}	0.56 ± 0.76 {0.05–3.77}	99.4 ± 24.7 {58–146}
Disorder						
	Childhood epilepsy with centrotemporal spikes	6 [2]	2 (0.33)	98.7 {87.9, 109.4}	0.19 {0.13, 0.25}	96 {88, 104}
	Panayiotopoulos syndrome	3 [0]	0 (0)	N/A	N/A	N/A
	Epilepsy with coexisting generalized and focal abnormalities	2 [0]	0 (0)	N/A	N/A	N/A
	Focal epilepsy evolving to epileptic encephalopathy with continuous spike-and-wave during sleep or related disorder	8 [7]	41 (5.13)	117 ± 18.8 {80.1–160.2}	0.50 ± 0.71 {0.05–3.77}	95.5 ± 28.5 {52–186}
	Other focal epilepsies with various etiologies	21 [5]	14 (0.67)	109.2 ± 17.4 {82–140.6}	0.37 ± 0.27 {0.12–1.02}	109 ± 29.4 {64–172}
	EEG spikes without clinical seizures	10 [0]	0 (0)	N/A	N/A	N/A

pt(s), patient(s); (), group mean; [], pts having at least one spike with ripples; {}, range; N/A, not applicable; ±, mean and standard deviation.

TABLE 2 | Identification of ripples in Sessions A and B.

			Session A: ripples identified by a combination of filtered EEG and time-frequency analysis		**Sum**	**Statistics (Fisher's exact test)**
			Present (Group A-R)	**Absent (Group A-N)**		
Session B: ripples identified in EEG″ traces	Strict criterion (clear ripples alone)	Detected	11	0	11	$p < 0.0001$
		Not detected	46	443	489	
	Extended criterion (clear and/or uncertain ripples)	Detected	23	1	24	$p < 0.0001$
		Not detected	34	442	476	
Sum			57	443	500	

with continuous spike-and-wave during sleep and related disorders tended to have associated ripples in the present study, but ripple-laden spikes were rare and variable in children with other types of disorders, as already reported (Ohuchi et al., 2019). The presence of only 57 spikes with ripples in Group A-R suggests that ripples are generally rare events that should have a special meaning.

The EEG' and EEG″ traces can be regarded as FIR-filtered EEG data, but they have particular meanings. EEG data are summed potentials that are generated by many neurons. The EEG' traces that show the degree of instantaneous change in the EEG may represent the driving forces behind the EEG changes, which may reflect the net amount of synaptic input at the moment more so than the raw EEG data. The EEG″ traces show the tendency for changes in the EEG' or possibly the direction of EEG changes that are taking place. This type of viewpoint for EEG is expected to increase the utility of EEG.

There are limitations and unsolved questions in the present study. The number of spike samples, particularly spikes with ripples, was not large, and we need to involve much more spike- and non-spike-data to clarify the effects of the EEG″ method. We used a Δt of 2 ms because the sampling rate was 500 Hz, but the selection of Δt may influence the results. We have not yet determined the best Δt for EEG″. Additionally, we have not compared the effects of various options for the numerical

approximation of the second derivative. We should address these questions in the future.

The inter-rater agreement in Session B was modest, suggesting that experience is needed to share the common knowledge and observe EEG″ traces. The EEG″ method was new to the reviewers, and establishment of a consensus standard regarding its interpretation is another future issue. This is why judgment was not based on consensus in Session B, which is in contrast to Session A that involved the already established analysis method, i.e., the combination of TFA and an FIR. When reviewers are accustomed to the EEG″ method, the quality of identification may improve.

Roehri et al. (2016) investigated several methods of whitening, including the first derivative, but not the second derivative, to improve the detectability of HFOs. The present EEG″ method is very simple, and there might be more sophisticated methods that have better performance in detecting HFOs compared to EEG″. Excluding the possibility of "false ripples," however, has not been rigorously pursued to the best of our knowledge. If this EEG″ method is used as an adjunctive tool in addition to the information about ordinary filtered or whitened EEG, then the preciseness with which the ripples may be identified will be improved. Despite all these limitations, we hope to add the numerical differentiation of EEG as another way to review EEGs that include spike-associated ripples and other types of high frequencies. Because there are pitfalls of bias in the detection of scalp HFOs (Gerner et al., 2020), we would like to refine the EEG differentiation method to develop a methodology to avoid such pitfalls and to make scalp HFOs a truly useful biomarker in the future.

CONCLUSION

Numerical differentiation of EEG data would provide proof for the presence of such unusually fast oscillations or ripples over the scalp and support the importance of this electrophysiological phenomenon.

DATA AVAILABILITY STATEMENT

The raw data supporting the conclusions of this article will be made available by the authors, without undue reservation.

ETHICS STATEMENT

The studies involving human participants were reviewed and approved by the Okayama University Ethics Committee (approval No. 1911-024). Written informed consent from the participants' legal guardian/next of kin was not required to participate in this study in accordance with the national legislation and the institutional requirements.

AUTHOR CONTRIBUTIONS

KK designed the methodology, conducted the analysis, and wrote the manuscript. KK and TA served as EEG reviewers in Session A. TS and HT reviewed the data in Session B. All authors contributed to the article and approved the submitted version.

FUNDING

KK was supported by Grants-in-Aid from the Ministry of Education, Culture, Sports, Science and Technology, Japan (MEXT KAKENHI Grant Number 15H05874 and JSPS KAKENHI Grant Number 21K07754) and by Health and Labour Research Grants from the Ministry of Health, Labour and Welfare, Japan (Research program on rare and intractable diseases, Grant number JPMH20FC1039).

ACKNOWLEDGMENTS

We thank Professor Jean Gotman and Dr. Nicolás von Ellenrieder at the Montreal Neurological Institute, McGill University, Canada for their important suggestions.

SUPPLEMENTARY MATERIAL

The Supplementary Material for this article can be found online at: https://www.frontiersin.org/articles/10.3389/fnhum.2021.696882/full#supplementary-material

Supplementary Figure 1 | Time–frequency analysis of sample EEG data. **(A)** A spectral panel including two artifacts (arrowhead and arrow) that were produced from the EEG data at F4–C4, which is shown in **Figure 1**. **(B)** Spectral data including a spike with ripples (arrow) that were produced from the EEG data at Cz–Pz, which is shown in **Figure 2**.

REFERENCES

Akiyama, T., McCoy, B., Go, C. Y., Ochi, A., Elliott, I. M., Akiyama, M., et al. (2011). Focal resection of fast ripples on extraoperative intracranial EEG improves seizure outcome in pediatric epilepsy. *Epilepsia* 52, 1802–1811. doi: 10.1111/j.1528-1167.2011.03199.x

Andrade-Valenca, L. P., Dubeau, F., Mari, F., Zelmann, R., and Gotman, J. (2011). Interictal scalp fast oscillations as a marker of the seizure onset zone. *Neurology* 77, 524–531. doi: 10.1212/WNL.0b013e318228bee2

Bénar, C. G., Chauvière, L., Bartolomei, F., and Wendling, F. (2010). Pitfalls of high-pass filtering for detecting epileptic oscillations: a technical note on "false" ripples. *Clin. Neurophysiol.* 121, 301–310. doi: 10.1016/j.clinph.2009.10.019

Bernardo, D., Nariai, H., Hussain, S. A., Sankar, R., Salamon, N., Krueger, D. A., et al. (2018). Visual and semi-automatic non-invasive detection of interictal fast ripples: a potential biomarker of epilepsy in children with tuberous sclerosis complex. *Clin. Neurophysiol.* 129, 1458–1466. doi: 10.1016/j.clinph.2018.03.010

Frauscher, B., Bartolomei, F., Kobayashi, K., Cimbalnik, J., van 't Klooster, M. A., Rampp, S., et al. (2017). High-frequency oscillations: the state of clinical research. *Epilepsia* 58, 1316–1329. doi: 10.1111/epi.13829

Gerner, N., Thomschewski, A., Marcu, A., Trinka, E., and Höller, Y. (2020). Pitfalls in scalp high-frequency oscillation detection from long-term

EEG monitoring. *Front. Neurol.* 11:432. doi: 10.3389/fneur.2020.00432

Jacobs, J., Zijlmans, M., Zelmann, R., Chatillon, C. E., Hall, J., Olivier, A., et al. (2010). High-frequency electroencephalographic oscillations correlate with outcome of epilepsy surgery. *Ann. Neurol.* 67, 209–220. doi: 10.1002/ana.21847

Kobayashi, K., Akiyama, T., Oka, M., Endoh, F., and Yoshinaga, H. (2015). A storm of fast (40-150 Hz) oscillations during hypsarrhythmia in West syndrome. *Ann. Neurol.* 77, 58–67. doi: 10.1002/ana.24299

Kobayashi, K., Watanabe, Y., Inoue, T., Oka, M., Yoshinaga, H., and Ohtsuka, Y. (2010). Scalp-recorded high-frequency oscillations in childhood sleep-induced electrical status epilepticus. *Epilepsia* 51, 2190–2194. doi: 10.1111/j.1528-1167.2010.02565.x

Kobayashi, K., Yoshinaga, H., Toda, Y., Inoue, T., Oka, M., and Ohtsuka, Y. (2011). High-frequency oscillations in idiopathic partial epilepsy of childhood. *Epilepsia* 52, 1812–1819. doi: 10.1111/j.1528-1167.2011.03169.x

Nariai, H., Hussain, S. A., Bernardo, D., Motoi, H., Sonoda, M., Kuroda, N., et al. (2020). Scalp EEG interictal high frequency oscillations as an objective biomarker of infantile spasms. *Clin. Neurophysiol.* 131, 2527–2536. doi: 10.1016/j.clinph.2020.08.013

Ohuchi, Y., Akiyama, T., Matsuhashi, M., and Kobayashi, K. (2019). High-frequency oscillations in a spectrum of pediatric epilepsies characterized by sleep-activated spikes in scalp EEG. *Clin. Neurophysiol.* 130, 1971–1980. doi: 10.1016/j.clinph.2019.08.001

Roehri, N., Lina, J. M., Mosher, J. C., Bartolomei, F., and Benar, C. G. (2016). Time-frequency strategies for increasing high-frequency oscillation detectability in intracerebral EEG. *IEEE Trans. Biomed. Eng.* 63, 2595–2606. doi: 10.1109/TBME.2016.2556425

Shibata, T., Yoshinaga, H., Akiyama, T., and Kobayashi, K. (2016). A study on spike focus dependence of high-frequency activity in idiopathic focal epilepsy in childhood. *Epilepsia Open* 1, 121–129. doi: 10.1002/epi4.12014

Thomschewski, A., Hincapié, A. S., and Frauscher, B. (2019). Localization of the epileptogenic zone using high frequency oscillations. *Front. Neurol.* 10:94. doi: 10.3389/fneur.2019.00094

van Klink, N. E., van't Klooster, M. A., Leijten, F. S., Jacobs, J., Braun, K. P., and Zijlmans, M. (2016). Ripples on rolandic spikes: a marker of epilepsy severity. *Epilepsia* 57, 1179–1189. doi: 10.1111/epi.13423

von Ellenrieder, N., Beltrachini, L., Perucca, P., and Gotman, J. (2014). Size of cortical generators of epileptic interictal events and visibility on scalp EEG. *Neuroimage* 94, 47–54. doi: 10.1016/j.neuroimage.2014.02.032

Zelmann, R., Lina, J. M., Schulze-Bonhage, A., Gotman, J., and Jacobs, J. (2014). Scalp EEG is not a blur: it can see high frequency oscillations although their generators are small. *Brain Topogr.* 27, 683–704. doi: 10.1007/s10548-013-0321-y

Conflict of Interest: The authors declare that the research was conducted in the absence of any commercial or financial relationships that could be construed as a potential conflict of interest.

frontiers in Human Neuroscience

METHODS
published: 21 June 2021
doi: 10.3389/fnhum.2021.691821

Prefrontal Theta-Phase Synchronized Brain Stimulation With Real-Time EEG-Triggered TMS

Pedro Caldana Gordon[1,2], Sara Dörre[1,2], Paolo Belardinelli[1,2,3], Matti Stenroos[4], Brigitte Zrenner[1,2], Ulf Ziemann[1,2] and Christoph Zrenner[1,2]*

[1] Department of Neurology and Stroke, University of Tübingen, Tübingen, Germany, [2] Hertie Institute for Clinical Brain Research, University of Tübingen, Tübingen, Germany, [3] CIMeC, Center for Mind/Brain Sciences, University of Trento, Rovereto, Italy, [4] Department of Neuroscience and Biomedical Engineering, Aalto University School of Science, Espoo, Finland

OPEN ACCESS

Edited by:
Shozo Tobimatsu,
Kyushu University, Japan

Reviewed by:
Keiichi Kitajo,
National Institute for Physiological Sciences (NIPS), Japan
Takashi Hanakawa,
Kyoto University, Japan
Andrea Pigorini,
University of Milan, Italy

***Correspondence:**
Ulf Ziemann
ulf.ziemann@uni-tuebingen.de

Specialty section:
This article was submitted to Brain Imaging and Stimulation, a section of the journal Frontiers in Human Neuroscience

Received: 07 April 2021
Accepted: 27 May 2021
Published: 21 June 2021

Citation:
Gordon PC, Dörre S, Belardinelli P, Stenroos M, Zrenner B, Ziemann U and Zrenner C (2021) Prefrontal Theta-Phase Synchronized Brain Stimulation With Real-Time EEG-Triggered TMS. Front. Hum. Neurosci. 15:691821. doi: 10.3389/fnhum.2021.691821

Background: Theta-band neuronal oscillations in the prefrontal cortex are associated with several cognitive functions. Oscillatory phase is an important correlate of excitability and phase synchrony mediates information transfer between neuronal populations oscillating at that frequency. The ability to extract and exploit the prefrontal theta rhythm in real time in humans would facilitate insight into neurophysiological mechanisms of cognitive processes involving the prefrontal cortex, and development of brain-state-dependent stimulation for therapeutic applications.

Objectives: We investigate individual source-space beamforming-based estimation of the prefrontal theta oscillation as a method to target specific phases of the ongoing theta oscillations in the human dorsomedial prefrontal cortex (DMPFC) with real-time EEG-triggered transcranial magnetic stimulation (TMS). Different spatial filters for extracting the prefrontal theta oscillation from EEG signals are compared and additional signal quality criteria are assessed to take into account the dynamics of this cortical oscillation.

Methods: Twenty two healthy participants were recruited for anatomical MRI scans and EEG recordings with 18 composing the final analysis. We calculated individual spatial filters based on EEG beamforming in source space. The extracted EEG signal was then used to simulate real-time phase-detection and quantify the accuracy as compared to post-hoc phase estimates. Different spatial filters and triggering parameters were compared. Finally, we validated the feasibility of this approach by actual real-time triggering of TMS pulses at different phases of the prefrontal theta oscillation.

Results: Higher phase-detection accuracy was achieved using individualized source-based spatial filters, as compared to an average or standard Laplacian filter, and also by detecting and avoiding periods of low theta amplitude and periods containing a phase reset. Using optimized parameters, prefrontal theta-phase synchronized TMS of DMPFC was achieved with an accuracy of ±55°.

Conclusion: This study demonstrates the feasibility of triggering TMS pulses during different phases of the ongoing prefrontal theta oscillation in real time. This method is relevant for brain state-dependent stimulation in human studies of cognition. It will also enable new personalized therapeutic repetitive TMS protocols for more effective treatment of neuropsychiatric disorders.

Keywords: EEG, TMS, prefrontal cortex, brain-state dependent stimulation, non-invasive brain stimulation, theta rhythm, brain oscillations

INTRODUCTION

Synchronous oscillatory activity between neuronal populations allows information exchange and the strengthening of connections through neuroplasticity (Harris et al., 2003; Buzsaki and Draguhn, 2004). These neuronal oscillations are ubiquitous in the functioning brain cortex and can be observed with the aid of several tools, including non-invasive recordings such as electroencephalography (EEG) and magnetoencephalography. Different oscillatory patterns predominate in different cortical areas and are modulated by the individual's states and behavior, suggesting that each oscillatory mode has specific physiological functions. Specifically, oscillatory activity in the theta frequency band (4–7 Hz), which can be found in brain areas such as the prefrontal cortex and hippocampus, has been correlated with several cognitive processes, making it a phenomenon of interest for developing diagnostics and treatment of neuropsychiatric disorders (Lisman and Buzsaki, 2008; Sauseng et al., 2010; Cavanagh and Frank, 2014).

Advances on understanding the relationship between cognition and neuronal oscillations in the theta band have mainly relied on studies in animal models. Early research has demonstrated spatial memory deficits following the loss of theta rhythm in the hippocampus (Winson, 1978). Moreover, the hippocampal theta oscillation has been found to be significantly phase-locked to the neuronal firing of large populations of neurons in the medial prefrontal cortex (Siapas et al., 2005), with different phases corresponding to different states of excitability. Accordingly, neuronal spiking has been observed predominantly in specific theta-phases depending on the brain region (Klausberger et al., 2004; Fujisawa and Buzsaki, 2011), with stimulation applied in different phases of theta oscillation yielding differential profiles of neuroplasticity (Pavlides et al., 1988; Holscher et al., 1997; Hyman et al., 2003). Together, these observations support the notion that different phases of theta oscillations represent distinct excitability states of neuronal populations, which would enable effective neuronal communication and different opportunities of plasticity induction (for comprehensive review see Fries, 2015). Studies in human subjects have confirmed the presence of a marked theta rhythm in the frontal midline EEG channels, originating from the anterior part of the superior frontal gyrus and anterior cingulate cortex (Ishii et al., 1999; Onton et al., 2005). Concomitant EEG measures and task performance confirmed an association between prefrontal theta dynamics and cognition, showing increasing power of theta oscillations and connectivity enhancement within prefrontal cortices, as well as between prefrontal and parietal cortices during tasks that required heavier memory loads (Onton et al., 2005; Sauseng et al., 2007). Intracranial recordings from patients undergoing invasive procedures further support the association between theta rhythm dynamics and cognition in humans, as well as phase-specific preferences for neuronal firing (Kahana et al., 1999; Rizzuto et al., 2006; Rutishauser et al., 2010; Lega et al., 2012; Zavala et al., 2018).

Given the role of different phases of the prefrontal theta oscillation, interfering with this oscillatory mode by applying non-invasive brain stimulation in a phase-specific manner may prove to be a relevant asset for modulating human brain function. This concept has previously been explored by our group, demonstrating that transcranial magnetic stimulation (TMS) in humans evokes differential responses depending on the phase of an ongoing local low-frequency EEG oscillation. Specifically, it has been found that the negative peak of the sensorimotor μ-oscillation represents a state of higher responsivity compared to the positive peak and random phase, as TMS during the negative peak evoked higher-amplitude motor potentials, and repetitive TMS induced long-term potentiation-like effects, which was made possible by using a real-time phase-detection algorithm (Schaworonkow et al., 2018; Zrenner et al., 2018). Here, we aim to develop a method to enable phase-specific stimulation according to the prefrontal theta oscillation.

However, differences in the characteristics of prefrontal theta and sensorimotor μ-oscillations require significant changes to the methods involved in the real-time phase-detection. Firstly, despite theta oscillations being prominently observed in EEG prefrontal regions, the signal-to-noise ratio (SNR) is usually lower than the SNR for the sensorimotor μ-oscillation in the alpha-frequency band. Lower SNR leads to increased vulnerability of the measured signal to interference from other oscillatory sources, either local or via volume conduction, which increases the estimation error of the phase of the theta oscillation of interest, while also decreasing the accuracy of the real-time phase-detection algorithm (Zrenner et al., 2020). Additionally, cortical theta oscillations have been found to occur in limited time lengths, sometimes described as bursts, which can last from a couple of cycles up to 2 seconds, which translates into a signal prone to sporadic shifts in amplitude and phase resetting (Kahana et al., 1999; Rizzuto et al., 2006; Rutishauser et al., 2010). This poses a challenge for any phase-estimation method, as one cannot rely on extrapolations from long windows of data, given that longer windows are more likely to contain periods of interference or a phase reset. Addressing these issues is particularly relevant for designing

an accurate real-time phase-detection algorithm aimed at the prefrontal theta oscillation. Therefore, such algorithm should include methods to reliably extract the theta oscillation from the cortical region of interest and to guarantee that the input signal to the real-time system corresponds to a stable oscillation, implying a signal length free from theta amplitude shifts and phase resets, which might compromise proper phase detection.

We propose here adaptations to the real-time phase detection method presented previously (Zrenner et al., 2018), in order to account for the characteristics of the prefrontal theta oscillation, and thereby enable real-time EEG-triggered TMS targeting of specific phases of the theta oscillation. We also assess the benefit of using an individual EEG spatial filter, based on the subject's anatomical MRI and EEG source activity estimation, designed to extract the signal of interest from the dorsomedial prefrontal cortex (DMPFC) in real time, as opposed to using a standard EEG montage. We also propose additional trigger constraints, which allow the real-time phase detection algorithm to detect instabilities in the theta oscillation, only triggering pulses during stable theta oscillation with adequate amplitude and without phase resets. We hope that our findings will enable future studies into the physiology of the human theta oscillation as well as new theta phase-dependent therapeutic neuromodulation.

MATERIALS AND METHODS

Subjects and Design

Twenty-two healthy individuals were recruited. Inclusion criteria were the absence of past or current psychiatric or neurological diseases. Exclusion criteria were current treatment with drugs acting on the central nervous system, presence or prior history of alcohol or illicit drugs abuse, and pregnancy. Two subjects were excluded due to excessive sleepiness, and two due to excessive eye movements and muscular activity during the experiment. The final sample included 18 subjects (11 female) with a mean age ($\pm$1 SD) of 24 $\pm$ 3.3 years. All subjects provided written informed consent prior to participation, and the study was conducted in accord with the Declaration of Helsinki approved by the ethics committee of the medical faculty of the University of Tübingen (716/2014BO2).

EEG and TMS

Scalp EEG was recorded with a 126-channel TMS compatible Ag/AgCl sintered ring electrode cap (EasyCap GmbH, Germany) in the International 10-5 EEG system arrangement (Oostenveld et al., 2011), with reference and ground electrodes placed at positions FCz and CPz, respectively. A 24-bit biosignal amplifier was used for EEG recordings, at a sampling rate of 5 kHz (NeurOne Tesla with Digital Out Option, Bittium Biosignals Ltd., Finland), in DC mode. TMS was delivered using a MagPro XP Stimulator (MagVenture A/S, Denmark) connected to a figure-of-eight coil (Cool-B65, inner coil winding diameter 35 mm) with biphasic pulses of 300 μs width.

Experimental Session

The experiment was conducted in a quiet room with the subjects sitting comfortably in a reclined chair, instructed to keep their eyes open. Experimental measurements involved a series of 3 EEG recordings. The first recording consisted of 8 min of resting-state EEG. This signal was used for the covariance matrix calculation, required for the design of the individualized source-based spatial filter, as explained in the next sub-section. This recording was also used to later test different parameters of the real-time phase estimation algorithm, in simulating real-time phase estimation offline, also explained below.

The second recording also involved resting-state EEG, but here we used the real-time phase-estimation algorithm to mark the EEG recording in real-time whenever the conditions for triggering at either the negative or positive peak of the ongoing theta oscillation were met. Sufficient data was recorded to include 100 markers for each phase condition. The procedure was designed to enable the quantification of the real-time algorithm's accuracy by comparing the predicted phase with a post-hoc "gold-standard" phase estimate. This was necessary as the real-time algorithm is essentially "predictive," relying on preceding signal only, which reduces the accuracy of the phase estimate (Blackwood et al., 2018; Zrenner et al., 2020). By analyzing the same signal *post hoc*, including data before and after the time point of interest, with standard signal-processing methods, the accuracy of the real-time estimate for a given signal can be assessed (details are provided below). It is important that the signal contains only trigger markers, but not actual TMS pulses, as stimulus artifacts and evoked cortical responses distort the post-stimulus signal, which cannot then be used for a *post hoc* phase estimate. Nonetheless, this method enables a reliable estimate of actual phase targeting accuracy, given that the marker placement in non-stimulated epochs follows exactly the same procedure and constraints as for the stimulated epochs (Bergmann et al., 2012; Zrenner et al., 2018).

The third part of the experiment consisted of the application of 480 EEG-triggered single biphasic TMS pulses to the DMPFC using the real-time phase detection algorithm to trigger pulses to either the positive peak, negative peak or random phases of the theta oscillation, 160 pulses per condition. The coil was separated from the scalp using an 11 mm plastic spacer that was mounted on the EEG electrodes to prevent direct contact of the TMS coil with the electrodes and reduce possible artifacts (Ruddy et al., 2017). Pulses were applied with an intensity of 120% of the resting motor threshold (RMT) (Groppa et al., 2012) and a minimum interstimulus interval of 2.5 s.

Imaging and Head Model

Extraction of brain activity from DMPFC was achieved by using an individual source-based spatial filter (filter W_{ind}). For this purpose, all subjects underwent MRI using a 3T Siemens PRISMA scanner, with T1- and T2-weighted anatomical sequences, required for the EEG forward model. The neuronavigation system (Localite GmbH, Sankt Augustin, Germany) was used to locate the left DMPFC (Dunlop et al., 2015), identified by the MNI coordinates (−4, 52, 36)

(Baetens et al., 2017; Piva et al., 2019). Individual MRIs were segmented and meshed using the Fieldtrip toolbox (Oostenveld et al., 2011), which relies on the software packages FreeSurfer and HCP workbench (Fischl, 2012). Meshes were imported into MATLAB R2018b (Mathworks Ltd., United States) and a forward model for EEG was built using a customized pipeline (Stenroos and Sarvas, 2012; Stenroos and Nummenmaa, 2016). Positions of all 126 electrodes were pinpointed manually using the neuronavigation system, and then projected onto the scalp surface mesh. A three-compartment volume conductor model was constructed using the boundary element method comprising the intracranial space (conductivity 0.33 S/m), skull (0.0041 S/m), and scalp (0.33 S/m). Cortical source activity was represented as primary current density on the boundary of white and gray matter, discretized into approximately 16,000 cortical source dipoles, each oriented perpendicular to the cortical surface. Signal topographies for all these dipoles were computed yielding a 126 × 16,000 leadfield matrix L, which quantifies how the source activity at each cortex location contributes to the voltage distribution on the sensor array. Cortical dipoles within 1 cm diameter centered in the left DMPFC coordinates were set as the region of interest for the EEG source activity estimation.

EEG Source Activity Estimation

A linear constrained minimum variance (LCMV) beamformer was used to estimate source activity at the relevant locations in source space (Van Veen et al., 1997). With constrained source orientations, the source amplitude $s(r,t)$ in location r at time-instant t is obtained by

$$s\,(r,\,t) = w^T\,(r)\,E(t), \tag{1}$$

where E is the array of measured EEG signals, and w is the spatial filter vector defined as

$$w = \frac{l^T\,(r)\,C^{-1}}{l^T\,(r)\,C^{-1}l(r)}, \tag{2}$$

where $l(r)$ is the topography of a elementary source dipole at location r, i.e., the corresponding column of the leadfield matrix L, and C is the signal covariance matrix, which was in this study calculated on 8 min of resting-state EEG data.

Spatial filters W and estimated time-course s were calculated for the selected dipoles in the region of interest. The individual filter W_{ind} is constructed using only those columns of the leadfield matrix L corresponding to the dipoles located within the left DMPFC. As this procedure depends on the covariance matrix of the acquired signal and on source topographies, which in turn depend on the head conductivity geometry and sensor positions with respect to the sources, each spatial filter is specifically calculated for each single session and subject. For the purpose of plotting, the results obtained from source estimation for each subject was then pooled and warped into a common MNI space for group average across subjects.

We used the resting state EEG data to estimate the source of the theta oscillation in the cortical surface by performing a spectral analysis at source level, using the individual head models and LCMV beamforming. Spectral power was estimated using the multi-taper method on contiguous data segments 5 s long with 5 tapers and a time half-bandwidth parameter of 3 yielding a power spectral density estimate of the full spectrum. Fractal (aperiodic) background noise was estimated using the Irregular Resampling Auto-Spectral Analysis (IRASA) method (Wen and Liu, 2016) with factors 1.1–2.9 in steps of 0.1 and excluding 2.0, as implemented by the Fieldtrip toolbox. SNR was computed by subtracting the fractal (aperiodic) component from the full spectrum (Donoghue et al., 2020).

Spatial Filters Comparison

In order to test the relevance of using an individual source-based spatial filter, the filter W_{ind}, we compared its properties with that from three non-individual spatial filters. The first of these filters involved the grand-average of the coefficient weights of the filter W_{ind}, channel by channel, across all subjects, resulting in the filter W_{avg}, which was applied as a generic spatial filter for all subjects. A simpler approach was to use the electrode with the highest coefficient weight in the filter W_{avg} as the center of a Hjorth montage (electrode AFF1h; coefficient weight = 1), with surrounding electrodes suppressing the signal (AFp1, AFF2h, FFC1h, AFF5h; coefficient weights = −1/4), resulting in the filter W_H, similarly to what has been done to detect the sensorimotor μ-oscillation (Zrenner et al., 2018). Finally, the simplest method was to consider solely the signal from the AFF1h electrode, resulting in the filter W_A. These spatial filters were compared with regard to the expected cortical areas they are sensitive to, performed by multiplying each individual filter by the whole leadfield matrix L, yielding a sensitivity profile over the cortical mesh. Furthermore, sensitivity profiles were normalized within subjects by means of a z-transform, subtracting the sensitivity of each dipole by the individual's average and divided by its standard deviation. The same procedure was applied to the individual electrodes in the sensor level, to better illustrate the conformation of the spatial filters. The correlation coefficient between the filters' sensitivity profiles across all the cortical surface was calculated on the individual subject level, as an estimate of similarity between these filters. The resulting correlation coefficients were then statistically compared. To summarize, the filters of interest were: (A) W_A, single electrode (AFF1h), with an average reference, (B) W_H, Hjorth-style Surface Laplacian montage centered on AFF1h (Hjorth, 1975; Tenke and Kayser, 2012), (C) W_{avg}, Non-individual beamforming (the average of the individual filter across all subjects), (D) W_{ind}, Individual source based spatial filter,

Each spatial filter was applied to resting-state EEG data in order to characterize and compare the resulting oscillation. The signal was first down-sampled to 250 Hz as done in the real-time phase estimation algorithm (see below). In order to compare the signal resulting from each filter with regards to their spectral distribution, a spectral analysis was performed using the same IRASA procedure as described above, allowing an estimate of the SNR. Total SNR in the theta band (5–8 Hz) from each filter was then statistically compared between the signals. The following analysis was performed to assess the stability of the theta oscillation extracted using different spatial filters, estimating the signal length of the theta oscillation between

phase resets: the signal was zero-phase (forward and backward) filtered using a theta band-pass filter (5–8 Hz pass-band, FIR order 250) and Hilbert transformed to yield the analytic signal. The complex angle (corresponding to instantaneous phase) was unwrapped (using the Matlab "unwrap" command) yielding phase progression of the signal with the slope corresponding to instantaneous frequency (radians/Hz), and the second derivative as a measure of the stability of the oscillation's phase progression: A value around zero represents stable phase progression, whereas phase slips are indicated by brief deviations from zero (possibly representing physiological phase resetting; see also Freeman: Origin, structure, and role of background EEG activity. Part 1 and 2; Freeman, 2004a,b, or interference from other sources). To detect phase slips in the signal using this procedure, the absolute value of the second derivative was taken and a threshold of higher than 5 times above the median was defined. From this, the distribution of the durations of stable periods between phase-slips was determined and statistically compared between the spatial filters (after log-transformation to reduce skew of the distribution).

Real-Time Phase Estimation Algorithm

EEG theta phase was estimated in real-time by downsampling the spatially filtered signal to 250 Hz and analyzing sliding windows of data with length of 256 samples (1,024 ms), applying the following steps every 4 ms to yield an instantaneous phase estimate: (1) zero-phase forward and backward filtering with an FIR 5–8 Hz band-pass filter of order 80, (2) removal of 35 samples from the epoch's window closest to the marker in order to reduce filtering edge effects, (3) autoregressive forward, Yule-Walker method, prediction of order 15 and the total predicted interval of 268 ms (140 ms for the removed edge, and 128 ms into the future to avoid edge effects from the Hilbert transform), (4) Hilbert transform. TMS was triggered when the estimated phase fell into a predetermined range and two further conditions were met: a minimum of 1 s had passed since the previous stimulus and no signal artifacts were detected (explained below). We chose the theta band as 5–8 Hz instead of the classical 4–7 Hz due to pilot experiments indicating a theta peak of the prefrontal signal as extracted with our spatial filters around 6–7 Hz, which was confirmed in the final results (see section "Results," **Figure 2**). A similar procedure was used previously for real-time estimation of sensorimotor μ-oscillation phase in the alpha band (Zrenner et al., 2018), but further adapted as described below.

Additional constraints were implemented to take into account the presence of muscle and eye blink artifacts when targeting more frontal sources and the intrinsic fluctuations characteristic to the theta oscillation. The algorithm included the following constraints to prevent inappropriate triggering of TMS: (1) Eye movement detection: The low frequency and high amplitude of eye movements and blinks could bias the phase detection algorithm and lead to inappropriate triggering. Eye blinks were detected by determining the maximum range within a 50 ms sliding window of the voltage potentials between four sensor pairs around the eyes (EOG1-Fp1, EOG1-Fp2, EOG2-Fp1, EOG2-Fp2), and taking the sum, with a threshold criterion of 250 μV. Therefore, TMS triggers were blocked for the following 700 ms after an eye blink was identified. (2) Muscle artifacts: If any of the EEG channels exceeded a range threshold within the window of analysis, signal quality was deemed to be affected by cranial muscle or movements artifacts. General EEG artifacts were detected when any channel exceeded a maximum range within a sliding window of 100 ms. This threshold was adjusted manually during the measurement due to fluctuations in the signal's amplitude during the experiment. (3) Phase stability of theta oscillation: constraints were added for the system to only send a trigger if no phase reset was detected in the previous 500 ms. Phase reset was determined by analyzing phase progression in a sliding 1 s window as follows: The signal was downsampled to 250 Hz, band-pass filtered in the theta range (5–8 Hz, FIR filter order 80, forward and backward), and converted to an analytic signal using the Hilbert transform. Instantaneous phase was unwrapped and (accounting for edge effects from the band-pass filter) instantaneous frequency was determined from phase progression over discrete 16 ms steps (units of Hz). The average squared difference between subsequent instantaneous frequencies across 16 ms steps was calculated and used as an "oscillation stability" criterion for the real-time phase-detection. (4) Theta amplitude: A user adjustable amplitude threshold prevented application of stimuli during periods where no reliably detectable theta oscillation was present. During the experiment, the general EEG artifacts and amplitude threshold were adjusted manually to track fluctuations and maintain a consistent stimulation rate. The implementation of the manually adjusted threshold was necessary as the intensity of the EEG background noise shifted throughout the experiment, probably due to change in the impedance of the electrodes and subjects' muscular activity, which changes the profile of spectral power and limits the possibility of establishing a static threshold. For the real-time phase-detection, we set the amplitude threshold to the mean of the minimum and maximum power of the theta band. For the *post hoc* comparison of different algorithms, the theta amplitude threshold was set as the 50% quantile with regards to the whole signal.

Simulating the Performance of the Phase Estimation Methods

In order to investigate the accuracy of the phase estimation method with different sets of parameters, we used the resting-state EEG data and applied the algorithm described above post-hoc, mimicking the real-time situation. This was performed by overlapping segments of 1,024 ms duration which were selected every 5 ms, and having the phase corresponding to the last sample of each segment estimated using the same procedure as described in the preceding section. The resulting estimated phase was then compared with the "gold-standard phase," obtained by using the whole signal, which involved data before and after each time point of interest (zero-phase forward and backward 5–8 Hz FIR band-pass filter of order 1,000, and Hilbert transform). The difference between the estimated and the gold-standard phases serves as an error measure to compare the accuracy of different

real-time phase estimation methods. We also calculated the proportion of instances when the distance between the estimated phase and the gold-standard phase was less than 45° to further quantify the accuracy of the phase estimation methods. Also, the "gold standard phases" were compared between spatial filters, calculating the correlation coefficient between the phases of the signal yielded by each spatial filter at individual level, as an estimate of phase agreement of the signal from these filters. The resulting correlation coefficients were then statistically compared.

Phase estimation error from the real-time phase estimation was assessed *post hoc* for signals extracted using the spatial filters. Then, for the signal extracted using the individual filter W_{ind}, the impact of additional constraints on phase estimation accuracy was assessed comparing the following conditions: individual source based spatial filter without constraints W_{ind}, as above; application of the phase stability constraint; application of the theta amplitude constraint; application of both the phase stability and amplitude constraints.

Real-Time Closed-Loop Data Processing Set-Up

Real-time data acquisition, data processing and TMS trigger control were implemented using a custom-built dedicated digital biosignal, executed on a dedicated xPC Target PC running the Simulink Real-Time operating system (DFI-ACP CL630-CRM mainboard). For the purpose of the real-time phase detection, EEG data was sent to a real-time processor through a real-time UDP interface at a packet rate of 5,000 Hz (one sample per channel) (Zrenner et al., 2018). The signal from left DMPFC was extracted using individual spatial filters based on LCMV beamforming (filter W_{ind}), for which all electrodes were used, with the exception of the ones in the outer rim (electrodes with labels 9 and 10 in the International 10–5 EEG system).

Statistics

All statistical analyses were performed using MATLAB R2018b (Mathworks Ltd., United States), first involving the assessment of the data distribution's pattern. Data following a normal distribution were analyzed using parametric methods (ANOVA, followed by *post hoc* pairwise comparisons when appropriate). Data not following a normal distribution were log-transformed and analyzed using parametric methods, as above, in the case the log-transformed distribution was normal. When this was not the case, the original data was then analyzed using non-parametric methods (Kruskal-Wallis test, followed by *post hoc* pairwise comparisons when appropriate). The correlation analyses were performed using Pearson correlation. Phase accuracy is reported as circular standard deviation. Threshold for statistical significance was set as $p < 0.05$.

RESULTS

From the 8-min resting-state EEG signal, we observed that the spectral power in the theta band was more prominent in prefrontal regions, as expected (**Figure 1A**). Given the particular interest in the DMPFC for its role in cognition and as possible anatomical target for brain stimulation interventions, we designed it as the source of the signal of interest for the calculation of the filter W_{ind} (**Figure 1B**).

Performance of Spatial Filters

The average of the W_{ind} filters across all subjects had high amplitude positive coefficients in a central group of electrodes centered around AFFh1, Fz and F1, vs. a surrounding area of electrodes with negative coefficients (**Figure 2**). Accordingly, the average of the sensitivity profiles shows that the W_{ind} filters are particularly sensitive to the anterior part of the left superior gyrus, corresponding to the left DMPFC, as expected. Slight inter-individual differences in the W_{ind} filter's coefficient weights conformation and the respective cortical sensitivity profile can be seen in the individual data (see individual filters in **Supplementary Material**). When comparing different spatial filters, at first glance, the sensitivity profiles of all filters appear to share the same characteristics, with higher sensitivity to the region around the left DMPFC. However, by basing this on a grand-average result, we might miss relevant differences in the individual results. To account for that, we performed an intra-subject correlation analysis of the sensitivity profiles and compared the resulting correlation coefficients. This revealed a significantly lower correlation between the sensitivity profiles from the W_{ind} filter and other filters, compared to the correlation between these other filters (**Table 1**). This suggests that, on an individual scale, the individual filters W_{ind} are more sensitive to different regions of the cortex, compared to the non-individual filters.

This particularity of the W_{ind} filter is probably responsible for considerable differences in the spatially filtered signal, compared to other filters, as observed in the power spectra of the yielded signal. Using only a single electrode as source (W_A), the resulting average power spectrum reveals the theta oscillation with little distinction with the alpha oscillation, both with lower power than higher frequency beta oscillations (**Figure 2A**). Using a Hjorth montage centered around that channel (W_H) successfully suppresses the alpha, but with little gain to the SNR of theta (**Figure 2B**). Using the average of the individual filters, there is some gain in the theta SNR (W_{avg}, **Figure 2C**). It is only when using the respective individual filters W_{ind} that we obtain a significantly higher SNR in the theta band (**Figure 2D**). On an important note, here we observe that, regardless of the spatial filter used, the average frequency peak of the local theta oscillation is around 6–7 Hz. The phase correlation was highest between the W_{avg} and W_{ind} filters, followed by W_H and other filters, and the lowest phase correlation being between W_A and other filters (**Table 2**).

The analysis of the stability of theta oscillation also shows difference between the yielded signal from the spatial filters. The intervals of theta oscillation between phase-slips were significantly longer in the signal from the individual source-based spatial filter. Interference from other cortical oscillations could have affected the phase progression estimation of the theta oscillation, leading to an overestimation of phase slips and thus shorter epochs between these events, especially in the signal from non-individualized filters (**Figure 2**).

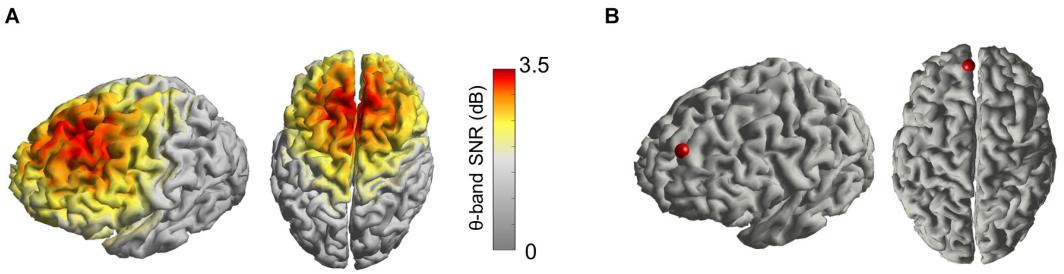

FIGURE 1 | (A) Average distribution of the signal-to-noise ratio (SNR) of the theta oscillation projected in the source space, including all 18 subjects, plotted on an averaged cortical model. **(B)** Cortical site (red dot) set as the region of interest for the EEG source activity estimation, centered on the left DMPFC.

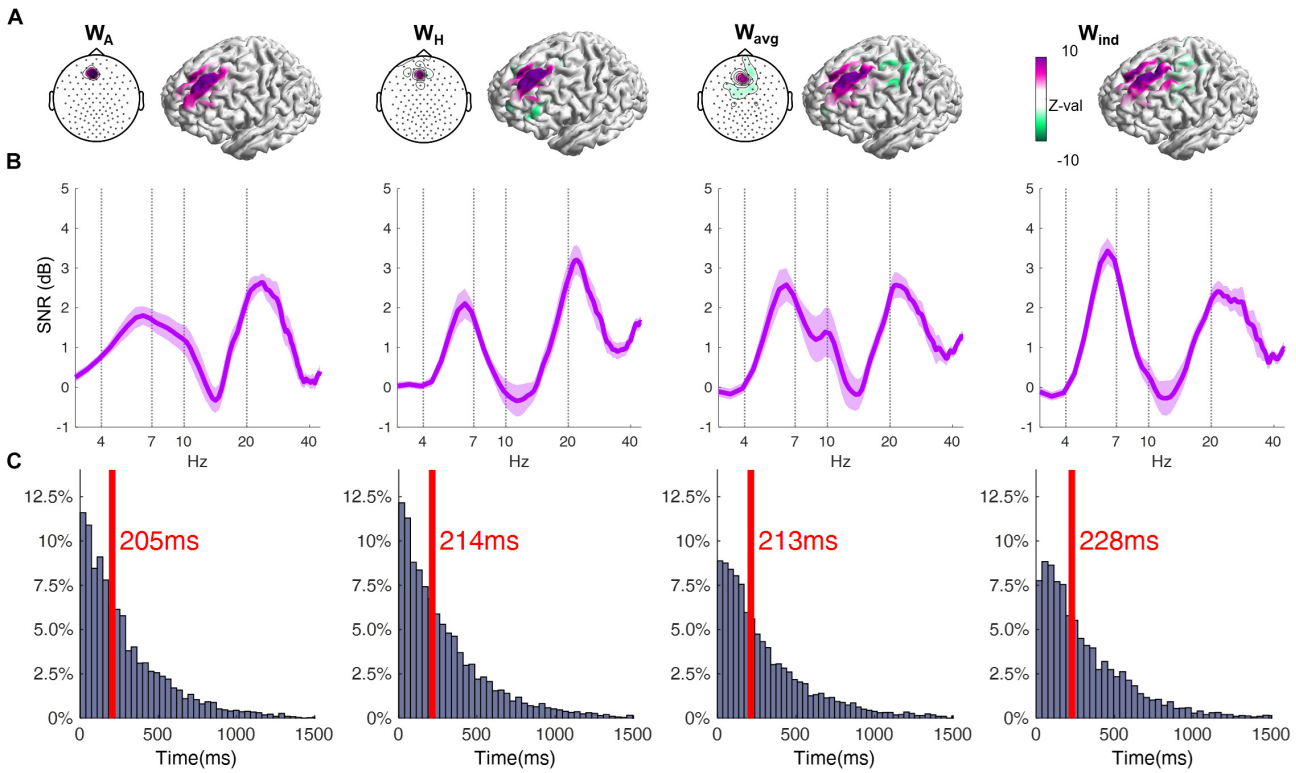

FIGURE 2 | (A) Topographical plot displaying the EEG channels' coefficient weighs of the respective filter. Cortical surface plots show the sensitivity profile of the respective filter, averaged across all subjects. The coefficient weights are given in arbitrary units, and are here normalized across all individuals using the standard score (z-value). Note that for the W_{ind} filter the values are different for each subject, and its average is depicted in W_{avg}. Also, results using the W_{ind} filter involved the application of the individual filter for each subject, and thus cannot be shown as a single topographical plot. **(B)** Power spectra of the resting-state EEG signal, obtained by using the respective spatial filters, averaged across all subjects (shaded area corresponds to ± 1 SEM). Data is depicted in form of Signal-to-Noise-Ratio. (ANOVA, $p = 0.0055$; *post-hoc* $W_A = W_H < W_{ind}$). **(C)** Distribution of the time lengths of epochs between phase slip events of the theta oscillation. Red line and text indicate the median of the respective distribution (ANOVA, $p = 0.0009$; *post-hoc* $W_A < W_H = W_{avg} < W_{ind}$).

Spatial Filters and Theta Oscillation Constraints in the Phase-Detection Algorithm

Here we investigate the procedures that may optimize the accuracy of the phase-detection method. We define the "accuracy" as deviation of the phase indicated by the real-time algorithm with respect to the "gold-standard phase," with higher accuracy representing higher overall agreement between these phases.

The choice of spatial filter significantly impacted the phase estimation, with increased accuracy observed when using the W_{ind} filters, followed by the use of W_{avg} filters, and with the lowest accuracy when using the W_A and W_H filters (**Figure 3**). Note that the difference is not in terms of the average phase error itself (i.e., the average difference between the estimated phase and the gold-standard) but in the standard deviation of that difference. In other words, on average all conditions have a very high accuracy, with the error close to 0 degrees. However,

TABLE 1 | Correlation matrix showing the comparison of the correlation coefficients between sensitivity profiles from the respective filters, averaged across all subjects (ANOVA, p = 0.0025; post-hoc [W_{ind} vs. W_A, W_H, W_{avg}] < [W_H vs. W_A]† < [W_{avg} vs. W_A, W_H]††).

	W_A	W_H	W_{avg}	W_{ind}
W_A	1	0.69†	0.73††	0.48
W_H		1	0.74††	0.46
W_{avg}			1	0.55
W_{ind}				1

TABLE 2 | Correlation matrix showing the correlation coefficients of the phases of prefrontal theta oscillation in the signal resulting from the respective filters, averaged across all subjects (Kruskal-Wallis test, p < 0.0001; post-hoc [W_A vs. W_H, W_{avg}, W_{ind}] < [W_H vs. W_{avg}, W_{ind}] † < [W_{avg} vs. W_{ind}] ††).

	W_A	W_H	W_{avg}	W_{ind}
W_A	1	0.02	0.05	0.03
W_H		1	0.15†	0.12†
W_{avg}			1	0.25††
W_{ind}				1

higher standard deviations mean that a larger proportion of trials had a higher phase estimation error. This can be exemplified by calculating the proportion of instances where the phase error exceeded the pre-established threshold. Setting a limit of ± 45°, we observe that either when using the W_A and W_H filters, 48% of the phase estimations are within that limit, whereas when using the W_{ind} filter, this number rises to 52% (**Figure 3**).

A limitation of this method is that the "gold-standard" signal was different for each filter. Therefore, each of the phase-detection simulations was compared with respect to the "gold-standard" signal yielded by the same filter. As a consequence, the method does not take into account the possibility that the yielded signal, instead of detecting the actual prefrontal theta, might correspond to other oscillatory modes from different cortical regions. Therefore, if we were to assume that the W_{ind} is more sensitive to the true underlying prefrontal theta, the actual increase in the phase accuracy by using the W_{ind} in comparison to filters W_A and W_H might be much larger. This possibility is strengthened by the findings of low correlation between the filters' sensitivity profiles, and also by the lower phase stability of the theta oscillations yielded by non-individualized filters (**Figure 2**). Finally, we investigated the correlation between the phases of the theta oscillation at the same given epochs in the signal from these filters, and observed a low correlation between the theta phases from the W_A and the W_H compared with other filters, with the highest agreement being between W_{avg} and W_{ind}, further suggesting that other oscillations of non-interest are confounding the phase estimation when non-individual filters are used to extract the signal.

We also aimed to further increase the accuracy of the phase-detection by taking into account the dynamics of the prefrontal theta oscillation, which involved adding the phase stability and amplitude threshold constrains to guarantee that the phase-detection would be performed during stable signal segments. These constrains were observed to individually contribute to the increase of the phase-detection accuracy (**Figure 3**).

Performance in Real-Time

As a proof of concept, we proceeded to applying the real-time phase-detection algorithm using the specifications above, including the W_{ind} filter as well as phase stability and amplitude constraints, in order to deliver theta phase-specific TMS pulses to the left DMPFC. By analyzing the resulting signal from the real-time phase-detection, we observed that the averaged signal of the pre-stimulus epochs closely resembles the simulations shown in **Figure 3**, with at least 2 distinct theta cycles observed prior to the trigger, peak amplitude between −200 to −100 ms with respect to the TMS trigger (**Figure 4A**). By estimating the theta phase using whole epochs, "gold-standard phase," we can observe the phase of the theta oscillation where each trigger was placed, thus allowing proper estimation of the real-time phase-detection accuracy. The results showed values similar to the accuracies obtained in the simulation, with 55.7% of the estimations being within ± 45° accuracy in the negative peak, and 56.4% in the positive peak (**Figure 4B**).

When observing the signal in the epochs where real TMS was applied, we notice that the averaged pre-stimulus signal resembles the simulations and the non-stimulated epochs, as expected. Moreover, we also see a massive electrical artifact caused by the TMS pulse in the EEG and the consequent brain response to direct stimulation. These can severely distort the phase estimation, which is the reason behind the need for accuracy tests to be performed on non-stimulated epochs, marking the EEG as if a real TMS pulse was applied.

DISCUSSION

The objective of this study was to develop a method to apply TMS phase-locked to the ongoing theta oscillation of the left DMPFC of healthy human subjects. We have adapted our previous algorithm, designed to detect the phases of the sensorimotor μ-rhythm in real-time, to now trigger stimuli phase-locked to the ongoing prefrontal theta oscillation. Importantly, this was possible by taking into consideration the individual anatomical location of the signal's source and the particularities of the theta oscillation dynamics.

For this purpose, we used individual filters based on source for extracting the EEG signal in real time from the region of interest. The higher SNR in the theta band of the signal yielded by the individual filters suggest a higher accuracy in detecting the signal from the DMPFC (**Figure 2**). Moreover, the estimated sensitivity profile of the individual filters presented a low correlation with other filters. This suggests that individual differences in the variables used to produce the filter (cortical anatomy, EEG electrodes position over the scalp, resting-state EEG signal and its covariance matrix) are relevant to

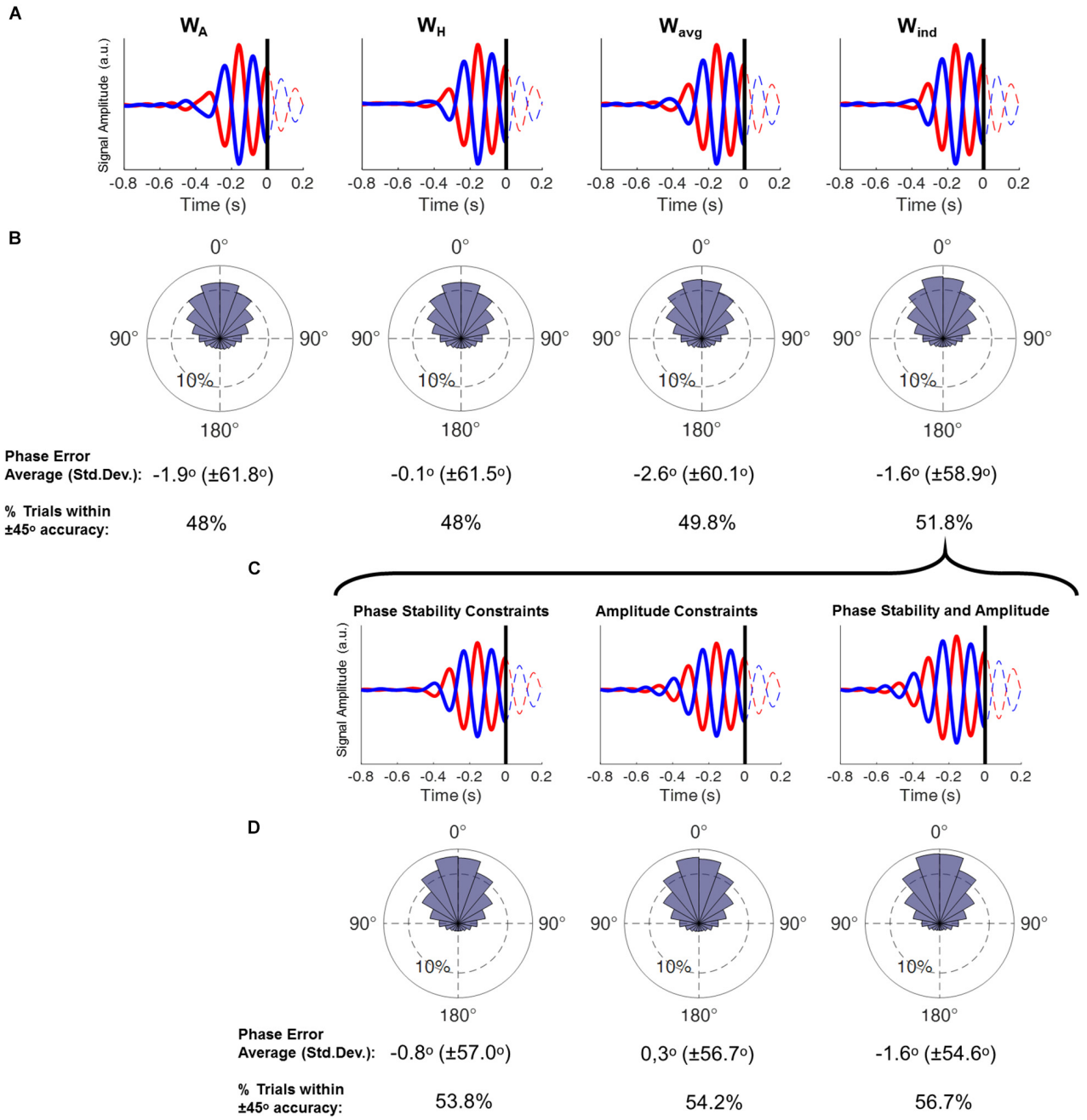

FIGURE 3 | (A) Time course plots display the averaged epochs obtained by running the real-time phase detection algorithm with resting-state EEG, with data obtained by using each spatial filter. Here only trials that were classified as positive peak (red) and negative peak (blue) were included. Time = 0 refers to the time point the theta phase was being estimated. Columns display the results from each spatial filter. **(B)** Phase histograms show the accuracy of the phase estimation from each spatial filter, obtained by subtracting the estimated phase of all epochs by their corresponding "gold-standard" phase (phase-bin width 20°, inner ring corresponds to 10% of the total trials). Below are the circular averages and standard deviations of the results, and the proportion of epochs within ± 45° accuracy (ANOVA, $p = 0.0025$; *post-hoc* $W_A = W_H < W_{avg} < W_{ind}$). **(C)** Time course plots display the averaged epochs obtained by running the real-time phase detection algorithm with resting-state EEG (as in **A**), with data obtained by using the W_{ind} filter and followed by different signal constraints: Phase stability, signal amplitude and both phase stability and amplitude constraints. **(D)** Phase histograms show the accuracy of the phase estimation (as in **B**) from the signal after application of each constraint (ANOVA, $p = 0.0002$; *post-hoc* [NO constraints] < [phase stability] = [amplitude] < [phase stability AND amplitude]).

be taken into account in designing a spatial filter to detect prefrontal theta oscillation. This personalized approach might have been responsible for a significantly higher accuracy in the real-time phase detection algorithm when this filter was applied (**Figure 3**), as the higher SNR in the theta band provided by this filter is expected to increase the accuracy

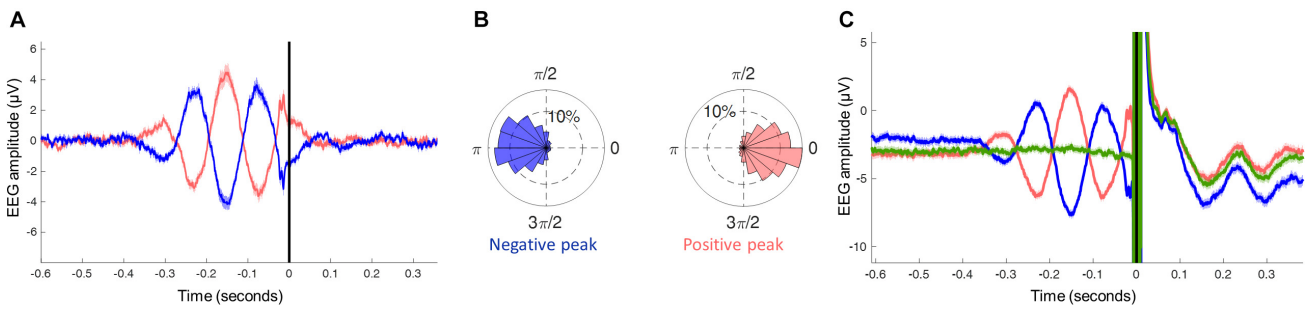

FIGURE 4 | (A) EEG signal generated by the individual filter W_{ind}, averaged across all subjects and trials around the trigger (time 0 s) located by the phase detection algorithm in the non-stimulated trials (red: positive peak; blue: negative peak). **(B)** Phase histogram of the estimated phases of the oscillation in the theta band at the time of the trigger, divided by trials triggered on the negative peak and positive peak (phase-bin width 20°, inner ring corresponds to 10% of the total trials). **(C)** EEG signal generated by the individual filter W_{ind}, averaged across all subjects and trials around the trigger (time 0 s) located by the phase detection algorithm in the stimulated trials (red: positive peak; blue: negative peak; green: random phase). Note the large TMS artifact and TMS-evoked EEG potentials.

of phase detection compared to other filters (Zrenner et al., 2020). However, for the purposes of estimating the phase accuracy, the signal for both the phase-detection simulation and for obtaining the "gold-standard phases" were produced by the same respective filter being examined. This means that the estimated accuracy does not account for the possibility that other oscillatory activities might be overriding the phase-detection, meaning that the phase inaccuracy with respect to the "real prefrontal theta" might be even greater. Properly identifying the "real theta" originating from the DMPFC would need to involve invasive electrophysiological recordings, and is beyond our present possibilities. Nevertheless, we can estimate a possible best candidate based on the indirect evidences available. At first, assuming that the preferential oscillatory mode region of interest is in the theta band, we can suppose that both the individual filters and its grand average are likely to be more accurate in extracting the "real prefrontal theta" than the other filter options, given the higher SNR of that oscillation in the yielded signal. This is reflected in the higher correlation between the phases of the theta oscillation of the signal yielded by these filters, with little agreement with the phases produced by the Hjorth montage and even smaller when using a single electrode, further suggesting that the signals being enhanced by these filters are of different origin. Finally, the lower stability of theta oscillations observed in the signal from non-individual filters suggests the existence of considerable interference with other oscillatory activities, falsely resembling theta phase slips. Conversely, longer durations of stable theta oscillation epochs were observed using the individual filter, which are closer to what has been reported in a previous study using invasive cortical recordings, with theta oscillation durations of on average 650 ms (Kahana et al., 1999). These reported values, however, are far above what we obtained, which is expected given that the signal was obtained during the execution of a continuous visuospatial task, which is more likely to recruit more stable theta oscillation, compared to the resting state used in our experiment. Moreover, the values reported in the aforementioned study were obtained through invasive recordings, which provides considerable protection from contamination from distant oscillatory signals compared to scalp EEG. Interestingly, the upper limit (95% percentile) of stable theta epochs was found to be around 1,500 ms in both our results and the aforementioned report (Kahana et al., 1999).

Taking into consideration the transient nature of the theta oscillation also significantly increased the method's accuracy. Creating constraints to avoid triggering during epochs of low theta power or theta phase shifts were independently responsible for increasing the accuracy (**Figure 3**). The relevance of these phenomena can also be seen in the final results: When averaging the non-stimulated trials, at least two cycles of an oscillation in the theta frequency-band prior to the stimulus marker can clearly be identified (**Figure 4C**). It should be noted that phase-locking to the sensorimotor μ-rhythm yields a continuous oscillation pattern, which extends up to 4–5 cycles prior to the trigger (Zrenner et al., 2018). This is not expected in phase-locking to the prefrontal theta rhythm, as this oscillation, as already mentioned, was found to occur in well-defined epochs of only a few hundred milliseconds, prone to sporadic shifts in amplitude and phase resetting (Kahana et al., 1999; Rizzuto et al., 2006; Rutishauser et al., 2010), resulting in the oscillatory activity averaging out the further it is from the time point of interest (TMS trigger). The application of these constraints was necessary to properly achieve accurate real-time phase-detection of the prefrontal theta oscillation. The resulting algorithm was found to be effective, with its accuracy in triggering at the desired phase being comparable to previously published phase-triggering algorithms (Siegle and Wilson, 2014; Blackwood et al., 2018; Zrenner et al., 2018; Madsen et al., 2019), and in line with the limitations imposed by the SNR of the data (Zrenner et al., 2020).

A limitation of this study is that we did not analyze the response signal produced by the different stimulation conditions. Although the stimuli applied to different phases of theta might have led to different cortical responses, it is exceedingly challenging to investigate these differences in the EEG signal response, given that the ongoing oscillations influence the resulting signal (Desideri et al., 2019). Differences

in stimulating opposite phases of the prefrontal theta oscillation could be better detected by methods unbiased by the pre-stimulus EEG, such as functional MRI or near-infrared spectroscopy. Another unbiased output is behavioral performance. It has been shown that TMS pulses applied during different phases of the prefrontal theta oscillation have different effects on cognition. More precisely, after applying a series of TMS pulses to subjects performing a working memory task, the accuracy of trials was influenced by the phase of the prefrontal theta during which the TMS pulse was delivered (Berger et al., 2019). Although that study relied on estimating the phase of each trial *post hoc*, by using the method described here it is possible to investigate the effects of cortical stimulation during specific theta phases on cognition in real-time. The method can also be applied in differentially modulating cortical plasticity. The particular role of the theta rhythm in frontal cortex neuroplasticity has inspired the development of a stimulation protocol that delivers repetitive TMS bursts of 50 Hz at a carrier frequency of 5 Hz, and was termed accordingly theta-burst stimulation (TBS) (Huang et al., 2005). Nevertheless, despite the clinical success of TBS, it has not been shown to be superior to standard repetitive TMS protocols (Blumberger et al., 2018). One possible reason is that, although the stimulation is applied in a theta-frequency band, it does not take into account the phase of the ongoing endogenous oscillation. Future studies should determine whether EEG-informed brain-state-dependent repetitive TMS, targeting, e.g., the negative peak of the theta-rhythm in prefrontal cortex indeed leads to neuroplastic changes that are significantly different when compared to random-phase stimulation. The capability of applying repetitive theta phase-locked cortical stimuli demonstrated in this study could potentially be used as neuroplasticity inducing non-invasive brain stimulation, with potential clinical applications.

CONCLUSION

Results support the feasibility of synchronizing TMS accurately to a specific phase of the local theta oscillation in DMPFC informed by EEG data analyzed in real time and source space. They may also be relevant for devising EEG-informed personalized therapeutic repetitive TMS protocols for effective treatment of neuropsychiatric disorders.

DATA AVAILABILITY STATEMENT

The raw data supporting the conclusions of this article will be made available by the authors, without undue reservation.

ETHICS STATEMENT

The studies involving human participants were reviewed and approved by Ethik-Kommission an der Medizinischen Fakultät Eberhard-Karls-Universität Tübingen. The patients/participants provided their written informed consent to participate in this study.

AUTHOR CONTRIBUTIONS

CZ, PG, and UZ conceived the study and designed the study protocol. CZ, PG, and BZ set-up the experiment and obtained ethical approval. PB, CZ, MS, and PG designed the algorithms for experiments and analyses. PB created the headmodels. PG and SD conducted the experiments and analyzed the data. CZ, PG, and BZ performed the spectral analysis. All authors contributed to the writing of the manuscript.

FUNDING

The authors acknowledge administrative supported by the Anna Kempf and Dragana Galevska. CZ acknowledges support from the Clinician Scientist Program at the Faculty of Medicine at the University of Tübingen (Grant 391-0-0). The project has received funding from the European Research Council (ERC Synergy) under the European Union's Horizon 2020 Research and Innovation Programme (ConnectToBrain; grant agreement no. 810377), and from an EXIST Transfer of Research grant by the German Federal Ministry for Economic Affairs and Energy (Grant 03EFJBW169).

SUPPLEMENTARY MATERIAL

The Supplementary Material for this article can be found online at: https://www.frontiersin.org/articles/10.3389/fnhum.2021.691821/full#supplementary-material

REFERENCES

Baetens, K. L., Ma, N., and Van Overwalle, F. (2017). The dorsal medial prefrontal cortex is recruited by high construal of non-social stimuli. *Front. Behav. Neurosci.* 11:44. doi: 10.3389/fnbeh.2017.00044

Berger, B., Griesmayr, B., Minarik, T., Biel, A. L., Pinal, D., Sterr, A., et al. (2019). Dynamic regulation of interregional cortical communication by slow brain oscillations during working memory. *Nat. Commun.* 10:4242. doi: 10.1038/s41467-019-12057-0

Bergmann, T. O., Molle, M., Schmidt, M. A., Lindner, C., Marshall, L., Born, J., et al. (2012). EEG-guided transcranial magnetic stimulation reveals rapid shifts in motor cortical excitability during the human sleep slow oscillation. *J. Neurosci.* 32, 243–253. doi: 10.1523/JNEUROSCI.4792-11.2012

Blackwood, E., Lo, M. C., and Alik Widge, S. (2018). Continuous phase estimation for phase-locked neural stimulation using an autoregressive model for signal prediction. *Conf. Proc. IEEE Eng. Med. Biol. Soc.* 2018, 4736–4739. doi: 10.1109/EMBC.2018.8513232

Blumberger, D. M., Vila-Rodriguez, F., Thorpe, K. E., Feffer, K., Noda, Y., Giacobbe, P., et al. (2018). Effectiveness of theta burst versus high-frequency repetitive transcranial magnetic stimulation in patients with depression (THREE-D): a randomised non-inferiority trial. *Lancet* 391, 1683–1692. doi: 10.1016/S0140-6736(18)30295-2

Buzsaki, G., and Draguhn, A. (2004). Neuronal oscillations in cortical networks. *Science* 304, 1926–1929. doi: 10.1126/science.1099745

Cavanagh, J. F., and Frank, M. J. (2014). Frontal theta as a mechanism for cognitive control. *Trends Cogn. Sci.* 18, 414–421. doi: 10.1016/j.tics.2014.04.012

Desideri, D., Zrenner, C., Ziemann, U., and Belardinelli, P. (2019). Phase of sensorimotor mu-oscillation modulates cortical responses to transcranial magnetic stimulation of the human motor cortex. *J. Physiol.* 597, 5671–5686. doi: 10.1113/JP278638

Donoghue, T., Haller, M., Peterson, E. J., Varma, P., Sebastian, P., Gao, R., et al. (2020). Parameterizing neural power spectra into periodic and aperiodic components. *Nat. Neurosci.* 23, 1655–1665. doi: 10.1038/s41593-020-00744-x

Dunlop, K., Gaprielian, P., Blumberger, D., Daskalakis, Z. J., Kennedy, S. H., Giacobbe, P., et al. (2015). MRI-guided dmPFC-rTMS as a treatment for treatment-resistant major depressive disorder. *J. Vis. Exp.* 102, e53129. doi: 10.3791/53129

Fischl, B. (2012). FreeSurfer. *Neuroimage* 62, 774–781. doi: 10.1016/j.neuroimage.2012.01.021

Freeman, W. J. (2004a). Origin, structure, and role of background EEG activity. Part 1. Analytic amplitude. *Clin. Neurophysiol.* 115, 2077–2088. doi: 10.1016/j.clinph.2004.02.029

Freeman, W. J. (2004b). Origin, structure, and role of background EEG activity. Part 2. Analytic phase. *Clin. Neurophysiol.* 115, 2089–2107. doi: 10.1016/j.clinph.2004.02.028

Fries, P. (2015). Rhythms for cognition: communication through coherence. *Neuron* 88, 220–235. doi: 10.1016/j.neuron.2015.09.034

Fujisawa, S., and Buzsaki, G. (2011). A 4 Hz oscillation adaptively synchronizes prefrontal, VTA, and hippocampal activities. *Neuron* 72, 153–165. doi: 10.1016/j.neuron.2011.08.018

Groppa, S., Oliviero, A., Eisen, A., Quartarone, A., Cohen, L. G., Mall, V., et al. (2012). A practical guide to diagnostic transcranial magnetic stimulation: report of an IFCN committee. *Clin. Neurophysiol.* 123, 858–882. doi: 10.1016/j.clinph.2012.01.010

Harris, K. D., Csicsvari, J., Hirase, H., Dragoi, G., and Buzsaki, G. (2003). Organization of cell assemblies in the hippocampus. *Nature* 424, 552–556. doi: 10.1038/nature01834

Hjorth, B. (1975). An on-line transformation of EEG scalp potentials into orthogonal source derivations. *Electroencephalogr. Clin. Neurophysiol.* 39, 526–530. doi: 10.1016/0013-4694(75)90056-5

Holscher, C., Anwyl, R., and Rowan, M. J. (1997). Stimulation on the positive phase of hippocampal theta rhythm induces long-term potentiation that can Be depotentiated by stimulation on the negative phase in area CA1 in vivo. *J. Neurosci.* 17, 6470–6477. doi: 10.1523/jneurosci.17-16-06470.1997

Huang, Y.-Z., Edwards, M. J., Rounis, E., Bhatia, K. P., and Rothwell, J. C. (2005). Theta burst stimulation of the human motor cortex. *Neuron* 45, 201–206.

Hyman, J. M., Wyble, B. P., Goyal, V., Rossi, C. A., and Hasselmo, M. E. (2003). Stimulation in hippocampal region CA1 in behaving rats yields long-term potentiation when delivered to the peak of theta and long-term depression when delivered to the trough. *J. Neurosci.* 23, 11725–11731. doi: 10.1523/jneurosci.23-37-11725.2003

Ishii, R., Shinosaki, K., Ukai, S., Inouye, T., Ishihara, T., Yoshimine, T., et al. (1999). Medial prefrontal cortex generates frontal midline theta rhythm. *Neuroreport* 10, 675–679. doi: 10.1097/00001756-199903170-00003

Kahana, M. J., Sekuler, R., Caplan, J. B., Kirschen, M., and Madsen, J. R. (1999). Human theta oscillations exhibit task dependence during virtual maze navigation. *Nature* 399, 781–784. doi: 10.1038/21645

Klausberger, T., Marton, L. F., Baude, A., Roberts, J. D., Magill, P. J., and Somogyi, P. (2004). Spike timing of dendrite-targeting bistratified cells during hippocampal network oscillations in vivo. *Nat. Neurosci.* 7, 41–47. doi: 10.1038/nn1159

Lega, B. C., Jacobs, J., and Kahana, M. (2012). Human hippocampal theta oscillations and the formation of episodic memories. *Hippocampus* 22, 748–761. doi: 10.1002/hipo.20937

Lisman, J., and Buzsaki, G. (2008). A neural coding scheme formed by the combined function of gamma and theta oscillations. *Schizophr. Bull.* 34, 974–980. doi: 10.1093/schbul/sbn060

Madsen, K. H., Karabanov, A. N., Krohne, L. G., Safeldt, M. G., Tomasevic, L., and Siebner, H. R. (2019). No trace of phase: corticomotor excitability is not tuned by phase of pericentral mu-rhythm. *Brain Stimul.* 12, 1261–1270. doi: 10.1016/j.brs.2019.05.005

Onton, J., Delorme, A., and Makeig, S. (2005). Frontal midline EEG dynamics during working memory. *Neuroimage* 27, 341–356. doi: 10.1016/j.neuroimage.2005.04.014

Oostenveld, R., Fries, P., Maris, E., and Schoffelen, J. M. (2011). FieldTrip: Open source software for advanced analysis of MEG, EEG, and invasive electrophysiological data. *Comput. Intell. Neurosci.* 2011:156869. doi: 10.1155/2011/156869

Pavlides, C., Greenstein, Y. J., Grudman, M., and Winson, J. (1988). Long-term potentiation in the dentate gyrus is induced preferentially on the positive phase of theta-rhythm. *Brain Res.* 439, 383–387. doi: 10.1016/0006-8993(88)91499-0

Piva, M., Velnoskey, K., Jia, R., Nair, A., Levy, I., and Chang, S. W. (2019). The dorsomedial prefrontal cortex computes task-invariant relative subjective value for self and other. *Elife* 8:e44939. doi: 10.7554/eLife.44939

Rizzuto, D. S., Madsen, J. R., Bromfield, E. B., Schulze-Bonhage, A., and Kahana, M. J. (2006). Human neocortical oscillations exhibit theta phase differences between encoding and retrieval. *Neuroimage* 31, 1352–1358. doi: 10.1016/j.neuroimage.2006.01.009

Ruddy, K. L., Woolley, D. G., Mantini, D., Balsters, J. H., Enz, N., and Wenderoth, N. (2017). Improving the quality of combined EEG-TMS neural recordings: Introducing the coil spacer. *J. Neurosci. Methods* 294, 34–39. doi: 10.1016/j.jneumeth.2017.11.001

Rutishauser, U., Ross, I. B., Mamelak, A. N., and Schuman, E. M. (2010). Human memory strength is predicted by theta-frequency phase-locking of single neurons. *Nature* 464, 903–907. doi: 10.1038/nature08860

Sauseng, P., Griesmayr, B., Freunberger, R., and Klimesch, W. (2010). Control mechanisms in working memory: a possible function of EEG theta oscillations. *Neurosci. Biobehav. Rev.* 34, 1015–1022. doi: 10.1016/j.neubiorev.2009.12.006

Sauseng, P., Hoppe, J., Klimesch, W., Gerloff, C., and Hummel, F. C. (2007). Dissociation of sustained attention from central executive functions: local activity and interregional connectivity in the theta range. *Eur. J. Neurosci.* 25, 587–593. doi: 10.1111/j.1460-9568.2006.05286.x

Schaworonkow, N., Caldana Gordon, P., Belardinelli, P., Ziemann, U., Bergmann, T. O., and Zrenner, C. (2018). mu-Rhythm extracted with personalized EEG Filters correlates with corticospinal excitability in real-time phase-triggered EEG-TMS. *Front. Neurosci.* 12:954. doi: 10.3389/fnins.2018.00954

Siapas, A. G., Lubenov, E. V., and Wilson, M. A. (2005). Prefrontal phase locking to hippocampal theta oscillations. *Neuron* 46, 141–151. doi: 10.1016/j.neuron.2005.02.028

Siegle, J. H., and Wilson, M. A. (2014). Enhancement of encoding and retrieval functions through theta phase-specific manipulation of hippocampus. *Elife* 3, e03061. doi: 10.7554/eLife.03061

Stenroos, M., and Nummenmaa, A. (2016). Incorporating and compensating cerebrospinal fluid in surface-based forward models of magneto- and electroencephalography. *PLoS One* 11:e0159595. doi: 10.1371/journal.pone.0159595

Stenroos, M., and Sarvas, J. (2012). Bioelectromagnetic forward problem: isolated source approach revis(it)ed. *Phys. Med. Biol.* 57, 3517–3535. doi: 10.1088/0031-9155/57/11/3517

Tenke, C. E., and Kayser, J. (2012). Generator localization by current source density (CSD): implications of volume conduction and field closure at intracranial and scalp resolutions. *Clin. Neurophysiol.* 123, 2328–2345. doi: 10.1016/j.clinph.2012.06.005

Van Veen, B. D., van Drongelen, W., Yuchtman, M., and Suzuki, A. (1997). Localization of brain electrical activity via linearly constrained minimum variance spatial filtering. *IEEE Trans. Biomed. Eng.* 44, 867–880. doi: 10.1109/10.623056

Wen, H., and Liu, Z. (2016). Separating fractal and oscillatory components in the power spectrum of neurophysiological signal. *Brain Topogr.* 29, 13–26. doi: 10.1007/s10548-015-0448-0

Winson, J. (1978). Loss of hippocampal theta rhythm results in spatial memory deficit in the rat. *Science* 201, 160–163. doi: 10.1126/science.663646

Zavala, B., Jang, A., Trotta, M., Lungu, C. I., Brown, P., and Zaghloul, K. A. (2018). Cognitive control involves theta power within trials and beta power across trials in the prefrontal-subthalamic network. *Brain* 141, 3361–3376. doi: 10.1093/brain/awy266

Zrenner, C., Desideri, D., Belardinelli, P., and Ziemann, U. (2018). Real-time EEG-defined excitability states determine efficacy of TMS-induced plasticity in human motor cortex. *Brain Stimul.* 11, 374–389. doi: 10.1016/j.brs.2017.11.016

Zrenner, C., Galevska, D., Nieminen, J. O., Baur, D., Stefanou, M. I., and Ziemann, U. (2020). The shaky ground truth of real-time phase estimation. *Neuroimage* 214:116761. doi: 10.1016/j.neuroimage.2020.116761

Conflict of Interest: PG, CZ, and BZ report funding through the EXIST translational research program from the German Federal Ministry for Economic Affairs and Energy, with the goal of commercializing the real-time EEG-TMS device used in this study and CZ and BZ report an interest in and employment by the spin-off company resulting from this grant (sync2brain GmbH, Tübingen). UZ received grants from the German Ministry of Education and Research (BMBF), European Research Council (ERC), German Research Foundation (DFG), Janssen Pharmaceuticals NV and Takeda Pharmaceutical Company Ltd., and consulting fees from Bayer Vital GmbH, Pfizer GmbH, and CorTec GmbH, all not related to this work.

The remaining authors declare that the research was conducted in the absence of any commercial or financial relationships that could be construed as a potential conflict of interest.

frontiers in Human Neuroscience

ORIGINAL RESEARCH
published: 22 October 2021
doi: 10.3389/fnhum.2021.748893

A Long Time Constant May Endorse Sharp Waves and Spikes Over Sharp Transients in Scalp Electroencephalography: A Comparison of After-Slow Among Different Time Constants Concordant With High-Frequency Activity Analysis

*Shamima Sultana[1], Takefumi Hitomi[1,2], Masako Daifu Kobayashi[1], Akihiro Shimotake[1], Masao Matsuhashi[3], Ryosuke Takahashi[1] and Akio Ikeda[3]**

[1] Department of Neurology, Graduate School of Medicine, Kyoto University, Kyoto, Japan, [2] Department of Clinical Laboratory Medicine, Graduate School of Medicine, Kyoto University, Kyoto, Japan, [3] Department of Epilepsy, Movement Disorders and Physiology, Graduate School of Medicine, Kyoto University, Kyoto, Japan

OPEN ACCESS

Edited by:
Shozo Tobimatsu, Kyushu University, Japan

Reviewed by:
Naoki Akamatsu, International University of Health and Welfare, Narita, Japan
Nuttida Rungratsameetaweemana, Salk Institute for Biological Studies, United States

***Correspondence:**
Akio Ikeda
akio@kuhp.kyoto-u.ac.jp

Specialty section:
This article was submitted to Brain Imaging and Stimulation, a section of the journal Frontiers in Human Neuroscience

Received: *28 July 2021*
Accepted: *28 September 2021*
Published: *22 October 2021*

Citation:
Sultana S, Hitomi T, Daifu Kobayashi M, Shimotake A, Matsuhashi M, Takahashi R and Ikeda A (2021) A Long Time Constant May Endorse Sharp Waves and Spikes Over Sharp Transients in Scalp Electroencephalography: A Comparison of After-Slow Among Different Time Constants Concordant With High-Frequency Activity Analysis. Front. Hum. Neurosci. 15:748893. doi: 10.3389/fnhum.2021.748893

Objective: To clarify whether long time constant (TC) is useful for detecting the after-slow activity of epileptiform discharges (EDs): sharp waves and spikes and for differentiating EDs from sharp transients (Sts).

Methods: We employed 68 after-slow activities preceded by 32 EDs (26 sharp waves and six spikes) and 36 Sts from 52 patients with partial and generalized epilepsy (22 men, 30 women; mean age 39.08 ± 13.13 years) defined by visual inspection. High-frequency activity (HFA) associated with the apical component of EDs and Sts was also investigated to endorse two groups. After separating nine Sts that were labeled by visual inspection but did not fulfill the amplitude criteria for after-slow of Sts, 59 activities (32 EDs and 27 Sts) were analyzed about the total area of after-slow under three TCs (long: 2 s; conventional: 0.3 s; and short: 0.1 s).

Results: Compared to Sts, HFA was found significantly more with the apical component of EDs ($p < 0.05$). The total area of after-slow in all 32 EDs under TC 2 s was significantly larger than those under TC 0.3 s and 0.1 s ($p < 0.001$). Conversely, no significant differences were observed in the same parameter of 27 Sts among the three different TCs. Regarding separated nine Sts, the total area of after-slow showed a similar tendency to that of 27 Sts under three different TCs.

Significance: These results suggest that long TC could be useful for selectively endorsing after-slow of EDs and differentiating EDs from Sts. These findings are concordant with the results of the HFA analysis. Visual inspection is also equally good as the total area of after-slow analysis.

Keywords: epileptiform discharge, total area, total duration, paroxysmal depolarization shifts, high-frequency activity

KEY POINTS

- Precise detection of EDs is important for patients with epilepsy.
- The long TC setting is appropriate to augment the after-slow activity of EDs.
- The findings may endorse the operational definitions of EDs and Sts.
- These findings are also consistent with the analysis of HFA.

INTRODUCTION

Electroencephalography (EEG) is a useful clinical examination for the diagnosis of epilepsy since it is the only clinically available examination to delineate the paroxysmal depolarization shifts (PDS). Appropriate EEG readings, especially for the detection of epileptiform discharges (EDs), are crucial for making the diagnosis of epilepsy (Winesett and Benbadis, 2008; Gil-Nagel and Abou-Khalil, 2012). According to the guidelines of the International Federation of Clinical Neurophysiology (IFCN), EDs are defined as transient activity that is outstanding from background activity with a pointed peak at a conventional paper speed or time scale, mainly negative component, and durations from 20 to less than 70 ms for spikes and from 70 to 200 ms for sharp waves (Brazier et al., 1961; Noachtar et al., 1999). However, it is sometimes still inaccurate even for certified electroencephalographers to distinguish EDs from morphologically resembling normal or non-specific sharply contoured waveforms, namely, sharp transients (Sts) (Janca et al., 2014). On the other hand, EDs are usually accompanied by a subsequent slow wave referred to as an "after-slow wave," which is helpful to identify EDs and to aid such differentiation (Winesett and Benbadis, 2008; Selwa, 2010). According to the study by Aykut et al. (2020), they found that three criteria: waves with spiky morphology, followed by an after-slow wave and voltage map suggesting a source in the brain, providing the best diagnostic value with specificity over 95% (Aykut et al., 2020). However, this study did not investigate the degree of after-slow activity to define EDs.

Clinical EEG technology has developed over the past several decades. Digital EEG has become common because of the advantages of recording, reviewing, and storing EEG data (Nuwer, 1997). Thus, current digital EEG data are recorded, analyzed, and interpreted by using a wide range of time constant (TC), as clinically needed (Maus et al., 2011; Constantino and Rodin, 2012). If long TC is chosen (e.g., 2 s), slow activities are not deleted as compared with the conventional settings (Fisch and Spehlmann, 1999; Sinha et al., 2016). This may be beneficial for detecting slow EEG activities (Misra and Kalita, 2005), including the after-slow activity of EDs. However, the degree of detection of the after-slow activity of EDs under different TC conditions has not been systematically analyzed. To the best of our knowledge, there was no study about the endorsement of the definition of Sts with less after-slow as compared with EDs.

In this study at first, we investigate whether long TC is useful for detecting the after-slow activity of EDs and for differentiating EDs from Sts as compared with conventional TC settings and whether the current operational definition of EDs and Sts is appropriate. The target activities must be visually identified and selected "typical" patterns inspected by EEG experts. It is because, despite recent advances in information technology, EEG interpretation still requires trained EEG experts to define clinically useful specific EEG results, and then we tried to endorse the EEG experts' judge by means of parameter analysis of waveform analysis. Second, recent technological advancement of digital EEG has aided the analysis of high-frequency activity (HFA) even in the scalp EEG (Kobayashi et al., 2004; Shibata et al., 2016). As HFA is considered to have an association with epileptogenicity (Shibata et al., 2016), we also examine the relationship of HFA with EDs and Sts for the endorsement of these two groups. Once those two approaches of this study would provide positive results, we may skip complicated HFA analysis, and only simple visual analysis by means of long TC may be practically useful.

MATERIALS AND METHODS

Study Design and Participants

We retrospectively analyzed randomly selected 55 routine EEGs from 52 patients (22 men, 30 women; mean age ± SD, 39.08 ± 13.13 years; age range, 18–80 years) with partial and generalized epilepsy. All EEGs were recorded at the Kyoto University Hospital from June 2013 to July 2017. Among the 52 epilepsy patients, 37 were clinically diagnosed as having partial epilepsy (temporal = 12, frontal = 13, parietal = 3, and other lobes or in combination = 9) and 15 as having generalized epilepsy (idiopathic generalized epilepsy = 6, symptomatic generalized epilepsy = 5, genetic epilepsy with febrile seizure plus = 1, and other generalized epilepsy = 3). We included both partial and generalized epilepsy since we tried to extract the common feature of EDs and Sts regardless of epilepsy classification. The study protocol was approved by the Institutional Review Board of the Kyoto University (No. R0603).

Electroencephalography Recording

Conventional digital EEGs by using the scalp electrodes were recorded for at least 30 min (EEG-1100 Neurofax; Nihon Kohden, Tokyo, Japan). Conventional Ag/AgCl scalp electrodes with a diameter of 10 mm were used. The Fp1, Fp2, Fz, F3, F4, F7, F8, Cz, C3, C4, T3, T4, Pz, P3, P4, T5, T6, O1, O2, A1, and A2 electrodes were placed according to the International 10–20 system. In addition, T1 and T2 electrodes (Silverman, 1965) were placed in 12 EEGs. The EEG data were recorded with a sampling rate of 500 Hz, the high-frequency filter of 120 Hz, and TC of 2 s (13 EEGs) or 10 s (42 EEGs). The impedance of all the electrodes was kept below 5 kΩ. EEG was reviewed and the EEG report was made by the certified electroencephalographer.

Selection of Electroencephalography Activities

First, we reviewed the EEGs with the sensitivity of 10 μV, TC of 0.3 s (regardless of the recording TC condition of EEGs),

and a high-frequency filter of 120 Hz and averaged reference montage of all the electrodes by using the review software of the Nihon Kohden. Second, we randomly selected the typical samples (for EDs: clear apical component with large after-slow; for Sts: clear apical component with small after-slow) of 68 EEG activities according to annotations that had been already labeled only for the clinical purposes through visual inspection by the certified electroencephalographers to avoid the selection biases. Because of these reasons, the adopted number of samples is limited since we respected the initial impression and decision of electroencephalographers. The 68 visually defined EEG samples consisted of 32 EDs [26 sharp waves (all focal), six spikes (5: focal and 1: generalized)], and 36 Sts (all focal). Third, we adopted the criteria used for the EDs (sharp waves and spikes) as follows: (1) standing out from the background, (2) the amplitude of after-slow component being > 50% of the amplitude of the immediately preceding apical component, and (3) total duration of apical component up to 200 ms. Then, we differentiated sharp waves and spikes based on the total duration of the apical component (spikes: < 70 ms and sharp waves: 70–200 ms).

With respect to the criteria for the Sts, only the difference from the criteria of EDs was that the amplitude of the after-slow component had to be < 50% compared to the apical component. According to these amplitude-quantitative criteria, 59 samples (32 EDs and 27 Sts) out of 68 samples (32 EDs and 36 Sts) fulfilled these criteria (Analysis A in **Figure 1**). On the other hand, the remaining nine Sts showed that the amplitude of the after-slow component was > 50% compared to the apical component and, thus, only compatible as visually defined samples. They were labeled as "borderline Sts" and separately analyzed (Analysis B in **Figure 1**).

The definition of after-slow activity was as follows: slow activity immediately following the apical component and the similar distribution and the same polarity as the preceding apical component (Selwa, 2010).

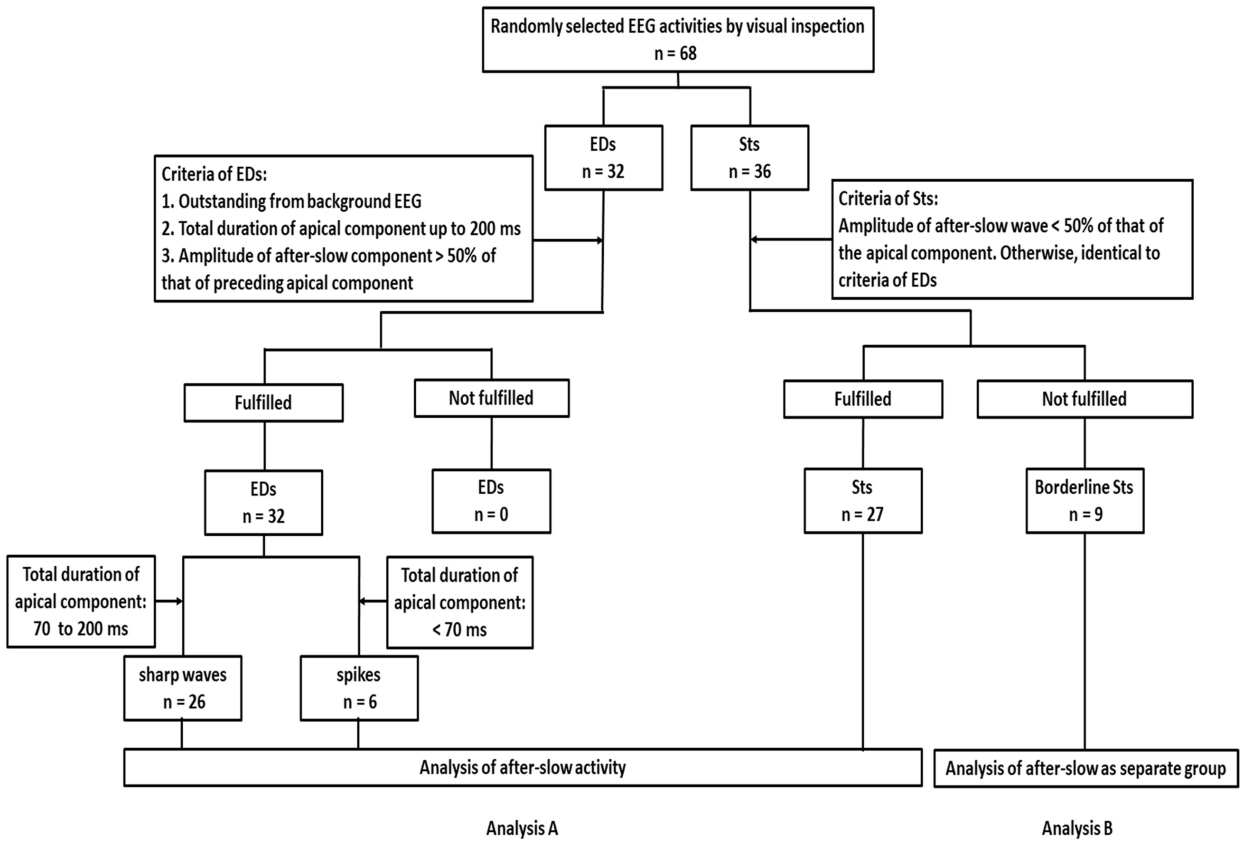

FIGURE 1 | Flow diagram of recruitment and classification of epileptiform discharges [epileptiform discharges (EDs): sharp waves and spikes] and sharp transients (Sts) based on the criteria of this study. First, a random selection of typical samples of 68 Electroencephalography (EEG) activities is done according to the annotations that have been already labeled for clinical purposes by visual inspection. The 68 EEG activities consist of 32 EDs and 36 Sts. Then the following criteria are adopted for EDs: (1) outstanding from the background EEG, (2) total duration of apical component up to 200 ms, and (3) the amplitude of after-slow component being > 50% of the amplitude of the immediately preceding apical component. About the criteria for the Sts, the amplitude of the after-slow component has to be < 50% that of the apical component. Otherwise, identical to criteria of EDs. Analysis A, according to these amplitude-quantitative criteria, among 68 activities, 32 EDs and 27 Sts fulfill the criteria. Then sharp waves and spikes are differentiated based on the total duration of the apical component (sharp waves: 70–200 ms and spikes: < 70 ms) and analysis of after-slow activities is performed. Analysis B, the remaining nine Sts do not fulfill the amplitude criteria but are visually defined, so that they are labeled as borderline Sts. They are considered and analyzed as a separate group.

Analysis of Electroencephalography Activities

After selecting the 59 EEG samples, the 5 s EEG segments including the selected activities were chosen, and the following analysis was performed by using averaged reference montage of all the electrodes (MATLAB version R2015b; MathWorks, Natick, MA, United States). We visually selected one channel with the maximum apical component. In the case of the contaminated artifacts, no clear onset or end of either apical or after-slow component or the absence of an outstanding after-slow wave, then the second maximum apical activity in a different channel was selected (eight activities). For analysis with different TC, we adopted three different TC conditions (long TC: 2 s; conventional TC: 0.3 s; and short TC: 0.1 s).

After selecting the channel, the apical and after-slow components were divided into two segments—half-wave 1 (HW1; the ascending phase) and half-wave 2 (HW2; the descending phase) —by the peak detection algorithm (**Figure 2**). Next, the amplitudes of the apical and after-slow components were calculated by taking the onset of the apical component as the baseline point (**Figure 2**). The duration of each HW1 and HW2 was measured by defining the time between the corresponding minima and peak. The total duration of the apical and after-slow components was calculated as the sum of the durations of HW1 and HW2, respectively (**Figure 2**; Dingle et al., 1993; Rakhade et al., 2007).

About the analysis of after-slow activity, i.e., amplitude vs. total area, we finally adopted only the total area as an analysis parameter under the three different TCs by using the double tangent line method (**Figure 3A**). We did not adopt the amplitude because the baseline point of background activity for amplitude measurement varied very much when the display TC was changed.

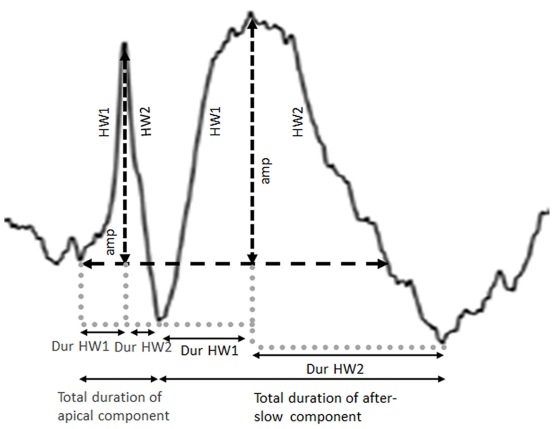

FIGURE 2 | Definition of amplitude (amp) and total duration calculated for both the apical and after-slow wave components. Each apical and after-slow wave component is divided into two segments, half-wave 1 (HW1: the ascending phase) and half-wave 2 (HW2: the descending phase), by the peak detection algorithm, and the amplitudes of the apical and after-slow wave components are calculated. The duration of each half-wave (Dur HW1 and Dur HW2) is calculated by defining the time between the corresponding minima and peak.

Analysis of Borderline Sharp Transients

About nine Sts that did not fulfill the amplitude criteria of Sts were labeled as "borderline Sts" (Analysis B in **Figure 1**). Similar to Analysis A in **Figure 1**, the total area of the after-slow activities was analyzed under the three different TCs.

Analysis of High-Frequency Activity

For further endorsement of two groups of EDs and Sts, HFA associated with the apical component of the EDs and Sts was also investigated (MATLAB version R2017b; MathWorks, Natick, MA, United States). Before analysis of HFA for appropriate averaged montage, if the EEG signal of a certain electrode was found to be accompanied by any artifact, the electrode channel with artifact was excluded from the reference channels of the averaged montage (8 EDs and 15 Sts). We tested two frequency bands, one with a low-frequency filter with 40 Hz and the other with an 80 Hz, zero-phase bidirectional fourth-order Butterworth filter. HFA was defined as an event of at least two consecutive peaks in these frequency bands, amplitude greater than -2 SD from the baseline, interval less than 0.03 and 0.015 s for 40 and 80 Hz, respectively. HFA was examined within the period of 50 ms before and 50 ms after the visually defined peak of the apical component. If HFA (40 or 80 Hz or both) was found within or some overlapping with this period, HFA was considered as associated with the apical component of EDs and Sts.

Statistical Analysis

To evaluate the differences in the total area of the after-slow activity among the three different TCs, we conducted the Friedman test followed by the Dunn–Bonferroni *post hoc* tests for pair wise comparison of EDs and Sts separately. We also compared the total area and total duration of the after-slow activity between EDs and Sts under the TC 0.3 s condition by using the Mann–Whitney *U*-test.

To examine the relationship between the width of apical component and size of after-slow, Kendall's tau-b correlation analysis with scatter plots was done between the total area of after-slow of EDs and Sts under three different TCs and a total duration of apical component (calculated in TC 0.3 s), separately.

To assess the difference of HFA between EDs and Sts, we performed Pearson's chi-squared analysis of all 68 activities (32 EDs and 36 Sts). It was also checked for 59 activities (32 EDs and 27 Sts) after excluding borderline nine Sts from 68 samples, separately. $p < 0.05$ was considered as statistically significant.

RESULTS

Analysis of Total Area of After-Slow Among the Three Different Time Constant Conditions

Regarding the total area of 59 after-slow, 40 activities (preceded by 26 sharp waves, six spikes, and eight Sts) showed the largest total area under TC 2s (**Figures 3B–D** and Analysis A in **Figure 4**). On the other hand, two and 17 after-slow activities (all

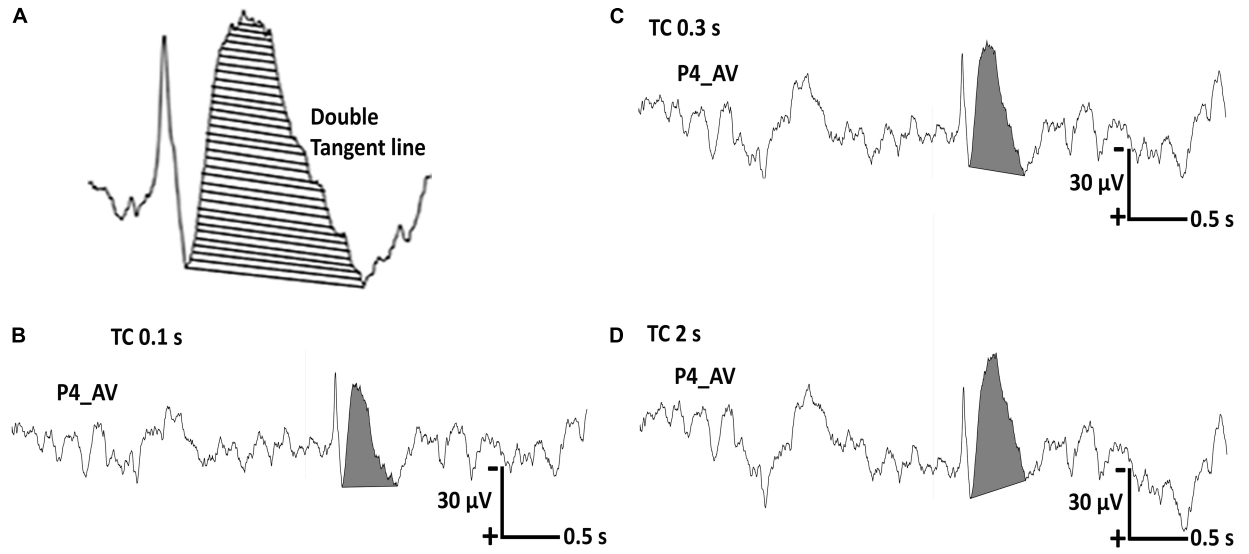

FIGURE 3 | Representative regional sharp wave in one patient with a recording time constant (TC) of 10 s. **(A)** The total area of the after-slow is calculated using the double tangent line method. **(B)** The total area of the after-slow under TC 0.1 s is 9.6837 μVs. **(C,D)** The same parameter under TC 0.3 s is 13.8499 μVs and that under TC 2 s is 15.6579 μVs, respectively.

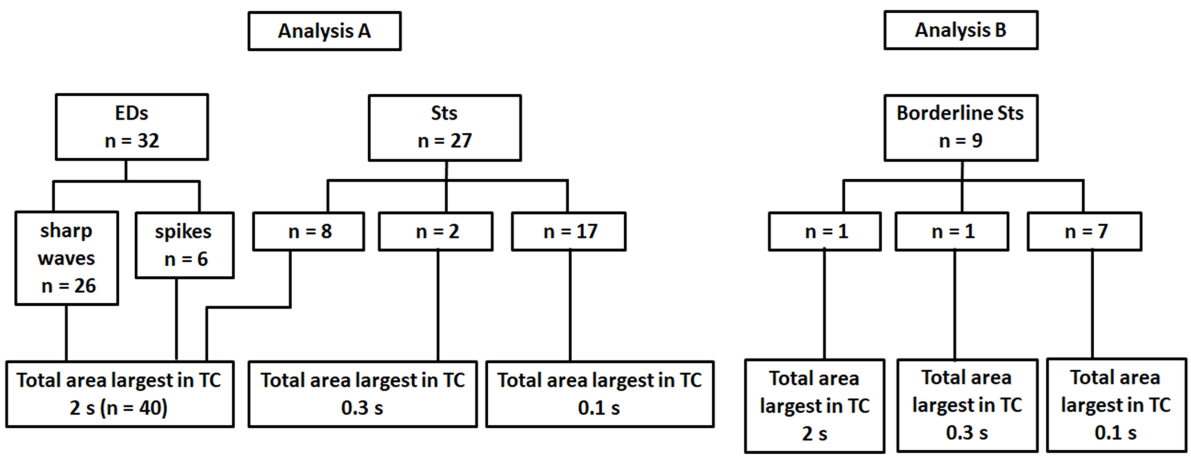

FIGURE 4 | The total area of after-slow activities of 32 EDs and 36 Sts under three different TC conditions. Analysis A, the after-slow activities of all 32 EDs (26 sharp waves and six spikes) show the largest total area under TC 2 s. Among 27 Sts, eight, two, and 17 after-slow activities show the largest total area under TCs 2, 0.3, and 0.1 s, respectively. Analysis B, about the after-slow activities of nine borderline Sts, one, one, and seven activities show the largest total area under TCs 2, 0.3, and 0.1 s, respectively.

preceded by Sts) showed the largest total area under TCs 0.3 and 0.1 s, respectively (Analysis A in **Figure 4**).

Figure 5 showed the representative waveforms of the after-slow of EDs and Sts in different TCs. It was visually evident that compared with Sts, the after-slow of EDs displayed with TC 2 s was exaggerated than that with TC 0.3 s which can be helpful to differentiate EDs and Sts visually. As for EDs, after Bonferroni adjustments, the total area of the after-slow was significantly larger under TC 2 s (mean ± SD: 25.25 ± 13.35 μVs) than under 0.3 s (21.98 ± 10.30 μVs) ($p < 0.001$) and 0.1 s (16.78 ± 7.79 μVs) ($p < 0.001$), and it was significantly larger under TC 0.3 s than that under TC 0.1 s ($p < 0.001$) (**Figure 6**). By contrast, no significant differences were seen in the same parameter of Sts among three different TCs (TC 2 s: 6.88 ± 5.81 μVs, TC 0.3 s: 6.87 ± 5.69 μVs, and TC 0.1 s: 7.09 ± 5.82 μVs) ($p > 0.05$) (**Figure 7**).

Analysis of Total Area and Total Duration of After-Slow With Time Constant of 0.3 s

The EDs showed a significantly larger total area of the after-slow (21.98 ± 10.30 μVs) as compared with those of Sts (6.87 ± 5.69 μVs) under TC 0.3 s ($p < 0.001$) according to their definition. In addition, the total duration

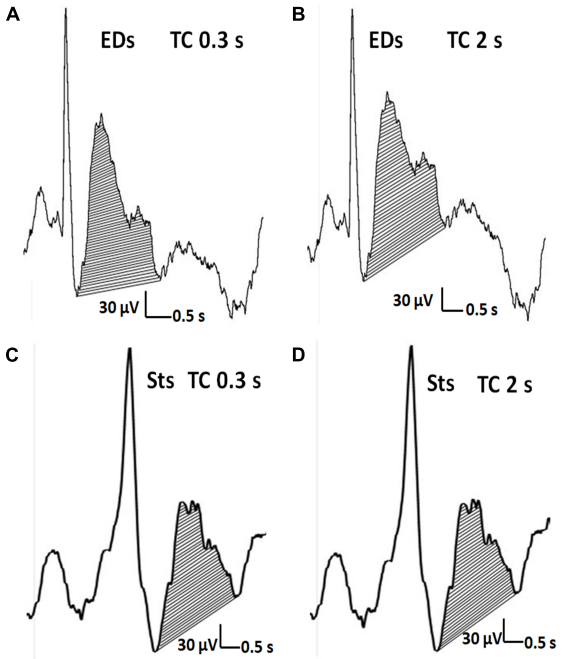

FIGURE 5 | The distinction of EDs from Sts. **(A,C)** The after-slow wave of an EDs (>50% of the amplitude of preceding activity) and Sts (<50% of the amplitude of preceding activity). **(A,B)** Concerning EDs, the after-slow wave is exaggerated with TC of 2 s compared with TC of 0.3 s. **(C,D)** In contrast, the much lesser after-slow wave of Sts is almost the same as one with TC of 2 s.

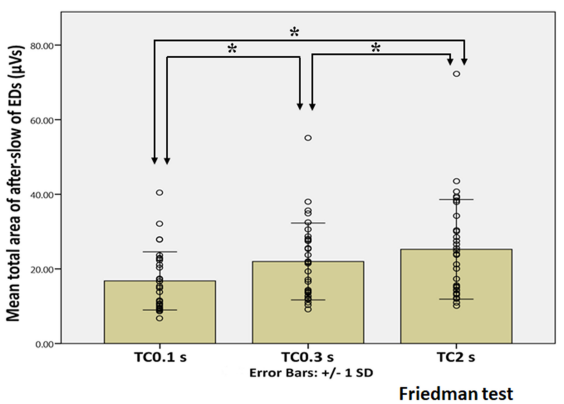

FIGURE 6 | Statistical analysis of the total area of the after-slow of EDs under three different TC conditions. X and Y axes show three different TCs and the mean total area of the after-slow of EDs, respectively, error bars indicate ± 1 SD and the circle shows the total area of each EDs in three different TCs. The total area of the after-slow under TC 2 s is significantly larger than those under TC 0.3 s and 0.1 s ($p < 0.001$). The same parameter is also significantly larger under TC 0.3 s than under TC 0.1 s ($p < 0.001$). *Indicates statistical significance.

of the after-slow of EDs (437.19 ± 125.07 ms) was also significantly longer as compared with Sts (285.41 ± 144.21 ms) ($p < 0.001$).

With respect to the correlation analysis, no significant relationship was found in any combination between total area

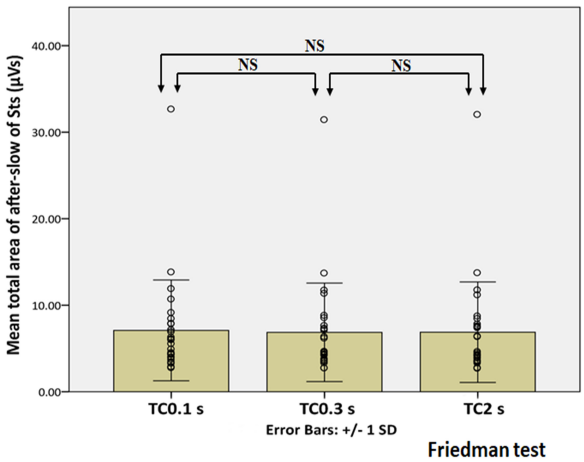

FIGURE 7 | Statistical analysis of the total area of the after-slow of Sts under three different TCs. X and Y axes show three different TCs and the mean total area of the after-slow of Sts, respectively, error bars indicate ± 1 SD, and the circle shows the total area of each Sts in three different TCs. No significant difference is observed under three different TCs. NS indicates not statistically significant.

of after-slow and total duration of apical component in EDs (TC 2 s: τb = 0.219; TC 0.3 s: τb = 0.223 and TC 0.1 s: τb = 0.235) and Sts (TC 2 s: τb = −0.191; TC 0.3 s: τb = −0.129 and TC 0.1 s: τb = −0.077), respectively, as shown by scatter plots in **Supplementary Figures 1, 2**.

It was initially concerned that the apical component of EDs may have a longer duration, and thus, they may be accompanied by larger after-slow, but it did not happen. Neither happened in the case of Sts. It simply convinced us that visually defined EDs and Sts could have a similar range of duration of apical components between each other and the degree of after-slow is independent of the apical components *per se*.

Analysis of Borderline Sharp Transients

About the nine after-slow activities of borderline Sts, one, one, and seven activities showed the largest total area under TCs 2, 0.3, and 0.1 s, respectively (Analysis B in **Figure 4**). Thus, nine borderline Sts showed a similar tendency to that of 27 Sts under three different TCs.

High-Frequency Activity Analysis

About the analysis of HFA, among all 68 activities (32 EDs and 36 Sts), HFA was found with the apical component of 21 EDs (65.6%) and 12 Sts (33.3%). In the Pearson's chi-squared analysis of all 68 activities (32 EDs and 36 Sts), it was found that the HFA was significantly more often with the apical component of EDs as compared with Sts ($p = 0.008$) (**Figure 8**). Furthermore, after exclusion of borderline nine Sts (32 EDs and 27 Sts), HFA remains significantly more associated with EDs (21 activities, 65.6%) in comparison to Sts (nine activities, 33.3%) ($p = 0.013$) (**Figure 9**).

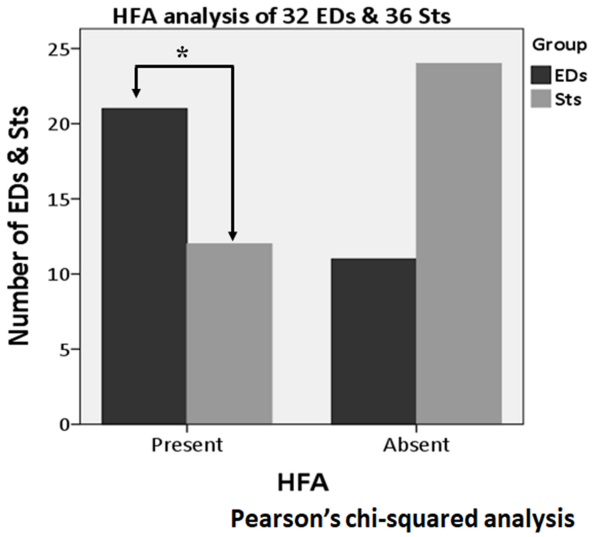

FIGURE 8 | High-frequency activity (HFA) analysis of all 68 activities (32 EDs and 36 Sts). Compared to Sts (12 activities), HFA is found significantly more often with the apical component of EDs (21 activities) (p = 0.008). *Indicates statistical significance.

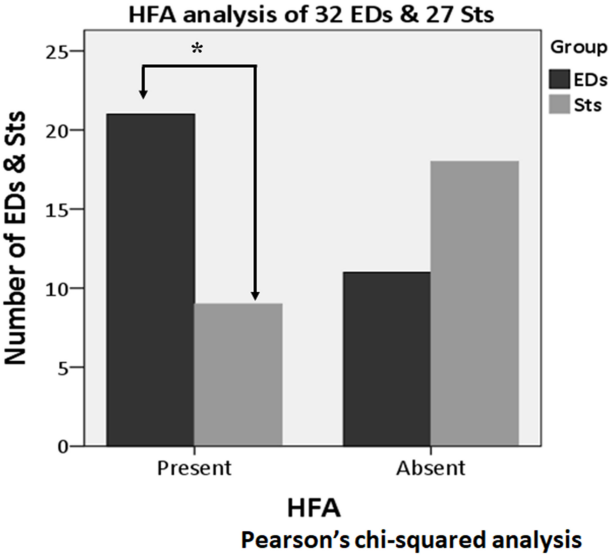

FIGURE 9 | High-frequency activity analysis of 59 activities (32 EDs and 27 Sts) after excluding borderline nine Sts. HFA is significantly more associated with EDs (21 activities) as compared with Sts (nine activities) (p = 0.013). *Indicates statistical significance.

DISCUSSION

In this study, we demonstrated two main findings for the real world's patient EEG data. First, the total area of the after-slow activity of EDs with long TC (2 s) was significantly larger than that of conventional (0.3 s) and short (0.1 s) TCs. By contrast, no significant difference in the same parameter of Sts was observed. Second, the total duration of the after-slow activity of EDs was also significantly longer than that of Sts.

Change in the Total Area of the After-Slow Under Long Time Constant

To the best of our knowledge, this is the first systematic study to disclose that long TC is useful for defining EDs by the total area of the after-slow in comparison with Sts. Although EDs showed a significantly larger total area of the after-slow than that of Sts even with TC 0.3 s, our findings indicate that the enlarged total area in long TC is also a useful biomarker to differentiate EDs from Sts, especially when equivocal after-slow waves are observed by TC 0.3 or 0.1 s (**Figures 5A,C**). Our findings further support the IFCN guideline stating that the low filter should be set to 0.16 Hz or less for recording except for specific or difficult clinical conditions (Nuwer et al., 1998).

Regarding EDs recorded from scalp EEG as field potentials, the apical component reflects the synchronized intracellular PDS, i.e., giant, abnormal excitatory postsynaptic potentials from the generator point of view, mainly occurring in the cortical pyramidal neurons. They are immediately followed by hyperpolarized activity as the recurrent inhibition that corresponds to after-slow activity at least in the experimental data (Engel, 1989). Therefore, even in the clinical EEG, after-slow is also an important parameter for defining EDs. On the other hand, possible generator mechanisms of Sts depend on its definition as follows. Namely, it is noted that (a) very ill-defined EDs and (b) the pyramidal neurons in the cerebral cortices that generate physiological oscillations at frequencies similar to spikes (i.e., beta oscillations and mu rhythms), can be prominent in certain regions (Janca et al., 2014). For EDs, the total duration of after-slow was significantly longer than that of Sts as indicated in result section "Analysis of Total Area and Total Duration of After Slow with Time Constant of 0.3 s." Compared to physiological EEG activity, the hyperpolarized activity immediately after PDS contains a slower frequency band because of prolonging depression in the excitability during this phase as described in previous human intracranial EEG studies (Neckelmann et al., 2000; Urrestarazu et al., 2006; Matsumoto et al., 2013; Von Ellenrieder et al., 2016). Based on these findings, our findings suggest that long TC may be useful for the selective enhancement of hyperpolarized activity (after-slow) immediately after PDS (EDs).

There may be some speculation that the augmentation of after-slow activity of EDs by changing TC setting is related to the longer total duration of apical component of EDs in addition to after-slow as described later. However, in this study, the total duration of the apical component did not correspond to the changes of the total area of after-slow in EDs and Sts (**Supplementary Figures 1, 2**).

Total Duration of the After-Slow Under the Conventional Time Constant Condition (0.3 s)

Epileptiform discharges are defined to show clearer after-slow than Sts; therefore, the total duration was also significantly longer

in EDs. The total duration may also be a useful parameter for differentiating after-slow activities of EDs from those of Sts.

Analysis of Borderline Sharp Transients

With respect to the analysis of borderline nine Sts, the total area of after-slow activities showed a similar tendency to that of 27 Sts under three different TC conditions. It may imply that certified electroencephalographers visually inspected mainly the total area rather than the amplitude of after-slow activities that practically leads to the correct conclusion. Namely, although certified electroencephalographers explicitly understand the amplitude criteria, they implicitly make the judgment by the factor of total area. It may validate the total area as the important criteria to differ between EDs and Sts.

About the differences in the total area of the after-slow activity of all 36 Sts among three different TCs, although the total area of after-slow under TC 0.1 s (mean ± SD: 6.85 ± 5.37 μVs) was significantly larger than that under 2 s (6.60 ± 5.35 μVs) (p = 0.003), there were no significant differences between any other comparisons after Bonferroni adjustments. So, under long TC (2 s) setting the after-slow of Sts remain almost similar to that of under TC 0.3 s.

High-Frequency Activity Analysis

High-frequency activity is considered to be associated with epileptogenicity (Shibata et al., 2016) because the increase of HFA is usually seen with the apical component of EDs (Kobayashi et al., 2009). As there is no definite characterization of HFA, the less strict inclusion criteria of two consecutive peaks were adopted in this study.

With respect to the other types of benign Sts such as benign focal EDs in childhood (Beaussart, 1972; Lüders et al., 1987) and benign epileptiform transients of sleep (White et al., 1977), these benign activities are usually accompanied by lower amplitude after-slow than that of the preceding apical component. To the best of our knowledge, as there is no clear definition or criteria of Sts with small after-slow except for anecdotal impression or experience like 50% of borderline, we initially selected the amplitude of after-slow more and less than 50% that of preceding apical component as the criteria of EDs and Sts, respectively. However, in this study, HFA analysis showed a clearer association with EDs than with Sts, which further justifies the differentiation of these two groups (EDs and Sts).

Limitations

This study has some limitations. First, it was a retrospective study based on a relatively small number of EEG activities in a single institute. In addition, no specific patients were selected other than having epilepsy. Therefore, further studies with larger populations of patients from homogeneous clinical backgrounds would be warranted to confirm the present findings and to further clarify its clinical significance based on epilepsy classifications, namely, generalized and partial epilepsy. Second, we randomly chose relatively typical EDs and Sts waveforms, and also the number of each sample from each patient was relatively small. We purposely excluded pure spike without after-slow, since the pure spike is atypical except for repetitive spikes or polyspikes. Nevertheless, these waveforms are less frequent. Future studies involving these waveforms would also be necessary to clarify the utility in practical EEG settings. Third, we tentatively chose the amplitude of after-slow more and less than 50% that of the preceding apical component to differentiate EDs and Sts, respectively. Further studies in the clinical setting are needed to confirm the current findings and to define the criteria of EDs and Sts more precisely. Nevertheless, the consistent results using HFA could warrant the present finding. Fourth, in this study, we did not inspect possible mechanisms of neurons associated with different TC. Hence, future studies regarding these patterns of neuronal activity from the viewpoint of seizure would be useful to understand EDs further in the scalp EEG. Finally, long TC may provide or exaggerates not only after-slow activities, but also slower artifacts such as movements, sweat, slow eye movement, electrode lead wire movement, and so on. These slower artifacts may interfere with the interpretation of after-slow activities if their frequency is close to the frequency of after-slow.

Even though we take all of those limitations into account, the current study may shed the light on the useful approach of after-slow activity with a long TC of 2 s in scalp EEG to differentiate between EDs and Sts that was supported by HFA analysis.

CONCLUSION

In this study, the EEG analysis showed that a long TC setting for EEG display is beneficial for differentiating after-slow activities between EDs and Sts. These findings are derived from the results of analysis on the total area of after-slow and supported by findings of HFA analysis. These findings at least may endorse the current operational definitions of EDs and Sts, and also the IFCN guidelines (1998). Total area rather than the amplitude of the after-slow was much more consistent with a visual inspection of EDs and Sts. Future studies to validate the clinical significance of current findings are, therefore, warranted.

MEETINGS IN WHICH THE STUDY HAS BEEN PRESENTED

Preliminary results of this study were presented at 71st American Epilepsy Society Annual Meeting, Washington D.C., the United States of America, December 1–5, 2017; at XXIII World Congress of Neurology, Kyoto, Japan, September 16–21, 2017 and at the 50th Congress of the Japan Epilepsy Society, Shizuoka, Japan, October 7–9, 2016.

DATA AVAILABILITY STATEMENT

The raw data supporting the conclusions of this article will be made available by the authors, without undue reservation.

ETHICS STATEMENT

The studies involving human participants were reviewed and approved by the institutional review board of Kyoto University (No. R0603). Written informed consent for participation was not required for this study in accordance with the national legislation and the institutional requirements.

AUTHOR CONTRIBUTIONS

SS did the initiation and planning of the project, did data collection and analysis, wrote the first draft of the manuscript, edited subsequent drafts, and created figures. TH aided in the planning of the project, verified the analytical methods, and edited the manuscripts. MD and AS provided additional patient information. MM contributed to the production of scripts for analyzing data from EEG. RT contributed to conception and design. AI contributed to the initiation and conceptualization of the project, supervised the findings of this study, and edited the manuscript. All authors contributed to the article and approved the submitted version.

FUNDING

TH reports grants from MEXT (KAKENHI 20K07902) from the Japan Society for the Promotion of Science (JSPS) and the Japan Epilepsy Research Foundations during the conduct of this study. AI reports grants from MEXT (KAKENHI 19803574) from the Japan Society for the Promotion of Science (JSPS).

SUPPLEMENTARY MATERIAL

The Supplementary Material for this article can be found online at: https://www.frontiersin.org/articles/10.3389/fnhum.2021.748893/full#supplementary-material

Supplementary Figure 1 | Scatter plot with linear regression fit (solid line) and a 95% CI (dashed lines) for the correlation between the total area of the after-slow of all 32 EDs (26 sharp waves and six spikes) under three different TC conditions and total duration of the apical component under TC 0.3 s. No significant relation is observed between total duration of apical component under TC 0.3 s and total area of after-slow in **(A)** TCs 2 s ($\tau b = 0.219$), **(B)** 0.3 s ($\tau b = 0.223$), and **(C)** 0.1 s ($\tau b = 0.235$), respectively.

Supplementary Figure 2 | The same graph is made for 27 Sts. No significant relation is found between the total duration of the apical component under TC 0.3 s and total area of after-slow in **(A)** TCs 2 s ($\tau b = -0.191$), **(B)** 0.3 s ($\tau b = -0.129$), and **(C)** 0.1 s ($\tau b = -0.077$), respectively.

REFERENCES

Aykut, M., Tankisi, H., Duez, L., Sejer, V., Udupi, A., Wennberg, R., et al. (2020). Clinical Neurophysiology Optimized set of criteria for defining interictal epileptiform EEG discharges. *Clin. Neurophysiol.* 131, 2250–2254. doi: 10.1016/j.clinph.2020.06.026

Beaussart, M. (1972). Benign epilepsy of children with rolandic (centro-temporal) paroxysmal foci a clinical entity, study of 221 cases. *Epilepsia* 13, 795–811. doi: 10.1111/j.1528-1157.1972.tb05164.x

Brazier, M. A. B., Cobb, W. A., Fischgold, H., Gastaut, H., Gloor, P., Hess, R., et al. (1961). Preliminary proposal for an EEG terminology by the terminology committee of the international federation for electroencephalography and clinical neurophysiology. *Electroencephalogr. Clin. Neurophysiol.* 13, 646–650.

Constantino, T., and Rodin, E. (2012). Peri-ictal and interictal, intracranial infraslow activity. *J. Clin. Neurophysiol.* 29, 298–308. doi: 10.1097/WNP.0b013e3182624289

Dingle, A. A., Jones, R. D., Carroll, G. J., and Fright, W. R. A. (1993). Multistage system to detect epileptiform activity in the EEG. *IEEE Trans. Biomed. Eng.* 40, 1260–1268. doi: 10.1109/10.250582

Engel, J. J. (1989). *Seizures and Epilepsy*, 1st Edn. Philadelphia, PA: F. A. Davis Company.

Fisch, B. J., and Spehlmann, R. (1999). *Fisch and Spehlmann's EEG Primer: Basic Principles of Digital and Analog EEG*, 3rd Edn. Amsterdam: Elsevier.

Gil-Nagel, A., and Abou-Khalil, B. (2012). "Electroencephalography and video-electroencephalography," in *Handbook Clinical Neurology*, Vol. 107, eds H. Stefan and W. H. Theodore (Amsterdam: Elsevier), 323–345. doi: 10.1016/B978-0-444-52898-8.00020-3

Janca, R., Jezdik, P., Cmejla, R., Tomasek, M., Worrell, G. A., Stead, M., et al. (2014). Detection of interictal epileptiform discharges using signal envelope distribution modelling: application to epileptic and non-epileptic intracranial recordings. *Brain Topogr.* 28, 172–183. doi: 10.1007/s10548-014-0379-1

Kobayashi, K., Jacobs, J., and Gotman, J. (2009). Detection of changes of high-frequency activity by statistical time-frequency analysis in epileptic spikes. *Clin. Neurophysiol.* 120, 1070–1077. doi: 10.1016/j.clinph.2009.03.020

Kobayashi, K., Oka, M., Akiyama, T., Inoue, T., Abiru, K., Ogino, T., et al. (2004). Very fast rhythmic activity on scalp EEG associated with epileptic spasms. *Epilepsia* 45, 488–496. doi: 10.1111/j.0013-9580.2004.45703.x

Lüders, H., Lesser, R. P., Dinner, D. S., and Morris, H. H. (1987). "Benign focal epilepsy of childhood," in *Epilepsy Electroclinical Syndromes*, eds H. Lüders and R. P. Lesser (London: Springer), 303–346. doi: 10.1007/978-1-4471-1401-7_13

Matsumoto, A., Brinkmann, B. H., Stead, S. M., Matsumoto, J., Kucewicz, M. T., Marsh, W. R., et al. (2013). Pathological and physiological high-frequency oscillations in focal human epilepsy. *J. Neurophysiol.* 110, 1958–1964. doi: 10.1152/jn.00341.2013

Maus, D., Epstein, C. M., and Herman, S. T. (2011). "Digital EEG," in *Niedermeyer's Electroencephalogr. Basic Principles of Clinical Application Relation Fields*, 6th Edn, eds E. Niedermeyer, D. L. Schomer, and F. H. L. da Silva (Philadelphia, PA: Wolters Kluwer Health/Lippincott Williams & Wilkins), 119–141.

Misra, U. K., and Kalita, J. (2005). *Clinical Electroencephalography*, 1st Edn. Amsterdam: Elsevier India Pvt. Limited.

Neckelmann, D., Amzica, F., and Steriade, M. (2000). Changes in neuronal conductance during different components of cortically generated spike-wave seizures. *Neuroscience* 96, 475–485. doi: 10.1016/S0306-4522(99)00571-0

Noachtar, S., Binnie, C., Ebersole, J., Mauguière, F., Sakamoto, A., and Westmoreland, B. (1999). A Glossary of terms most commonly used by clinical electroencephalographers and proposal for the report form for the EEG Findings. The international federation of clinical neurophysiology. *Electroencephalogr. Clin. Neurophysiol.* 52, 21–41. doi: 10.1055/s-2003-812583

Nuwer, M. (1997). Assessment of digital EEG, quantitative EEG, and EEG brain mapping: report of the American Academy of Neurology and the American Clinical Neurophysiology Society. *Neurology* 49, 277–292.

Nuwer, M. R., Comi, G., Emerson, R., Fuglsang-Frederiksen, A., Guérit, J.-M., Hinrichs, H., et al. (1998). IFCN standards for digital recording of clinical EEG. *Electroencephalogr. Clin. Neurophysiol.* 106, 259–261. doi: 10.1016/S0013-4694(97)00106-5

Rakhade, S. N., Shah, A. K., Agarwal, R., Yao, B., Asano, E., and Loeb, J. A. (2007). Activity-dependent gene expression correlates with interictal spiking in human neocortical epilepsy. *Epilepsia* 48, 86–95. doi: 10.1111/j.1528-1167.2007.01294.x

Selwa, L. M. (2010). "Epileptiform activity, seizures and epilepsy syndromes," in *Readiing EEGs A Pract. Approach*, eds L. J. J. Greenfield, J. D. Geyer, and P. R. Carney (Philadelphia, PA: Lippincott Williams & Wilkins), 93–134.

Shibata, T., Yoshinaga, H., Akiyama, T., and Kobayashi, K. (2016). A study on spike focus dependence of high-frequency activity in idiopathic focal epilepsy in childhood. *Epilepsia Open* 1, 121–129. doi: 10.1002/epi4.12014

Silverman, D. (1965). The anterior temporal electrode and the ten-twenty system. *Am. J. EEG Technol.* 5, 11–14. doi: 10.1080/00029238.1965.11080641

Sinha, S. R., Sullivan, L., Sabau, D., San-Juan, D., Dombrowski, K. E., Halford, J. J., et al. (2016). American clinical neurophysiology society guideline 1: minimum technical requirements for performing clinical electroencephalography. *J. Clin. Neurophysiol.* 33, 303–307. doi: 10.1097/WNP.0000000000000308

Urrestarazu, E., Jirsch, J. D., LeVan, P., Hall, J., and Gotman, J. (2006). High-frequency intracerebral EEG activity (100-500 Hz) following interictal spikes. *Epilepsia* 47, 1465–1476. doi: 10.1111/j.1528-1167.2006.00618.x

Von Ellenrieder, N., Frauscher, B., Dubeau, F., and Gotman, J. (2016). Interaction with slow waves during sleep improves discrimination of physiologic and pathologic high-frequency oscillations (80-500 Hz). *Epilepsia* 57, 869–878. doi: 10.1111/epi.13380

White, J. C., Langston, J. W., and Pedley, T. A. (1977). Benign epileptiform transients of sleep: clarification of the small sharp spike controversy. *Neurology* 27, 1061–1068. doi: 10.1212/wnl.27.11.1061

Winesett, S., and Benbadis, S. R. (2008). Which electroencephalogram patterns are commonly misread as epileptiform? *TouchneurologyCom* 3, 101–104. doi: 10.17925/ENR.2008.03.02.101

Conflict of Interest: AI and MM were members of the Department of Epilepsy, Movement Disorders and Physiology which is the Industry-Academia Collaboration Courses, supported by the Eisai Co., Ltd., Nihon Kohden Corporation, Otsuka Pharmaceutical Co., and UCB Japan Co., Ltd.

The remaining authors declare that the research was conducted in the absence of any commercial or financial relationships that could be construed as a potential conflict of interest.

Publisher's Note: All claims expressed in this article are solely those of the authors and do not necessarily represent those of their affiliated organizations, or those of the publisher, the editors and the reviewers. Any product that may be evaluated in this article, or claim that may be made by its manufacturer, is not guaranteed or endorsed by the publisher.

frontiers in Behavioral Neuroscience

ORIGINAL RESEARCH
published: 03 November 2021
doi: 10.3389/fnbeh.2021.750869

Heterogeneous GAD65 Expression in Subtypes of GABAergic Neurons Across Layers of the Cerebral Cortex and Hippocampus

*Yuki Kajita and Hajime Mushiake**

Department of Physiology, Graduate School of Medicine, Tohoku University, Sendai, Japan

Gamma-aminobutyric acid (GABA), a major inhibitory transmitter in the central nervous system, is synthesized via either of two enzyme isoforms, GAD65 or GAD67. GAD65 is synthesized in the soma but functions at synaptic terminals in an activity-dependent manner, playing a distinct role in excitatory-inhibitory balance. However, the extent to which each GABAergic subtype expresses GAD65 in the resting state remains unclear. In this study, we compared GAD65 expression among six GABAergic subtypes: NPY^+, $nNOS^+$, PV^+, SOM^+, CR^+, and CCK^+. According to the results, the GABAergic subtypes were classified into two groups per region based on GAD65 expression levels: high-expression (NPY^+ and $nNOS^+$) and low-expression groups (PV^+, SOM^+, CR^+, and CCK^+) in the cerebral cortex and high-expression (NPY^+, $nNOS^+$, and CCK^+) and low-expression groups (PV^+, SOM^+, and CR^+) in the hippocampus. Moreover, these expression patterns revealed a distinct laminar distribution in the cerebral cortex and hippocampus. To investigate the extent of GAD65 transport from the soma to synaptic terminals, we examined GAD65 expression in colchicine-treated rats in which GAD65 was synthesized in the soma but not transported to terminals. We found a significant positive correlation in GAD65 expression across subtypes between colchicine-treated and control rats. In summary, each GABAergic subtype exhibits a distinct GAD65 expression pattern across layers of the cerebral cortex and hippocampus. In addition, the level of GAD65 expression in the soma can be used as a proxy for the amount of GAD65 in the cytoplasm. These findings suggest that exploration of the distinct profiles of GAD65 expression among GABAergic subtypes could clarify the roles that GABAergic subtypes play in maintaining the excitatory-inhibitory balance.

Keywords: cerebral cortex, GABAergic subtype, GAD65, hippocampus, rat

OPEN ACCESS

Edited by:
Shozo Tobimatsu,
Kyushu University, Japan

Reviewed by:
Hideo Hagihara,
Fujita Health University, Japan
Ileana Hanganu-Opatz,
University of Hamburg, Germany

***Correspondence:**
Hajime Mushiake
hmushiak@med.tohoku.ac.jp

Specialty section:
This article was submitted to Pathological Conditions, a section of the journal Frontiers in Behavioral Neuroscience

Received: *31 July 2021*
Accepted: *16 September 2021*
Published: *03 November 2021*

Citation:
Kajita Y and Mushiake H (2021) Heterogeneous GAD65 Expression in Subtypes of GABAergic Neurons Across Layers of the Cerebral Cortex and Hippocampus. Front. Behav. Neurosci. 15:750869. doi: 10.3389/fnbeh.2021.750869

INTRODUCTION

The inhibitory neurotransmitter gamma-aminobutyric acid (GABA) is widely distributed in the central nervous system and is synthesized from glutamate via two isoforms of glutamic acid decarboxylase (GAD): GAD67 and GAD65. These two isoforms are encoded by distinct genes but are co-expressed in most GABAergic interneurons (Erlander et al., 1991; Feldblum et al., 1993). The mRNA (Dicken et al., 2015) and protein (Rimvall et al., 1993) expression of GAD67 is closely

related to GABA content, as GAD67 is responsible for basal and tonic GABA synthesis (Asada et al., 1997; Chattopadhyaya et al., 2007; Obata et al., 2008). On the other hand, GAD65 has a high affinity for the cofactor pyridoxal 5′-phosphate (Martin and Rimvall, 1993), and localizes strongly in axon terminals rather than in the soma (Esclapez et al., 1994). In addition, repeated electrical stimulation has been shown to increase GABA contents and its release (Bowdler et al., 1983) while increasing GAD65 expression (Jinno and Kosaka, 2009). These previous data suggest that GAD65 expression is closely related to activity-dependent and phasic GABA synthesis.

GAD67 and GAD65 expression are not evenly distributed within GABAergic neurons in various brain regions, including the cerebral cortex and hippocampus (Esclapez et al., 1994; Hendrickson et al., 1994; Houser and Esclapez, 1994). In particular, GAD65 expression in the soma is heterogeneous compared with that of GAD67 (Guo et al., 1997). Although the drivers of GAD65 expression remain unknown, this heterogeneous expression may depend on the diversity of GABAergic neuron properties. One previous study showed that GAD65 expression is lower in calcium-binding protein parvalbumin-positive (PV^+) cells in the hippocampus (Fukuda et al., 1997), suggesting that GAD65 expression depends on the interneuron subtype. GABAergic neurons are classified into multiple subtypes in addition to PV^+ cells based on chemical markers (Hendry et al., 1984; Gonchar and Burkhalter, 1997; Kubota and Kawaguchi, 1997; Jinno et al., 2001; Kawaguchi and Kondo, 2002; Gonchar et al., 2007). Elucidating the relationship between GABAergic subtypes and GAD65 expression would clarify the roles of GABAergic subtypes in activity-dependent and phasic inhibition under pathological conditions such as epileptic seizures and mental disorders.

To achieve this purpose, we compared GAD65 expression among several subtypes of neurons in the cerebral cortex and hippocampus under normal conditions. Although a variety of markers can be used to identify GABAergic subtypes, we followed the classification described in previous reports (Druga, 2009; Tricoire et al., 2010; Rudy et al., 2011; Tricoire and Vitalis, 2012; Perrenoud et al., 2013; Tremblay et al., 2016) and analyzed the following six subtypes: PV^+ neurons, somatostatin-positive (SOM^+) neurons, calretinin-positive (CR^+) neurons, cholecystokinin-positive (CCK^+) neurons, neuropeptide Y-positive (NPY^+) neurons, and neuronal nitric oxide synthase-positive ($nNOS^+$) neurons. This classification system was shared between the cerebral cortex and hippocampus. We also compared the laminar distribution of GAD65 expression by dividing the cerebral cortex and hippocampus into three layers: the superficial layer, pyramidal layer and deep layer. Additionally, to confirm that somatic expression reflects expression throughout the cytoplasm, we performed the same experiments using colchicine, which blocks axonal transport.

Briefly, each GABAergic subtype exhibited a distinct GAD65 expression pattern across the cerebral cortical and hippocampal layers. Additionally, GAD65 expression in the soma of different subtypes was significantly and positively correlated between colchicine-treated and control rats.

MATERIALS AND METHODS

Animals

We used male 8–12 weeks old Long-Evans rats (Institute for Animal Reproduction, Kasumigaura, Ibaraki, Japan, http://www.iar.or.jp) weighing 300–500 *g* each. These rats were housed in groups in a temperature- and humidity-controlled room under a 12-h-light/12-h-dark cycle with food and water available *ad libitum*. Efforts were made to minimize the number of animals used, as well as their pain and discomfort. All animal treatments were approved by the Tohoku University Committee for Animal Research, Seiryo Campus (Sendai, Japan).

Intraventricular Injection of Colchicine

To block axonal transport, colchicine (Sigma-Aldrich, Tokyo, Japan) dissolved in saline (100 μg/10 μl) was stereotactically injected 5 μl of solution into the bilateral lateral ventricle of the brain. Control group was injected equal (5 μl) volume of saline into the bilateral lateral ventricle of the brain. The surgery was performed under inhalation anesthesia with isoflurane (1–3%, Pfizer, Tokyo, Japan). 2 days later, the brains were processed for immunohistochemical investigation, as described below.

Tissue Preparation

Under deep nembutal anesthesia (Somnopentyl, 250 mg/kg body weight, intraperitoneally, Kyoritsu Seiyaku Co., Ltd., Tokyo Japan), the rats were transcardially perfused with saline containing 2 IU/mL heparin and then with 4% paraformaldehyde in 0.1M phosphate buffer (pH 7.4). The brains were removed and post-fixed in formaldehyde solution for 24 h at 4°C. Then, the brains were immersed in 30% sucrose solution in phosphate-buffered saline (PBS) for at least 24 h, and coronal sections (30 μm thick) were cut using a cryostat (Leica CM1950, Leica Microsystems, Nussloch, Germany).

Immunohistochemistry

The sections were washed in PBS for 10 min. After blocking with 3% bovine serum albumin in PBS for 1 h, the sections were incubated with primary antibodies overnight at 4°C and washed with PBS. The following antibodies were used in this study: mouse monoclonal anti-GAD65 antibody (1:300, BD Biosciences, San Jose, CA, United States), rabbit polyclonal anti-parvalbumin antibody (1:500, Abcam, Cambridge, United Kingdom), rabbit polyclonal anti-somatostatin antibody (1:500; Peninsula Lab, San Carlos, CA, United States), rabbit polyclonal anti-calretinin antibody (1:500, Proteintech group, Inc., Chicago, IL, United States), rabbit polyclonal anti-cholecystokinin antibody (1:100, Cloud-Clone Corp, Carlsbad, CA, United States), rabbit polyclonal anti-neuropeptide Y antibody (1:100, Proteintech group, Inc.), rabbit polyclonal anti-neuronal nitric oxide synthase antibody (1:800, Merck-Millipore, Temecula, CA, United States) and rabbit polyclonal anti-vesicular GABA transporter (VGAT) antibody (1:500, Gene Tex, Los Angeles, CA, United States). After washing three times with PBS, the brain sections were incubated with an

appropriate species-specific secondary antibody for 1 h—Alexa Fluor 488-conjugated goat anti-mouse immunoglobin (Ig) G (1:200, Abcam) or Alexa Fluor 647-conjugated goat anti-rabbit IgG (1:200, Merck-Millipore)—and then with 4′,6-diamidino-2-phenylindole dihydrochloride (DAPI) solution (1:500, Dojindo, Kamimashiki, Japan). After three washes with PBS, the sections

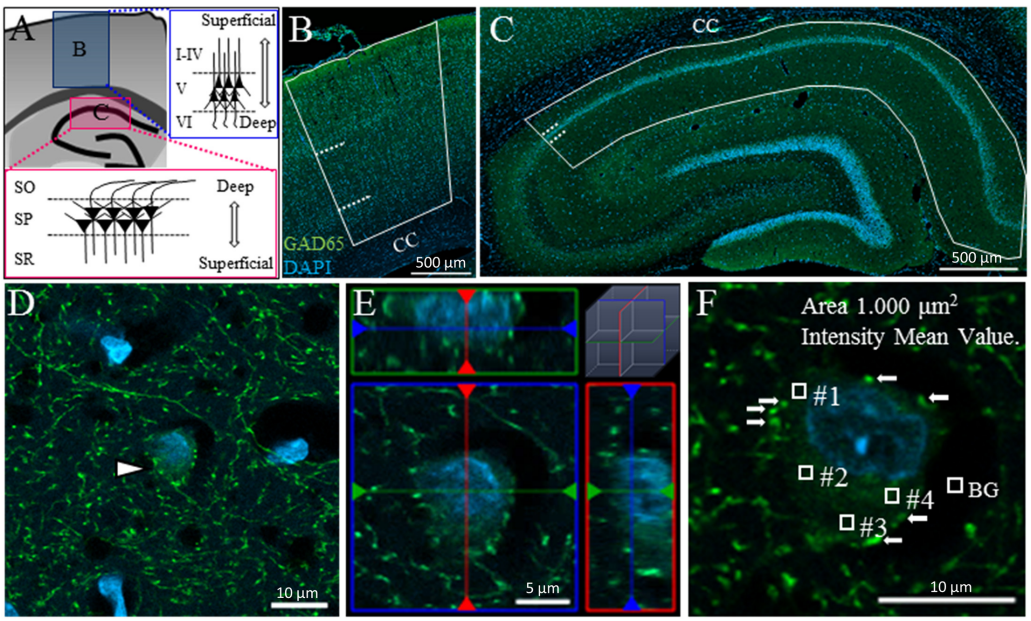

FIGURE 1 | Measuring GAD65 staining intensity in somata in the cerebral cortex and hippocampus. Schematic drawing of a coronal section of an adult rat brain showing the cerebral cortex (**A:** upper inset **B**) and hippocampus (**A:** lower inset **C**). The cerebral cortex and hippocampus were each divided into three layers. Solid lines and dashed lines indicate the region of interest and the boundaries between layers, respectively, in the cerebral cortex **(B)** and hippocampus **(C)**. The area of GAD65 expression in the soma was surrounded by synaptic buttons in the 2D (**D:** arrowhead) and 3D images (**E:** ortho-image from the *x*, *y*, and *z* planes). The level of GAD65 expression was calculated by subtracting the background (BG) intensity from the average intensity of four squares **(F)**. CC, corpus callosum.

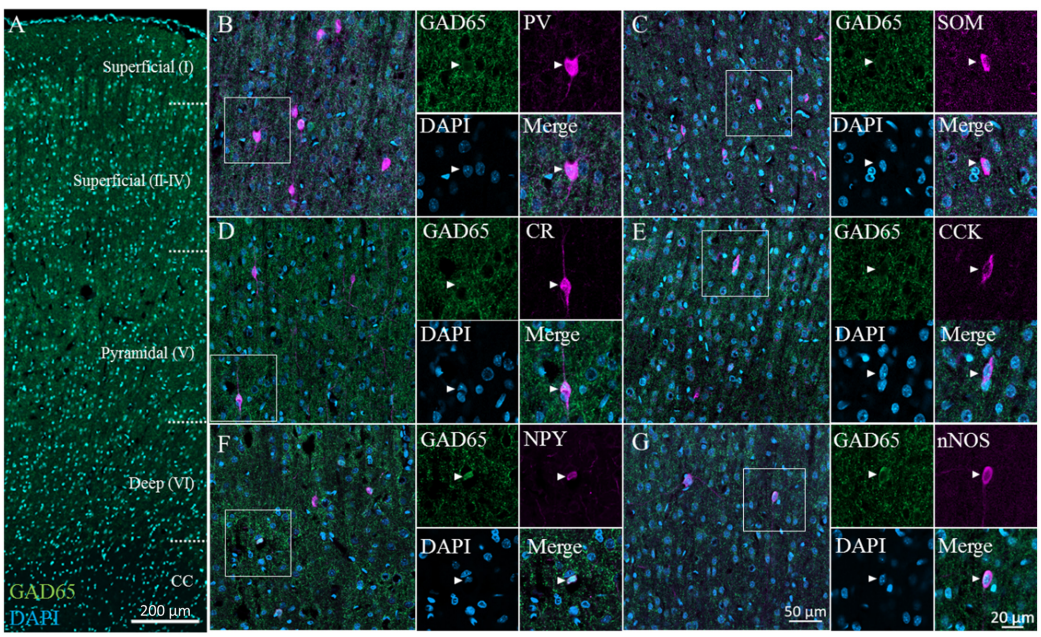

FIGURE 2 | GAD65 expression in each GABAergic subtype in the cerebral cortex. Double immunofluorescence image of GAD65 (green) and DAPI (blue) signals **(A)**. Triple immunofluorescence images showing GAD65 expression (green); positive signals for PV, SOM, CR, CCK, NPY, or nNOS (magenta); and DAPI staining (blue) in the superficial (II–IV) layer **(B–G)**. White squares indicate the regions enlarged in the panels on the right, and arrowheads indicate somata.

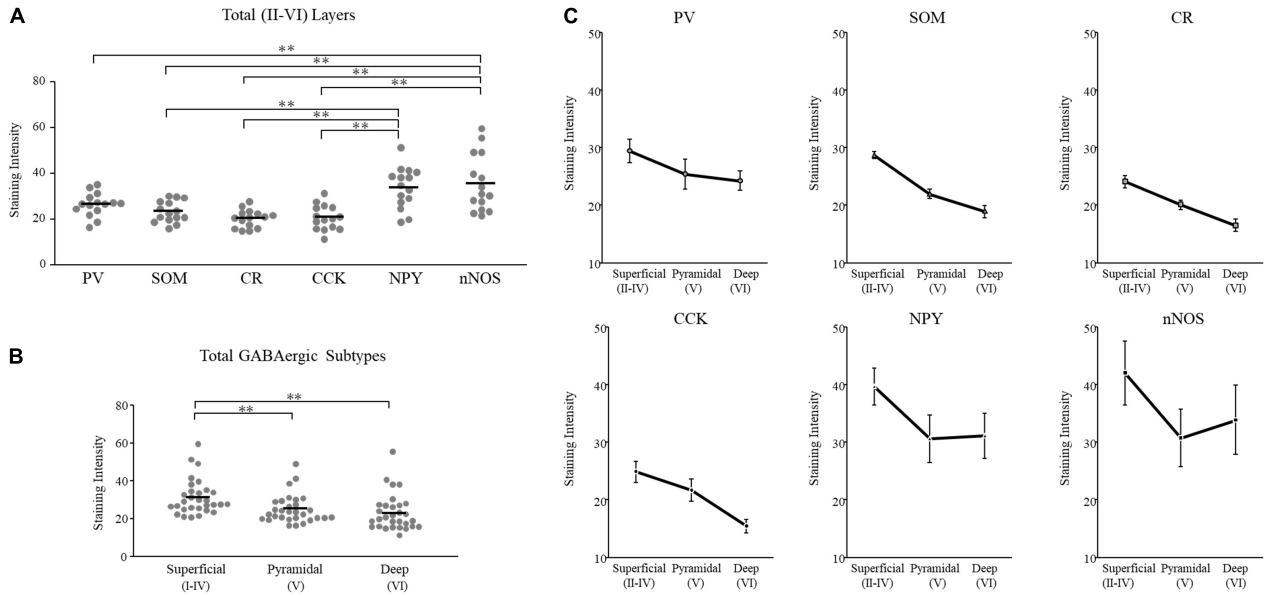

FIGURE 3 | GAD65 expression in each GABAergic subtype across layers of the cerebral cortex (n = 5 brains). The average intensity of GAD65 immimostaining among six GABAergic subtypes **(A)**. The average intensity of GAD65 immunostaining among the superficial (II–IV), pyramidal (V), and deep (VI) layers **(B)**. The average intensity of GAD65 immunostaining across layers of the cerebral cortex among six GABAergic subtypes **(C)**. Error bars indicate SEM. Two-way ANOVA followed by Bonferroni's tests was used to compare the expression level. $^{**}p < 0.01$.

TABLE 1 | GAD65 Expression in Cerebral Cortical Layers Based on GAD65 Staining Intensity.

Layer	Subtypes	Mean Intensity of GAD65*	Numbers of Cells in each GAD65-Intensity Range**								Subtypes ratio (%)
			0–10	11–20	21–30	31–40	41–50	51–60	61–70	71–255	Total	
Superficial (I)	CR	27.95 ± 3.15	2	9	11	4	2	0	1	0	29	52.72
	nNOS	70.04 ± 11.32	0	1	3	5	3	6	0	8	26	47.27
Superficial (II–IV)	PV	29.34 ± 2.09	0	47	97	58	41	10	2	2	257	25.90
	SOM	28.63 ± 0.60	10	51	64	38	19	7	2	1	192	19.35
	CR	24.00 ± 1.09	12	76	67	32	15	3	0	0	205	20.66
	CCK	24.77 ± 1.89	6	37	32	26	1	1	0	0	103	10.38
	NPY	39.63 ± 3.27	2	13	41	37	21	14	12	3	143	14.41
	nNOS	41.94 ± 5.61	1	15	23	26	10	7	7	3	92	9.27
Pyramial (V)	PV	25.40 ± 2.59	4	70	118	45	10	0	0	0	247	38.35
	SOM	21.90 ± 0.82	12	68	55	15	2	0	0	0	152	23.60
	CR	20.02 ± 0.82	8	36	22	5	1	0	0	0	72	11.18
	CCK	21.57 ± 1.96	5	20	16	5	2	0	0	0	48	7.45
	NPY	30.54 ± 4.08	2	23	34	11	9	3	2	1	85	13.19
	nNOS	30.70 ± 4.96	0	12	13	4	6	4	0	1	40	6.21
Deep (VI)	PV	24.19 ± 1.68	6	52	86	42	4	0	0	0	190	31.09
	SOM	18.87 ± 1.09	25	73	41	9	1	0	0	0	149	24.38
	CR	16.46 ± 1.10	19	44	13	2	0	1	0	0	79	12.92
	CCK	15.40 ± 1.20	14	21	16	1	1	0	0	0	53	8.67
	NPY	31.05 ± 3.91	3	23	31	25	10	4	3	4	103	16.85
	nNOS	33.83 ± 6.01	1	5	13	6	6	3	3	0	37	6.05

**Mean of five brains (Five rats).*
***Total cells from five brains (Total 2302 cells).*

were mounted using Fluoromount (Diagnostic BioSystems, Pleasanton, CA, United States).

Quantification and Imaging

Tissue Observation

We observed samples under a confocal microscope (Zeiss LSM 800, Carl Zeiss, Jena, Germany) with a 20 × (NA 0.80) or 63 × (NA 1.4) objective lens (LSM 800, Carl Zeiss). Images were captured using a charge-coupled device camera (Axio-Cam MRm, Carl Zeiss), transferred to a computer, and analyzed using ZEN software (Carl Zeiss).

Definition of Layers of the Cerebral Cortex and Hippocampus

In the cerebral cortex, we examined the primary motor area, primary somatosensory area and posterior parietal association area. Since we could not reliably divide these cortical areas, we did not analyze the differences among these cerebral cortical areas. For the same reason, we also divided the cortex into three layers (Layer II, III, and IV are not distinguished) the superficial (II–IV), pyramidal (V), and deep (VI) layers (**Figure 1A**: upper inset; **Figure 1B**). Layer I was not included in the superficial layer in this study, as this layer contains very few cells of GABAergic subtypes other than CR^+ and $nNOS^+$ neurons (Kubota et al., 2011).

In the hippocampus, we examined the CA1 region in the dorsal hippocampus. The hippocampal CA1 region was divided into three layers: the superficial [stratum radiatum (SR)], pyramidal [stratum pyramidale (SP)], and deep [stratum oriens (SO)] layers (**Figure 1A**: lower inset; **Figure 1C**).

Evaluation of GAD65 Expression in the Soma Using Serial *z*-Stack Sections

We measured the intensity of GAD65 expression in somata but not in synaptic buttons. In two-dimensional (2D) images, distinguishing GAD65 expression in the soma from that in synaptic buttons is technically difficult. **Figure 1D** shows an example of a GAD65-positive ($GAD65^+$: green) cell in the hippocampus (arrowhead). The nucleolus was stained with DAPI (blue). GAD65 expression was observed in the soma and perisomatic region. Such perisomatic staining shows synaptic buttons (axon terminals) as somatic inputs because GAD65 is localized to axon terminals but not to dendrites (Kanaani et al., 2002).

To distinguish the GAD65 staining in somata from that in axon terminals, we followed the criteria proposed by Jinno and Kosaka (2009). According to their criteria, we captured serial stacks of optical sections at 1-μm intervals using confocal microscopy with a *z*-stack system, as cell bodies (>2 μm) appear in multiple adjacent sections, whereas buttons (<2 μm) do not appear in more than two optical sections. To validate these criteria for GAD65 staining, we reconstructed the $GAD65^+$ cell in a three-dimensional (3D) image (**Figure 1E**) and then confirmed that these criteria can be used to successfully distinguish between GAD65 expression in the soma and that in synaptic buttons. The reconstruction of 3D images has been described previously (Kajita et al., 2017).

To measure GAD65 intensity in the soma, we randomly set four squares within each soma, avoiding the nucleus and buttons (arrows), and measured the average intensity within those squares (0, no signal; 255, maximum level; **Figure 1F**). The average intensity over the four squares was used as the datapoint for GAD65 intensity after the subtraction of background signals. To avoid measuring out-of-focus cells, we selected only cells with clear DAPI staining. To measure GAD65 intensity in the synaptic buttons, we selected the 50 synaptic buttons from VGAT staining, and the average intensity was used as the data point after the subtraction of background signals. The density of VGAT was measured in unit area (/100 μm^2). The average density of 25 unit areas was used as the datapoint for VGAT density per brain. Data were collected in Excel (Microsoft, Redmond, WA, United States) for further analysis. All data were calculated with the truncation of numbers beyond the third or fourth decimal place.

Statistical Analysis

We used IBM SPSS Statistics for Windows software (version 21.0 [released 2012], IBM Corp., Armonk, NY, United States) for statistical analysis and performed Welch's *t*-test, Mann–Whitney *U* Test, two-way analysis of variance (ANOVA) followed by Bonferroni's *post hoc* tests, and Pearson's correlation test. Values are presented as the mean ± standard error of the mean (SEM). Groups were compared using thresholds for significance of 0.05 and 0.01.

RESULTS

GAD65 Expression Levels Among GABAergic Subtypes and Layers of the Cerebral Cortex

We immunostained for GAD65 in the cerebral cortex; a typical image captured via confocal microscopy is shown in **Figure 2A** (GAD65: green; DAPI: blue). GAD65 expression was detected throughout the imaged region, except in the corpus callosum. All six GABAergic subtypes were detected across layers II–VI. On the other hand, only CR^+ and $nNOS^+$ neurons were detected in layer I. We present representative high-magnification images of the six GABAergic subtypes in the superficial (II–IV) layer in **Figures 2B–G**, which show triple signals of GAD65 immunofluorescence (green), the GABAergic subtype (magenta), and DAPI staining (blue).

We plotted GAD65 intensity among the six subtypes present in those three layers in **Figure 3**. Further details are provided in **Table 1**.

GAD65 Expression Was High in NPY^+ and $nNOS^+$ Neurons and Low in PV^+, SOM^+, CR^+, and CCK^+ Neurons Across Layers of the Cerebral Cortex

To examine subtype- and layer-related specificity, we statistically analyzed the GAD65 staining intensity using two-way ANOVA (subtype × layer). The statistical analysis showed significant main effects due to the subtype and layer type (subtypes: $p = 0.000$; layers: $p = 0.000$), but their interaction was not significant.

To compare the GAD65 staining intensity among the six subtypes, we performed multiple comparison analysis using Bonferroni's *post hoc* method. The GAD65 staining intensity was significantly higher in NPY$^+$ and nNOS$^+$ neurons than in other subtypes (NPY$^+$ vs. SOM$^+$, p = 0.001; vs. CR$^+$, p = 0.000; vs. CCK$^+$, p = 0.000), (nNOS$^+$ vs. PV$^+$, p = 0.006; vs. SOM$^+$, p = 0.000; vs. CR$^+$, p = 0.000; vs. CCK$^+$, p = 0.000; **Figure 3A**). The difference between NPY$^+$ and PV$^+$ neurons was not quite significant. In the superficial (I) layer, Welch's t-test revealed that the GAD65 staining intensity was

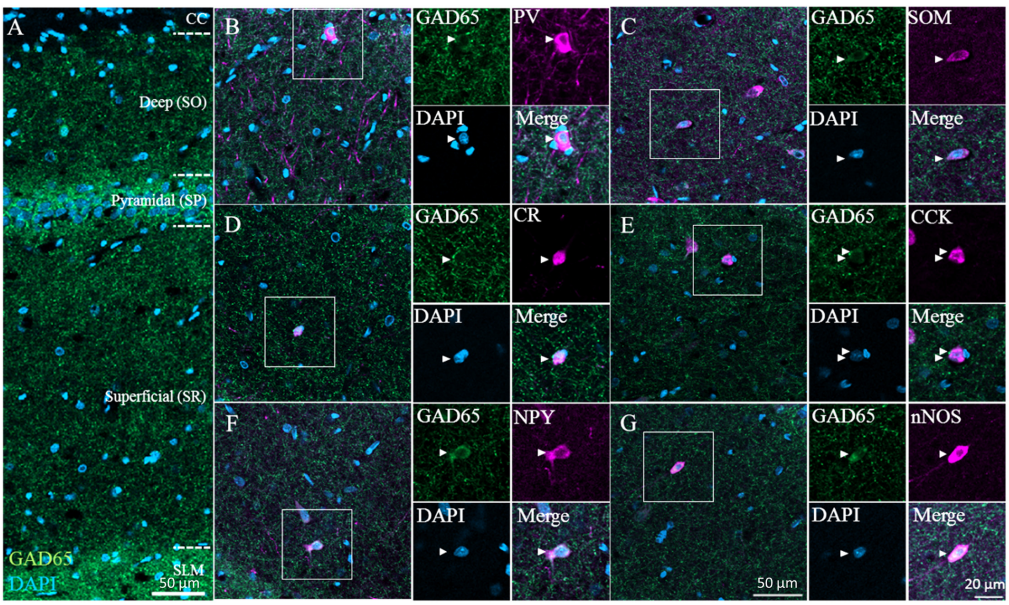

FIGURE 4 | GAD65 expression in each GABAergic subtype in the hippocampus. Double immunofluorescence image showing GAD65 (green) and DAPI (blue) signals **(A)**. Triple immunofluorescence images showing GAD65 expression (green); positive signals for PV, SOM, CR, CCK, NPY, or nNOS (magenta); and DAPI staining (blue) in the superficial (SR) layer **(B–G)**. White squares indicate the regions enlarged in the panels on the right, and arrowheads indicate somata. CC, corpus callosum; SO, stratum oriens; SP, stratum pyramidale; SR, stratum radiatum; and SLM, stratum lacunosum-moleculare.

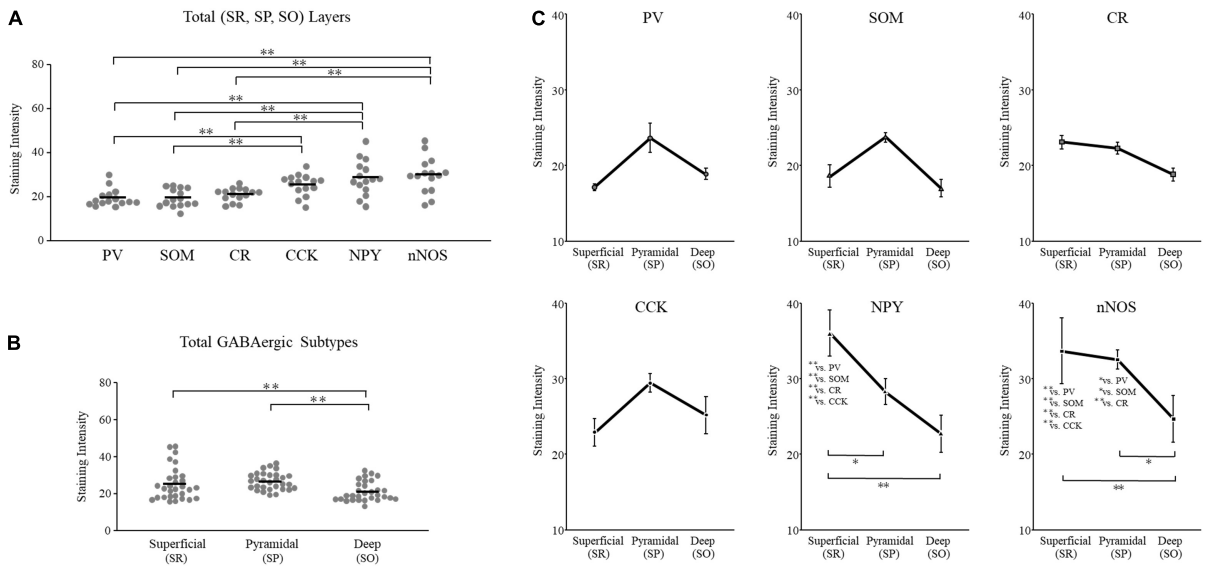

FIGURE 5 | GAD65 expression in each GABAergic subtype across layers of the hippocampus (n = 5 brains). The average intensity of GAD65 immunostaining among six GABAergic subtypes **(A)**. The average intensity of GAD65 immunostaining among the superficial (SR), pyramidal (SP), and deep (SO) layers **(B)**. The average intensity of GAD65 immunostaining across layers of the cerebral cortex among six GABAergic subtypes **(C)**. SO, stratum oriens; SP, stratum pyramidale; and SR, stratum radiatum. Error bars indicate SEM. Two-way ANOVA followed by Bonferroni's tests was used to compare the expression level. *p < 0.05. **p < 0.01.

significantly higher in nNOS$^+$ neurons than in CR$^+$ neurons ($p = 0.018$).

Based on these statistical analysis, we classified GABAergic subtypes into two groups: high GAD65 (NPY$^+$ and nNOS$^+$) and low GAD65 (PV$^+$, SOM$^+$, CR$^+$, and CCK$^+$) neurons in the cerebral cortex.

GAD65 Expression Was Higher in the Superficial Layer Than in Other Layers of the Cerebral Cortex

To compare the GAD65 staining intensity among layers of the cerebral cortex, we performed multiple comparison analysis using Bonferroni's *post hoc* method. The GAD65 staining intensity was significantly higher in the superficial (II–IV) layer than in the pyramidal (V; $p = 0.002$) and deep (VI; $p = 0.000$) layers (**Figure 3B**).

Based on these results, GAD65 expression is higher in the superficial layer than in other layers of the cerebral cortex. The GAD65 staining intensity among layers in each subtype was shown in **Figure 3C**. In the cerebral cortex there was no significant interaction (subtype × layer). We did not perform statistical analysis among the six subtypes in each three layer, or among three layers in each six subtype.

GAD65 Expression Among GABAergic Subtypes Across Layers of the Hippocampus

Next, we immunostained for GAD65 in the CA1 region of the hippocampus; a typical image from confocal microscopy can be seen in **Figure 4A** (GAD65: green; DAPI: blue). GAD65 expression was detected across the entire region excluding the corpus callosum. We detected all six GABAergic subtypes, and high-magnification examples of each subtype as observed in the superficial (SR) layer can be found in **Figures 4B–G**, which show triple signals of GAD65 immunofluorescence (green), the GABAergic subtype (magenta), and DAPI staining (blue).

We plotted the GAD65 staining intensity among the six subtypes and three layers in **Figure 5**. Further details are provided in **Table 2**.

GAD65 Expression Was Layer Specific and High in NPY$^+$, nNOS$^+$, and CCK$^+$ Neurons but Low in PV$^+$, SOM$^+$, and CR$^+$ Neurons

To examine subtype- and layer-related specificity, we statistically analyzed the GAD65 staining intensity using two-way ANOVA (subtype × layer). The statistical analysis indicated significant main effects due to the subtype and layer type (subtypes: $p = 0.000$; layers: $p = 0.000$). The interaction was also significant (subtype × layer: $p = 0.002$).

To compare the GAD65 staining intensity among the six subtypes, we performed multiple comparison analysis using Bonferroni's *post hoc* method. The GAD65 staining intensity was significantly higher in NPY$^+$, nNOS$^+$, and CCK$^+$ neurons than in other subtypes (NPY$^+$ vs. PV$^+$, $p = 0.000$; vs. SOM$^+$, $p = 0.000$; vs. CR$^+$, $p = 0.000$; nNOS$^+$ vs. PV$^+$, $p = 0.000$; vs. SOM$^+$, $p = 0.000$; vs. CR$^+$, $p = 0.000$; CCK$^+$ vs. PV$^+$, $p = 0.006$; vs. SOM$^+$, $p = 0.005$; **Figure 5A**). No significant difference was found between CCK$^+$ and CR$^+$ neurons.

However, these main effects were qualified by a significant interaction between subtype and layer type. Therefore, we compared the GAD65 staining intensity among the six subtypes for each layer using Bonferroni's *post hoc* tests. In the superficial (SR) layer, the GAD65 staining intensity was significantly higher in NPY$^+$ (NPY$^+$ vs. PV$^+$, $p = 0.000$; vs. SOM$^+$, $p = 0.000$;

TABLE 2 | GAD65 Expression in Hippocampal Layers Based on GAD65 Staining Intensity.

Layer	Subtypes	Mean Intensity of GAD65*	Numbers of Cells in each GAD65-Intensity Range**								Subtypes ratio (%)
			0–10	11–20	21–30	31–40	41–50	51–60	61–70	71–255	Total	
Superficial (SR)	PV	17.11 ± 0.40	26	30	19	4	2	0	0	0	81	7.97
	SOM	18.59 ± 1.50	12	34	14	6	1	1	0	0	68	6.69
	CR	23.08 ± 0.85	44	131	91	44	21	5	1	1	338	33.26
	CCK	22.87 ± 1.82	19	115	65	31	13	8	0	0	251	24.70
	NPY	36.03 ± 3.06	5	17	39	44	26	14	9	5	159	15.64
	nNOS	33.66 ± 4.36	0	30	34	22	14	9	5	5	119	11.71
Pyramidal (SP)	PV	23.65 ± 1.93	31	158	127	76	17	2	1	2	414	34.10
	SOM	23.75 ± 0.66	3	21	22	7	4	0	0	0	57	4.69
	CR	22.25 ± 0.76	28	128	100	37	11	1	0	1	306	25.20
	CCK	29.44 ± 1.21	2	24	45	34	15	4	0	0	124	10.21
	NPY	28.25 ± 1.70	13	55	58	35	18	12	2	0	193	15.89
	nNOS	32.53 ± 1.29	1	8	53	33	17	6	1	1	120	9.88
Deep (SO)	PV	18.77 ± 0.86	58	153	84	24	5	0	0	0	324	21.92
	SOM	16.96 ± 1.13	106	303	106	22	3	1	0	0	541	36.60
	CR	18.80 ± 1.09	34	126	53	17	2	0	0	0	232	15.69
	CCK	25.18 ± 2.42	8	35	51	27	8	1	1	0	131	8.86
	NPY	22.69 ± 2.42	23	83	60	18	7	4	0	2	197	13.32
	nNOS	24.70 ± 3.08	1	23	16	9	2	2	0	0	53	3.58

**Mean of five brains (Five rats).*

***Total cells from five brains (Total 3708 cells).*

vs. CR^+, $p = 0.000$; vs. CCK^+, $p = 0.000$) and $nNOS^+$ neurons ($nNOS^+$ vs. PV^+, $p = 0.000$; vs. SOM^+, $p = 0.000$; vs. CR^+, $p = 0.005$; vs. CCK^+, $p = 0.004$; **Figure 5C**). In the pyramidal (SP) layer, the GAD65 staining intensity was significantly higher in $nNOS^+$ neurons than in all other subtypes ($nNOS^+$ vs. PV^+, $p = 0.033$; vs. SOM^+, $p = 0.037$; vs. CR^+, $p = 0.007$). By contrast, in the deep (SO) layer, no significant differences were found.

Based on these statistical analysis, we classified GABAergic subtypes into two groups: high GAD65 (NPY^+, $nNOS^+$, and CCK^+) and low GAD65 (PV^+, SOM^+, and CR^+) neurons in the hippocampus. In contrast to the cerebral cortex, these high expression levels are indicative of layer specificity. GAD65 expression in the superficial layer (SR) was higher in NPY^+ and $nNOS^+$ neurons, and GAD65 expression in the pyramidal layer (SP) was higher in $nNOS^+$ neurons than in other subtypes. In the deep layer (SO), GAD65 expression tended to be high in CCK^+ neurons, but no significant differences were noted.

GAD65 Expression Was Subtype Specific and Higher in the Superficial and Pyramidal Layers Than in the Deep Layer of the Hippocampus

To compare the GAD65 staining intensity among hippocampal layers, we performed multiple comparison analysis using Bonferroni's *post hoc* method. The GAD65 staining intensity was significantly higher in the superficial (SR) and pyramidal (SP) layers than in the deep (SO) layer (SR vs. SO, $p = 0.002$; SP vs. SO, $p = 0.000$; **Figure 5B**).

As described above, these main effects were qualified by a significant interaction between the subtype and layer type. Therefore, we compared the GAD65 staining intensity among layers for each subtype using Bonferroni's *post hoc* tests. In NPY^+ neurons, the GAD65 staining intensity was significantly higher in the superficial (SR) layer than in the other (SP and SO) layers (SR vs. SP, $p = 0.021$; SR vs. SO, $p = 0.000$; **Figure 5C**). In $nNOS^+$ neurons, the GAD65 staining intensity was significantly higher in the superficial (SR) and pyramidal (SP) layers than in the deep (SO) layer (SR vs. SO, $p = 0.006$: SP vs. SO, $p = 0.020$). In PV^+, SOM^+, CR^+, and CCK^+ neurons, the GAD65 staining intensity was not significantly different across layers.

Based on these results, GAD65 expression was higher in the superficial (SR) and pyramidal (SP) layers than in the deep (SO) layer. However, this laminar distribution was subject to subtype specificity. In NPY^+ neurons, GAD65 expression was high in the superficial (SR) layer. In $nNOS^+$ neurons, GAD65 expression was high in the superficial (SR) and pyramidal (SP) layers. In PV^+, SOM^+, and CCK^+ neurons, no significant differences were observed, but GAD65 expression tended to be high in the pyramidal (SP) layer.

GAD65 Expression in Different Subtypes Was Positively Correlated Between Colchicine-Treated and Control Brains

We examined GAD65 expression in somata but not in axon terminals. Investigating GAD65 expression in axon terminals is difficult because the SOM, NPY, and nNOS proteins cannot be clearly detected in axon terminals under confocal microscopy. To detect GAD65 expression throughout the cytoplasm including in axon terminals, we injected colchicine, an inhibitor of microtubule polymerization, into the lateral ventricle to block axonal transport. At 2 days after colchicine injection, the GAD65 staining (green) intensity increased in somata in the cerebral cortex (**Figures 6A-I, B-I**, arrowhead) and hippocampus (**Figures 6G-I, H-I**, arrowhead). On the other hand, the intensity of GAD65 decreased in the neuropil region of the cerebral cortex (**Figures 6A-II, B-II**, arrows) and hippocampus (**Figures 6G-II, H-II**, arrows). Welch's *t*-test showed the intensities of GAD65 clusters were significantly lower in colchicine-injected brains (**Figure 6C**, cerebral cortex: $p = 0.001$; **Figure 6I**, hippocampus: $p = 0.000$). In additions, the number of VGAT clusters (magenta) were not changed in colchicine-injected brains (**Figure 6D**, cerebral cortex; **Figure 6J**, hippocampus). VGAT is localized in inhibitory axon terminal (Chaudhry et al., 1998), suggesting that GAD65 was not transported to axon terminals and instead accumulated in somata. In these brains, we measured GAD65 expression in the six subtypes in the cerebral cortex (**Figure 6E**) and hippocampus (**Figure 6K**) and compared the results with control brains. In colchicine-injected brains, the intensities of GAD65 staining in somata were dramatically increased, but their distributions throughout the somata did not appear to show the major changes. Therefore, we determined that same quantitative method as control is applicable in them. GAD65 expression was compared using the mean value of the three layers in both colchicine-injected and control brains. Welch's *t*-test showed the intensities of GAD65 in somata were significantly higher in colchicine-injected brains (**Figure 6E**, cerebral cortex: PV, $p = 0.000$; SOM, $p = 0.004$; CR, $p = 0.026$; CCK, $p = 0.049$; NPY, $p = 0.000$; and nNOS, $p = 0.029$; **Figure 6K**, hippocampus: PV, $p = 0.001$; CCK, $p = 0.005$; NPY, $p = 0.003$; and nNOS, $p = 0.006$). The data of CR did not show normal distribution, and was detected the significant difference using Mann–Whitney *U* Test ($p = 0.008$). There was no significant difference in SOM^+ cells between colchicine-injected and control brains. Further details are provided in **Table 3**. Pearson's test showed significant positive correlations in the expression profile between colchicine-injected and control brains (**Figure 6F**, cerebral cortex: $r = 0.780$, $p = 0.003$; **Figure 6L**, hippocampus: $r = 0.889$, $p = 0.000$).

Based on these results, GAD65 expression in the soma and cytoplasm exhibited similar tendencies across all GABAergic subtypes, and the level of GAD65 expression in the soma can be used as a proxy for the level of GAD65 expression in the cytoplasm for all GABAergic subtypes.

DISCUSSION

In this study, we compared GAD65 expression among six GABAergic subtypes and found that GABAergic subtypes fell into two classes for each brain region from statistical analysis: a high-expression group (NPY^+ and $nNOS^+$) and a low-expression group (PV^+, SOM^+, CR^+, and CCK^+) in the cerebral cortex, and a high-expression group (CCK^+, NPY^+, and $nNOS^+$), and a low-expression group (PV^+, SOM^+, and

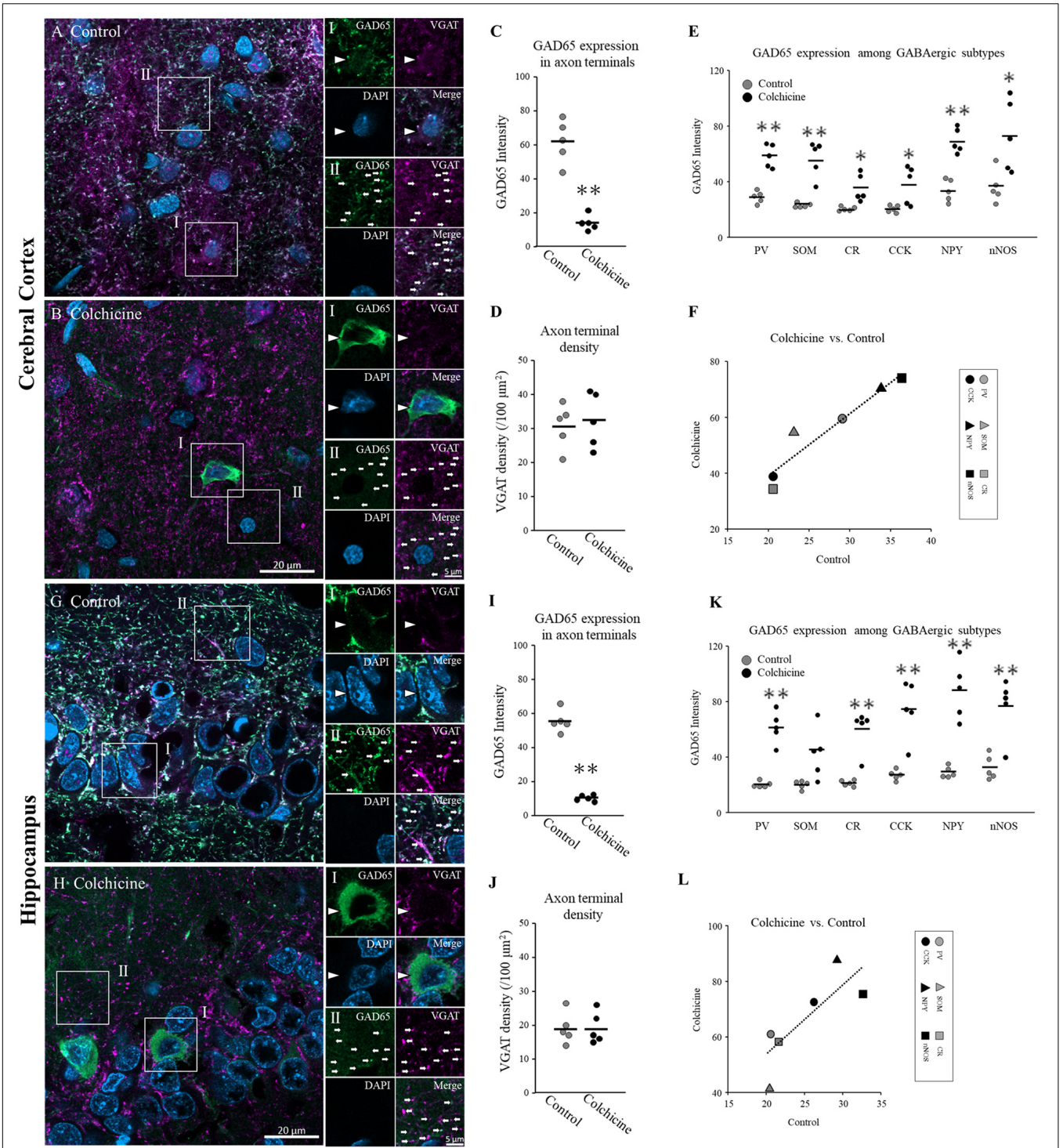

FIGURE 6 | GAD65 expression in the cerebral cortex and hippocampus of colchicine-treated rats (n = 5 brains). Triple immunofluorescence image showing GAD65 (green), VGAT (magenta), and DAPI (blue) signals (cerebral cortex: **A,B**; hippocampus: **G,H**). White squares (I: soma; II: neuropil) indicate the regions enlarged in the panels on the right, and arrowheads and arrows indicate somata and axon terminals, respectively. The average GAD65 immunostaining intensity in axon terminals (neuropil) in cerebral cortical layers **(C)** and hippocampal layers **(I)**. The density of VGAT immunostaining per unit area in cerebral cortical layers **(D)** and hippocampal layers **(J)**. The average GAD65 immunostaining intensity in soma in cerebral cortical layers **(E)** and hippocampal layers **(K)** among six GABAergic subtypes. Correlations in GAD65 staining intensities in six GABAergic subtypes in the cerebral cortex **(F)** and hippocampus **(L)** between the colchicine-injected group and the control group. Black bars indicate the mean value of five brains **(C–E,I–K)**. Error bars indicate SEM. Welch's t-test revealed was used for **(C,E,D,I,K,J)**. Mann–Whitney U Test was used for **(K)**. Pearson's correlation analysis was used for **(F,L)**. $^{*}p < 0.05$. $^{**}p < 0.01$.

TABLE 3 | GAD65 Expression in (A) Cerebral Cortical (B) Hippocampal layers based on GAD65 staining intensity in colchicine-injected rats.

(A) Cerebral Cortex

	Subtypes	Mean Intensity of GAD65*	Numbers of Cells in each GAD65-Intensity Range**										
			0–10	11–20	21–30	31–40	41–50	51–60	61–70	71–80	81–90	91–100	101–255	Total
Colchicine	PV	60.26 ± 3.71	0	1	7	14	24	23	21	15	6	3	0	114
	SOM	55.93 ± 5.82	2	7	12	3	3	5	4	4	8	10	10	68
	CR	35.65 ± 4.41	3	3	9	18	9	13	13	8	9	9	3	68
	CCK	37.51 ± 6.11	0	1	4	15	15	10	8	7	0	0	0	60
	NPY	69.49 ± 3.98	0	0	0	10	25	15	30	5	5	10	25	125
	nNOS	73.62 ± 11.61	0	0	8	0	6	12	3	3	5	10	18	65
Control	PV	29.07 ± 1.91	17	50	67	39	7	7	1	0	0	0	0	188
	SOM	23.10 ± 0.70	21	66	22	5	1	0	0	0	0	0	0	115
	CR	20.59 ± 0.69	9	27	18	6	3	0	0	0	0	0	0	63
	CCK	20.58 ± 1.13	7	17	14	9	0	0	0	0	0	0	0	47
	NPY	33.85 ± 3.55	0	18	23	20	5	4	5	1	0	0	0	76
	nNOS	36.38 ± 5.25	0	5	14	11	10	8	4	1	1	0	0	54

(B) Hippocampus

	Subtypes	Mean Intensity of GAD65*	Numbers of Cells in each GAD65-Intensity Range***										
			0–10	11–20	21–30	31–40	41–50	51–60	61–70	71–80	81–90	91–100	101–255	Total
Colchicine	PV	61.57 ± 5.12	0	15	17	25	21	12	14	10	6	6	28	154
	SOM	42.80 ± 8.16	18	11	23	17	6	10	3	3	2	1	6	100
	CR	59.98 ± 6.62	5	17	16	17	9	9	4	5	4	3	20	109
	CCK	73.79 ± 9.21	3	4	5	6	6	8	5	9	3	3	34	86
	NPY	88.11 ± 9.23	0	3	5	0	5	3	4	7	2	6	37	72
	nNOS	75.51 ± 9.51	5	8	11	12	6	8	11	3	7	6	32	109
Control	PV	20.41 ± 0.97	17	63	43	16	3	0	0	0	0	0	0	142
	SOM	20.19 ± 1.26	10	41	37	9	5	1	0	0	0	0	0	103
	CR	21.49 ± 0.95	16	52	34	16	5	1	1	0	0	0	0	125
	CCK	27.09 ± 1.60	5	26	31	21	5	5	1	0	0	0	0	94
	NPY	29.27 ± 1.81	6	23	25	16	10	4	2	1	1	0	0	88
	nNOS	32.64 ± 3.97	1	17	32	20	11	7	3	1	1	1	1	95

**Mean of five brains (Five rats).*
***Total cells from five brains (Colchicine: 529 cells, Control: 543 cells).*
****Total cells from five brains (Colchicine: 630 cells, Control: 647 cells).*

CR^+) in the hippocampus. There was a difference in the laminar distribution of GAD65 expression between the cortical and hippocampal layers.

Additionally, GAD65 expression across all GABAergic subtypes were significantly and positively correlated between control and colchicine-treated rats.

nNOS$^+$ and NPY$^+$ Neurons Express GAD65 at Higher Levels Than Do the Other Subtypes

Our results revealed that nNOS$^+$ and NPY$^+$ neurons express GAD65 at particularly high levels, whereas some major subtypes (PV^+/SOM^+/CR^+) express GAD65 at low levels in the cerebral cortex and hippocampus. This result is consistent with previous reports of PV^+ neurons having lower GAD65 expression than non-PV neurons in the mouse hippocampus (Fukuda et al., 1997). Candidates of these non-PV neurons having high GAD65 may include the nNOS$^+$ and NPY$^+$ neurons based on our findings. There was another previous report comparing synaptic-GAD65 and GAD67 expression among PV^+ basket neurons, PV^+ chandelier neurons and Calbindin-positive (CB^+) basket neurons in the monkey prefrontal cortex (Fish et al., 2011). They shows the higher synaptic expression of GAD65 in PV^+ basket neurons than in PV^+ chandelier neurons, and the same level of synaptic expression of GAD65 in PV^+ basket neurons as in CB^+ basket neurons. Because of different classification of GABAergic subtypes, it would be necessary to clarify distinct patterns of GAD65 expressions in synapse levels at multiple GABAergic subtype.

Neuropeptide Y is a neuromodulator with anti-seizure activity (Erickson et al., 1996; Baraban et al., 1997; Vezzani et al., 1999). Its anti-epileptic functions occur during the pre- and post-synaptic inhibition of excitatory neurons via Y1, Y2, and Y5 receptors

(Baraban, 2004). NPY belongs to the G-protein-coupled inwardly rectifying potassium receptor family (Paredes et al., 2003). The functions of neuromodulator/GABA co-release remain unclear, but generally, GABA transmission contributes to fine-tuning of the synaptic effects of neuromodulators (Horvath et al., 2001; Yu et al., 2015; Tritsch et al., 2016). Many NPY^+ neurons are excited by GABA in the hilus of the hippocampus (Fu and van den Pol, 2007), suggesting that NPY^+ cells are activated by GABA, which results in the increased release of not only GABA but also the co-expressed inhibitory neuromodulator NPY. Based on these reports, we suggest that the neural inhibitory functions of NPY are regulated by GAD65-dependent GABA release in pathological situations.

The pharmacological functions of nitric oxide (NO) in epileptic seizures remain controversial, but NO has been considered to act as a mediator of neurotoxic effects in several reports (Dawson et al., 1991; Marangoz et al., 1994; Penix et al., 1994; Schuman and Madison, 1994). nNOS has the function of evoking the release of several neurotransmitters, including acetylcholine, catecholamines, neuroactive amino acids and GABA (Kahn et al., 1997a,b). NO-evoked neurotransmitter release is mediated by two distinct release systems, a Ca^{2+}-dependent system and the reverse process of a Na^+-dependent carrier-mediated transport system (Garthwaite, 1991; Kuriyama and Ohkuma, 1995). NO has effects of decreasing GABA transaminase activity and increasing GABA expression (Jayakumar et al., 1999; Vega Rasgado et al., 2018). The relationship between presynaptic NO release and GABA remains largely unknown, but as with NPY, NO, and GABA release may be related to the regulation of overexcited neurons in some pathological states. The high concentrations of GAD65 in $nNOS^+$ and NPY^+ neurons may be needed to support a rapid response to neuromodulators when necessary.

Additionally, SOM is an anti-epileptic neuropeptide in the hippocampus (Boehm and Betz, 1997; Schweitzer et al., 1998; Tallent and Siggins, 1999). GABA-mediated activation of NPY^+ neurons may increase the release of SOM (Fu and van den Pol, 2007), as SOM/NPY co-expression has been observed in a subset of GABAergic neurons in the hippocampus (Köhler et al., 1987). However, GAD65 expression was not high in SOM^+ neurons according to our results, indicating that the release of SOM is not associated with GAD65-dependent GABA release.

Laminar Distributions of GAD65 in the Cerebral Cortex and Hippocampus

In the cerebral cortex, we found that GAD65 expression is higher in the superficial layer than in the other layers for all GABAergic subtypes. Pyramidal neurons project their dendrites into the superficial layer to receive amino-acid or monoamine signals from other parts of the cortex or extra-cortical regions. Inhibitory dendritic signals from local GABAergic neurons are essential for mediating these inputs and maintaining a normal neural state (Northoff and Mushiake, 2020). Therefore, high GAD65 expression in neurons in the superficial layer may play a crucial role in suppressing cortical over-excitation. This idea is consistent with a report stating that local GABAergic inhibition drives the elasticity of ictal progression and that cortical seizures occur in superficial layers prior to deep layers during lateral seizure spread (Wenzel et al., 2017). Additionally, GAD65 expression was found to be higher in the pyramidal layer of the visual cortex of 1-week-old cats (Mower and Guo, 2001), but higher expression was detected in the superficial layer in adults (Guo et al., 1997). This pattern change may reflect flexible regulation of GAD65 for maintaining a normal state during the growth of neural circuits.

In the hippocampus, we observed that GAD65 expression was higher in the superficial layer than in the deep layer only in $nNOS^+$ and NPY^+ neurons. Dendrites of hippocampal pyramidal neurons in the superficial layer receive glutamatergic Schaffer collateral inputs from the CA3 region. In the hippocampal CA1 region, GABAergic neurons expressing nNOS/NPY are known as Ivy cells (Price et al., 2005; Tricoire and Vitalis, 2012). Ivy cells provide widespread synaptic and extra-synaptic slow inhibition of the dendrites of CA1 pyramidal neurons (Fuentealba et al., 2008; Lapray et al., 2012). The number of Ivy cells was significantly reduced in the hippocampus of pilocarpine-induced epileptic rats. Interestingly, the number of PV^+ neurons was not changed in this model (Orbán-Kis et al., 2015). These findings suggest that $nNOS^+$ and NPY^+ neurons in the superficial layer may play a critical role in suppressing ictal progression in the hippocampus. Same as $nNOS^+$ and NPY^+ neurons, in PV^+, SOM^+, CR^+ and CCK^+ neurons, they also showed the tendency of distinct GAD65 expression among layers. These results are consistent with a previous report stating that both PV^+ and non-PV neurons exhibit distinct laminar distribution of GAD65 in the deep and pyramidal layer (Fukuda et al., 1997).

Measurement of GAD65 Expression in the Soma

We noted that strong GAD65 fluorescence often accumulated in the perinuclear region. This localization may reflect GAD65 protein undergoing a hydrophobic posttranslational modification and becoming anchored to the cytosolic face of the Golgi membranes (Kanaani et al., 2008).

Based on this feature, we considered it inappropriate to compare GAD65 expression through measurement of its mean intensity inside a traced outline of the soma, as described in previous report (Jinno and Kosaka, 2009). GABAergic neurons have different soma size depending on subtypes (González-Albo et al., 2001). This affects the ratio of the Golgi membrane occupying the soma differs among GABAergic subtypes. To avoid this problem, we quantified GAD65 expression from the average intensity of four squares (details are provided in the section "Materials and Methods"); this method is considered less susceptible to the effects of soma size.

GAD65 Expression in the Soma Can Be Used as a Proxy for Its Level in the Cytoplasm

GAD65 localizes to both the soma and axon terminal, and thus, the amount of GAD65 in the soma does not necessarily reflect the total number of GAD65 molecules throughout the cytoplasm.

As reported previously, there are two possible drivers of high GAD65 expression in the soma: a high synthesis rate or slow transport to the axon terminals (Esclapez et al., 1993). The inhibition of axonal transport by colchicine enhances GAD65 immunoreactivity in the soma (Wang et al., 2014). We found that GAD65 expression in the soma across neuronal subtypes was significantly and positively correlated between colchicine-treated and control brains, suggesting that GAD65 expression in the soma can be used as a proxy for the overall amount of GAD65 in the cytoplasm. It is important to consider the possibility that the colchicine injections might have caused abnormal effects on not only axonal transport but also protein synthesis or metabolism, as colchicine is neurotoxic (Sutula et al., 1983). Neural excitation caused by colchicine might affect the GAD65 expression, because temporal lobe epilepsy caused by pilocarpine is reported to increase GAD65 expression (Esclapez and Houser, 1999). In additions, GABAergic neurons may have differing colchicine sensitivities based on their morphologies and localization patterns. In this study, we injected colchicine into the lateral ventricle of the brain. Layers near the lateral ventricle might have thus been vulnerable to drug effects. In future research, synaptic protein levels can be detected directly using super-resolution fluorescence microscopy. Complementary data should be obtained through several methods.

GAD65-Expression in Subtypes Contributes Understanding of Pathological States

High GAD65 expression in NOS^+ and NPY^+ neurons has important implications. As noted in the introduction, GAD65 is associated with activity-dependent GABA release, whereas GAD67 is associated with spontaneous GABA release (Tian et al., 1999; Jinno and Kosaka, 2009). Our findings suggest that $nNOS^+$ and NPY^+ neurons are closely associated with activity-dependent GABA release. Among GABAergic subtypes, PV^+ neurons are considered a pivotal subtype based on previous studies using subtype-specific GAD67-knockout or -knockdown models (Kuki et al., 2015; Lazarus et al., 2015). However, no studies to date have examined the functions of GAD65 in $nNOS^+$ and NPY^+ neurons. In humans, electroconvulsive therapy increases the seizure threshold (Sackeim, 1999) and GABA expression in the brain (Sanacora et al., 2003). According to our findings, GAD65 expression may increase in $nNOS^+$ and NPY^+ neurons, resulting in increased GABA expression and a higher seizure threshold. This study demonstrates the baseline level of GAD65 expression at the resting state of various GABAergic subtypes. In the future, the relationships between GABAergic subtypes and pathological states should be studied, as GABAergic subtypes play distinct roles in excitatory-inhibitory balance under normal and pathological conditions, including epileptic seizures and mental disorders.

DATA AVAILABILITY STATEMENT

The raw data supporting the conclusions of this article will be made available by the authors, without undue reservation.

ETHICS STATEMENT

The animal study was reviewed and approved by the Institute for Animal Experimentation of Tohoku University (Permission number: 2019 IDOU-291-03).

AUTHOR CONTRIBUTIONS

YK and HM conceived and designed the experiments, wrote the manuscript, and contributed to the article and approved the submitted version. YK performed the experiments and analyzed the data. Both authors contributed to the article and approved the submitted version.

FUNDING

This work was supported by a JSPS KAKENHI grant (Numbers 20K16614 and 19H03337) and MEXT KAKENHI grant (Number JP16H06276: Platform of Advanced Animal Model Support).

REFERENCES

Asada, H., Kawamura, Y., Maruyama, K., Kume, H., Ding, R. G., Kanbara, N., et al. (1997). Cleft palate and decreased brain gamma-aminobutyric acid in mice lacking the 67-kDa isoform of glutamic acid decarboxylase. *Proc. Natl. Acad. Sci. U.S.A.* 94, 6496–6499. doi: 10.1073/pnas.94.12.6496

Baraban, S. C. (2004). Neuropeptide Y and epilepsy: recent progress, prospects and controversies. *Neuropeptides* 38, 261–265. doi: 10.1016/j.npep.2004.04.006

Baraban, S. C., Hollopeter, G., Erickson, J. C., Schwartzkroin, P. A., and Palmiter, R. D. (1997). Knock-out mice reveal a critical antiepileptic role for neuropeptide Y. *J. Neurosci.* 17, 8927–8936.

Boehm, S., and Betz, H. (1997). Somatostatin inhibits excitatory transmission at rat hippocampal synapses via presynaptic receptors. *J. Neurosci.* 17, 4066–4075.

Bowdler, J. M., Green, A. R., Minchin, M. C., and Nutt, D. J. (1983). Regional GABA concentration and [3H]-diazepam binding in rat brain following repeated electroconvulsive shock. *J. Neural Transm.* 56, 3–12. doi: 10.1007/BF01243369

Chattopadhyaya, B., Di Cristo, G., Wu, C. Z., Knott, G., Kuhlman, S., Fu, Y., et al. (2007). GAD67-mediated GABA synthesis and signaling regulate inhibitory synaptic innervation in the visual cortex. *Neuron* 54, 889–903. doi: 10.1016/j.neuron.2007.05.015

Chaudhry, F. A., Reimer, R. J., Bellocchio, E. E., Danbolt, N. C., Osen, K. K., Edwards, R. H., et al. (1998). The vesicular GABA transporter, VGAT, localizes to synaptic vesicles in sets of glycinergic as well as GABAergic neurons. *J. Neurosci.* 18, 9733–9750.

Dawson, V. L., Dawson, T. M., London, E. D., Bredt, D. S., and Snyder, S. H. (1991). Nitric oxide mediates glutamate neurotoxicity in primary cortical cultures. *Proc. Natl. Acad. Sci. U.S.A.* 88, 6368–6371. doi: 10.1073/pnas.88.14.6368

Dicken, M. S., Hughes, A. R., and Hentges, S. T. (2015). Gad1 mRNA as a reliable indicator of altered GABA release from orexigenic neurons in the hypothalamus. *Eur. J. Neurosci.* 42, 2644–2653. doi: 10.1111/ejn.13076

Druga, R. (2009). Neocortical inhibitory system. *Folia Biol.* 55, 201–217.

Erickson, J. C., Clegg, K. E., and Palmiter, R. D. (1996). Sensitivity to leptin and susceptibility to seizures of mice lacking neuropeptide Y. *Nature* 381, 415–421. doi: 10.1038/381415a0

Erlander, M. G., Tillakaratne, N. J., Feldblum, S., Patel, N., and Tobin, A. J. (1991). Two genes encode distinct glutamate decarboxylases. *Neuron* 7, 91–100. doi: 10.1016/0896-6273(91)90077-d

Esclapez, M., and Houser, C. R. (1999). Up-regulation of GAD65 and GAD67 in remaining hippocampal GABA neurons in a model of temporal lobe epilepsy. *J. Comp. Neurol.* 412, 488–505.

Esclapez, M., Tillakaratne, N. J., Kaufman, D. L., Tobin, A. J., and Houser, C. R. (1994). Comparative localization of two forms of glutamic acid decarboxylase and their mRNAs in rat brain supports the concept of functional differences between the forms. *J. Neurosci.* 14(3 Pt 2), 1834–1855.

Esclapez, M., Tillakaratne, N. J., Tobin, A. J., and Houser, C. R. (1993). Comparative localization of mRNAs encoding two forms of glutamic acid decarboxylase with nonradioactive in situ hybridization methods. *J. Comp. Neurol.* 331, 339–362. doi: 10.1002/cne.903310305

Feldblum, S., Erlander, M. G., and Tobin, A. J. (1993). Different distributions of GAD65 and GAD67 mRNAs suggest that the two glutamate decarboxylases play distinctive functional roles. *J. Neurosci. Res.* 34, 689–706. doi: 10.1002/jnr.490340612

Fish, K. N., Sweet, R. A., and Lewis, D. A. (2011). Differential distribution of proteins regulating GABA synthesis and reuptake in axon boutons of subpopulations of cortical interneurons. *Cereb. Cortex* 21, 2450–2460. doi: 10.1093/cercor/bhr007

Fu, L. Y., and van den Pol, A. N. (2007). GABA excitation in mouse hilar neuropeptide Y neurons. *J. Physiol.* 579(Pt 2), 445–464. doi: 10.1113/jphysiol.2002.019356

Fuentealba, P., Begum, R., Capogna, M., Jinno, S., Márton, L. F., Csicsvari, J., et al. (2008). Ivy cells: a population of nitric-oxide-producing, slow-spiking GABAergic neurons and their involvement in hippocampal network activity. *Neuron* 57, 917–929. doi: 10.1016/j.neuron.2008.01.034

Fukuda, T., Heizmann, C. W., and Kosaka, T. (1997). Quantitative analysis of GAD65 and GAD67 immunoreactivities in somata of GABAergic neurons in the mouse hippocampus proper (CA1 and CA3 regions), with special reference to parvalbumin-containing neurons. *Brain Res.* 764, 237–243. doi: 10.1016/s0006-8993(97)00683-5

Garthwaite, J. (1991). Glutamate, nitric oxide and cell-cell signalling in the nervous system. *Trends Neurosci.* 14, 60–67. doi: 10.1016/0166-2236(91)90022-m

Gonchar, Y., and Burkhalter, A. (1997). Three distinct families of GABAergic neurons in rat visual cortex. *Cereb. Cortex* 7, 347–358. doi: 10.1093/cercor/7.4.347

Gonchar, Y., Wang, Q., and Burkhalter, A. (2007). Multiple distinct subtypes of GABAergic neurons in mouse visual cortex identified by triple immunostaining. *Front. Neuroanat.* 1:3. doi: 10.3389/neuro.05.003.2007

González-Albo, M. C., Elston, G. N., and DeFelipe, J. (2001). The human temporal cortex: characterization of neurons expressing nitric oxide synthase, neuropeptides and calcium-binding proteins, and their glutamate receptor subunit profiles. *Cereb. Cortex* 11, 1170–1181. doi: 10.1093/cercor/11.12.1170

Guo, Y., Kaplan, I. V., Cooper, N. G., and Mower, G. D. (1997). Expression of two forms of glutamic acid decarboxylase (GAD67 and GAD65) during postnatal development of the cat visual cortex. *Brain Res. Dev. Brain Res.* 103, 127–141. doi: 10.1016/s0165-3806(97)81789-0

Hendrickson, A. E., Tillakaratne, N. J., Mehra, R. D., Esclapez, M., Erickson, A., Vician, L., et al. (1994). Differential localization of two glutamic acid decarboxylases (GAD65 and GAD67) in adult monkey visual cortex. *J. Comp. Neurol.* 343, 566–581. doi: 10.1002/cne.903430407

Hendry, S. H., Jones, E. G., DeFelipe, J., Schmechel, D., Brandon, C., and Emson, P. C. (1984). Neuropeptide-containing neurons of the cerebral cortex are also GABAergic. *Proc. Natl. Acad. Sci. U.S.A.* 81, 6526–6530. doi: 10.1073/pnas.81.20.6526

Horvath, T. L., Pu, S., Dube, M. G., Diano, S., and Kalra, S. P. (2001). A GABA-neuropeptide Y (NPY) interplay in LH release. *Peptides* 22, 473–481. doi: 10.1016/s0196-9781(01)00343-6

Houser, C. R., and Esclapez, M. (1994). Localization of mRNAs encoding two forms of glutamic acid decarboxylase in the rat hippocampal formation. *Hippocampus* 4, 530–545. doi: 10.1002/hipo.450040503

Jayakumar, A. R., Sujatha, R., Paul, V., Asokan, C., Govindasamy, S., and Jayakumar, R. (1999). Role of nitric oxide on GABA, glutamic acid, activities of GABA-T and GAD in rat brain cerebral cortex. *Brain Res.* 837, 229–235. doi: 10.1016/s0006-8993(99)01692-3

Jinno, S., Kinukawa, N., and Kosaka, T. (2001). Morphometric multivariate analysis of GABAergic neurons containing calretinin and neuronal nitric oxide synthase in the mouse hippocampus. *Brain Res.* 900, 195–204. doi: 10.1016/s0006-8993(01)02292-2

Jinno, S., and Kosaka, T. (2009). Neuronal circuit-dependent alterations in expression of two isoforms of glutamic acid decarboxylase in the hippocampus following electroconvulsive shock: a stereology-based study. *Hippocampus* 19, 1130–1141. doi: 10.1002/hipo.20576

Kahn, R. A., Panah, M., Kiffel, S., and Weinberger, J. (1997a). Modulation of ischemic excitatory neurotransmitter and gamma-aminobutyric acid release during global temporary cerebral ischemia by local nitric oxide synthase inhibition. *Anesth. Analg.* 84, 1004–1010. doi: 10.1097/00000539-199705000-00010

Kahn, R. A., Panah, M., and Weinberger, J. (1997b). Modulation of ischemic excitatory neurotransmitter and gamma-aminobutyric acid release during global temporary cerebral ischemia by selective neuronal nitric oxide synthase inhibition. *Anesth. Analg.* 84, 997–1003. doi: 10.1097/00000539-199705000-00009

Kajita, Y., Kojima, N., Koganezawa, N., Yamazaki, H., Sakimura, K., and Shirao, T. (2017). Drebrin E regulates neuroblast proliferation and chain migration in the adult brain. *Eur. J. Neurosci.* 46, 2214–2228. doi: 10.1111/ejn.13668

Kanaani, J., el-Husseini, A.-D., Aguilera-Moreno, A., Diacovo, J. M., Bredt, D. S., and Baekkeskov, S. (2002). A combination of three distinct trafficking signals mediates axonal targeting and presynaptic clustering of GAD65. *J. Cell Biol.* 158, 1229–1238. doi: 10.1083/jcb.200205053

Kanaani, J., Patterson, G., Schaufele, F., Lippincott-Schwartz, J., and Baekkeskov, S. (2008). A palmitoylation cycle dynamically regulates partitioning of the GABA-synthesizing enzyme GAD65 between ER-Golgi and post-Golgi membranes. *J. Cell Sci.* 121(Pt 4), 437–449. doi: 10.1242/jcs.011916

Kawaguchi, Y., and Kondo, S. (2002). Parvalbumin, somatostatin and cholecystokinin as chemical markers for specific GABAergic interneuron types in the rat frontal cortex. *J. Neurocytol.* 31, 277–287. doi: 10.1023/a:1024126110356

Köhler, C., Eriksson, L. G., Davies, S., and Chan-Palay, V. (1987). Co-localization of neuropeptide tyrosine and somatostatin immunoreactivity in neurons of individual subfields of the rat hippocampal region. *Neurosci. Lett.* 78, 1–6. doi: 10.1016/0304-3940(87)90551-9

Kubota, Y., and Kawaguchi, Y. (1997). Two distinct subgroups of cholecystokinin-immunoreactive cortical interneurons. *Brain Res.* 752, 175–183. doi: 10.1016/s0006-8993(96)01446-1

Kubota, Y., Shigematsu, N., Karube, F., Sekigawa, A., Kato, S., Yamaguchi, N., et al. (2011). Selective coexpression of multiple chemical markers defines discrete populations of neocortical GABAergic neurons. *Cereb. Cortex* 21, 1803–1817. doi: 10.1093/cercor/bhq252

Kuki, T., Fujihara, K., Miwa, H., Tamamaki, N., Yanagawa, Y., and Mushiake, H. (2015). Contribution of parvalbumin and somatostatin-expressing GABAergic neurons to slow oscillations and the balance in beta-gamma oscillations across cortical layers. *Front. Neural Circ.* 9:6. doi: 10.3389/fncir.2015.00006

Kuriyama, K., and Ohkuma, S. (1995). Role of nitric oxide in central synaptic transmission: effects on neurotransmitter release. *Jpn. J. Pharmacol.* 69, 1–8. doi: 10.1254/jjp.69.1

Lapray, D., Lasztoczi, B., Lagler, M., Viney, T. J., Katona, L., Valenti, O., et al. (2012). Behavior-dependent specialization of identified hippocampal interneurons. *Nat. Neurosci.* 15, 1265–1271. doi: 10.1038/nn.3176

Lazarus, M. S., Krishnan, K., and Huang, Z. J. (2015). GAD67 deficiency in parvalbumin interneurons produces deficits in inhibitory transmission and network disinhibition in mouse prefrontal cortex. *Cereb. Cortex* 25, 1290–1296. doi: 10.1093/cercor/bht322

Marangoz, C., Ayyildiz, M., and Ağar, E. (1994). Evidence that sodium nitroprusside possesses anticonvulsant effects mediated through nitric oxide. *Neuroreport* 5, 2454–2456. doi: 10.1097/00001756-199412000-00012

Martin, D. L., and Rimvall, K. (1993). Regulation of gamma-aminobutyric acid synthesis in the brain. *J. Neurochem.* 60, 395–407. doi: 10.1111/j.1471-4159.1993.tb03165.x

Mower, G. D., and Guo, Y. (2001). Comparison of the expression of two forms of glutamic acid decarboxylase (GAD67 and GAD65) in the visual cortex of normal and dark-reared cats. *Brain Res. Dev. Brain Res.* 126, 65–74. doi: 10.1016/s0165-3806(00)00139-5

Northoff, G., and Mushiake, H. (2020). Why context matters? Divisive normalization and canonical microcircuits in psychiatric disorders. *Neurosci. Res.* 156, 130–140. doi: 10.1016/j.neures.2019.10.002

Obata, K., Hirono, M., Kume, N., Kawaguchi, Y., Itohara, S., and Yanagawa, Y. (2008). GABA and synaptic inhibition of mouse cerebellum lacking glutamate decarboxylase 67. *Biochem. Biophys. Res. Commun.* 370, 429–433. doi: 10.1016/j.bbrc.2008.03.110

Orbán-Kis, K., Szabadi, T., and Szilágyi, T. (2015). The loss of Ivy cells and the hippocampal input modulatory O-LM cells contribute to the emergence of hyperexcitability in the hippocampus. *Rom. J. Morphol. Embryol.* 56, 155–161.

Paredes, M. F., Greenwood, J., and Baraban, S. C. (2003). Neuropeptide Y modulates a G protein-coupled inwardly rectifying potassium current in the mouse hippocampus. *Neurosci. Lett.* 340, 9–12. doi: 10.1016/s0304-3940(03)00036-3

Penix, L. P., Davis, W., and Subramaniam, S. (1994). Inhibition of NO synthase increases the severity of kainic acid-induced seizures in rodents. *Epilepsy Res.* 18, 177–184. doi: 10.1016/0920-1211(94)90038-8

Perrenoud, Q., Rossier, J., Geoffroy, H., Vitalis, T., and Gallopin, T. (2013). Diversity of GABAergic interneurons in layer VIa and VIb of mouse barrel cortex. *Cereb. Cortex* 23, 423–441. doi: 10.1093/cercor/bhs032

Price, C. J., Cauli, B., Kovacs, E. R., Kulik, A., Lambolez, B., Shigemoto, R., et al. (2005). Neurogliaform neurons form a novel inhibitory network in the hippocampal CA1 area. *J. Neurosci.* 25, 6775–6786. doi: 10.1523/JNEUROSCI.1135-05.2005

Rimvall, K., Sheikh, S. N., and Martin, D. L. (1993). Effects of increased gamma-aminobutyric acid levels on GAD67 protein and mRNA levels in rat cerebral cortex. *J. Neurochem.* 60, 714–720. doi: 10.1111/j.1471-4159.1993.tb03206.x

Rudy, B., Fishell, G., Lee, S., and Hjerling-Leffler, J. (2011). Three groups of interneurons account for nearly 100% of neocortical GABAergic neurons. *Dev. Neurobiol.* 71, 45–61. doi: 10.1002/dneu.20853

Sackeim, H. A. (1999). The anticonvulsant hypothesis of the mechanisms of action of ECT: current status. *J. ECT* 15, 5–26.

Sanacora, G., Mason, G. F., Rothman, D. L., Hyder, F., Ciarcia, J. J., Ostroff, R. B., et al. (2003). Increased cortical GABA concentrations in depressed patients receiving ECT. *Am. J. Psychiatry* 160, 577–579. doi: 10.1176/appi.ajp.160.3.577

Schuman, E. M., and Madison, D. V. (1994). Nitric oxide and synaptic function. *Annu. Rev. Neurosci.* 17, 153–183. doi: 10.1146/annurev.ne.17.030194.001101

Schweitzer, P., Madamba, S. G., and Siggins, G. R. (1998). Somatostatin increases a voltage-insensitive K+ conductance in rat CA1 hippocampal neurons. *J. Neurophysiol.* 79, 1230–1238. doi: 10.1152/jn.1998.79.3.1230

Sutula, T., Goldschmidt, R., and Steward, O. (1983). Mechanisms of colchicine neurotoxicity in the dentate gyrus: dissociation of seizures and cell death. *Exp. Neurol.* 81, 683–693. doi: 10.1016/0014-4886(83)90335-7

Tallent, M. K., and Siggins, G. R. (1999). Somatostatin acts in CA1 and CA3 to reduce hippocampal epileptiform activity. *J. Neurophysiol.* 81, 1626–1635. doi: 10.1152/jn.1999.81.4.1626

Tian, N., Petersen, C., Kash, S., Baekkeskov, S., Copenhagen, D., and Nicoll, R. (1999). The role of the synthetic enzyme GAD65 in the control of neuronal gamma-aminobutyric acid release. *Proc. Natl. Acad. Sci. U.S.A.* 96, 12911–12916. doi: 10.1073/pnas.96.22.12911

Tremblay, R., Lee, S., and Rudy, B. (2016). GABAergic interneurons in the neocortex: from cellular properties to circuits. *Neuron* 91, 260–292. doi: 10.1016/j.neuron.2016.06.033

Tricoire, L., Pelkey, K. A., Daw, M. I., Sousa, V. H., Miyoshi, G., Jeffries, B., et al. (2010). Common origins of hippocampal Ivy and nitric oxide synthase expressing neurogliaform cells. *J. Neurosci.* 30, 2165–2176. doi: 10.1523/JNEUROSCI.5123-09.2010

Tricoire, L., and Vitalis, T. (2012). Neuronal nitric oxide synthase expressing neurons: a journey from birth to neuronal circuits. *Front. Neural Circ.* 6:82. doi: 10.3389/fncir.2012.00082

Tritsch, N. X., Granger, A. J., and Sabatini, B. L. (2016). Mechanisms and functions of GABA co-release. *Nat. Rev. Neurosci.* 17, 139–145. doi: 10.1038/nrn.2015.21

Vega Rasgado, L. A., Reyes, G. C., and Vega Díaz, F. (2018). Role of nitric oxide synthase on brain GABA transaminase activity and GABA levels. *Acta Pharm.* 68, 349–359. doi: 10.2478/acph-2018-0022

Vezzani, A., Sperk, G., and Colmers, W. F. (1999). Neuropeptide Y: emerging evidence for a functional role in seizure modulation. *Trends Neurosci.* 22, 25–30. doi: 10.1016/s0166-2236(98)01284-3

Wang, X., Gao, F., Zhu, J., Guo, E., Song, X., Wang, S., et al. (2014). Immunofluorescently labeling glutamic acid decarboxylase 65 coupled with confocal imaging for identifying GABAergic somata in the rat dentate gyrus-A comparison with labeling glutamic acid decarboxylase 67. *J. Chem. Neuroanat.* 6, 51–63. doi: 10.1016/j.jchemneu.2014.07.002

Wenzel, M., Hamm, J. P., Peterka, D. S., and Yuste, R. (2017). Reliable and elastic propagation of cortical seizures in vivo. *Cell Rep.* 19, 2681–2693. doi: 10.1016/j.celrep.2017.05.090

Yu, X., Ye, Z., Houston, C. M., Zecharia, A. Y., Ma, Y., Zhang, Z., et al. (2015). Wakefulness is governed by GABA and histamine cotransmission. *Neuron* 87, 164–178. doi: 10.1016/j.neuron.2015.06.003

Conflict of Interest: The authors declare that the research was conducted in the absence of any commercial or financial relationships that could be construed as a potential conflict of interest.

Publisher's Note: All claims expressed in this article are solely those of the authors and do not necessarily represent those of their affiliated organizations, or those of the publisher, the editors and the reviewers. Any product that may be evaluated in this article, or claim that may be made by its manufacturer, is not guaranteed or endorsed by the publisher.

frontiers in Human Neuroscience

ORIGINAL RESEARCH
published: 12 November 2021
doi: 10.3389/fnhum.2021.750329

After-Effects of Intermittent Theta-Burst Stimulation Are Differentially and Phase-Dependently Suppressed by α- and β-Frequency Transcranial Alternating Current Stimulation

Katsuya Ogata[1], Hisato Nakazono[2], Takuro Ikeda[3], Shin-ichiro Oka[3], Yoshinobu Goto[4] and Shozo Tobimatsu[5]*

[1] Department of Pharmacy, School of Pharmaceutical Sciences at Fukuoka, International University of Health and Welfare, Okawa, Japan, [2] Department of Occupational Therapy, Faculty of Medical Science, Fukuoka International University of Health and Welfare, Fukuoka, Japan, [3] Department of Physical Therapy, School of Health Sciences, Fukuoka International University of Health and Welfare, Fukuoka, Japan, [4] School of Medicine, International University of Health and Welfare, Naritaa, Japan, [5] Department of Orthoptics, Faculty of Medical Science, Fukuoka International University of Health and Welfare, Fukuoka, Japan

OPEN ACCESS

Edited by:
Ferdinand Binkofski,
RWTH Aachen University, Germany

Reviewed by:
Vera Moliadze,
University Medical Center Schleswig-Holstein, Germany
Gregor Thut,
University of Glasgow, United Kingdom
Makoto Suzuki,
Tokyo Kasei University, Japan
Thomas Kammer,
University of Ulm, Germany

***Correspondence:**
Katsuya Ogata
ogata_k@iuhw.ac.jp

Specialty section:
This article was submitted to Brain Imaging and Stimulation, a section of the journal Frontiers in Human Neuroscience

Received: 30 July 2021
Accepted: 25 October 2021
Published: 12 November 2021

Citation:
Ogata K, Nakazono H, Ikeda T, Oka S, Goto Y and Tobimatsu S (2021) After-Effects of Intermittent Theta-Burst Stimulation Are Differentially and Phase-Dependently Suppressed by α- and β-Frequency Transcranial Alternating Current Stimulation. Front. Hum. Neurosci. 15:750329. doi: 10.3389/fnhum.2021.750329

Intermittent theta-burst stimulation (iTBS) using transcranial magnetic stimulation (TMS) is known to produce excitatory after-effects over the primary motor cortex (M1). Recently, transcranial alternating current stimulation (tACS) at 10 Hz (α) and 20 Hz (β) have been shown to modulate M1 excitability in a phase-dependent manner. Therefore, we hypothesized that tACS would modulate the after-effects of iTBS depending on the stimulation frequency and phase. To test our hypothesis, we examined the effects of α- and β-tACS on iTBS using motor evoked potentials (MEPs). Eighteen and thirteen healthy participants were recruited for α and β tACS conditions, respectively. tACS electrodes were attached over the left M1 and Pz. iTBS over left M1 was performed concurrently with tACS. The first pulse of the triple-pulse burst of iTBS was controlled to match the peak (90°) or trough (270°) phase of the tACS. A sham tACS condition was used as a control in which iTBS was administered without tACS. Thus, each participant was tested in three conditions: the peak and trough of the tACS phases and sham tACS. As a result, MEPs were enhanced after iTBS without tACS (sham condition), as observed in previous studies. α-tACS suppressed iTBS effects at the peak phase but not at the trough phase, while β-tACS suppressed the effects at both phases. Thus, although both types of tACS inhibited the facilitatory effects of iTBS, only α-tACS did so in a phase-dependent manner. Phase-dependent inhibition by α-tACS is analogous to our previous finding in which α-tACS inhibited MEPs online at the peak condition. Conversely, β-tACS reduced the effects of iTBS irrespective of its phase. The coupling of brain oscillations and tACS rhythms is considered important in the generation of spike-timing-dependent

plasticity. Additionally, the coupling of θ and γ oscillations is assumed to be important for iTBS induction through long-term potentiation (LTP). Therefore, excessive coupling between β oscillations induced by tACS and γ or θ oscillations induced by iTBS might disturb the coupling of θ and γ oscillations during iTBS. To conclude, the action of iTBS is differentially modulated by neuronal oscillations depending on whether α- or β-tACS is applied.

Keywords: transcranial alternating current stimulation, transcranial magnetic stimulation, primary motor cortex, motor evoked potentials, intermittent theta burst stimulation, phase dependency, combined stimulation

INTRODUCTION

Transcranial alternating current stimulation (tACS) is a non-invasive brain stimulation (NIBS) method that uses alternating current over the scalp, typically without a direct current shift. An early report revealed that motor learning was modulated after 2–10 min of 0.4 mA tACS at 10 Hz but not 1, 15, 30, or 45 Hz, while motor evoked potentials (MEPs) were not modulated after stimulation at any of these frequencies (Antal et al., 2008). Following this study, the effects of tACS over the primary motor cortex (M1) have been investigated and their dependency on tACS frequency has been reported (Feurra et al., 2011). Specifically, tACS at 20 Hz but not 5, 10, or 40 Hz with 1 mA was effective during stimulation. These studies indicate that tACS effects depend on the stimulation intensity as well as duration and frequency. Although the underlying mechanisms that produce this frequency dependency have not been established, the entrainment of cortical oscillations may be involved (Herrmann et al., 2013). Subsequently, the effects have been suggested to depend on the phase (Guerra et al., 2016; Nakazono et al., 2016; Raco et al., 2016), which is in line with the entrainment of oscillations.

Theta-burst stimulation (TBS) is a patterned form of transcranial magnetic stimulation (TMS) in which triple-pulse bursts (typically 50 Hz) are repeated at 5 Hz (Huang et al., 2005). Continuous and intermittent TBS [cTBS, Intermittent theta-burst stimulation (iTBS)] result in cortical inhibition and excitation, respectively. The mechanisms underlying these TBS after-effects are not fully understood; however, long-term potentiation (LTP) or long-term depression (LTD) through N-methyl-D-aspartate receptor or γ-aminobutyric acid have been suggested to be important factors (Cárdenas-Morales et al., 2010; Rounis and Huang, 2020). The ability to modulate cortical excitability with a short stimulation duration popularized TBS, and it has been applied widely not only to the motor cortices, but also to other brain regions as a means to combat symptoms of psychiatric conditions such as depression (Blumberger et al., 2018; Rounis and Huang, 2020). However, the effects of TBS have been shown to be variable (Hamada et al., 2013), as with other methods of NIBS (Wiethoff et al., 2014; Guerra et al., 2020a). Latency differences resulting from different TMS current directions, which involve I-wave recruitment, have been proposed to contribute to the variability (Hamada et al., 2013), while cortical oscillations recorded by electroencephalography (EEG) have been shown to reflect cortical excitability indexed by MEP amplitudes (Khademi et al., 2018; Zrenner et al., 2018; Ogata et al., 2019). Thus, variability in cortical oscillations might influence NIBS effects. Indeed, repeated burst pulses of TMS that were synchronized to the peak phase of α-band EEG at the central region, which reflects endogenous cortical oscillations around the sensorimotor region, resulted in post-intervention MEP facilitation (Zrenner et al., 2018). Accordingly, we hypothesized that coupling iTBS with oscillations entrained by a specific phase of tACS could lead to more apparent after-effects. In a previous study, iTBS combined with γ-band (70 Hz) tACS resulted in an enhanced iTBS effect, while β-band (20 Hz) tACS did not modulate the iTBS effect in either direction (Guerra et al., 2018). However, the tACS phase was not aligned with the TMS pulses in that study. In our recent study (Nakazono et al., 2021), synchronized tACS with repetitive paired-pulse stimulation (rPPS) enhanced M1 excitability more than rPPS alone at the peak phase of 20-Hz tACS, but not at the trough phase. Conversely, 10-Hz tACS did not facilitate rPPS after-effects at either the peak or trough phases. Thus, the effects of tACS with rPPS are phase and frequency dependent. In this study, we investigated the synchronized effects of α- and β-frequency tACS when combined with iTBS.

MATERIALS AND METHODS

Participants

Eighteen healthy volunteers (men = 10, women = 8; age: 20–24 years) were recruited for the 10-Hz (α) tACS experiment and thirteen (men = 8, women = 5; age: 20–35 years) for the 20-Hz (β) tACS experiment. One individual participated in both experiments. The sample size was determined based on a recent systematic review that considered 82 iTBS studies with samples ranging from 2 to 77 participants (mean ± SD: 13.2 ± 10.8) (Chung et al., 2016). Thus, the current sample sizes were within the average range. All participants were right-handed by self-report, and none had a history of neuropsychological disorders. All participants gave their written informed consent following an explanation of the experiments in accordance with the Declaration of Helsinki. This study was approved by the Ethics Committee of Kyushu University and the International University of Health and Welfare.

Motor Evoked Potentials

Motor evoked potentials were recorded as in our previous studies (Nakazono et al., 2016; Hayashi et al., 2019; Ogata et al., 2019).

In brief, participants sat in a comfortable chair and kept their right hands relaxed. They were asked to keep their eyes open. MEPs were recorded from their right first dorsal interosseus muscle. Recordings were band-pass filtered between 10 and 3,000 Hz and sampled at 10 kHz. MEP data from 250 ms before TMS onset until 250 ms after TMS onset were stored on a Windows PC using Multiscope PSTH software ver. 1.7 (MedicalTry System, Tokyo, Japan) for offline analysis. Electromyographies (EMGs) were shown to the participants on a monitor as visual feedback. Single-pulse TMS was delivered with a monophasic Magstim 200 (Magstim Co., Ltd., Whitland, United Kingdom) with a figure-of-eight coil that was 70 mm in diameter. The TMS coil was placed over the left M1 hot spot with the handle pointing posterolaterally to approximately 45° from the midline. To ensure that the positions of the coils were constant throughout each session, their position and orientation were marked in pen on plastic wrap covering the scalp. The TMS intensity was adjusted to obtain 0.5–1.5 mV MEPs, which occurred at 53.1 ± 9.7% of maximum stimulator output (mean ± SD) for the α-tACS experiment and 53.6 ± 7.7% for the β-one. Twenty-four MEPs were obtained for each recording with an interstimulus interval of 5–7 s.

Intermittent Theta-Burst Stimulation

Intermittent theta-burst stimulation pulses were delivered using a Magstim SuperRapid system (Magstim Co., Ltd., Whitland, United Kingdom) with a figure-of-eight coil that was 70 mm in diameter. Three 50-Hz pulses with a 20-ms interval were repeated every 200 ms (5 Hz) for 2 s with an 8-s pause. Six hundred pulses (200 s) were delivered over the left M1 "hot spot" in each session. The stimulus intensity was set to 80% of the active motor threshold (Huang et al., 2005), which was determined as the minimum intensity needed to obtain 200 μV MEPs with weak contraction of the target muscle in at least 5 of 10 trials (Groppa et al., 2012). The active motor threshold was 50.1 ± 6.7% (mean ± SD) for the α-tACS experiment and 50.6 ± 6.6% for the β-one, respectively.

Transcranial Alternating Current Stimulation

Transcranial alternating current stimulation was administered as in our previous studies (Nakazono et al., 2016, 2021). Two 5 × 7 cm self-adhesive electrodes (PALS electrodes, Axelgaard Manufacturing Co., Ltd., Fallbrook, CA, United States) were attached with electrically conductive gel (Gelaid, Nihonkohden, Tokyo, Japan) over the left M1 hot spot and Pz according to the international 10–20 system (**Figure 1A**). tACS was delivered using a battery-driven current stimulator (DC Stimulator-Plus, NeuroConn GmbH, Ilmenau, Germany) with an intensity of 1 mA. The electrode size, position, and current intensity were chosen based on previous studies (Feurra et al., 2011; Helfrich et al., 2014; Guerra et al., 2016; Nakazono et al., 2016, 2021). The tACS duration was 260 s, and the stimulation began 60 s before iTBS onset and lasted until iTBS offset. The tACS current was ramped up and down in 5-s increments to reduce skin sensations.

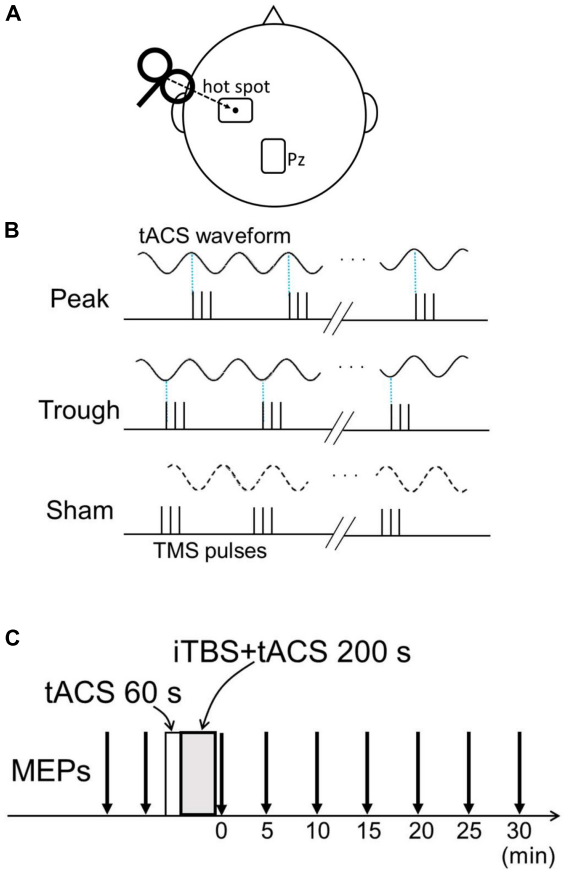

FIGURE 1 | Experimental setup. **(A)** Transcranial alternating current stimulation (tACS) electrode position and transcranial magnetic stimulation (TMS) coil configuration. The target electrode was placed over the left M1 "hot spot," and TMS was delivered over the target electrode. The reference electrode was placed over Pz. **(B)** Three conditions for the combined tACS/intermittent theta-burst stimulation (iTBS) pulses. On the basis of the tACS phase, the first of the three pulses was adjusted to 90° for the peak condition and to 270° for the trough condition. For the sham condition, tACS only lasted 20 s and was terminated before iTBS began. Thus, no tACS current flowed during iTBS. **(C)** Time course of the experiment. Baseline motor evoked potentials (MEPs) were obtained from two sessions comprising the recording of 24 MEPs before the combined stimulation. tACS began before iTBS and continued after iTBS onset for 200 s. After the intervention, 24 MEPs were recorded every 5 min for 30 min.

Procedures

Intermittent theta-burst stimulation was synchronized with α- and β-tACS in separate experiments. All participants completed three conditions in each experiment: peak (90°), trough (270°), and sham, where the sham condition comprised iTBS without tACS and was used as a control. For the first two conditions, the timing of the first iTBS pulse was controlled to match either the peak or trough phase of the tACS (**Figure 1B**). Because there was a slight delay of about 10 ms between the tACS phase and iTBS pulse in the combined 260 s stimulation without adjustment, we calculated the precise iTBS pulse time accordingly, enabling us to match the iTBS pulse with the tACS phase. The tACS waveforms and TMS pulses were recorded during combined stimulation,

and synchronization between the iTBS pulse and tACS phase was confirmed. In the sham condition, tACS was only administered for 20 s, and thus current did not flow during iTBS. Baseline MEP amplitudes were obtained in two 24-MEP sessions before the combined stimulation. After the combined stimulation, 24 MEPs were obtained for 30 min at 5-min intervals (i.e., 0, 5, 10, 15, 20, 25, 30 min after stimulation; **Figure 1C**). The different conditions took place at least 2 days apart, and the order of the three conditions (peak, trough, and sham) was randomized and counterbalanced across the participants. The order of the conditions was blinded only to the subjects; thus, the experiment had a single-blind, cross-over design.

Data Analysis

Motor evoked potential waveforms were visually checked, and trials with artifacts (about 50 μV or larger) during the 100 ms before TMS pulse onset were discarded. Fewer than 17% (4/24) trials were discarded in each session. Peak-to-peak amplitudes were measured and log-transformed to normalize their distribution, and then averaged for each recording (Nielsen, 1996; Avenanti et al., 2006; Feurra et al., 2011; Guerra et al., 2016; Nakazono et al., 2016; Borgomaneri et al., 2020). Mean MEP amplitudes after combined tACS/iTBS were normalized by subtracting the averaged amplitudes over the two baseline MEP sessions, as in previous studies (Avenanti et al., 2006; Goldsworthy et al., 2016; Borgomaneri et al., 2020). This was done because we intended to estimate the after-effects of tACS over those of iTBS, i.e., to compare MEPs modulated by combined iTBS and tACS (peak or trough) with those modulated by iTBS only (sham). The three stimulation conditions were compared using a linear mixed-effect (LME) model with fixed effects of time (0–30 min after combined stimulation) and phase condition (peak, trough, and sham), as well as the random effects of participant. When a main effect of phase condition was significant, pairwise comparisons were performed with the Holm–Bonferroni correction. A p-value less than 0.05 was considered to be significant. Error bars represent the standard error of the mean (SEM) throughout the study. The data from the α- and β-tACS experiments were analyzed separately. The baseline MEP amplitudes were also compared using a LME model with fixed effects of phase condition and the random effects of participant. Statistical analyses were carried out using R (R Core Team, 2020). Untransformed MEP amplitudes were also analyzed for comparison of the transformed MEP data.

RESULTS

Motor evoked potential waveforms from a representative participant are shown in **Figure 2A** for the α-tACS experiment. MEPs were enhanced after the sham (iTBS only) and trough conditions but not after the peak condition. The baseline amplitudes for α- and β-tACS were not significantly different ($p = 0.52$ and 0.32, respectively). Thus, MEP amplitudes that had been subtracted from baseline were used in the following analyses (as described in the Methods). The changes of mean

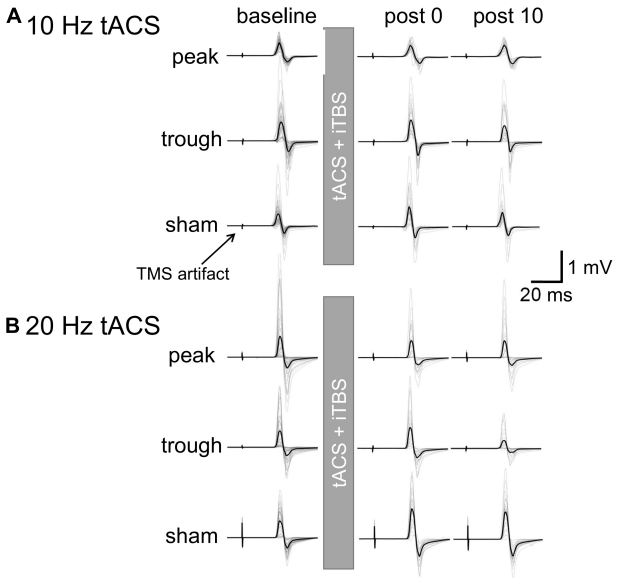

FIGURE 2 | Motor evoked potential waveforms from a representative participant for iTBS with α- or β-tACS. MEP waveforms are shown for the baseline and 0 and 10 min after the combined stimulation. Thick lines indicate the mean waveform calculated from 24 trials in each session. Thin lines indicate each of the 24 trials. **(A)** iTBS with α-tACS. MEPs increased after the trough and sham conditions but were suppressed after the peak condition. **(B)** iTBS with β-tACS. Compared with the sham condition, MEPs were inhibited after both the peak and trough conditions, which differed from the iTBS/α-tACS results. For actual data analysis, MEP amplitudes were measured for each trial, not for average waveforms.

log-transformed MEP amplitudes for α-tACS/iTBS from baseline values are shown in **Figure 3**. The synchronized stimulation resulted in phase-dependent effects. Mean MEP amplitudes for the sham and trough conditions were larger after α-tACS/iTBS (positive values). However, those for the peak condition were often lower than baseline (negative values). Therefore, MEP amplitudes were lower for the peak condition than for the trough or sham conditions. A LME model indicated a main effect of tACS condition ($F_{(2,357)} = 4.74$, $p = 0.009$, $\eta_p{}^2 = 0.03$). Furthermore, we found significant differences between the peak and sham conditions ($F_{(1,232)} = 10.4$, $p = 0.004$, 95% confidence interval (CI) = 0.029 – 0.118) and between the peak and trough conditions ($F_{(1,232)} = 5.15$, $p = 0.048$, 95% CI = 0.006 – 0.103), but not between the trough and sham conditions ($F_{(1,232)} = 0.57$, $p = 0.45$). These results indicate that synchronized tACS in the peak condition inhibited the effects of iTBS relative to the sham and trough conditions. The intercept of the data produced by the LME model, in which the sham stimulation was the control, was 0.05 ± 0.03 ($p = 0.1$). Thus, the MEP amplitudes after the sham condition were above zero, although this enhancement was not confirmed statistically. Of note, these results were obtained by the log-transformed MEP amplitudes followed by subtracting baseline values as described in the section "Data Analysis," but not by the raw MEP amplitudes.

Figure 2B shows the representative MEP waveforms for the β-tACS experiment. MEPs were enhanced after the sham

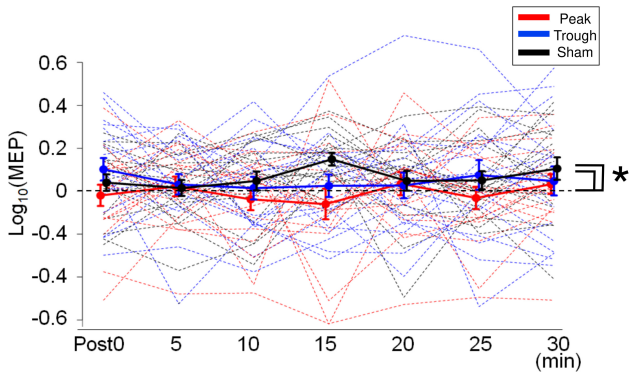

FIGURE 3 | Mean MEP amplitudes after iTBS/α-tACS. MEP amplitudes were log-transformed and normalized by the baseline amplitudes. Accordingly, positive values indicate enhancement after the stimulation while negative values imply MEP suppression. Thick solid lines represent mean amplitudes while dotted lines indicate the MEP amplitudes for each subject. MEP amplitudes after the sham and trough conditions were enhanced continuously after stimulation, while those after the peak condition were often suppressed. Accordingly, MEP amplitudes for the peak condition were lower than those for the sham and trough conditions. Error bars indicate standard errors of the mean (SEM). *$p < 0.05$.

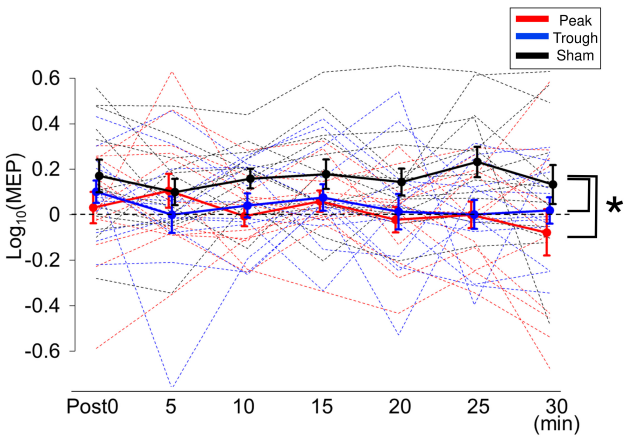

FIGURE 4 | Mean MEP amplitudes after iTBS/β-tACS. MEP amplitudes were processed in the same manner as that described in **Figure 3**. MEP amplitudes for the sham condition were clearly enhanced after the intervention, whereas those for the peak and trough conditions were not significantly modulated. Consequently, MEP amplitudes for the peak and trough conditions were lower than those for the sham condition. Error bars indicate SEM. *$p < 0.05$.

condition but not after the peak or trough conditions. As seen in **Figure 4**, β-tACS with iTBS modulated the mean MEP amplitudes, but not in the same way as with α-tACS. β-tACS/iTBS erased the iTBS effect, and MEP amplitudes in the peak and trough conditions remained unenhanced. A LME model revealed a main effect of the tACS condition ($F_{(2,257)} = 14.0$, $p < 0.001$, $\eta_p{}^2 = 0.10$). Further analysis showed a significant difference between the sham and peak conditions ($F_{(1,167)} = 28.0$, $p < 0.001$, 95% CI = 0.092 – 0.201) and between the sham and trough conditions ($F_{(1,167)} = 17.3$, $p < 0.001$, 95% CI = 0.065 – 0.181), but not between the peak and trough conditions ($F_{(1,167)} = 0.62$, $p = 0.43$). The intercept of the LME model, in which the sham was the control, was 0.18 ± 0.04 ($p < 0.001$), which indicates that the MEPs were enhanced in the sham condition. In sum, iTBS-induced enhancement of M1 excitability was inhibited when the stimulation was synchronized with 20-Hz tACS. This was irrespective of the tACS phase, which was unlike the phase-dependent inhibition seen with α-tACS synchronization. Again, these results were not found by the raw MEP amplitude analysis as in α-tACS experiment.

DISCUSSION

We investigated the effect of synchronizing α- and β-tACS with iTBS on M1 excitability. Our results revealed that (1) α-tACS suppressed iTBS in the peak condition, but not in the trough condition, and that (2) β-tACS inhibited iTBS-induced enhancement regardless of the tACS phase. Thus, we have demonstrated for the first time that α- and β-tACS modulate iTBS after-effects in both frequency and phase-dependent manners.

Online Effects of Transcranial Alternating Current Stimulation

Online effects of tACS have been reported to modulate cortical excitability in a frequency-dependent manner. For instance, Feurra et al. (2011) reported that while β-tACS effectively enhanced M1 excitability, other frequencies (5, 10, or 40 Hz) did not. Our previous study (Nakazono et al., 2016) also revealed frequency and phase-dependent effects of M1-tACS on the α and β bands: tACS at the peak phase was effective in differentiating the facilitatory effect of 20-Hz tACS from the inhibitory effect of α-tACS. Previous studies have reported online phase-dependent MEP modulation by β-tACS (Guerra et al., 2016; Raco et al., 2016; Schilberg et al., 2018), which is in line with the entrainment of cortical oscillations (Thut et al., 2011; Herrmann et al., 2013). However, the relationship between phase and MEP amplitudes was not consistent among previous studies. Taken together, the online effects of tACS are clear for α/β frequencies.

Combined Transcranial Alternating Current Stimulation and Intermittent Theta-Burst Stimulation

Following the significant online tACS effects discussed above, iTBS combined with γ-tACS was reported to enhance the effects of iTBS over M1, but the same was not true for β-tACS (Guerra et al., 2018). In that study, the tACS phase was not synchronized with the iTBS pulses. Thus, we assumed that β-tACS synchronized with iTBS might reveal facilitatory effects beyond what is seen after M1 iTBS. Indeed, we recently found that the facilitatory after-effects of rPPS over M1 were more pronounced with β-ACS when the TMS pulses were synchronized to the peak phase but not the trough phase

(Nakazono et al., 2021). Conversely, α-tACS did not significantly modulate the effects of rPPS. The inhibitory effect of cTBS on M1 was found to be greater with α-tACS when the TBS pulses were aligned to the trough phase than when they were aligned to the peak phase (Goldsworthy et al., 2016). Adding to these previous studies, our current results indicate that synchronization of α-tACS with iTBS suppressed M1 excitability compared with iTBS delivered in a phase-dependent manner. Specifically, MEP amplitudes in the peak condition were lower than those in the trough as well as the sham condition. Because α-tACS synchronized at the peak phase tended to suppress single-pulse MEPs (Nakazono et al., 2016), it is likely that the effect of iTBS was suppressed by the inhibitory effect of peak-phase α-tACS, but not trough-phase α-tACS. It has been proposed that α oscillations reflect pulsed inhibition or top-down inhibitory control, depending on their amplitudes and phases (Klimesch et al., 2007; Jensen and Mazaheri, 2010; Mazaheri and Jensen, 2010). In a previous study, depressive cTBS effects were enhanced by trough-phase α-tACS (Goldsworthy et al., 2016), which seems to contradict the current results. If peak-phase α-tACS has inhibitory effects *via* pulsed inhibition, trough-phase α-tACS could lead to less inhibitory or facilitatory effects. Cortical modulation by iTBS and cTBS may be derived from LTP and LTD-like mechanisms. While high-frequency bursts may be necessary to induce LTP-like modulation, overstimulation could reduce or reverse LTP-like effects (Wischnewski and Schutter, 2015). Thus, cTBS could cause LTD-like effects through overstimulating bursts, whereas 2-s iTBS pulses with 8-s intervals could induce cortical potentiation. In these circumstances, more efficient bursts of cTBS synchronized with the trough phase of tACS would lead to more overstimulation by continuous bursts, resulting in greater depression of cortical excitability. In contrast, less efficient iTBS bursts synchronized with the peak phase of tACS would disturb the induction of iTBS effects, as was observed in the current study.

In contrast to α-tACS, β-tACS suppressed the effects of iTBS regardless of the tACS phase. Although the reasons for this are unclear, given that unsynchronized β-tACS did not modulate the iTBS after-effects (Guerra et al., 2018), the synchronization of β-tACS appears to be critical for inhibiting iTBS over M1. β oscillations are thought to originate in the motor cortices, whereas α oscillations are thought to be generated by the somatosensory cortices (Salmelin et al., 1995). β oscillations over M1 have been suggested to reflect idling rhythm, response inhibition, or maintenance of the *status quo* (Engel and Fries, 2010). In pathological conditions such as Parkinson disease, exaggerated coupling of the local field potentials has been reported between β phase and γ oscillations in M1 (de Hemptinne et al., 2013). Therefore, excessive coupling of β-tACS and γ oscillations induced by iTBS might result in the suppression of iTBS effects. One of the proposed mechanisms through which tACS is thought to affect cortical excitation is spike-timing-dependent plasticity, in which the interaction between ongoing oscillatory activity and tACS is important for tACS effectiveness (Zaehle et al., 2010). The coupling of θ and γ rhythms is considered important for cortical functions such as cognitive processing (Canolty et al., 2006; Lisman, 2010) and is also assumed to be linked to the induction of TBS effects (Rounis and Huang, 2020). Taken together, unlike γ-tACS, entraining β oscillations with tACS might interfere with the coupling of θ and γ rhythms, which hampers LTP induction during iTBS (Guerra et al., 2018).

After-Effects of Transcranial Alternating Current Stimulation

Although our current results could be derived from an interaction between tACS and iTBS, another explanation involves additive tACS after-effects. tACS after-effects have been consistently reported in studies using much higher stimulation frequencies (140 Hz and 250 Hz tACS; Moliadze et al., 2010, 2012; Inukai et al., 2016; Guerra et al., 2020b). α- and β-tACS also induce after-effects on visual (Zaehle et al., 2010; Neuling et al., 2013; Vossen et al., 2015; Kasten et al., 2016; Nakazono et al., 2020) and auditory (Ahn et al., 2019; Wang et al., 2020) neurophysiological functions. Conversely, α- and β-tACS have not consistently been reported to produce after-effects on M1. Rjosk et al. (2016) reported that 20-Hz tACS over M1 for 20 min did not modulate MEP amplitudes or induce intracortical or interhemispheric inhibition. Several other studies have also failed to observe effects after α- and/or β-tACS (Antal et al., 2008; Feurra et al., 2011, 2019; Wach et al., 2013; Nakazono et al., 2016; Pozdniakov et al., 2021), yet other studies have observed effects after β-tACS. For example, 15-Hz tACS suppressed MEPs (Zaghi et al., 2010), and 1.5 mA or 2 mA 20-Hz tACS reportedly increased MEP amplitudes (Gallasch et al., 2018; Wischnewski et al., 2019a). Therefore, after-effects induced by α- and β-tACS are inconsistent and weak. This is especially true for tACS delivered with small 1-mA currents, as opposed to larger currents, as suggested by a meta-analysis (Wischnewski et al., 2019b). Taken together, the suppressive effects of tACS on iTBS do not result from tACS after-effects but rather are generated through the interaction between iTBS and tACS.

Limitations

There are several limitations to this study. First, neuronavigation was not available, and the TMS coil position was not monitored or recorded with a camera. However, the M1 hot spot was determined based on the standard protocol, and the position was marked with a pen to ensure the consistency of the TMS coil position throughout each session. Thus, we believe the TMS coil position variability to have been negligible. Second, the sample size was relatively small and slightly different between the α- and β-tACS experiments. However, this sample size was within the average range of other studies. Moreover, when the sample size in the α-tACS condition was limited to the first 13 subjects as in the β-tACS experiment, consistent results were obtained, i.e., a significant main effect of tACS condition ($F_{(2,257)} = 4.66$, $p = 0.01$). The differences were also significant between the peak and sham conditions ($F_{(1,167)} = 4.4$, $p = 0.037$) and between the peak and trough conditions ($F_{(1,167)} = 9.58$, $p = 0.002$), but not between the trough and sham conditions ($F_{(1,167)} = 0.93$,

$p = 0.34$). Thus, it is unlikely that the difference in the sample size between the α- and β-tACS experiments caused the differential results. Third, iTBS effects are facilitatory in general, and this was observed for the β-tACS but not the α-tACS experiment. Because iTBS effects are known to vary among subjects (Hamada et al., 2013), individual variation could have influenced the data. Marginal effects can be found for other NIBS protocols such as cTBS (Goldsworthy et al., 2016). However, because the tACS effects were statistically demonstrated for combined stimulation compared with iTBS only (sham condition), it is likely that tACS suppressed the effects of iTBS. Finally, the present results were not achieved by the untransformed data, but after the data transformation, where MEP amplitudes were log-transformed to normalize their distribution and subtracted by baseline values to estimate the after-effects. Although these transformations were employed in other researchers (Avenanti et al., 2006; Goldsworthy et al., 2016; Borgomaneri et al., 2020), the tACS effect on iTBS was thought to be weak considering the data transformation as well as small η_p^2. Therefore, our results should be interpreted with caution.

CONCLUSION

We explored the after-effects of iTBS synchronized with α- and β-tACS. We found phase-dependent suppression of iTBS at the peak phase for α-tACS, and phase-independent inhibition for β-tACS. We propose that cortical oscillations at α or β frequencies could interfere with iTBS activity through different mechanisms. Determining these differential mechanisms could provide new insights for understanding the mechanisms underlying iTBS, as well as other types of NIBS, and lead to more efficient protocols for enhancing cortical functions.

DATA AVAILABILITY STATEMENT

The raw data supporting the conclusions of this article will be made available by the authors, without undue reservation.

ETHICS STATEMENT

The studies involving human participants were reviewed and approved by the Ethics Committee of Kyushu University and the International University of Health and Welfare. The patients/participants provided their written informed consent to participate in this study.

AUTHOR CONTRIBUTIONS

KO, HN, and ST developed the concept for the experiments. KO, HN, TI, and S-IO collected and analyzed the data. KO and HN drafted the manuscript. TI, S-IO, YG, and ST provided comments to improve the manuscript. All authors contributed to the article and approved the submitted version.

FUNDING

This research was supported by the KAKENHI Grant Numbers 21K11174, 19H03977, 18K17720, and 18K07530.

ACKNOWLEDGMENTS

We thank Adam Phillips and Sydney Koke from Edanz (https://jp.edanz.com/ac) for editing a draft of this manuscript.

REFERENCES

Ahn, S., Mellin, J. M., Alagapan, S., Alexander, M. L., Gilmore, J. H., Jarskog, L. F., et al. (2019). Targeting reduced neural oscillations in patients with schizophrenia by transcranial alternating current stimulation. *Neuroimage* 186, 126–136. doi: 10.1016/j.neuroimage.2018.10.056

Antal, A., Boros, K., Poreisz, C., Chaieb, L., Terney, D., and Paulus, W. (2008). Comparatively weak after-effects of transcranial alternating current stimulation (tACS) on cortical excitability in humans. *Brain Stimul.* 1, 97–105. doi: 10.1016/j.brs.2007.10.001

Avenanti, A., Minio-Paluello, I., Minio Paluello, I., Bufalari, I., and Aglioti, S. M. (2006). Stimulus-driven modulation of motor-evoked potentials during observation of others' pain. *Neuroimage* 32, 316–324. doi: 10.1016/j.neuroimage.2006.03.010

Blumberger, D. M., Vila-Rodriguez, F., Thorpe, K. E., Feffer, K., Noda, Y., Giacobbe, P., et al. (2018). Effectiveness of theta burst versus high-frequency repetitive transcranial magnetic stimulation in patients with depression (THREE-D): a randomised non-inferiority trial. *Lancet* 391, 1683–1692. doi: 10.1016/S0140-6736(18)30295-2

Borgomaneri, S., Vitale, F., and Avenanti, A. (2020). Early motor reactivity to observed human body postures is affected by body expression, not gender. *Neuropsychologia* 146:107541. doi: 10.1016/j.neuropsychologia.2020.107541

Canolty, R. T., Edwards, E., Dalal, S. S., Soltani, M., Nagarajan, S. S., Kirsch, H. E., et al. (2006). High gamma power is phase-locked to theta oscillations in human neocortex. *Science* 313, 1626–1628. doi: 10.1126/science.1128115

Cárdenas-Morales, L., Nowak, D. A., Kammer, T., Wolf, R. C., and Schönfeldt-Lecuona, C. (2010). Mechanisms and applications of theta-burst rTMS on the human motor cortex. *Brain Topogr.* 22, 294–306. doi: 10.1007/s10548-009-0084-7

Chung, S. W., Hill, A. T., Rogasch, N. C., Hoy, K. E., and Fitzgerald, P. B. (2016). Use of theta-burst stimulation in changing excitability of motor cortex: a systematic review and meta-analysis. *Neurosci. Biobehav. Rev.* 63, 43–64. doi: 10.1016/j.neubiorev.2016.01.008

de Hemptinne, C., Ryapolova-Webb, E. S., Air, E. L., Garcia, P. A., Miller, K. J., Ojemann, J. G., et al. (2013). Exaggerated phase-amplitude coupling in the primary motor cortex in Parkinson disease. *Proc. Natl. Acad. Sci. U.S.A.* 110, 4780–4785. doi: 10.1073/pnas.1214546110

Engel, A. K., and Fries, P. (2010). Beta-band oscillations–signalling the status quo? *Curr. Opin. Neurobiol.* 20, 156–165. doi: 10.1016/j.conb.2010.02.015

Feurra, M., Bianco, G., Santarnecchi, E., Del Testa, M., Rossi, A., and Rossi, S. (2011). Frequency-dependent tuning of the human motor system induced by transcranial oscillatory potentials. *J. Neurosci.* 31, 12165–12170. doi: 10.1523/JNEUROSCI.0978-11.2011

Feurra, M., Blagoveshchensky, E., Nikulin, V. V., Nazarova, M., Lebedeva, A., Pozdeeva, D., et al. (2019). State-dependent effects of transcranial oscillatory currents on the motor system during action observation. *Sci. Rep.* 9:12858. doi: 10.1038/s41598-019-49166-1

Gallasch, E., Rafolt, D., Postruznik, M., Fresnoza, S., and Christova, M. (2018). Decrease of motor cortex excitability following exposure to a 20 Hz magnetic field as generated by a rotating permanent magnet. *Clin. Neurophysiol.* 129, 1397–1402. doi: 10.1016/j.clinph.2018.03.045

Goldsworthy, M. R., Vallence, A.-M., Yang, R., Pitcher, J. B., and Ridding, M. C. (2016). Combined transcranial alternating current stimulation and continuous theta burst stimulation: a novel approach for neuroplasticity induction. *Eur. J. Neurosci.* 43, 572–579. doi: 10.1111/ejn.13142

Groppa, S., Oliviero, A., Eisen, A., Quartarone, A., Cohen, L. G., Mall, V., et al. (2012). A practical guide to diagnostic transcranial magnetic stimulation: report of an IFCN committee. *Clin. Neurophysiol.* 123, 858–882. doi: 10.1016/j.clinph.2012.01.010

Guerra, A., López-Alonso, V., Cheeran, B., and Suppa, A. (2020a). Variability in non-invasive brain stimulation studies: reasons and results. *Neurosci. Lett.* 719:133330. doi: 10.1016/j.neulet.2017.12.058

Guerra, A., Pogosyan, A., Nowak, M., Tan, H., Ferreri, F., Di Lazzaro, V., et al. (2016). Phase dependency of the human primary motor cortex and cholinergic inhibition cancelation during beta tACS. *Cereb. Cortex* 26, 3977–3990. doi: 10.1093/cercor/bhw245

Guerra, A., Ranieri, F., Falato, E., Musumeci, G., Di Santo, A., Asci, F., et al. (2020b). Detecting cortical circuits resonant to high-frequency oscillations in the human primary motor cortex: a TMS-tACS study. *Sci. Rep.* 10:7695. doi: 10.1038/s41598-020-64717-7

Guerra, A., Suppa, A., Bologna, M., D'Onofrio, V., Bianchini, E., Brown, P., et al. (2018). Boosting the LTP-like plasticity effect of intermittent theta-burst stimulation using gamma transcranial alternating current stimulation. *Brain Stimul.* 11, 734–742. doi: 10.1016/j.brs.2018.03.015

Hamada, M., Murase, N., Hasan, A., Balaratnam, M., and Rothwell, J. C. (2013). The role of interneuron networks in driving human motor cortical plasticity. *Cereb. Cortex* 23, 1593–1605. doi: 10.1093/cercor/bhs147

Hayashi, R., Ogata, K., Nakazono, H., and Tobimatsu, S. (2019). Modified ischaemic nerve block of the forearm: use for the induction of cortical plasticity in distal hand muscles. *J. Physiol. (Lond.)* 597, 3457–3471. doi: 10.1113/JP277639

Helfrich, R. F., Schneider, T. R., Rach, S., Trautmann-Lengsfeld, S. A., Engel, A. K., and Herrmann, C. S. (2014). Entrainment of brain oscillations by transcranial alternating current stimulation. *Curr. Biol.* 24, 333–339. doi: 10.1016/j.cub.2013.12.041

Herrmann, C. S., Rach, S., Neuling, T., and Strüber, D. (2013). Transcranial alternating current stimulation: a review of the underlying mechanisms and modulation of cognitive processes. *Front. Hum. Neurosci.* 7:279. doi: 10.3389/fnhum.2013.00279

Huang, Y.-Z., Edwards, M. J., Rounis, E., Bhatia, K. P., and Rothwell, J. C. (2005). Theta burst stimulation of the human motor cortex. *Neuron* 45, 201–206. doi: 10.1016/j.neuron.2004.12.033

Inukai, Y., Saito, K., Sasaki, R., Tsuiki, S., Miyaguchi, S., Kojima, S., et al. (2016). Comparison of three non-invasive transcranial electrical stimulation methods for increasing cortical excitability. *Front. Hum. Neurosci.* 10:668. doi: 10.3389/fnhum.2016.00668

Jensen, O., and Mazaheri, A. (2010). Shaping functional architecture by oscillatory alpha activity: gating by inhibition. *Front. Hum. Neurosci.* 4:186. doi: 10.3389/fnhum.2010.00186

Kasten, F. H., Dowsett, J., and Herrmann, C. S. (2016). Sustained aftereffect of α-tACS lasts up to 70 min after stimulation. *Front. Hum. Neurosci.* 10:245. doi: 10.3389/fnhum.2016.00245

Khademi, F., Royter, V., and Gharabaghi, A. (2018). Distinct Beta-band oscillatory circuits underlie corticospinal gain modulation. *Cereb. Cortex* 28, 1502–1515. doi: 10.1093/cercor/bhy016

Klimesch, W., Sauseng, P., and Hanslmayr, S. (2007). EEG alpha oscillations: the inhibition-timing hypothesis. *Brain Res. Rev.* 53, 63–88. doi: 10.1016/j.brainresrev.2006.06.003

Lisman, J. (2010). Working memory: the importance of theta and gamma oscillations. *Curr. Biol.* 20, R490–R492. doi: 10.1016/j.cub.2010.04.011

Mazaheri, A., and Jensen, O. (2010). Rhythmic pulsing: linking ongoing brain activity with evoked responses. *Front. Hum. Neurosci.* 4:177. doi: 10.3389/fnhum.2010.00177

Moliadze, V., Antal, A., and Paulus, W. (2010). Boosting brain excitability by transcranial high frequency stimulation in the ripple range. *J. Physiol. (Lond.)* 588, 4891–4904. doi: 10.1113/jphysiol.2010.196998

Moliadze, V., Atalay, D., Antal, A., and Paulus, W. (2012). Close to threshold transcranial electrical stimulation preferentially activates inhibitory networks before switching to excitation with higher intensities. *Brain Stimul.* 5, 505–511. doi: 10.1016/j.brs.2011.11.004

Nakazono, H., Ogata, K., Kuroda, T., and Tobimatsu, S. (2016). Phase and frequency-dependent effects of transcranial alternating current stimulation on motor cortical excitability. *PLoS One* 11:e0162521. doi: 10.1371/journal.pone.0162521

Nakazono, H., Ogata, K., Takeda, A., Yamada, E., Kimura, T., and Tobimatsu, S. (2020). Transcranial alternating current stimulation of α but not β frequency sharpens multiple visual functions. *Brain Stimul.* 13, 343–352. doi: 10.1016/j.brs.2019.10.022

Nakazono, H., Ogata, K., Takeda, A., Yamada, E., Oka, S., and Tobimatsu, S. (2021). A specific phase of transcranial alternating current stimulation at the β frequency boosts repetitive paired-pulse TMS-induced plasticity. *Sci. Rep.* 11:13179. doi: 10.1038/s41598-021-92768-x

Neuling, T., Rach, S., and Herrmann, C. S. (2013). Orchestrating neuronal networks: sustained after-effects of transcranial alternating current stimulation depend upon brain states. *Front. Hum. Neurosci.* 7:161. doi: 10.3389/fnhum.2013.00161

Nielsen, J. F. (1996). Improvement of amplitude variability of motor evoked potentials in multiple sclerosis patients and in healthy subjects. *Electroencephalogr. Clin. Neurophysiol.* 101, 404–411.

Ogata, K., Nakazono, H., Uehara, T., and Tobimatsu, S. (2019). Prestimulus cortical EEG oscillations can predict the excitability of the primary motor cortex. *Brain Stimul.* 12, 1508–1516. doi: 10.1016/j.brs.2019.06.013

Pozdniakov, I., Vorobiova, A. N., Galli, G., Rossi, S., and Feurra, M. (2021). Online and offline effects of transcranial alternating current stimulation of the primary motor cortex. *Sci. Rep.* 11:3854. doi: 10.1038/s41598-021-83449-w

R Core Team (2020). *R: A Language and Environment for Statistical Computing*. Vienna: R Foundation for Statistical Computing.

Raco, V., Bauer, R., Tharsan, S., and Gharabaghi, A. (2016). Combining TMS and tACS for closed-loop phase-dependent modulation of corticospinal excitability: a feasibility study. *Front. Cell. Neurosci.* 10:143. doi: 10.3389/fncel.2016.00143

Rjosk, V., Kaminski, E., Hoff, M., Gundlach, C., Villringer, A., Sehm, B., et al. (2016). Transcranial alternating current stimulation at beta frequency: lack of immediate effects on excitation and interhemispheric inhibition of the human motor cortex. *Front. Hum. Neurosci.* 10:560. doi: 10.3389/fnhum.2016.00560

Rounis, E., and Huang, Y.-Z. (2020). Theta burst stimulation in humans: a need for better understanding effects of brain stimulation in health and disease. *Exp. Brain Res.* 238, 1707–1714. doi: 10.1007/s00221-020-05880-1

Salmelin, R., Hämäläinen, M., Kajola, M., and Hari, R. (1995). Functional segregation of movement-related rhythmic activity in the human brain. *Neuroimage* 2, 237–243.

Schilberg, L., Engelen, T., Ten Oever, S., Schuhmann, T., de Gelder, B., de Graaf, T. A., et al. (2018). Phase of beta-frequency tACS over primary motor cortex modulates corticospinal excitability. *Cortex* 103, 142–152. doi: 10.1016/j.cortex.2018.03.001

Thut, G., Schyns, P. G., and Gross, J. (2011). Entrainment of perceptually relevant brain oscillations by non-invasive rhythmic stimulation of the human brain. *Front. Psychol.* 2:170. doi: 10.3389/fpsyg.2011.00170

Vossen, A., Gross, J., and Thut, G. (2015). Alpha power increase after transcranial alternating current stimulation at alpha frequency (α-tACS) reflects plastic changes rather than entrainment. *Brain Stimul.* 8, 499–508. doi: 10.1016/j.brs.2014.12.004

Wach, C., Krause, V., Moliadze, V., Paulus, W., Schnitzler, A., and Pollok, B. (2013). Effects of 10 Hz and 20 Hz transcranial alternating current stimulation (tACS) on motor functions and motor cortical excitability. *Behav. Brain Res.* 241, 1–6. doi: 10.1016/j.bbr.2012.11.038

Wang, Y., Dong, G., Shi, L., Yang, T., Chen, R., Wang, H., et al. (2020). Depression of auditory cortex excitability by transcranial alternating current stimulation. *Neurosci. Lett.* 742:135559. doi: 10.1016/j.neulet.2020.135559

Wiethoff, S., Hamada, M., and Rothwell, J. C. (2014). Variability in response to transcranial direct current stimulation of the motor cortex. *Brain Stimul.* 7, 468–475. doi: 10.1016/j.brs.2014.02.003

Wischnewski, M., Engelhardt, M., Salehinejad, M. A., Schutter, D. J. L. G., Kuo, M.-F., and Nitsche, M. A. (2019a). NNDA receptor-mediated motor cortex plasticity after 20 Hz transcranial alternating current stimulation. *Cereb. Cortex* 29, 2924–2931. doi: 10.1093/cercor/bhy160

Wischnewski, M., and Schutter, D. J. L. G. (2015). Efficacy and time course of theta burst stimulation in healthy humans. *Brain Stimul.* 8, 685–692. doi: 10.1016/j.brs.2015.03.004

Wischnewski, M., Schutter, D. J. L. G., and Nitsche, M. A. (2019b). Effects of beta-tACS on corticospinal excitability: a meta-analysis. *Brain Stimul.* 12, 1381–1389. doi: 10.1016/j.brs.2019.07.023

Zaehle, T., Rach, S., and Herrmann, C. S. (2010). Transcranial alternating current stimulation enhances individual alpha activity in human EEG. *PLoS One* 5:e13766. doi: 10.1371/journal.pone.0013766

Zaghi, S., de Freitas Rezende, L., de Oliveira, L. M., El-Nazer, R., Menning, S., Tadini, L., et al. (2010). Inhibition of motor cortex excitability with 15 Hz transcranial alternating current stimulation (tACS). *Neurosci. Lett.* 479, 211–214. doi: 10.1016/j.neulet.2010.05.060

Zrenner, C., Desideri, D., Belardinelli, P., and Ziemann, U. (2018). Real-time EEG-defined excitability states determine efficacy of TMS-induced plasticity in human motor cortex. *Brain Stimul.* 11, 374–389. doi: 10.1016/j.brs.2017.11.016

Conflict of Interest: The authors declare that the research was conducted in the absence of any commercial or financial relationships that could be construed as a potential conflict of interest.

frontiers in Human Neuroscience

ORIGINAL RESEARCH
published: 15 December 2021
doi: 10.3389/fnhum.2021.787229

Magnetoencephalography Studies of the Envelope Following Response During Amplitude-Modulated Sweeps: Diminished Phase Synchrony in Autism Spectrum Disorder

Timothy P. L. Roberts[1], Luke Bloy[1], Song Liu[1], Matthew Ku[1], Lisa Blaskey[1] and Carissa Jackel[2]*

[1] Department of Radiology, Children's Hospital of Philadelphia, Philadelphia, PA, United States, [2] Department of Pediatrics, Children's Hospital of Philadelphia, Philadelphia, PA, United States

OPEN ACCESS

Edited by:
Shozo Tobimatsu, Kyushu University, Japan

Reviewed by:
Margot J. Taylor, Hospital for Sick Children, Canada
Hidetoshi Takahashi, Kôchi University, Japan

***Correspondence:**
Timothy P. L. Roberts
robertstim@chop.edu

Specialty section:
This article was submitted to Brain Imaging and Stimulation, a section of the journal Frontiers in Human Neuroscience

Received: *30 September 2021*
Accepted: *01 November 2021*
Published: *15 December 2021*

Citation:
Roberts TPL, Bloy L, Liu S, Ku M, Blaskey L and Jackel C (2021) Magnetoencephalography Studies of the Envelope Following Response During Amplitude-Modulated Sweeps: Diminished Phase Synchrony in Autism Spectrum Disorder. Front. Hum. Neurosci. 15:787229. doi: 10.3389/fnhum.2021.787229

Prevailing theories of the neural basis of at least a subset of individuals with autism spectrum disorder (ASD) include an imbalance of excitatory and inhibitory neurotransmission. These circuitry imbalances are commonly probed in adults using auditory steady-state responses (ASSR, driven at 40 Hz) to elicit coherent electrophysiological responses (EEG/MEG) from intact circuitry. Challenges to the ASSR methodology occur during development, where the optimal ASSR driving frequency may be unknown. An alternative approach (more agnostic to driving frequency) is the amplitude-modulated (AM) sweep in which the amplitude of a tone (with carrier frequency 500 Hz) is modulated as a sweep from 10 to 100 Hz over the course of ∼15 s. Phase synchrony of evoked responses, measured *via* intra-trial coherence, is recorded (by EEG or MEG) as a function of frequency. We applied such AM sweep stimuli bilaterally to 40 typically developing and 80 children with ASD, aged 6–18 years. Diagnoses were confirmed by DSM-5 criteria as well as autism diagnostic observation schedule (ADOS) observational assessment. Stimuli were presented binaurally during MEG recording and consisted of 20 AM swept stimuli (500 Hz carrier; sweep 10–100 Hz up and down) with a duration of ∼30 s each. Peak intra-trial coherence values and peak response frequencies of source modeled responses (auditory cortex) were examined. First, the phase synchrony or inter-trial coherence (ITC) of the ASSR is diminished in ASD; second, hemispheric bias in the ASSR, observed in typical development (TD), is maintained in ASD, and third, that the frequency at which the peak response is obtained varies on an individual basis, in part dependent on age, and with altered developmental trajectories in ASD vs. TD. Finally, there appears an association between auditory steady-state phase synchrony (taken as a proxy of neuronal circuitry integrity) and clinical assessment of language ability/impairment. We concluded that (1) the AM sweep stimulus provides a mechanism for probing ASSR in an unbiased fashion, during

developmental maturation of peak response frequency, (2) peak frequencies vary, in part due to developmental age, and importantly, (3) ITC at this peak frequency is diminished in ASD, with the degree of ITC disturbance related to clinically assessed language impairment.

Keywords: autism (ASD), magnetoencephalography (MEG), gamma-band activity, envelope following response, children

INTRODUCTION

Gamma-band (30–80 Hz) electrophysiological activity elicited from sensory cortices may provide a window into the maturity and viability of local neuronal circuitry. This in turn may be reflective of the balance between excitatory and inhibitory neuronal activity and, as such, the balance of excitatory and inhibitory neurotransmitters (particularly glutamate and GABA). The excitation/inhibition (E/I) imbalance theory has been suggested to be relevant to at least some individuals with ASD for nearly two decades (Rubenstein and Merzenich, 2003; Port et al., 2019; Sohal and Rubenstein, 2019). Thus, considerable attention has been paid to using gamma-band activity as a biomarker, for diagnostic, prognostic, or stratification use.

Eliciting gamma-band activity can be achieved through a variety of stimulation paradigms. The most prevalent paradigm for auditory cortex gamma activity is the auditory steady-state response (ASSR). The ASSR captures the entrainment of auditory cortex neural activity (Pantev et al., 1996; Gutschalk et al., 1999; Brugge et al., 2009; Weisz and Lithari, 2017) to the frequency and phase of auditory stimuli typically delivered as click trains or amplitude-modulated (AM) tones. Studies in adults have suggested that the ASSR is largest in response to presentations in the gamma range particularly at 40 Hz (Galambos et al., 1981; Picton et al., 2003). While the 40 Hz ASSR has been used to illustrate consistent gamma abnormalities in several neurodevelopmental disorders, principally schizophrenia (Brenner et al., 2003; Hong et al., 2004; Light et al., 2006; Hamm et al., 2011; Lenz et al., 2011; Edgar et al., 2014), studies focused on ASD have been more inconsistent (Rojas et al., 2006; Wilson et al., 2007; Edgar et al., 2016; Ono et al., 2020; Seymour et al., 2020; Stroganova et al., 2020).

Initial work examining the ASSR in ASD observed reduced 40 Hz ASSR in children and adolescents (7–17 years) diagnosed with ASD (Wilson et al., 2007) and also in adults (>30 years) diagnosed with ASD and their first-degree relatives (Rojas et al., 2008). A later study, focused on adolescents and early adulthood (14–20 years), similarly found reduced 40 Hz ASSR in participants with ASD (Seymour et al., 2020). Despite the consistent observation of reduced ASSR in adolescent and older populations, studies focused on younger participants have not observed such differences. Examining a large cohort of 7–15-year-old boys, Edgar et al. (2016) did not reveal group differences in ASSR, though bilateral associations with age were observed, as was a right hemispheric dominance of the ASSR responses. Similar age associations and lack of significant group differences have been reported in 7–12-year-old boys (Stroganova et al., 2020) and in 5–7-year-old participants (Ono et al., 2020). Given that the auditory system is still developing through early adulthood, with the 40 Hz ASSR reaching its maximum around 22 years of age (Cho et al., 2015), it may not be surprising that atypical ASSR in neurodevelopmental disorders, such as ASD, do not manifest until later in their maturation (De Stefano et al., 2019).

One possible limitation to previous studies using 40 Hz modulated stimuli in younger children is the question of "optimum" driving frequency for eliciting an ASSR response. While 40 Hz seems canonical for adults, inter-individual variation, especially as a function of development, may compromise the efficiency of a strictly 40 Hz focus. To address this, the "envelope following response (EFR)" has been proposed (Artieda et al., 2004) in which a steady-state stimulus slowly undergoes swept increase of its modulation frequency (e.g., from 10 to 100 Hz, over the course of ∼15 s). Such a stimulus provides a constant "steady-state" stimulus while allowing identification of an "optimal" driving frequency (ascertained by maximum evoked phase coherence), which may occur at 40 Hz, or a frequency slightly lower or higher.

This study examines the neural response to an AM sinusoidal 500 Hz carrier tone. The frequency of the amplitude modulation was continuously swept from 10 to 100 Hz and then back from 100 to 10 Hz over the course of a 30-s stimulus. This approach allowed the peak phase synchrony, or inter-trial coherence (ITC), for each participant to be determined optimally (and not at an arbitrarily predefined frequency) and examined further. In both ASD and typical development (TD) groups, we hypothesized a moderate maturation of peak ASSR frequency over the age range of 6–18 years. More generally, we hypothesized that individuals with ASD[1] would demonstrate diminished "peak" ITC, reflecting compromised integrity (or delayed maturation) of the local neuronal circuitry of the auditory cortex. Furthermore, we hypothesized that compromise of such neuronal circuitry would have behavioral sequelae in assessments of language ability/impairment.

MATERIALS AND METHODS

A total of 80 children with ASD and 40 age-matched TD controls participated in this study. The age range included spanned 6–18 years – refer to **Table 1** for demographic information and degree of matching. All studies were approved by the institutional

[1]Individuals on the autism spectrum, their parents, and professionals in the field have unique and overlapping opinions regarding the use of person-first (e.g., children with ASD) or identity first (e.g., autistic child) language (Kenny et al., 2016). With respect for divided opinions, we used both terms in this study.

TABLE 1 | Demographic information.

	TD	ASD
N	40 (6F)	80 (12F)
Handedness	34R, 6L, 0A	69R, 8L, 3A
Age	11.94 ± 0.44	11.72 ± 0.26
NVIQ	**113.24 ± 2.23**	**100.84 ± 1.85**
Equivalent FSIQ (WISC GAI/DAS-II GCA)	**115.32 ± 2.53**	**97.92 ± 2.13**
CELF-CLSS	**108.79 ± 2.00**	**93.36 ± 2.14**
SCQ	**2.63 ± 0.4**	**18.53 ± 0.68**
SRS (T-score)	**42.84 ± 0.72**	**73.44 ± 1.32**
ADOS-CSS	**1.32 ± 0.13**	**6.99 ± 0.2**

Bold indicates significant differences.

IRB, and written consent was obtained from parents/caregivers, while assent was obtained from participants, over the age of 7 years, who were competent to provide it.

All participants with ASD had an existing ASD diagnosis, made according to DSM criteria by expert clinicians in the autism specialty practices of medical centers in a large metropolitan area. The diagnosis was confirmed at the time of study participation using gold-standard diagnostic tools, including the Autism Diagnostic Observation Schedule (ADOS-2; Lord et al., 2012) and parent report on the Social Communication Questionnaire (SCQ; Rutter et al., 2003). Dimensional symptom severity ratings were obtained *via* the ADOS-2 Calibrated Severity Score (CSS; Gotham et al., 2009) and parent report on the Social Responsiveness Scale (SRS-2; Constantino and Gruber, 2012).

Data were collected over an extended time period (∼5 years) during which standard diagnostic tests underwent version (as well as protocol) changes: for both the ASD and TD cohorts, cognitive ability was characterized by indices of non-verbal, verbal, and overall intellectual functioning (**Table 1**), using the Wechsler Intelligence Scale-Fourth Edition (WISC-IV; Wechsler, 2003), the Wechsler Intelligence Scale-Fifth Edition (WISC-V; Wechsler, 2014), or the Differential Ability Scale-Second Edition (DAS-II; Elliott, 2007), depending on the time of study participation. Psychometrics suggest acceptable index-level correlations (r = 0.73–0.93) between these tests, all of which are standardized to an average of 100 and SD of 15 (Kuriakose, 2014). Language understanding and expression were evaluated using the core language standard score (CELF-CLSS) from the Clinical Evaluation of Language Fundamentals (CELF-4/CELF-5; Semel et al., 2006, 2013).

To rule out global cognitive delay in both the TD and ASD groups, participants were required to score at or above the second percentile (SS > 70) on the non-verbal composite score of the cognitive assessment administered. Inclusion criteria for all participants included English as their first language. Inclusion criteria for the children with TD included no significant cognitive impairment (described above), no history of neurodevelopmental or psychiatric conditions (e.g., ADHD, learning or language disorder, and depression/anxiety), and scoring below the cutoffs for ASD on all domains of the ADOS-2 (Lord et al., 2012) as well as on parent questionnaires of ASD symptoms (SCQ; Rutter et al., 2003 and SRS-2; Constantino and Gruber, 2012). Additional exclusion criteria for all participants included known neurological disorders (e.g., cerebral palsy and epilepsy), severe tics, and severe head trauma; sensory (e.g., hearing and visual) impairments (e.g., by parent report/medical records); known genetic conditions with a very high incidence of ASD (e.g., Fragile X syndrome and 22q11 deletion syndrome) and premature birth (earlier than gestation of 34 weeks) or significant birth complications.

Stimuli

Auditory stimuli consisted of sweeps of 30 s duration in which a 500 Hz sinusoidal tone was AM at a rate that increased uniformly between 10 and 100 Hz over the first 15 s (up trials) and then decreased uniformly from 100 to 10 Hz over the remaining 15 s (Down trials). Of note, 20 such tone sweep pairs were presented with an intervening rest/silence period of 9 s for an overall acquisition time of ∼13 min. Stimuli were presented binaurally at the 45 dB sensation level, SL (after individually determining hearing detection thresholds) using Etymotic ER3A transducers and eartip inserts, after amplification and attenuation using TDT series 3 equipment (Tucker Davis Technologies, FL, United States).

Magnetoencephalography Recording

Recordings were made using a CTF 275-channel whole head biomagnetometer (CTF, Coquitlam, BC, Canada) at a sample rate of 1,200 Hz/channel, housed in a magnetically shielded room, MSR (Vacuumschmelze, Germany). Synthetic third-order gradiometer noise reduction was employed. To facilitate source analysis, a digitized head shape consisting of three anatomical landmarks (i.e., nasion and left and right preauricular points) as well as an additional 200+ points on the scalp and face was obtained for each participant using the fast-track probe position identification system (Polhemus, Colchester, VT, United States).

Magnetoencephalography Analysis

Magnetoencephalography data were analyzed using the MNE-Python analysis toolbox (Gramfort et al., 2013, 2014). As *sensor*-based analysis of MEG reflects the superposition of activity from multiple brain regions, fine-grained analysis of the temporal features, such as measures of phase coherence, is optimally performed in the *source* rather than sensor space (Hoechstetter et al., 2004; Srinivasan et al., 2006).

Prior to source localization, independent component analysis (ICA; Winkler et al., 2015; Ablin et al., 2018) was used to detect and remove eye-blink and cardiac artifacts. Sensor waveforms were then filtered (0.1–150 Hz) and epochs defined (-1 to 15 s) relative to the onset of the up and down sweeps, resulting in 20 up and 20 down sweep trial trials. To facilitate source localization, an anatomical (1 mm × 1 mm × 1 mm isotropic resolution) MRI (MPRAGE – TE/TR/TI: 2.87 ms/1,900 ms/1,050 ms) was acquired from each participant. Subject-specific single shell head models were created from the MRI data of each participant. Freesurfer (Fischl, 2012) watershed segmentation was used to identify the inner skull surface, and a single shell boundary element model (BEM) forward model was

computed. MRI to MEG co-registration was achieved using three fiducial points and further refined using an iterative closest point registration to align acquired digitized head shape points and outer scalp surface of the subject as defined by MRI. A regional source model, with 46 (23-per hemisphere) regional sources (Glasser et al., 2016), along with the Minimum Norm Estimator (MNE; Wang et al., 1992; Hämäläinen and Ilmoniemi, 1994) was used to estimate total power and ITC (Stapells et al., 1987) separately for the up and down trials. For each participant, the peak ITC value was determined, as was the corresponding AM stimulation frequency for both up and down trials.

Statistical treatment: Linear mixed model (LMM) with fixed effects of group, sweep direction, hemisphere with age as a covariate, and subject as a random effect was performed on ITC at the peak of the ASSR response and on the peak frequency itself. To assess the association between MEG measures and behavioral/clinical assessments of language ability, the CLSS of the CELF was included as a covariate, along with age.

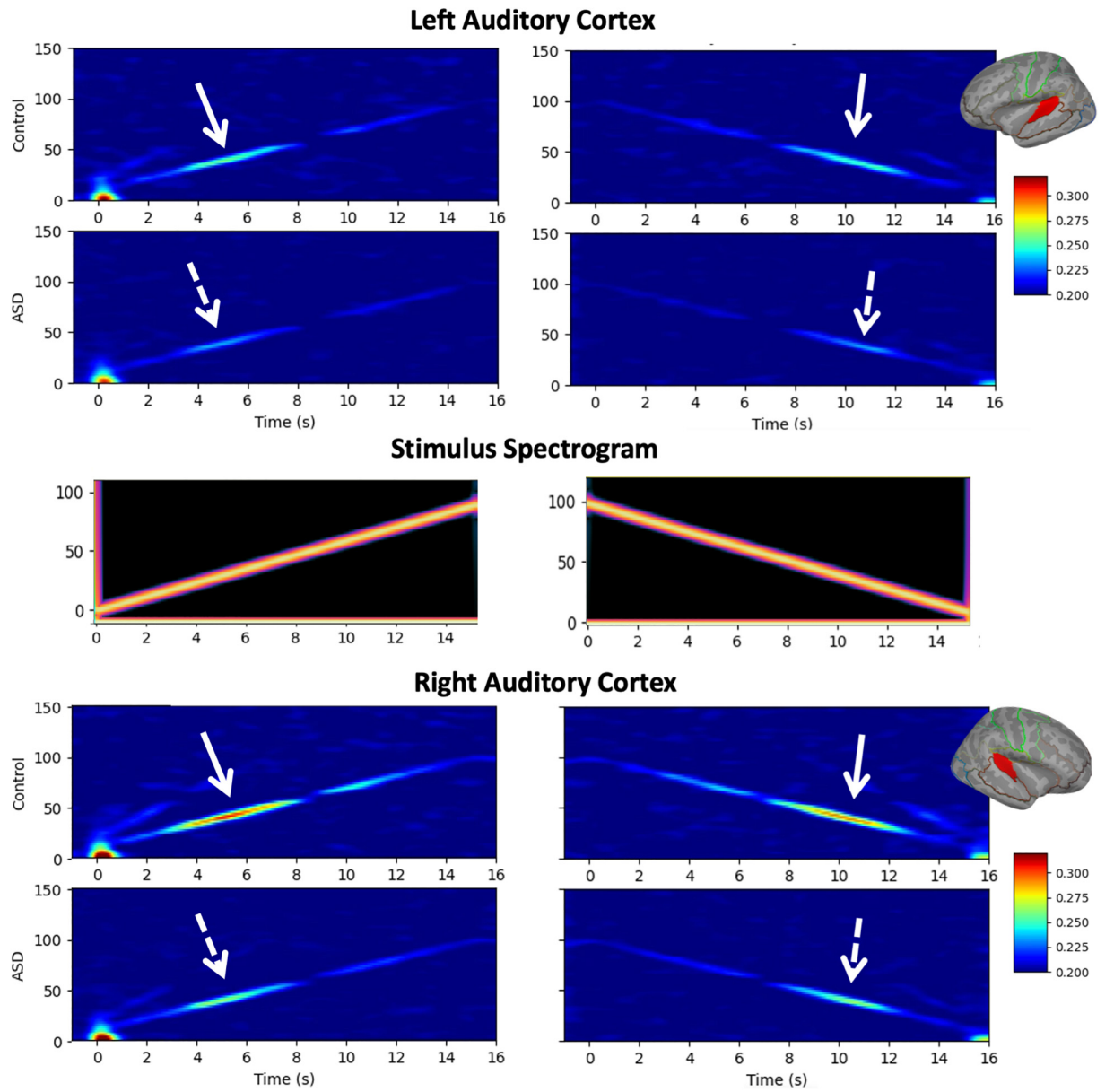

FIGURE 1 | Grand average time-frequency plots [typical development (TD) and autism spectrum disorder (ASD)] of inter-trial coherence (ITC) are shown for the left (**top**) and right (**bottom**) auditory cortices and the up/down sweep directions (**left/right**), as is the spectrogram of the stimuli (**middle**). While increased ITC is visible at all frequencies, the maximal response occurs in the low gamma range (30–50 Hz) where decreased ITC in the ASD group compared to TD is also evident bilaterally, and in both sweep directions.

RESULTS

The ASD vs. TD groups did not differ on age (ASD = 11.72 ± 0.26 years, TD = 11.94 ± 0.44 years, $p = 0.672$), and there was no significant difference in distribution of handedness (ASD = 69R, 8L, 3Ambi; TD = 34R, 6L, 0Ambi; chi-squared $p = 0.354$) or sex (ASD = 68 M, 12 F; TD = 34 M, 6 F; chi-squared $p = 1.00$). As expected, groups did significantly differ ($p < 0.01$) on neuropsychological measures known to be affected in the ASD phenotype, such as language ability (CELF-4/5), full scale and non-verbal-IQ (WISC-IV/V or DAS-II), and ADOS-CSS (Shumway et al., 2012; **Table 1**).

Figure 1 shows grand average time-frequency ITC responses as a function of time/modulation frequency for both up and down sweeps, for left and right hemispheres, and children with TD vs. ASD. Diminished responses in children with ASD are evident in both hemispheres in the 30–50 Hz range. Notably, in general, left hemispheric responses to seem weaker than right hemispheric responses, while relative group differences between TD and ASD appear to persist across hemispheres.

A LMM (fixed effects of group, sweep direction, hemisphere with age as a covariate, and subject as a random effect) interrogating the amount of ITC at the peak of the ASSR response revealed significantly reduced ITC in ASD (ASD = 0.288 ± 0.005, TD = 0.311 ± 0.008, $p = 0.015$), a significant difference between hemispheres (LH = 0.280 ± 0.005, RH = 0.318 ± 0.005, $p < 0.001$) as well as a significant group × hemisphere interaction ($p = 0.045$; **Figure 2**). As expected, no significant effects of sweep direction (or any of its interactions) were observed (up: 0.301 ± 0.005 and down: 0.297 ± 0.005, $p = 0.15$). Significant effects of age (0.120 ± 0.005 per year; $p < 0.001$) as well as age × hemisphere ($p < 0.001$) and age × group ($p < 0.001$) interactions were also observed.

Post hoc analysis examining ITC separately in the left and right hemispheres observed that bilateral effects of age were somewhat more profound in the right hemisphere (0.015 ± 0.002 per year, $p < 0.001$) than in the left hemisphere (0.009 ± 0.002 per year, $p < 0.001$). Group differences were also more profound in the right hemisphere (ASD = 0.304 ± 0.007, TD = 0.333 ± 0.010, and $p < 0.001$), compared to the left hemisphere (ASD = 0.272 ± 0.005, TD = 0.289 ± 0.006, $p = 0.029$) as was the interaction between group and age (RH: 0.008 ± 0.002 per year, $p = 0.0017$, LH: 0.005 ± 0.002 per year, $p = 0.0023$).

Similar LMMs revealed no main effect of diagnostic group on peak ASSR response frequency; moreover, when projected to the mean age of 11.8 years, both groups exhibited responses

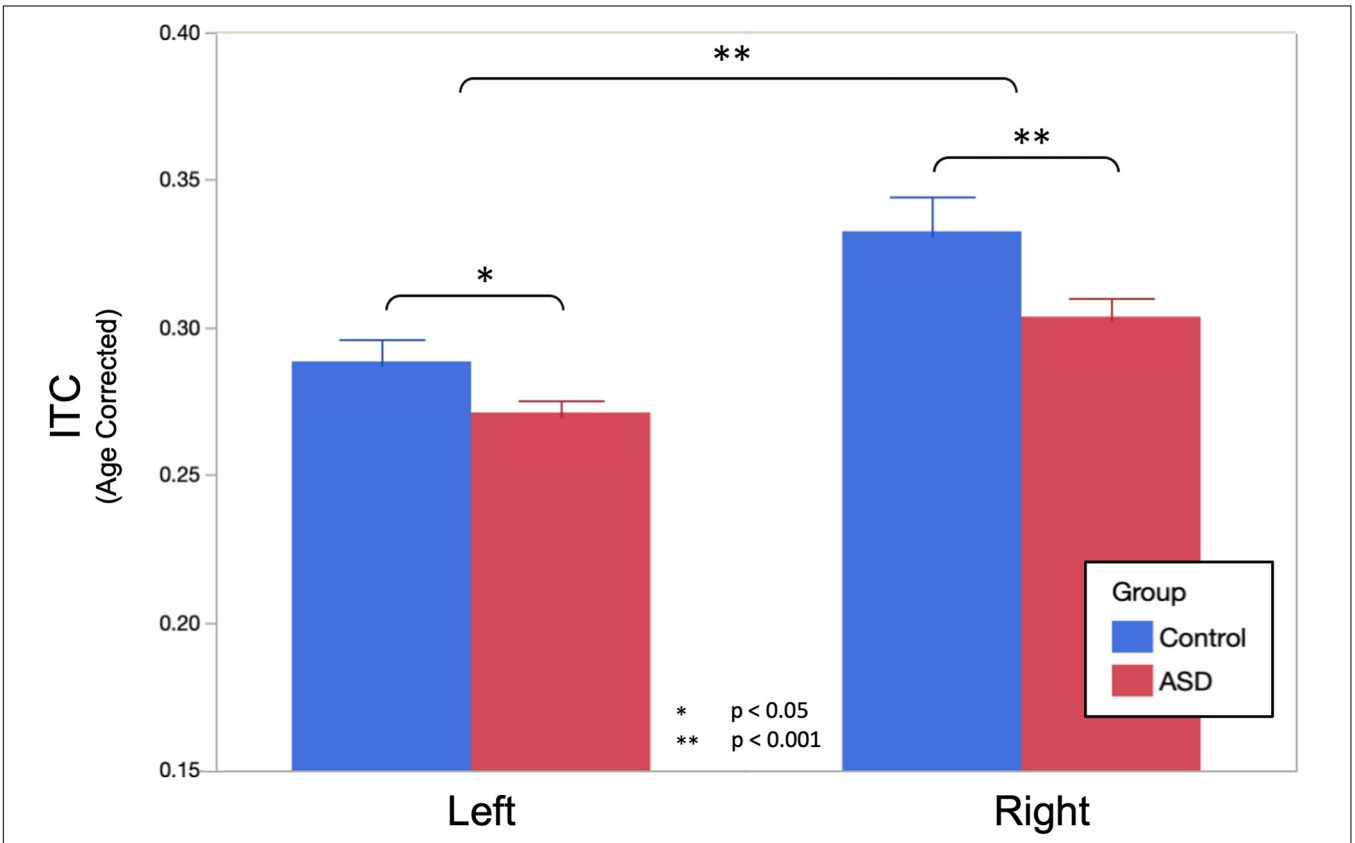

FIGURE 2 | Age corrected auditory steady-state response (ASSR) ITC (to the population mean 11.8 years) at the peak of the ASSR is shown. Omnibus linear mixed models (LMMs) reveal significantly reduced ITC in ASD (main effect of group, $p = 0.015$) and the left hemisphere (main effect of the hemisphere, $p < 0.001$). *Post hoc* analysis in each hemisphere indicated that group differences were more profound in the right hemisphere ($p < 0.001$), compared to the left hemisphere ($p = 0.029$), but significant in both.

very close to the canonical 40 Hz (ASD = 39.39 ± 0.47 Hz, TD = 40.05 ± 0.66 Hz, and p = 0.416). There was also no significant influence of hemisphere on peak ASSR response frequency (LH = 39.99 ± 0.49 Hz, RH = 39.45 ± 0.49 Hz, and p = 0.326). Similarly, there was no effect of sweep direction on peak ASSR response frequency (up = 39.86 ± 0.49 Hz, down = 39.58 ± 0.49 Hz, and p = 0.609). Although peak ASSR response frequency was very close to 40 Hz at the *projected* mean age of 11.8 years, significant effects of age (0.45 Hz/year and p = 0.005) and an age × hemisphere interaction (an additional 0.28 Hz/year in the right hemisphere) were observed.

Based on *a priori* hypotheses of atypical developmental trajectories in participants with ASD (Wolff et al., 2012; Edgar et al., 2015; Berman et al., 2016), the relationship between age and peak ASSR frequency was investigated separately in both groups. Individual LMM models (age, hemisphere, and age × hemisphere) were used in each group, revealing significant age (0.64 Hz/year and p = 0.027) and age × hemisphere (additional 0.33 Hz/year in right hemisphere and p = 0.0466) effects in TD, while in the ASD group, there was reduced evidence for maturation of peak ASSR frequency (0.26 Hz/year and p = 0.15) or age × hemisphere interactions (additional 0.256 Hz/year in right hemisphere and p = 0.06). This suggests that for the younger children in the cohort, the use of a canonical 40 Hz driving frequency stimulus would have potentially yielded suboptimal responses (for a 6-year old, the peak ASSR response frequency would be ∼36 Hz), as well as pointing to a group difference in the rate of maturation of the peak response frequency in ASD vs. TD. **Figure 3** illustrates the age dependence of peak ASSR response frequency in both TD and ASD.

Given the high degree of heterogeneity in the language abilities of children diagnosed with ASD and the putative relationship between the ASSR and auditory cortex function, we examined the relationship between peak ASSR ITC value and a behavioral/clinical language ability index: the CLSS of the CELF. LMMs (fixed effects of age, hemisphere, sweep direction, their interactions, and CELF-CLSS with subject as a random effect) were applied separately in the TD and ASD groups. Similar to above, age, hemisphere, and age × hemisphere were significant in both TD and ASD. Additionally, the effect of CELF-CLSS (0.0005 ± 0.0002 and p = 0.048) was significant within the ASD group. For visualization purposes (**Figure 4**), these models were used to project the ITC value to the population mean (11.8 years) and collapsed across the hemisphere and sweep direction (Correlation of ASSR ITC with CELF-CLSS within the ASD cohort – **Figure 4**).

DISCUSSION

The main finding of this study is that auditory gamma-band responses, especially in terms of phase synchrony (ITC), are diminished in ASD compared with age-matched

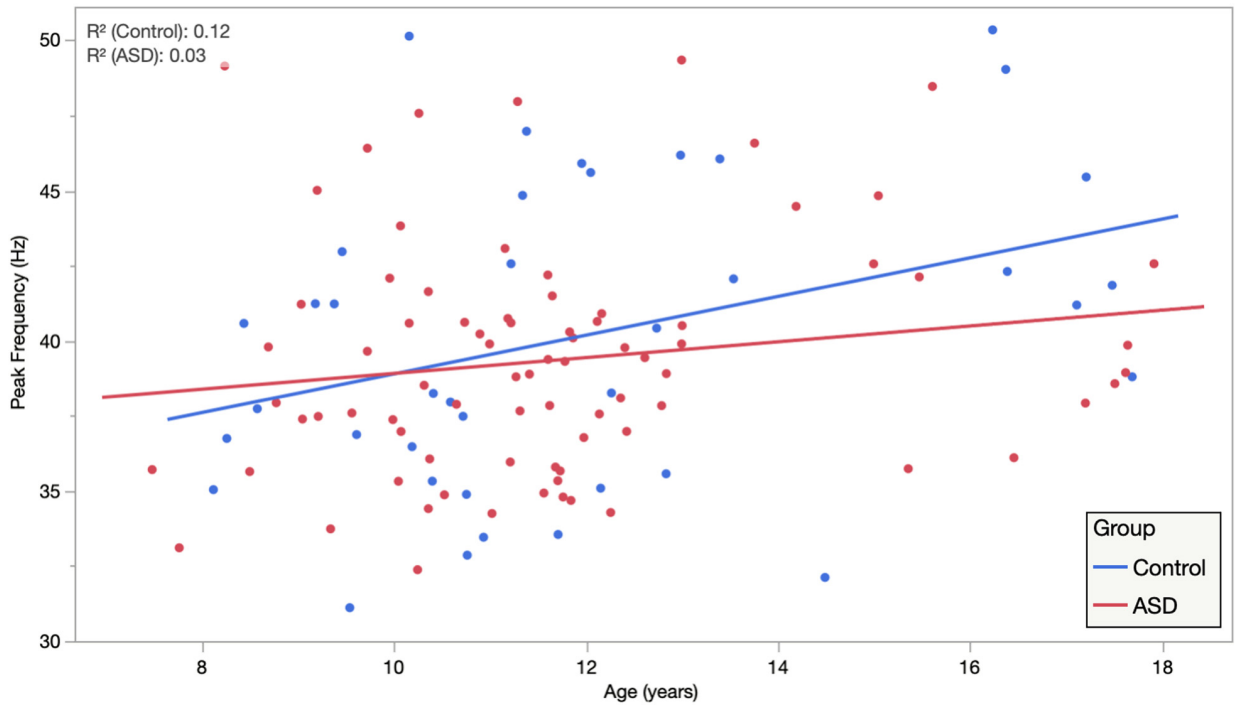

FIGURE 3 | Auditory steady-state response peak ITC frequency, averaged across hemisphere and condition, is plotted against age, illustrating significant age dependence in TD and diminished age dependence in ASD. Importantly, while this suggests that for the younger children a canonical 40 Hz driving frequency stimulus may be suboptimal. It also indicates clear heterogeneity/individuality in the peak ASSR frequency at all ages and possibly also points to an atypical maturational trajectory in ASD as a group.

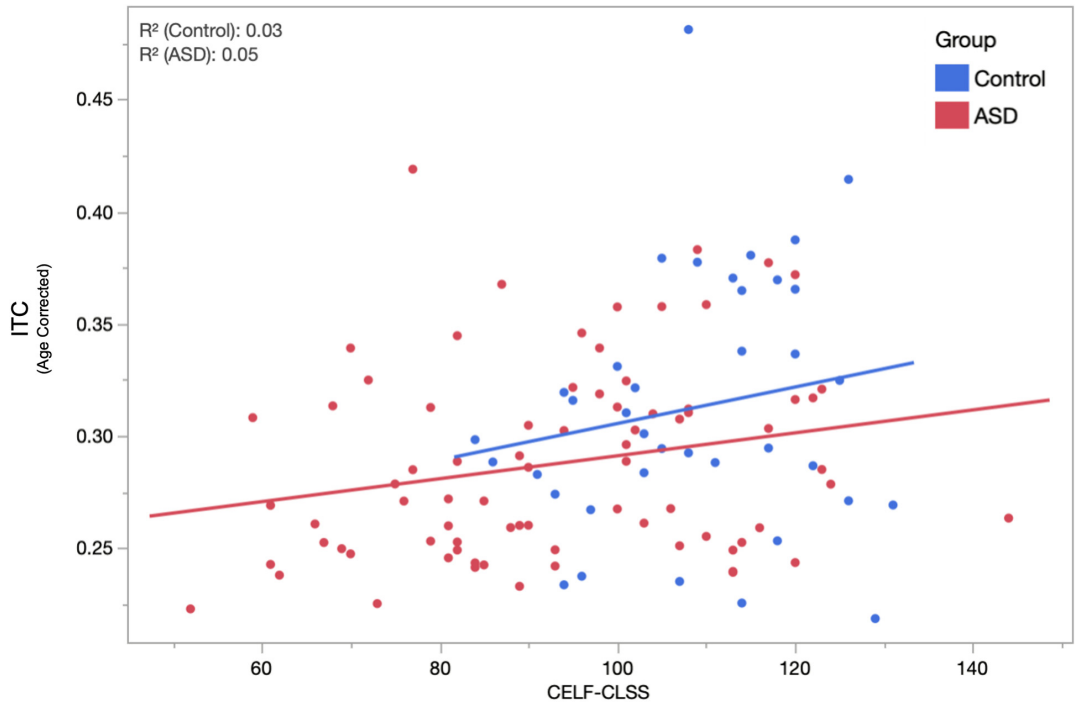

FIGURE 4 | The relationship between age-corrected ASSR ITC (to the population mean 11.8 years, averaged across hemisphere and condition) and assessment of language function (CELF-CLSS) is shown for both ASD and TD groups. Within the ASD group, a significant (p = 0.048) positive correlation (increases in ITC indicated increases in language function) was observed. While failing to reach significance (over the narrower range of CELF-CLSS scores encountered), a similar positive relationship is also observed in TD.

TD peers. This is in line with the hypothesis that part of the ASD phenotype stems from an imbalance of excitation and inhibition in the neural circuitry of sensory systems, with such imbalance leading to diminished network capacity to establish coherent electrophysiological oscillatory activity in response to repeated stimuli, with subsequent behavioral/clinical sequelae.

Other findings suggest a developmental trajectory to the optimal driving frequency to elicit ASSR responses such that, especially in younger children, modulation at the canonical 40 Hz may not be optimal for eliciting high signal-to-noise ratio (SNR) responses. Furthermore, the slope of this developmental maturation of ASSR peak frequency appears to be significantly lower in ASD, suggesting either a slower maturation or perhaps the existence of multiple subpopulations encompassing both near-typical developmental trajectories and near-asymptotic ones; only further, longitudinal studies can resolve this on an individual basis.

Moreover, in this large and heterogeneous cohort of children/adolescents with ASD, the peak ASSR ITC (diminished relative to TD peers) was found to correlate with clinical assessment of language impairment, with decreased phase synchrony indicating decreased language performance (with a slope of 0.0005 units of ITC per point on the CELF core language index), suggesting that this electrophysiological signature, putatively mechanistically associated with E/I imbalance, has a clinical/behavioral consequence and thus, meets some of the criteria needed for a diagnostic/prognostic biomarker, at least for the functional domain of language impairment, in ASD.

Given the sample population differences between ASD and TD cohorts in both IQ and language ability, it is not unambiguously possible to ascribe observed differences in brain signals (auditory cortex phase synchrony) to ASD diagnosis alone. It is very likely that such signatures relate to brain activity anomalies shared between ASD and other neuropsychiatric conditions and developmental disorders. Nonetheless, brain signatures of clinical impairment likely point to atypical neuronal circuitry underlying observable behavior. Also, despite similar proportions in both ASD and TD groups, a limitation of this study is the relatively small fraction of female participants, precluding statistical evaluation of sex differences in EFR/ASSR measures.

Additionally, while the main findings of this study might well have been identified with more conventional 40 Hz stimulus paradigms, this study supports the use of the EFR paradigm (a swept-modulation tone), especially in children, to account for individual differences in network maturation and to optimize the collection of signatures of neural synchrony. This might be especially significant for yet younger populations. It is possible that individual differences in optimal ASSR driving frequency might account for some divergent reports on ASSR responsiveness in the literature. It is likely that a narrower frequency sweep (perhaps 30–50 Hz) EFR stimulus might suffice to capture the gamma-band response as well as further define the "resonance width" of the optimal driving frequency.

In summary, electrophysiological responses (particularly, the ITC) elicited by ASSR paradigms reveal anomalies in ASD reflecting the atypical activity of neuronal local circuitry. Furthermore, the magnitude of these anomalies appears to be associated with clinical/behavioral sequelae (namely language impairment). The EFR approach accounts for inter-individual differences in peak ASSR response frequency, attributable to the developmental trajectory or otherwise, and thus, represents a less-biased approach to probing neuronal circuit integrity.

DATA AVAILABILITY STATEMENT

The raw data supporting the conclusions of this article will be made available by the authors, without undue reservation.

ETHICS STATEMENT

The studies involving human participants were reviewed and approved by Children's Hospital of Philadelphia Institutional Review Board. Written informed consent to participate in this study was provided by the participants' legal guardian/next of kin.

AUTHOR CONTRIBUTIONS

TR was responsible for the conception of the study, statistical analysis, and wrote the first draft of the manuscript. LuB was responsible for development of data processing pipelines, performed statistical analysis, and edited the manuscript. SL contributed to preprocessing analysis methods and development of figures. MK conducted primary data preprocessing and analysis. LiB conducted neuropsychological assessments and edited the manuscript. CJ provided clinical interpretation on ASD. All authors contributed to the article and approved the submitted version.

FUNDING

This research was supported by the grants of NIH R01-DC008871 and NIH P50-HD105354.

REFERENCES

Ablin, P., Cardoso, J.-F., and Gramfort, A. (2018). Faster independent component analysis by preconditioning with Hessian approximations. *IEEE Tran. Signal Process.* 66, 4040–4049.

Artieda, J., Valencia, M., Alegre, M., Olaziregi, O., Urrestarazu, E., and Iriarte, J. (2004). Potentials evoked by chirp-modulated tones: a new technique to evaluate oscillatory activity in the auditory pathway. *Clin. Neurophysiol.* 115, 699–709. doi: 10.1016/j.clinph.2003.10.021

Berman, J. I., Edgar, J. C., Blaskey, L., Kuschner, E. S., Levy, S. E., Ku, M., et al. (2016). Multimodal diffusion-MRI and MEG assessment of auditory and language system development in autism spectrum disorder. *Front. Neuroanat.* 10:30. doi: 10.3389/fnana.2016.00030

Brenner, C. A., Sporns, O., Lysaker, P. H., and O'Donnell, B. F. (2003). EEG synchronization to modulated auditory tones in schizophrenia, schizoaffective disorder, and schizotypal personality disorder. *Am. J. Psychiatry* 160, 2238–2240. doi: 10.1176/appi.ajp.160.12.2238

Brugge, J. F., Nourski, K. V., Oya, H., Reale, R. A., Kawasaki, H., Steinschneider, M., et al. (2009). Coding of repetitive transients by auditory cortex on Heschl's gyrus. *J. Neurophysiol.* 102, 2358–2374.

Cho, R. Y., Walker, C. P., Polizzotto, N. R., Wozny, T. A., Fissell, C., Chen, C. M., et al. (2015). Development of sensory gamma oscillations and cross-frequency coupling from childhood to early adulthood. *Cereb. Cortex (New York, NY)* 25, 1509–1518. doi: 10.1093/cercor/bht341

Constantino, J. N., and Gruber, C. P. (2012). *Social Responsiveness Scale*, Second Edn. Torrance, CA: Western Psychological Services.

De Stefano, L. A., Schmitt, L. M., White, S. P., Mosconi, M. W., Sweeney, J. A., and Ethridge, L. E. (2019). Developmental effects on auditory neural oscillatory synchronization abnormalities in autism spectrum disorder. *Front. Integr. Neurosci.* 13:34. doi: 10.3389/fnint.2019.00034

Edgar, J. C., Chen, Y. H., Lanza, M., Howell, B., Chow, V. Y., Heiken, K., et al. (2014). Cortical thickness as a contributor to abnormal oscillations in schizophrenia? *Neuroimage Clin.* 4, 122–129. doi: 10.1016/j.nicl.2013.11.004

Edgar, J. C., Fisk, C. L. IV, Berman, J. I., Chudnovskaya, D., Liu, S., Pandey, J., et al. (2015). Auditory encoding abnormalities in children with autism spectrum disorder suggest delayed development of auditory cortex. *Mol. Autism* 6:69.

Edgar, J. C., Fisk, C. L. IV, Liu, S., Pandey, J., Herrington, J. D., Schultz, R. T., et al. (2016). Translating adult electrophysiology findings to younger patient populations: difficulty measuring 40-Hz auditory steady-state responses in typically developing children and children with autism spectrum disorder. *Dev. Neurosci.* 38, 1–14. doi: 10.1159/000441943

Elliott, C. D. (2007). *Differential Ability Scales*, Second Edn. San Antonio, TX: Harcourt.

Fischl, B. (2012). FreeSurfer. *Neuroimage* 62, 774–781. doi: 10.1016/j.neuroimage.2012.01.021

Galambos, R., Makeig, S., and Talmachoff, P. J. (1981). A 40-Hz auditory potential recorded from the human scalp. *Proc. Natl. Acad. Sci. U.S.A.* 78, 2643–2647. doi: 10.1073/pnas.78.4.2643

Glasser, M. F., Coalson, T. S., Robinson, E. C., Hacker, C. D., Harwell, J., Yacoub, E., et al. (2016). A multi-modal parcellation of human cerebral cortex. *Nature* 536, 171–178.

Gotham, K., Pickles, A., and Lord, C. (2009). Standardizing ADOS scores for a measure of severity in autism spectrum disorders. *J. Autism Dev. Disord.* 39, 693–705. doi: 10.1007/s10803-008-0674-3

Gramfort, A., Luessi, M., Larson, E., Engemann, D. A., Strohmeier, D., Brodbeck, C., et al. (2013). MEG and EEG data analysis with MNE-Python. *Front. Neurosci.* 7:267. doi: 10.3389/fnins.2013.00267

Gramfort, A., Luessi, M., Larson, E., Engemann, D. A., Strohmeier, D., Brodbeck, C., et al. (2014). MNE software for processing MEG and EEG data. *Neuroimage* 86, 446–460. doi: 10.1016/j.neuroimage.2013.10.027

Gutschalk, A., Mase, R., Roth, R., Ille, N., Rupp, A., Hähnel, S., et al. (1999). Deconvolution of 40 Hz steady-state fields reveals two overlapping source activities of the human auditory cortex. *Clin. Neurophysiol.* 110, 856–868. doi: 10.1016/s1388-2457(99)00019-x

Hämäläinen, M. S., and Ilmoniemi, R. J. (1994). Interpreting magnetic fields of the brain: minimum norm estimates. *Med. Biol. Eng. Comput.* 32, 35–42.

Hamm, J. P., Gilmore, C. S., Picchetti, N. A., Sponheim, S. R., and Clementz, B. A. (2011). Abnormalities of neuronal oscillations and temporal integration to low- and high-frequency auditory stimulation in schizophrenia. *Biol. Psychiatry* 69, 989–996.

Hoechstetter, K., Bornfleth, H., Weckesser, D., Ille, N., Berg, P., and Scherg, M. (2004). BESA source coherence: a new method to study cortical oscillatory coupling. *Brain Topogr.* 16, 233–238. doi: 10.1023/b:brat.0000032857.55223.5d

Hong, L. E., Summerfelt, A., McMahon, R., Adami, H., Francis, G., Elliott, A., et al. (2004). Evoked gamma band synchronization and the liability for schizophrenia. *Schizophr. Res.* 70, 293–302. doi: 10.1016/j.schres.2003.12.011

Kenny, L., Hattersley, C., Molins, B., Buckley, C., Povey, C., and Pellicano, E. (2016). Which terms should be used to describe autism? Perspectives from the UK autism community. *Autism* 20, 442–462. doi: 10.1177/1362361315588200

Kuriakose, S. (2014). Concurrent validity of the WISC-IV and DAS-II in children with autism spectrum disorder. *J. Psychoedu. Assess.* 32, 283–294. doi: 10.1177/0734282913511051

Lenz, D., Fischer, S., Schadow, J., Bogerts, B., and Herrmann, C. S. (2011). Altered evoked gamma-band responses as a neurophysiological marker of schizophrenia? *Int. J. Psychophysiol.* 79, 25–31.

Light, G. A., Hsu, J. L., Hsieh, M. H., Meyer-Gomes, K., Sprock, J., Swerdlow, N. R., et al. (2006). Gamma band oscillations reveal neural network cortical coherence dysfunction in schizophrenia patients. *Biol. Psychiatry* 60, 1231–1240. doi: 10.1016/j.biopsych.2006.03.055

Lord, C., Rutter, M., DiLavore, P. C., Risi, S., Gotham, K., and Bishop, S. (2012). *Autism Diagnostic Observation Schedule*, 2nd Edn. Torance, CA: Western Psychological Services.

Ono, Y., Kudoh, K., Ikeda, T., Takahashi, T., Yoshimura, Y., Minabe, Y., et al. (2020). Auditory steady-state response at 20?Hz and 40?Hz in young typically developing children and children with autism spectrum disorder. *Psychiatry Clin. Neurosci.* 74, 354–361. doi: 10.1111/pcn.12998

Pantev, C., Roberts, L. E., Elbert, T., Ross, B., and Wienbruch, C. (1996). Tonotopic organization of the sources of human auditory steady-state responses. *Hear. Res.* 101, 62–74. doi: 10.1016/s0378-5955(96)00133-5

Picton, T. W., John, M. S., Dimitrijevic, A., and Purcell, D. (2003). Human auditory steady-state responses. *Int. J. Audiol.* 42, 177–219.

Port, R. G., Oberman, L. M., and Roberts, T. P. (2019). Revisiting the excitation/inhibition imbalance hypothesis of ASD through a clinical lens. *Br. J. Radiol.* 92:20180944. doi: 10.1259/bjr.20180944

Rojas, D. C., Maharajh, K., Teale, P. D., Kleman, M. R., Benkers, T. L., Carlson, J. P., et al. (2006). Development of the 40Hz steady state auditory evoked magnetic field from ages 5 to 52. *Clin. Neurophysiol.* 117, 110–117. doi: 10.1016/j.clinph.2005.08.032

Rojas, D. C., Maharajh, K., Teale, P., and Rogers, S. J. (2008). Reduced neural synchronization of gamma-band MEG oscillations in first-degree relatives of children with autism. *BMC Psychiatry* 8:66. doi: 10.1186/1471-244X-8-66

Rubenstein, J. L. R., and Merzenich, M. M. (2003). Model of autism: increased ratio of excitation/inhibition in key neural systems. *Genes Brain Behav.* 2, 255–267.

Rutter, M., Bailey, A., and Lord, C. (2003). *The Social Communication Questionnaire: Manual*. Los Angeles, CA: Western Psychological Services.

Semel, E. M., Wiig, E. H., and Secord, W. (2006). *CELF 4: Clinical Evaluation of Language Fundamentals 4*. San Antonio, TX: Pearson Education Inc.

Semel, E. M., Wiig, E. H., and Secord, W. (2013). *CELF 5: Clinical Evaluation of Language Fundamentals 5*. San Antonio, TX: The Psychological Corporation.

Seymour, R. A., Rippon, G., Gooding-Williams, G., Sowman, P. F., and Kessler, K. (2020). Reduced auditory steady state responses in autism spectrum disorder. *Mol. Autism* 11:56.

Shumway, S., Farmer, C., Thurm, A., Joseph, L., Black, D., and Golden, C. (2012). The ADOS calibrated severity score: relationship to phenotypic variables and stability over time. *Autism Res.* 5, 267–276. doi: 10.1002/aur.1238

Sohal, V. S., and Rubenstein, J. L. R. (2019). Excitation-inhibition balance as a framework for investigating mechanisms in neuropsychiatric disorders. *Mol. Psychiatry* 24, 1248–1257. doi: 10.1038/s41380-019-0426-0

Srinivasan, R., Winter, W. R., and Nunez, P. L. (2006). Source analysis of EEG oscillations using high-resolution EEG and MEG. *Prog. Brain Res.* 159, 29–42. doi: 10.1016/s0079-6123(06)59003-x

Stapells, D. R., Makeig, S., and Galambos, R. (1987). Auditory steady-state responses: threshold prediction using phase coherence. *Electroencephalogr. Clin. Neurophysiol.* 67, 260–270. doi: 10.1016/0013-4694(87)90024-1

Stroganova, T. A., Komarov, K. S., Sysoeva, O. V., Goiaeva, D. E., Obukhova, T. S., Ovsiannikova, T. M., et al. (2020). Left hemispheric deficit in the sustained neuromagnetic response to periodic click trains in children with ASD. *Mol. Autism* 11:100. doi: 10.1186/s13229-020-00408-4

Wang, J. Z., Williamson, S. J., and Kaufman, L. (1992). Magnetic source images determined by a lead-field analysis: the unique minimum-norm least-squares estimation. *IEEE Trans. Bio Med. Eng.* 39, 665–675. doi: 10.1109/10.142641

Wechsler, D. (2003). *Wechsler Intelligence Scale for Children*, 4th Edn. San Antonio, TX: Psychological Corporation.

Wechsler, D. (2014). *Wechsler Intelligence Scale for Children*, 5th Edn. San Antonio, TX: Psychological Corporation.

Weisz, N., and Lithari, C. (2017). Amplitude modulation rate dependent topographic organization of the auditory steady-state response in human auditory cortex. *Hear. Res.* 354, 102–108. doi: 10.1016/j.heares.2017.09.003

Wilson, T. W., Rojas, D. C., Reite, M. L., Teale, P. D., and Rogers, S. J. (2007). Children and adolescents with autism exhibit reduced MEG steady-state gamma responses. *Biol. Psychiatry* 62, 192–197. doi: 10.1016/j.biopsych.2006.07.002

Winkler, I., Debener, S., Müller, K., and Tangermann, M. (2015). "On the influence of high-pass filtering on ICA-based artifact reduction in EEG-ERP," in *Proceedings of the 2015 37th Annual International Conference of the IEEE Engineering in Medicine and Biology Society (EMBC)* (Piscataway, NJ: IEEE). doi: 10.1109/EMBC.2015.7319296

Wolff, J. J., Gu, H., Gerig, G., Elison, J. T., Styner, M., Gouttard, S., et al. (2012). Differences in white matter fiber tract development present from 6 to 24 months in infants with autism. *Am. J. Psychiatry* 169, 589–600. doi: 10.1176/appi.ajp.2011.11091447

Conflict of Interest: TR declares equity in Prism Clinical Imaging and Proteus Neurodynamics. He serves as a consultant/medical advisory board member for CTF, Ricoh, Spago Nanomedicine, Avexis and Acadia Pharmaceuticals.

The remaining authors declare that the research was conducted in the absence of any commercial or financial relationships that could be construed as a potential conflict of interest.

Publisher's Note: All claims expressed in this article are solely those of the authors and do not necessarily represent those of their affiliated organizations, or those of the publisher, the editors and the reviewers. Any product that may be evaluated in this article, or claim that may be made by its manufacturer, is not guaranteed or endorsed by the publisher.

frontiers in Behavioral Neuroscience

ORIGINAL RESEARCH
published: 17 February 2022
doi: 10.3389/fnbeh.2022.751053

D1 Receptor Mediated Dopaminergic Neurotransmission Facilitates Remote Memory of Contextual Fear Conditioning

*Nae Saito[1,2], Makoto Itakura[3] and Toshikuni Sasaoka[1]**

[1] Department of Comparative and Experimental Medicine, Brain Research Institute, Niigata University, Niigata, Japan, [2] Department of Molecular and Cellular Medicine, Graduate School of Medical and Dental Sciences, Niigata University, Niigata, Japan, [3] Department of Biochemistry, Kitasato University School of Medicine, Sagamihara, Japan

Dopaminergic neurotransmission *via* dopamine D1 receptors (D1Rs) is considered to play an important role not only in reward-based learning but also in aversive learning. The contextual and auditory cued fear conditioning tests involve the processing of classical fear conditioning and evaluates aversive learning memory. It is possible to evaluate aversive learning memory in two different types of neural transmission circuits. In addition, when evaluating the role of dopaminergic neurotransmission *via* D1R, to avoid the effects in D1R-mediated neural circuitry alterations during development, it is important to examine using mice who D1R expression in the mature stage is suppressed. Herein, we investigated the role of dopaminergic neurotransmission *via* D1Rs in aversive memory formation in contextual and auditory cued fear conditioning tests using D1R knockdown (KD) mice, in which the expression of D1Rs could be conditionally and reversibly controlled with doxycycline (Dox) treatment. For aversive memory, we examined memory formation using recent memory 1 day after conditioning, and remote memory 4 weeks after conditioning. Furthermore, immunostaining of the brain tissues of D1RKD mice was performed after aversive footshock stimulation to investigate the distribution of activated c-Fos, an immediate-early gene, in the hippocampus (CA1, CA3, dentate gyrus), striatum, amygdala, and prefrontal cortex during aversive memory formation. After aversive footshock stimulation, immunoblotting was performed using hippocampal, striatal, and amygdalar samples from D1RKD mice to investigate the increase in the amount of c-Fos and phosphorylated SNAP-25 at Ser187 residue. When D1R expression was suppressed using Dox, behavioral experiments revealed impaired contextual fear learning in remote aversion memory following footshock stimulation. Furthermore, expression analysis showed a slight increase in the post-stimulation amount of c-Fos in the hippocampus and striatum, and a significant increase in the amount of phosphorylated SNAP-25 in the hippocampus, striatum, and prefrontal cortex before and after stimulation. These findings indicate that deficiency in D1R-mediated dopaminergic neurotransmission is an important factor in impairing contextual fear memory formation for remote memory.

Keywords: dopamine D1 receptor (D1R), aversive memory, remote memory, c-Fos, SNAP-25

OPEN ACCESS

Edited by:
Atsushi Nambu,
National Institute for Physiological Sciences (NIPS), Japan

Reviewed by:
Hotaka Fukushima,
Tokyo University of Agriculture, Japan
Akinobu Suzuki,
University of Toyama, Japan

***Correspondence:**
Toshikuni Sasaoka
sasaoka@bri.niigata-u.ac.jp

Specialty section:
This article was submitted to Pathological Conditions, a section of the journal Frontiers in Behavioral Neuroscience

Received: *31 July 2021*
Accepted: *21 January 2022*
Published: *17 February 2022*

Citation:
Saito N, Itakura M and Sasaoka T (2022) D1 Receptor Mediated Dopaminergic Neurotransmission Facilitates Remote Memory of Contextual Fear Conditioning. Front. Behav. Neurosci. 16:751053. doi: 10.3389/fnbeh.2022.751053

INTRODUCTION

Dopamine neurotransmission through D1Rs and D1-like receptors is thought to play an important role in aversive memory (El-Ghundi et al., 2001; Ortiz et al., 2010; Sarinana et al., 2014; Soares-Cunha et al., 2016b; Schultz, 2019). On the other hand, dopamine neurotransmission through D2 dopamine receptors (D2Rs) and D2-like receptors is also thought to play an important role in aversive memory (Bromberg-Martin et al., 2010; Danjo et al., 2014; Yamaguchi et al., 2015; Soares-Cunha et al., 2016b; Kawahata et al., 2021).

To date, it has been reported that the direct and indirect pathways of the basal ganglia are composed of medium spiny neurons expressing D1R and D2R, respectively (Gerfen et al., 1990), and that dopamine neurotransmission through D1R mediates behavioral promotion and reward learning, while dopamine neurotransmission through D2R mediates behavioral suppression and aversive learning (Kravitz and Kreitzer, 2012; Volman et al., 2013). However, in recent years, these concepts have been re-evaluated, and the complexity of the basal ganglia circuit has been investigated (Calabresi et al., 2014; Soares-Cunha et al., 2016a,b; Shin et al., 2018).

D1R knockout (KO) mice or genetically modified mice, including conditional D1R knockdown mice using drug administration or the Cre-loxP system, have been utilized to elucidate the role of dopamine transmission through D1R in fear conditioning (El-Ghundi et al., 2001; Ortiz et al., 2010; Ikegami et al., 2014). However, the results of these analyses have been inconsistent, and the role of D1R-mediated dopamine neurotransmission in the hippocampus, amygdala, prefrontal cortex, and striatum remains to be fully elucidated.

In this study, we investigated the effects of D1R suppression on long-term memory of contextual and auditory cued fear conditioning as aversive learning in mature mice, as well as the role of D1Rs in the hippocampus, dorsomedial striatum (DMS), prelimbic region of medial prefrontal cortex (mPFC), and basal amygdala (BA). Fear conditioning memory tests were conducted 1 day after conditioning to examine recent memories and 4 weeks after conditioning to evaluate remote memories in long-term memory to investigate the effect of D1Rs suppression. Specifically, we observed the expression of c-Fos that is involved in the molecular mechanisms of learning and memory and is rapidly expressed during long-term memory formation (Milanovic et al., 1998; Tischmeyer and Grimm, 1999; Fleischmann et al., 2003; Miyashita et al., 2018). Contextual fear memories require the hippocampus, amygdala, striatum, and mPFC (Goshen et al., 2011; Ikegami et al., 2014; Stubbendorff et al., 2019; Mizuno et al., 2020), and auditory cued fear memories require the amygdala or striatum and do not depend on the hippocampus (Phillips and LeDoux, 1992; Pare et al., 2004; Goshen et al., 2011). Different neural circuits are thought to be important for contextual fear conditioning and auditory cued fear conditioning. In this study, we examined the effects of the suppression of D1R expression on fear memory formation in contextual and auditory cued fear conditioning in mature mice and compared the results of this study with results regarding aversive memory formation in the passive avoidance test reported previously (Saito et al., 2020). Furthermore, we analyzed the phosphorylation of synaptosomal-associated protein of 25 kDa (SNAP-25) at Ser187, which is involved in cognitive function and stress (Genoud et al., 1999; Yamamori et al., 2014), and investigated the effects of D1R suppression on aversive memory formation.

MATERIALS AND METHODS

Mice

C57BL/6 mice were purchased from CLEA Japan (Tokyo, Japan). The generation of D1R knockdown (KD) mice (D1R homozygous knockout/Tet/Off system-based compound-transgenic mice) was performed following previously published protocols (Chiken et al., 2015; Okubo et al., 2018; Saito et al., 2020). Only male mice were used in the contextual and cued fear conditioning tests.

Mice were maintained under a 12 h light/dark cycle (lights on at 7:00 AM), with *ad libitum* access to food and water in specific-pathogen-free conditions. All experiments were performed in accordance with the guidelines of the National Institutes of Health and the Ministry of Education, Culture, Sports, Science and Technology (MEXT) of Japan, and in compliance with the protocol that was reviewed by the Institutional Animal Care and Use Committee and approved by the President of Niigata University (Permit Number: SA00954) as previously described (Saito et al., 2020).

Grouping and Doxycycline (Dox) Treatment

In D1RKD mice, 2.0 mg/mL doxycycline (Dox; Sigma Aldrich, United States) was used to knock down D1R expression, as previously described (Chiken et al., 2015; Okubo et al., 2018; Saito et al., 2020). For mice treated with Dox, Dox was administered *via* drinking water containing 5% sucrose for 4 weeks prior to behavioral tests and until the completion of the conditioning experiment (see section "Contextual and Auditory Cued Fear Conditioning Test," **Figures 1A**, **2A**), after which all mice received drinking water without Dox for the remainder period. Mice that were not treated with Dox received Dox-free water for the entire duration of the experiment. After termination of Dox administration, the expression level of D1Rs recovered to the same level as that before Dox administration (Chiken et al., 2015).

In the contextual and auditory cued fear conditioning test, D1RKD mice were assigned to D1RKD Dox (−) and D1RKD Dox (+) groups. D1RKD Dox (−) mice were used with ten mice per group. D1RKD Dox (+) were used with six and eight mice in recent and remote phase tests, respectively; six and ten wild-type (WT) mice were used as the control group in recent and remote phase tests, respectively.

In the immunohistochemical analysis, D1RKD mice were assigned to the following four groups: D1RKD Dox (−) Stimulation (−) (n = 3), D1RKD Dox (−) Stimulation (+) (n = 3), D1RKD Dox (+) Stimulation (−) (n = 3), and D1RKD Dox (+) Stimulation (+) (n = 3); two groups of WT mice,

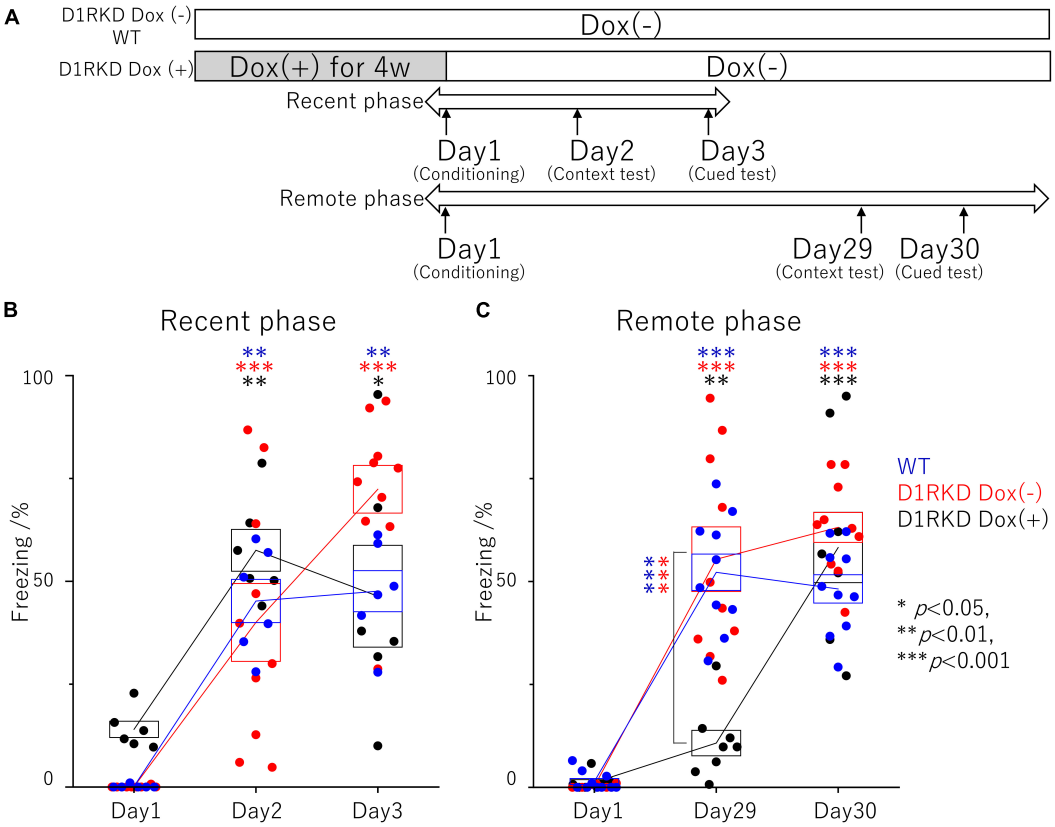

FIGURE 1 | Contextual and auditory cued fear conditioning test. **(A)** Experimental schedule. In the D1RKD Dox (+) group, Dox (2 mg/mL) was administered for 4 weeks prior to the commencement of the experiment and until after the completion of conditioning as the learning session on Day 1, with mice provided drinking water without Dox thereafter. The D1RKD Dox (–) and wild-type (WT) groups were always given only Dox-free water. Conditioning on Day 1, context test on Day 2, and auditory cued test on Day 3 were conducted for recent phase tests in all three groups [WT; $n = 6$, D1RKD Dox (–); $n = 10$, D1RKD Dox (+); $n = 6$]. On the other hand, Conditioning on Day 1, context test on Day 29, and cued test on Day 30 were conducted for remote phase tests in all three groups [WT; $n = 10$, D1RKD Dox (–); $n = 10$, D1RKD Dox (+); $n = 8$]. **(B)** In the recent phase tests, the freezing time of mice was recorded for all three groups during the context tests of Day 2 and the auditory cued tests of Day 3 as the test session, $^{*}p < 0.05$; $^{**}p < 0.01$; $^{***}p < 0.001$. **(C)** In the remote phase tests, the freezing time of mice was recorded for all three groups during the context tests of Day 29 and the auditory cued tests of Day 30 as the learning session. The blue circles indicate the values of WT groups, the red circles indicate the values of D1RKD Dox (–) groups, the black circles indicate the values of D1RKD Dox (+) groups, $^{**}p < 0.01$; $^{***}p < 0.001$.

Stimulation (−) ($n = 3$) and Stimulation (+) ($n = 3$), were used as the control groups.

In the immunoblot analysis, D1RKD mice were assigned to the following six groups: D1RKD Dox (−) Stimulation (−) ($n = 3$), D1RKD Dox (−) Stimulation (+) ($n = 3$), D1RKD Dox (+) Stimulation (−) ($n = 3$), D1RKD Dox (+) Stimulation (+) ($n = 3$), D1RKD Dox (+→−) Stimulation (−) ($n = 3$), D1RKD Dox (+→−) Stimulation (+) ($n = 3$); two groups of WT mice, Stimulation (−) ($n = 3$) and Stimulation (+) ($n = 3$), were used as control groups.

Contextual and Auditory Cued Fear Conditioning Test

A computer-controlled fear conditioning system was used for contextual and auditory cued fear conditioning tests (O'Hara & Co., Japan). A clear chamber (16 × 14 × 10 cm) for conditioning and contextual tests was set in a sound-insulating box (30 lux) with white walls. A white chamber (17 × 10 × 10 cm) for auditory cued tests was placed in a sound-insulating box (30 lux) with black walls. Mice were subjected to a conditioning session for 5 min on Day 1, a contextual test session for 5 min on Day 2 or Day 29, and an auditory cued test session for 5 min on Day 3 or Day 30.

In the conditioning session, a tone (65 dB, white noise) was presented for 20 s, and a mild footshock (0.3 mA, 2 s) was presented in the last 2 s through a floor grid. This process was performed three times for 5 min each. The mice were returned to their home cages 60 s after shock termination. Before the initial tone and footshock presentation and in the contextual test session, mice were placed back into a clear chamber used in the conditioning session for 5 min without footshock or tone stimulus. In the auditory cued test session, the mice were placed in a white chamber. A tone stimulus was presented for 2 min after 2 min of placing the mice in the white chamber. The behaviors of the mice were monitored using a CCD camera, and freezing behaviors were analyzed using Time FZ2 software (O'Hara & Co., Tokyo, Japan).

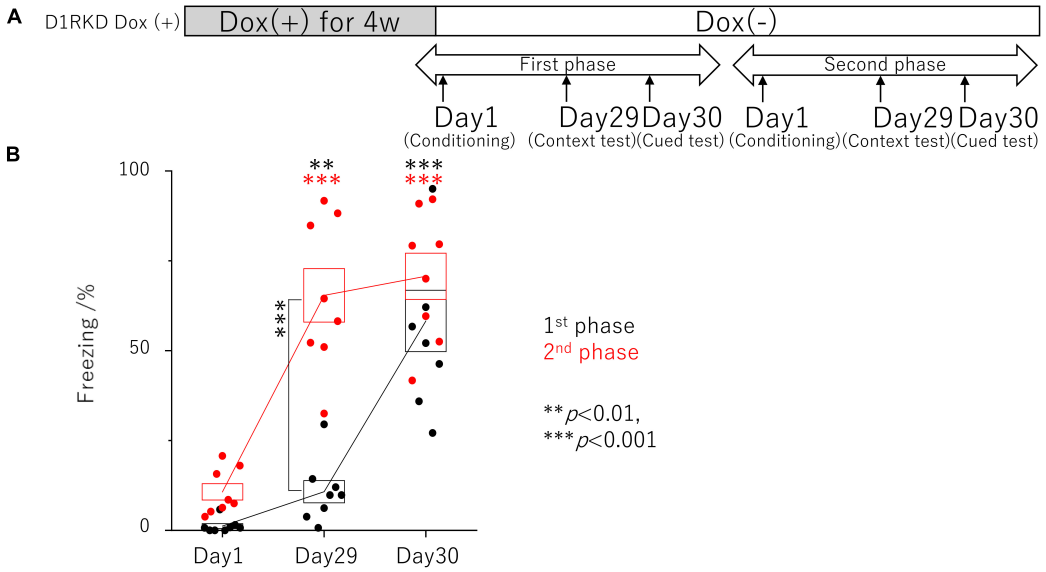

FIGURE 2 | Contextual and auditory cued fear conditioning test with the same mice for remote phase. **(A)** Experimental schedule. Experiments were conducted only in the D1RKD Dox (+) group (n = 8) and the experiments of the 1st phase and 2nd phase were performed with the same mice. Dox (2 mg/mL) was administered for 4 weeks prior to the commencement of the experiment and until after the completion of conditioning as the learning session on Day 1, with mice provided drinking water without Dox thereafter. Conditioning on Day 1, contextual test on Day 29, and auditory cued test on Day 30 conducted for 1st phase and 2nd phase tests, respectively. **(B)** In 1st phase and 2nd phase, the freezing time of mice was recorded during the contextual tests of Day 29, and the auditory cued tests of Day 30 as the test session with the same mice, respectively. The black circles indicate the values in 1st phase, and the red circles indicate the values in 2nd phase, $^{**}p < 0.01$; $^{***}p < 0.001$.

Treatment Prior to Histochemistry and Immunoblot

Footshock stimulation was carried out in a fear conditioning system or a step-through-type apparatus, comprising light and dark compartments separated by a removable door for the passive avoidance test (O'Hara & Co., Japan). In the fear conditioning system, each mouse was placed in the same way as in the fear conditioning tests. In the passive avoidance apparatus, each mouse was placed in the dark compartment and received a 2 s 0.3 mA electric footshock. Brain samples were collected 1 h after the footshock stimulus was delivered.

Histochemistry and Cell Counting

D1RKD mice and WT mice were anesthetized with a mixture of medetomidine hydrochloride [0.75 mg/kg body weight (BW)], midazolam (4 mg/kg BW), and butorphanol tartrate (5 mg/kg BW). The mice were then perfused with phosphate-buffered saline (PBS, pH 7.4) and 4% paraformaldehyde in 0.1 M phosphate buffer (PB, pH 7.4) through the left ventricle. The brains were removed, post-fixed overnight in 4% paraformaldehyde in 0.1 M PB (pH 7.4), and equilibrated overnight with 30% sucrose in 0.1 M PB (pH 7.4) at 4°C. The brains were embedded in OCT compound (Sakura Finetek, Japan), frozen over isopropanol (FUJIFILM Wako Pure Chemical Corporation, Japan) in liquid nitrogen, and cut on a cryostat CM1950 (Leica, Germany) into 40 μm thick coronal sections. Free-floating sections were treated with 3% H_2O_2 and 10% methanol in PB (pH 7.4) for 10 min and then blocked with 5% Blocking One (Nacalai Tesque) in 0.1% Triton in PBS (PBST) for 1 h after washing with PBS. Sections were incubated at 4°C with a polyclonal rabbit anti c-Fos antibody (1: 600, Cell Signaling) in blocking solution overnight, washed with PBST, and then incubated with biotinylated goat anti rabbit IgG (1: 300, Jackson Laboratories, United States) for 2 h. Thereafter, sections were incubated for 1 h with Vectastain Elite ABC Kit (Vector Laboratories, United States), washed with PBST, and then incubated with SIGMAFAST 3,3'-diaminobenzidine (DAB) (Sigma Aldrich, United States). After washing with distilled water, sections were mounted on glass slides, counterstained with 0.5% methyl green (FUJIFILM Wako Pure Chemical Corporation, Japan), and washed with distilled water. Finally, immunostained sections on mounted slides were fixed by serial dehydration in alcohol and lemosol and mounted using Softmount (FUJIFILM Wako Pure Chemical Corporation, Japan). Images of immunostained sections were acquired using a BZ-9000 microscope (Keyence, Japan) with BZ-II Analyzer software (Keyence, Japan). Immunoreactive cells were counted bilaterally in three sections, each from three mice by an experimenter blinded to the treatment conditions.

Regions in the brain of mice examined by immunohistochemistry are shown in **Figure 3**, and c-Fos positive cells were counted within the red rectangles. Brain sections including hippocampus and amygdala (**Figure 3A**; bregma −1.34 to −2.06 mm), DMS (**Figure 3B**; bregma −0.10 to 0.98 mm), and prelimbic region of mPFC (**Figure 3C**; bregma 1.70 to 1.98 mm) were analyzed. To examine each region of the hippocampus in detail, the number of c-Fos

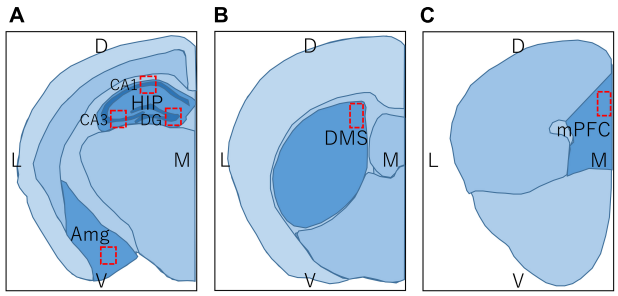

FIGURE 3 | Regions in the brain of mice used in immunohistochemistry and immunoblot. L, lateral; M, medial; D, dorsal; V, ventral; HIP, hippocampus; CA1, hippocampal CA1 region; CA3, hippocampal CA3 region; DG, dentate gyrus; Amg, amygdala; DMS, dorsomedial striatum; mPFC, medial prefrontal cortex. Brain section map of the hippocampus and amygdala (**A**; bregma –1.34 to –2.06 mm), DMS (**B**; bregma –0.10 to 0.98 mm), and prelimbic region of mPFC (**C**; bregma 1.70 to 1.98 mm). Rectangles in **(A–C)** represent the areas in which the number of c-Fos positive cells was counted.

positive cells within the rectangles (300 × 300 μm) in the CA1, CA3, and dentate gyrus (DG) regions were counted separately. The number of c-Fos positive cells in the BA, DMS, and mPFC were counted within the rectangles (500 × 500 μm, 300 × 300 μm, and 300 × 300 μm, respectively), as shown in **Figures 3A–C**, respectively.

Immunoblotting

D1RKD mice and WT mice were sacrificed by cervical dislocation, and their brains were removed. The brains were sliced coronally into 1 mm thick sections. Regions in the brains of mice used for immunoblotting are shown in **Figure 3**. However, in contrast to immunohistochemistry, for immunoblotting, the entire hippocampus was used, including both the dorsal and ventral sides (**Figure 3A**). In addition, the entire striatum, including the DMS and the entire amygdala, including the BA was used (**Figures 3A,B**). Hippocampal tissues containing CA1, CA3, and DG were collected from the sections of three mice. Striatum and amygdala tissues were obtained from the sections of three mice. Each tissue was homogenized in phase-transfer surfactant buffer (PTS, 12 mM sodium deoxycholate, 12 mM sodium N-dodecanoylsarcosinate, and 200 mM triethylammonium bicarbonate) with cOmplete EDTA-free protease inhibitor (Sigma Aldrich, United Kingdom), PhosStop (Sigma Aldrich, United Kingdom), and 1 mM EDTA. Homogenized proteins were quantified using a BCA kit (Wako, Japan). Homogenates were solubilized in sample buffer (125 mM Tris–HCl, pH 7.4, 3.3% glycerol, 2% SDS, and 50 mM DTT) and heated at 90°C for 5 min. The proteins were then separated on 5 – 20% polyacrylamide gel (ATTO, Japan) loaded at 5 μg in SDS sample buffer at 15 mA for 90 min. These gels were blotted onto PVDF membranes (Immobilon-P, Merck Millipore) in blotting buffer (192 mM glycine, 0.037% SDS, 20% methanol, 100 mM Tris–HCl, pH 8.8) at 20 V for 60 min, and then blocked with 5% non-fat milk in TBST (150 mM NaCl, 0.2% Tween 20, 20 mM Tris–HCl, pH 7.5) for 30 min at room temperature. These membranes were incubated with rabbit anti c-Fos antibody (1: 1,000, Cell Signaling), mouse anti actin antibody (1: 1,000, BD Biosciences, United States), rabbit anti SNAP-25 antibody (1 μg/ml) (Yamamori et al., 2011), or rabbit anti Phospho-SNAP-25 (Ser187) antibody (1: 500) (Iida et al., 2013) in 1% non-fat milk with TBST at 4°C overnight, washed with TBST, and then incubated with peroxidase-conjugated donkey anti-rabbit IgG (H + L) (1: 2,000, Jackson Laboratories, United States) or peroxidase-conjugated donkey anti-mouse IgG (H + L) (1: 1,000, Jackson Laboratories, United States) for 1 h. Immunoreacted samples were visualized using a chemiluminescent reagent (Chemi-Lumi One, Nacalai Tesque or Immobilon Western Chemiluminescent HRP, Sigma Aldrich), and images were acquired using a luminescence image analyzer (LAS 4000, GE Healthcare, Sweden) with ImageQuant TL software (GE Healthcare, Sweden).

Statistical Analysis

All data were analyzed using Origin 2021 (OriginLab, United States). Data from the contextual and auditory cued fear conditioning tests and cell counting data from immunohistochemistry were analyzed using the Mann-Whitney test. Immunoblot data were analyzed using the two sample *t* test. Significance was set at $p < 0.05$.

RESULTS

Contextual and Auditory Cued Fear Conditioning Test

The effect of suppressing D1R expression on fear memory formation was examined using a contextual and auditory cued fear conditioning test in the recent and remote phase (**Figure 1A**). First, recent phase examinations found significantly longer freezing responses in both the context test (Day 2) and auditory cued test (Day 3) than those before conditioning. There was no significant difference between the three groups on both the context test (Day 2) and auditory cued test (Day 3) (**Figure 1B**). Next, the remote phase contextual and auditory cued fear conditioning tests were conducted using different mice from those used in the recent phase tests. In the remote phase context tests (Day 29), D1RKD Dox (+) mice showed almost no freezing response, similar to before conditioning (Day 1). The freezing responses of D1RKD Dox (+) mice were clearly different from those of the other two groups (D1RKD Dox (−) and WT), while the freezing responses in the remote phase context tests (Day 29) of D1RKD Dox (−) and WT mice were increased and similar to those seen in the recent phase context tests (Day 2). On the other hand, D1RKD Dox (+) mice showed a significantly increased percentage of time spent freezing in the auditory cued tests (Day 30), which was equivalent to WT and D1RKD Dox (−) mice, albeit with some amount of variation (**Figure 1C**). Furthermore, D1RKD Dox (−) mice overexpressing D1Rs showed a significantly increased percentage of time spent freezing compared to WT mice in the auditory cued tests [Day 3 ($p < 0.05$), Day 30 ($p < 0.05$)].

In addition, the effects of recovery of D1R expression were examined using the same mice as those in the remote phase

contextual and auditory cued fear conditioning tests (**Figure 2A**). In the first test phase in the context tests (Day 29), D1RKD Dox (+) mice showed almost no freezing response, similar to before conditioning (Day 1) (**Figure 2B**). In the second test phase, following footshock conditioning on Day 1, D1RKD Dox (+) mice showed a significantly increased percentage of freezing on the context tests (Day 29). On the other hand, in the auditory cued fear conditioning test, both D1RKD mice with suppressed D1R expression in the first test phase and the same mice with recovering D1R expression in the second phase showed freezing behavior. These results using the same D1RKD mice were consistent with those obtained using different D1RKD mice (**Figure 2A**).

Immunohistochemistry

Representative immunohistochemical staining images of the hippocampus are shown in **Figure 4A**. Hippocampal CA1, CA3, and DG regions in **Figure 4** were enlarged and shown in **Supplementary Figures 1A–C**, respectively. Distributions of c-Fos positive cells in the hippocampus of WT and D1RKD Dox (−) mice with footshock stimulation by a fear conditioning (FC) or a passive avoidance (PA) apparatus were compared with those of the WT and D1RKD Dox (−) mice without stimulation. In the case of PA footshock stimulation, there was an increase in the number of c-Fos positive cells in a large area of the hippocampi of WT and D1RKD Dox (−) mice with footshock stimulation. In contrast, c-Fos positive cells were hardly observed in either case of D1RKD Dox (+) mice with or without stimulation (**Figure 4A**). In the case of FC footshock stimulation, the number of c-Fos-positive cells increased in a large area of the hippocampi of footshock-stimulated WT mice. In contrast, c-Fos-positive cells were not often observed in either D1RKD Dox (−) and D1RKD Dox (+) mice, with or without stimulation (**Figure 4A**). In both cases of PA and FC footshock stimulation, when the number of c-Fos positive cells was counted in all the CA1, CA3, and DG regions, there was a significant increase in the two groups (WT and D1RKD Dox (−) mice) when comparing the stimulated and unstimulated groups. However, the number of positive cells D1RKD Dox (−) mice was lower in FC than in PA. Moreover, in the case of PA apparatus, there was a little increase in the hippocampal CA1, CA3, and DG regions of the D1RKD Dox (+) mice group when comparing the stimulated and unstimulated groups (**Figure 4B**). In the case of FC footshock stimulation, the number of positive cells in the hippocampal CA1 and CA3 regions was slightly increased, but that in the DG region was almost unchanged (**Figure 4B**). In addition, the distributions of c-Fos positive cells in the DMS of WT, D1RKD Dox (−), and D1RKD Dox (+) mice with and without stimulation were found to be similar to those observed in the hippocampus as described above (**Figure 5A**). When the number of c-Fos positive cells was counted in DMS, there was a significant increase in the both groups (WT and D1RKD Dox (−) mice) when comparing the stimulated and unstimulated groups. However, there was a little increase in the DMS or hippocampus of the D1RKD Dox (+) mice group when comparing the stimulated and unstimulated groups (**Figure 5B**). In contrast, an apparent increase in the number of c-Fos positive cells was observed in the mPFC and BA in the mice of the three groups [WT, D1RKD Dox (−), and D1RKD Dox (+)] that received stimulation (**Figures 6A**, **7A**). Furthermore, the number of c-Fos positive cells in mice with stimulation was significantly different from that in mice without stimulation in the three groups ($p < 0.001$) (**Figures 6B**, **7B**).

Immunoblotting

Representative immunoblotting images are shown in **Figure 8**. First, in the case of FC footshock stimulation, c-Fos protein levels were greatly increased in both groups (WT, D1RKD Dox (−) mice), but the increase in c-Fos protein levels in D1RKD Dox (+) mice was quite small compared with those in WT and D1RKD Dox (−) mice in the hippocampus and striatum. Second, in the case of PA footshock stimulation, c-Fos protein levels were significantly increased in D1RKD Dox (−) mice, but those in D1RKD Dox (+) mice were relatively small (**Figure 8C**). These results were consistent with those of immunohistochemical analysis, except for the increase in the hippocampal CA1 region in the case of FC apparatus. Furthermore, c-Fos protein levels were also examined in D1RKD Dox (+→−) mice in which D1R expression was restored after termination of Dox administration. c-Fos protein levels tended to be similar to those in D1RKD Dox (−) mice before Dox administration. This result indicates that the restoration of D1R expression following suppression led to the recovery of the response to stimulation with respect to the induction of c-Fos expression.

In contrast, in the amygdala, the amount of c-Fos protein was greatly increased by stimulation in all four groups (WT, D1RKD Dox (−), D1RKD Dox (+), and D1RKD Dox (+→−) mice), and also these results were consistent with the results of immunohistochemical analysis, in the case of FC footshock stimulation. In the case of PA footshock stimulation, c-Fos protein levels increased slightly more than in the case of FC footshock stimulation, but the same tendency as that of FC stimulation was observed (**Figure 8C**). The amount of SNAP-25 protein was approximately the same in all four groups (WT, D1RKD Dox (−), D1RKD Dox (+), and D1RKD Dox (+→−) mice).

Next, in the case of FC footschock stimulation, the amount of phosphorylated SNAP-25 at Ser187 tended to decrease with stimulation in D1RKD Dox (−), D1RKD Dox (+→−), and D1RKD Dox (+) mice in all observed regions of the hippocampus, striatum, and amygdala. In addition, in the case of PA footshock stimulation, the amount of phosphorylated SNAP-25 at Ser187 significantly increased in D1RKD Dox (−), D1RKD Dox (+→−) mice in region of the striatum following stimulation. In contrast, in the hippocampus and amygdala, there were no significant changes. Interestingly, there was a large increase in the amount of phosphorylated SNAP-25 at Ser187 not only after stimulation but also before stimulation of the D1RKD Dox (+) mice compared to that in WT mice without stimulation. This result was prominent in regions of the striatum and amygdala (**Figures 8A,B,D**).

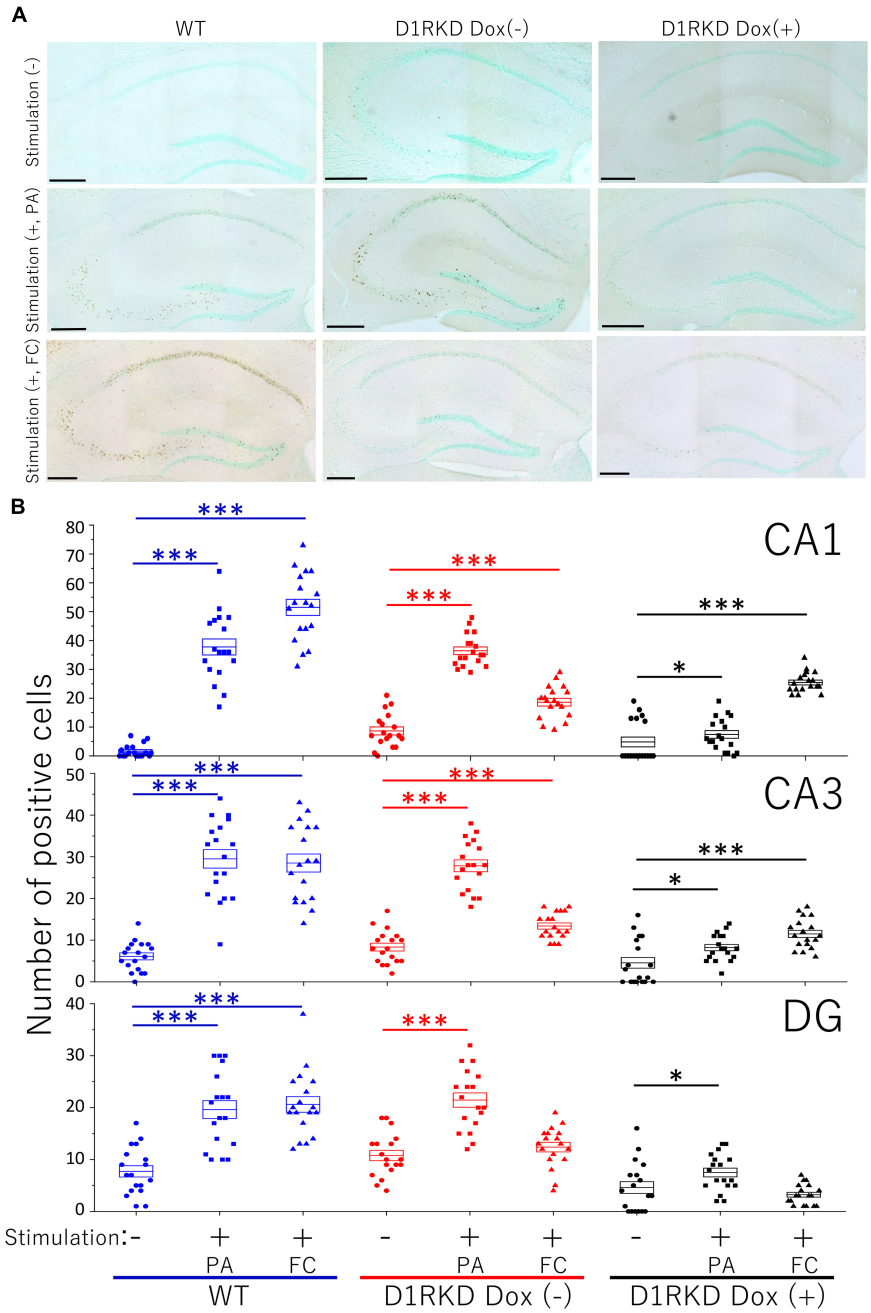

FIGURE 4 | Immunohistochemical analysis of c-Fos expression in the hippocampus (CA1, CA3, and DG) after 1 h of electric footshock stimulus using a step-through-type apparatus for the passive avoidance test (PA) or fear conditioning system (FC). **(A)** Representative immunohistochemical staining of c-Fos positive cells. Scale bar, 300 μm. **(B)** The number of positive cells in CA1, CA3, DG in immunohistochemistry. All groups, $n = 18$. The blue color indicates the values of WT groups, the red color indicates the values of D1RKD Dox (–) groups, and the black color indicates the values of D1RKD Dox (+) groups. The circle, square, and triangle indicate no stimulation, stimulation by PA, and stimulation by FC, respectively, $^{*}p < 0.05$; $^{***}p < 0.001$.

DISCUSSION

To date, D1R knockout (KO) mice or genetically modified mice, including conditional D1R knockout (cKO) mice using the Cre-loxP system have been utilized to elucidate the role of dopamine transmission through D1Rs in fear conditioning (El-Ghundi et al., 2001; Ortiz et al., 2010; Ikegami et al., 2014). However, the results of these analyses have been inconsistent, and the role of D1R-mediated dopamine neurotransmission in fear memory formation in the hippocampus, amygdala, prefrontal cortex, and striatum remains to be fully elucidated. In D1R KO mice, D1R is deficient from the beginning of development, and

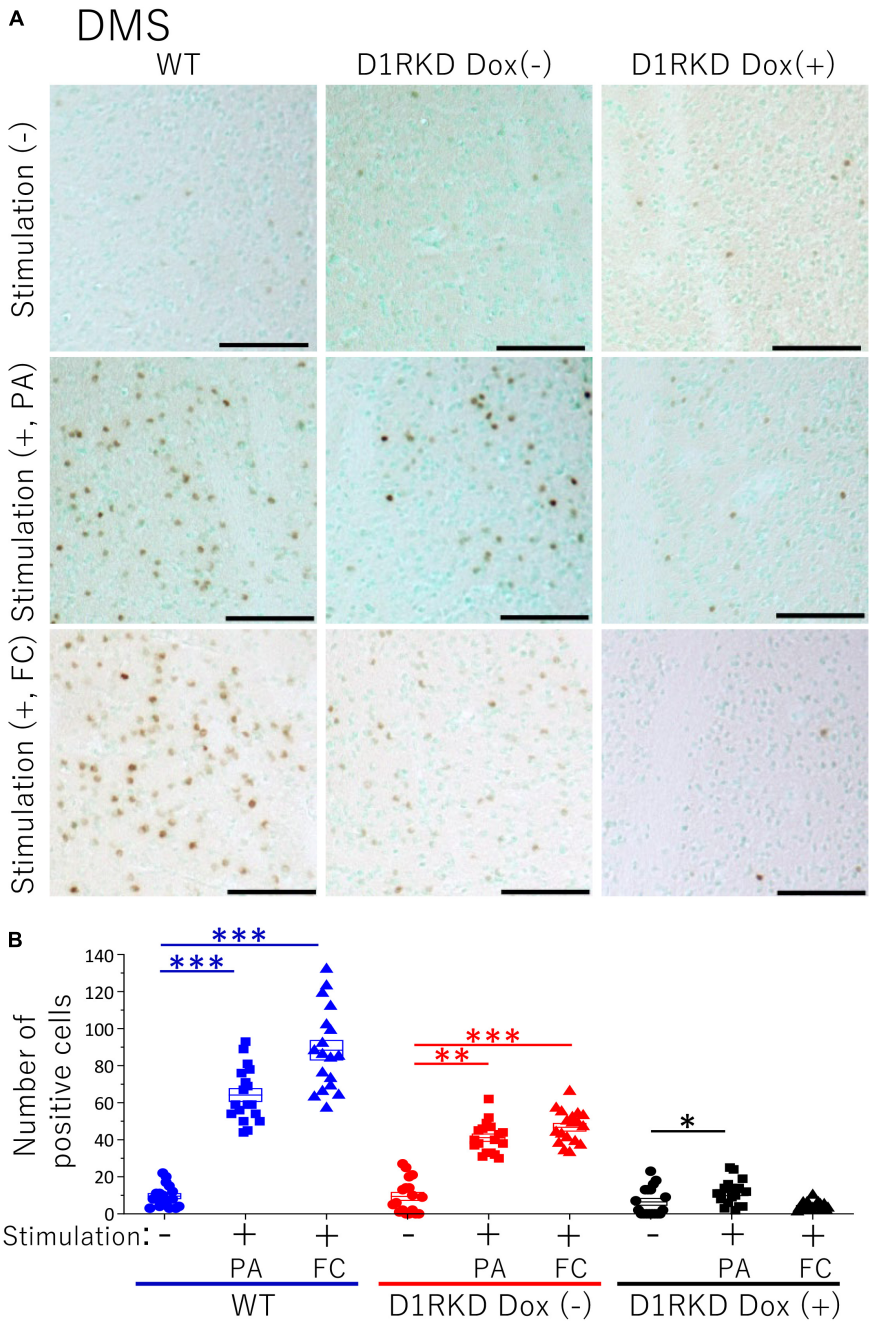

FIGURE 5 | Immunohistochemical analysis of c-Fos expression in DMS after 1 h of electric foot shock stimulus using a step-through-type apparatus for the passive avoidance test (PA) or fear conditioning system (FC). **(A)** Representative immunohistochemical staining of c-Fos positive cells. Scale bar, 100 μm. **(B)** The number of positive cells in DMS in immunohistochemistry. All groups, $n = 18$. The blue color indicates the values of WT groups, the red color indicates the values of D1RKD Dox (–) groups, and the black color indicates the values of D1RKD Dox (+) groups. The circle, square, and triangle indicate no stimulation, stimulation by PA, and stimulation by FC, respectively, $^{*}p < 0.05$; $^{**}p < 0.01$; $^{***}p < 0.001$.

compensatory mechanisms may have been affected. In the case of drug-induced suppression of D1R function, the effects may differ depending on the timing and method of administration and specificity of the drug to D1R. In addition, in the case of conditional knockout mice using Cre-loxP recombination, the timing of the induction of D1R deletion has a significant effect. Although few of these causes have been reported (Stiedl et al., 1999; Soares-Cunha et al., 2016b; Stubbendorff and Stevenson, 2020), it is considered that one of the causes is the timing of D1R elimination.

We have previously reported that D1R KO mice and D1RKD exhibited different impairments in motor function

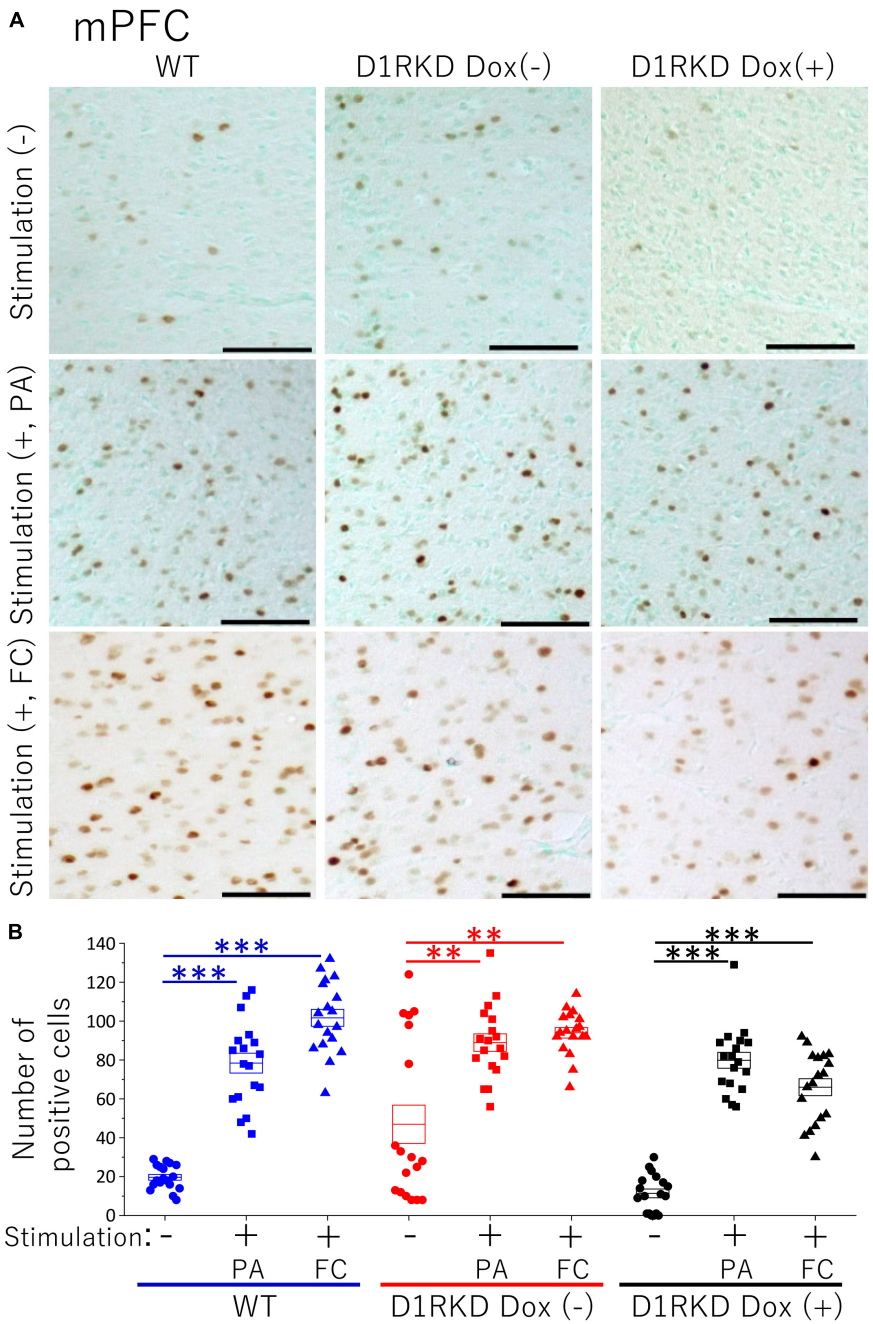

FIGURE 6 | Immunohistochemical analysis of c-Fos expression in mPFC after 1 h of electric footshock stimulus using a step-through-type apparatus for the passive avoidance test (PA) or fear conditioning system (FC). **(A)** Representative immunohistochemical staining of c-Fos positive cells. Scale bar, 100 μm. **(B)** The number of positive cells in mPFC in immunohistochemistry. All groups, $n = 18$. The blue color indicates the values of WT groups, the red color indicates the values of D1RKD Dox (–) groups, and the black color indicates the values of D1RKD Dox (+) groups. The circle, square, and triangle indicate no stimulation, stimulation by PA, and stimulation by FC, respectively, $^{**}p < 0.01$; $^{***}p < 0.001$.

(Okubo et al., 2018). In these D1RKD mice, D1R expression can be reversibly regulated from birth by administering Dox using the TET-OFF system (Chiken et al., 2015). Despite the same D1R deficiency, these mice showed significant differences in motor function depending on the timing of D1R suppression. First, we compared D1R KO mice, which are deficient in D1R from early development, with D1RKD mice, which underwent D1R suppression immediately after birth to examine motor function in early childhood. The basal motor activity of D1R KO mice was higher than that of WT and D1RKD mice, and no effect of D1R suppression on the basal motor activity was observed in D1RKD mice. In adulthood, the motor activity of D1R-deficient D1RKD

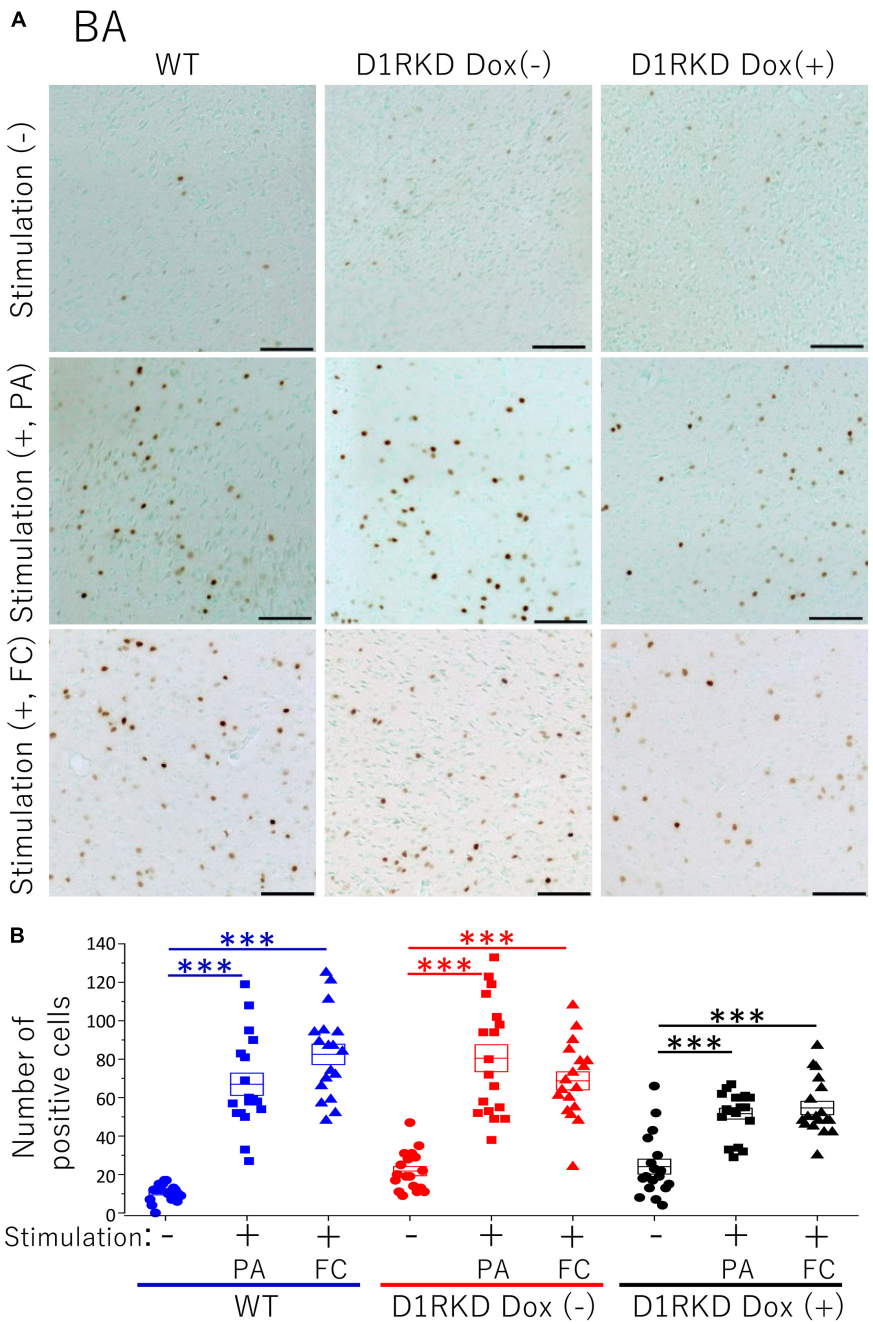

FIGURE 7 | Immunohistochemical analysis of c-Fos expression in BA after 1 h of electric footshock stimulus using a step-through-type apparatus for the passive avoidance test (PA) or fear conditioning system (FC). **(A)** Representative immunohistochemical staining of c-Fos positive cells. Scale bar, 100 μm. **(B)** The number of positive cells in BA in immunohistochemistry. All groups, $n = 18$. The blue color indicates the values of WT groups, the red color indicates the values of D1RKD Dox (–) groups, and the black color indicates the values of D1RKD Dox (+) groups. The circle, square, and triangle indicate no stimulation, stimulation by PA, and stimulation by FC, respectively, $^{***}p < 0.001$.

mice was lower than that of D1R KO, D1R-expressing D1RKD, and WT mice. On the other hand, the motor coordination of D1R-suppressed D1RKD mice was lower in childhood and adulthood than in WT and D1R KO mice. Although it is unclear which neural circuitry affects the behavioral phenotype, the prenatal stage is important for establishing the basis of motor function, suggesting that the role of dopamine neurotransmission *via* D1Rs is also in a developmental stage during growth. Therefore, the brain may develop compensatory mechanisms to avoid a functional decline in motor function due to D1Rs suppression, and it is possible that a similar phenomenon occurs in fear conditioning. This study used these D1RKD mice, which

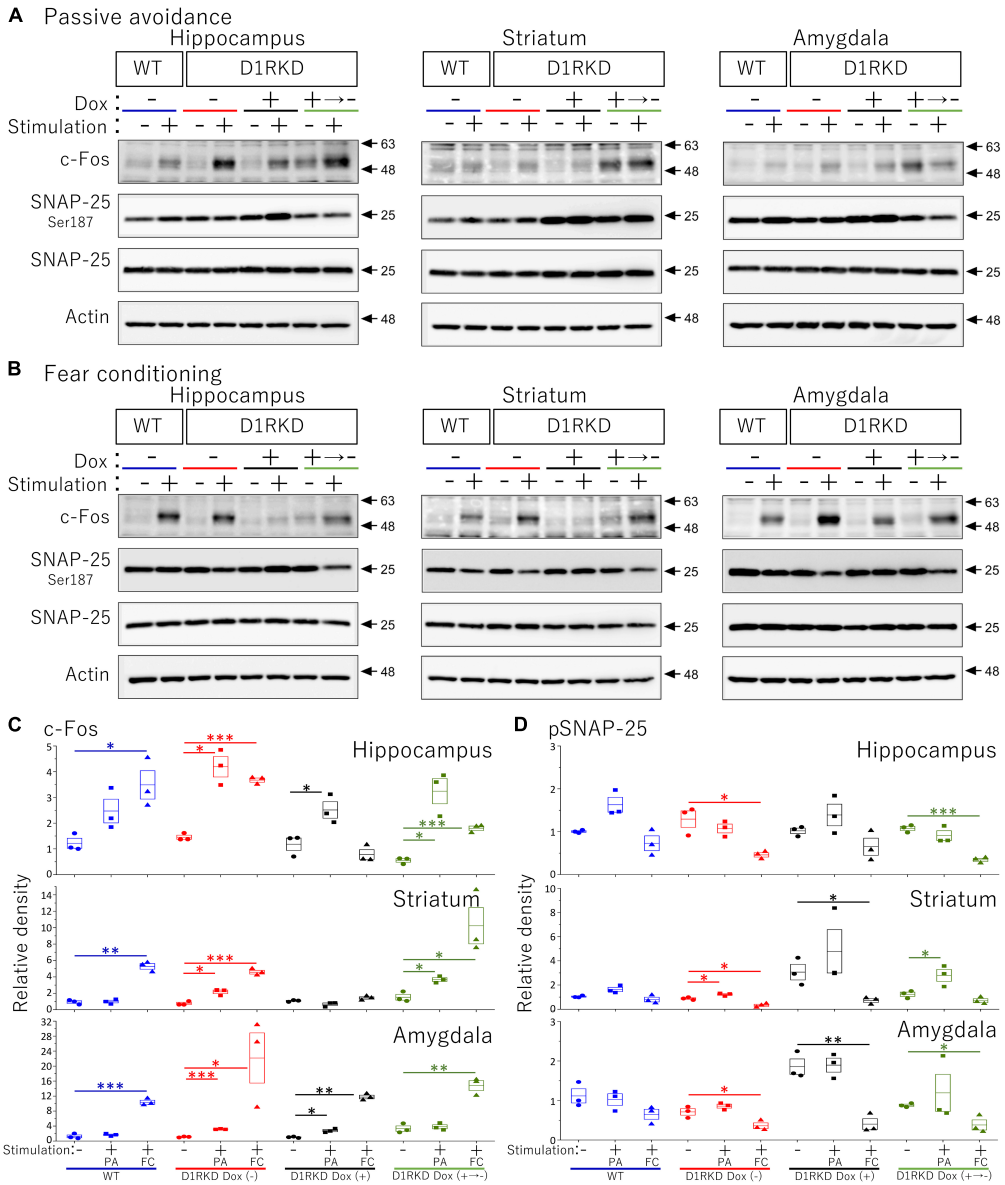

FIGURE 8 | Immunoblot analysis of c-Fos, SNAP-25 phosphorylation at Ser187, SNAP-25, and Actin expression in homogenates from the hippocampus, striatum, and amygdala after 1 h of electric footshock stimulus using a step-through-type apparatus for the passive avoidance test (PA) or fear conditioning system (FC). **(A)** Representative immunoblot images using the apparatus for PA. **(B)** Representative immunoblot images using the system for FC. Samples without electric footshock stimulus were used as controls. Actin was used as a loading control. **(C)** The relative band intensities of c-Fos. **(D)** The relative band intensities of SNAP-25 phosphorylation at Ser187. These band intensities were represented as the ratio of WT mice without stimulation as control of two type stimulation, separately. Actin was used as a loading control. Data shown are from three independent experiments. The blue color indicates the values of WT groups, the red color indicates the values of D1RKD Dox (–) groups, the black color indicates the values of D1RKD Dox (+) groups, and the green color indicates the values of D1RKD Dox (+→–). The circle, square, and triangle indicate no stimulation, stimulation by PA, and stimulation by FC, respectively. All groups, $n = 3$, $^{*}p < 0.05$; $^{**}p < 0.01$; $^{***}p < 0.001$.

allows D1R to be reversibly regulated from birth by administering Dox to focus on aversive memory formation during maturity and investigate the effects of D1R suppression.

In the present study, we found the following characteristics of the effect of dopamine neurotransmission *via* D1R on contextual fear memory and auditory cued fear memory. First, D1R suppression had no effect on test results for either recent (Day 3) or remote (Day 30) memories in the auditory cued fear conditioning test. The fact that the expression level of c-Fos in the amygdala was not affected by D1R suppression may be one of the causes. Dopamine neurons affect auditory cued fear memory (Jo et al., 2018); therefore, neurotransmission *via* D2Rs instead of D1Rs may be involved. The amount of phosphorylated SNAP-25 was increased in the amygdala before footshock stimulation, but this may not be involved in the amygdala-mediated neurotransmission

pathway following electric footshock. This result suggests that suppression of dopaminergic neurotransmission *via* D1R had minor if any effect on auditory cued fear memory formation. In contrast, overexpression of D1Rs had enhanced effects on recent (Day 3) or remote (Day 30) memories in the auditory cued fear conditioning test. This suggests that D1R-mediated dopaminergic neurotransmission may have a positive effect on the auditory cued fear memory. The alteration of c-Fos expression showed no effect of D1R overexpression, but the amount of phosphorylated SNAP-25 at Ser187 was significantly reduced by stimulation compared to WT mice. The expression of phosphorylated SNAP-25 at Ser187 has been reported to increase with stress (Yamamori et al., 2014), which is contrary to the predicted results. Therefore, elucidating the cause of this effect is a matter for future investigation. Second, although there was no effect of D1R suppression on the test results in contextual fear conditioning for recent memories (Day 2), there was a decrease in performance due to D1R suppression for remote memories (Day 29). In contextual fear conditioning, which is considered to be a hippocampal-dependent form of memory, the performance in the test of recent memory did not decrease despite the no increase in hippocampal c-Fos expression as the immunoblotting results, which is an unexpected result and unlike previously reported findings (Saito et al., 2020). However, when the hippocampus was observed in more detail by immunohistochemistry, the expression of c-Fos increased in the CA1 and CA3 regions, though not as much as in WT mice. In particular, the increase of the c-Fos expression in the CA1 region was significantly higher than in PA footshock stimulation. These results may have affected contextual fear conditioning for recent memories. In addition, recent memory in contextual fear conditioning has been reported to involve not only the hippocampus but also the striatum (Ikegami et al., 2014), amygdala, and mPFC. As shown in **Figures 6**, **7**, c-Fos expression was increased in the BA and mPFC in D1R-mediated neurotransmission deficits. In this study these results may not have affected contextual fear conditioning for recent memories by D1Rs suppression, as similar results were obtained with FC and PA footshock stimulation. Third, the performance based on remote memory in contextual fear conditioning was clearly reduced in the D1R-mediated neurotransmission-deficient state when compared to performance in control mice and was reversible such that the performance became equivalent to that of control mice when the D1R-mediated neurotransmission was restored (**Figures 1**, **2**). This is consistent with the fact that the expression of c-Fos in the hippocampus and striatum, and its upregulation by footshock stimulation, is reversible, and that it is reduced in the D1R-mediated neurotransmission-deficient state and becomes comparable to that in control mice when D1R-mediated neurotransmission is restored (**Figures 1**, **2**, **4**, **5**, **8**). As reported by previous studies (Saito et al., 2020), our results suggest that D1R-mediated neurotransmission in the hippocampus and striatum is important for the formation of remote memories in contextual fear conditioning.

In addition, although it was predicted that the expression level of SNAP-25 phosphorylation would decrease, similar to that of c-Fos due to D1R suppression it was found that SNAP-25 phosphorylation was unexpectedly elevated following D1R suppression compared to that in WT mice. Increased stress induces SNAP-25 phosphorylation (Yamamori et al., 2014). A form of plasticity that induces long-term potentiation involved in learning and memory mechanisms results in the phosphorylation of SNAP-25 (Genoud et al., 1999). However, in this study, D1R-suppressed mice had increased SNAP-25 phosphorylation levels in all observed regions, even before electrical stimulation. Phosphorylated SNAP-25 is a multifunctional protein that plays a role in several processes, such as neurite extension, regulation of ion channel function, and regulation of neurotransmitter release (Osen-Sand et al., 1993; Pozzi et al., 2008). Therefore, this may be mediated by a mechanism independent of the function of stress-related neurons (Yamamori et al., 2014). Furthermore, transient overexpression of SNAP-25 phosphorylation at Ser187 is responsible for its negative effects on calcium dynamics and provides a negative feedback mechanism through the inhibition of voltage-gated calcium channels (Pozzi et al., 2008). Changes in SNAP-25 activity are associated with cognitive deficits found in several disorders such as attention deficit hyperactivity disorder and schizophrenia (Mill et al., 2004; Gosso et al., 2006). Knockdown of SNAP-25 does not affect auditory cued fear memory but reduces long-term memory performance in context fear conditioning (Hou et al., 2004). In contrast, overexpression of SNAP-25 in the dorsal hippocampus reduced the performance of context fear conditioning (McKee et al., 2010). Furthermore, there was a significant decrease in SNAP-25 after 12 h of passive avoidance training (O'Sullivan et al., 2007). Therefore, SNAP-25 expression during memory formation must be tightly regulated, and excessive deviations from normal expression levels are thought to affect cognitive function (McKee et al., 2010). However, these have not been investigated for SNAP-25 phosphorylation at Ser187, and they did not mention whether the amount of phosphorylation affects cognitive function. Considering the effect of SNAP-25 on long-term memory in the hippocampus, the decrease in the amount of phosphorylated SNAP-25 before a new stimulus after the elevated amount before the previous stimulus and the increase in phosphorylated SNAP-25 after a new stimulus are considered to be important for memory formation. In the present study, we found that D1R suppression increased the amount of SNAP-25 phosphorylated at Ser187 before footshock stimulation, and when D1R expression was restored, the amount of SNAP-25 phosphorylated at Ser187 decreased to the same level as that in controls. This may be a result of the prevented downregulation of phosphorylated SNAP-25 from the previous stimulation-induced increase in the amount of phosphorylated SNAP-25 during memory formation, leading to reduced long-term memory in the contextual fear condition. The lack of post-stimulation increase in phosphorylated SNAP-25 due to overexpression of phosphorylated SNAP-25 before stimulation may also contribute to memory decline. SNAP-25 phosphorylation at Ser187 occurs *via* protein kinase C (PKC) (Shimazaki et al., 1996; Nagy et al., 2002). Therefore, investigating the relationship between SNAP-25 phosphorylation at Ser187, D1R, and PKC in long-term memory is a subject for future research.

In our previous study, we reported that in the passive avoidance test where mice were conditioned with the same intensity of footshock as in this study, they showed impairments in both recent and remote memories (Saito et al., 2020). In addition, the D1R-mediated neurotransmission deficit had less effect on the suppression of Arc expression in the hippocampus and a greater effect on the suppression of Arc expression in the cerebral cortex. Unlike the contextual fear conditioning test, the passive avoidance test, which uses the same footshock, may have affected the recent memory because it depends not only on the hippocampus but also on multiple regions such as the striatum, amygdala, and cortices (Lorenzini et al., 1996; Pittenger et al., 2006; Ortiz et al., 2010; Yao et al., 2021). In the contextual and auditory cued fear memories examined in this study, mice were conditioned using three repetitions of the same intensity of footshock, and their recent memory was comparable to that of control mice. However, their remote memory of contextual fear conditioning was impaired. The mice performed as well as control mice in the recent memory task but were impaired in the remote memory task following fear conditioning. These results suggest that the effect of D1R-mediated neurotransmission on the formation of recent context fear memories may depend on the upregulation of c-Fos expression by footshock stimulation, especially in the hippocampal CA1 and CA3 regions, or on the upregulation of c-Fos expression by footshock stimulation in other regions such as the striatum, amygdala, and mPFC, or both. Furthermore, D1R-mediated neurotransmission appears to be involved from the formation to the fixation of remote memory.

DATA AVAILABILITY STATEMENT

The raw data supporting the conclusions of this article will be made available by the authors, without undue reservation.

ETHICS STATEMENT

The animal study was reviewed and approved by the Institutional Animal Care and Use Committee, Niigata University, Japan. Written informed consent was obtained from the owners for the participation of their animals in this study.

AUTHOR CONTRIBUTIONS

NS and TS designed the research and wrote the manuscript. NS and MI performed the research and analyzed the data. All authors contributed to the article and approved the submitted version.

FUNDING

This work was supported by a Grant-in-Aid for Scientific Research from the Japan Society for the Promotion of Science (grant number 18H02540, TS); a Grant-in-Aid for Scientific Research on Innovative Areas [Non-linear Neuro-oscillology: Toward Integrative Understanding of Human Nature from the Ministry of Education, Culture, Sports, Science and Technology, Japan (grant number 16H01606, 18H04937; TS)]; Japan Agency for Medical Research and Development (AMED) (grant number JP21dm0207091, TS) and the Co-operative Study Program (grant number 19–201, 20–214, 21–215; TS) of the National Institute for Physiological Sciences.

ACKNOWLEDGMENTS

We thank Ayane Sasaki and the members of Department of Comparative and Experimental Medicine in the Brain Research Institute at Niigata University for their assistance and discussion.

SUPPLEMENTARY MATERIAL

The Supplementary Material for this article can be found online at: https://www.frontiersin.org/articles/10.3389/fnbeh.2022.751053/full#supplementary-material

REFERENCES

Bromberg-Martin, E. S., Matsumoto, M., and Hikosaka, O. (2010). Dopamine in motivational control: rewarding, aversive, and alerting. *Neuron* 68, 815–834. doi: 10.1016/j.neuron.2010.11.022

Calabresi, P., Picconi, B., Tozzi, A., Ghiglieri, V., and Di Filippo, M. (2014). Direct and indirect pathways of basal ganglia: a critical reappraisal. *Nat. Neurosci.* 17, 1022–1030. doi: 10.1038/nn.3743

Chiken, S., Sato, A., Ohta, C., Kurokawa, M., Arai, S., Maeshima, J., et al. (2015). Dopamine D1 receptor-mediated transmission maintains information flow through the cortico-striato-entopeduncular direct pathway to release movements. *Cereb. Cortex* 25, 4885–4897. doi: 10.1093/cercor/bhv209

Danjo, T., Yoshimi, K., Funabiki, K., Yawata, S., and Nakanishi, S. (2014). Aversive behavior induced by optogenetic inactivation of ventral tegmental area dopamine neurons is mediated by dopamine D2 receptors in the nucleus accumbens. *Proc. Natl. Acad. Sci. U.S.A.* 111, 6455–6460. doi: 10.1073/pnas.1404323111

El-Ghundi, M., O'dowd, B. F., and George, S. R. (2001). Prolonged fear responses in mice lacking dopamine D1 receptor. *Brain Res.* 892, 86–93. doi: 10.1016/s0006-8993(00)03234-0

Fleischmann, A., Hvalby, O., Jensen, V., Strekalova, T., Zacher, C., Layer, L. E., et al. (2003). Impaired long-term memory and NR2A-type NMDA receptor-dependent synaptic plasticity in mice lacking c-Fos in the CNS. *J. Neurosci.* 23, 9116–9122. doi: 10.1523/JNEUROSCI.23-27-09116.2003

Genoud, S., Pralong, W., Riederer, B. M., Eder, L., Catsicas, S., and Muller, D. (1999). Activity-dependent phosphorylation of SNAP-25 in hippocampal organotypic cultures. *J. Neurochem.* 72, 1699–1706. doi: 10.1046/j.1471-4159.1999.721699.x

Gerfen, C. R., Engber, T. M., Mahan, L. C., Susel, Z., Chase, T. N., Monsma, F. J. Jr., et al. (1990). D1 and D2 dopamine receptor-regulated gene expression of striatonigral and striatopallidal neurons. *Science* 250, 1429–1432. doi: 10.1126/science.2147780

Goshen, I., Brodsky, M., Prakash, R., Wallace, J., Gradinaru, V., Ramakrishnan, C., et al. (2011). Dynamics of retrieval strategies for remote memories. *Cell* 147, 678–689. doi: 10.1016/j.cell.2011.09.033

Gosso, M. F., De Geus, E. J. C., Van Belzen, M. J., Polderman, T. J. C., Heutink, P., Boomsma, D. I., et al. (2006). The SNAP-25 gene is associated with cognitive ability: evidence from a family-based study in two independent Dutch cohorts. *Mol. Psychiatry* 11, 878–886. doi: 10.1038/sj.mp.4001868

Hou, Q., Gao, X., Zhang, X., Kong, L., Wang, X., Bian, W., et al. (2004). SNAP-25 in hippocampal CA1 region is involved in memory consolidation. *Eur. J. Neurosci.* 20, 1593–1603. doi: 10.1111/j.1460-9568.2004.03600.x

Iida, Y., Yamamori, S., Itakura, M., Miyaoka, H., and Takahashi, M. (2013). Protein phosphatase 2A dephosphorylates SNAP-25 through two distinct mechanisms in mouse brain synaptosomes. *Neurosci. Res.* 75, 184–189. doi: 10.1016/j.neures.2013.01.002

Ikegami, M., Uemura, T., Kishioka, A., Sakimura, K., and Mishina, M. (2014). Striatal dopamine D1 receptor is essential for contextual fear conditioning. *Sci. Rep.* 4:3976. doi: 10.1038/srep03976

Jo, Y. S., Heymann, G., and Zweifel, L. S. (2018). Dopamine neurons reflect the uncertainty in fear generalization. *Neuron* 100, 916.e3–925.e3. doi: 10.1016/j.neuron.2018.09.028

Kawahata, I., Sekimori, T., Wang, H., Wang, Y., Sasaoka, T., Bousset, L., et al. (2021). Dopamine D2 long receptors are critical for caveolae-mediated α-synuclein uptake in cultured dopaminergic neurons. *Biomedicines* 9:49. doi: 10.3390/biomedicines9010049

Kravitz, A. V., and Kreitzer, A. C. (2012). Striatal mechanisms underlying movement, reinforcement, and punishment. *Physiology* 27, 167–177. doi: 10.1152/physiol.00004.2012

Lorenzini, C. A., Baldi, E., Bucherelli, C., Sacchetti, B., and Tassoni, G. (1996). Role of dorsal hippocampus in acquisition, consolidation and retrieval of rat's passive avoidance response: a tetrodotoxin functional inactivation study. *Brain Res.* 730, 32–39. doi: 10.1016/0006-8993(96)00427-1

McKee, A. G., Loscher, J. S., O'Sullivan, N. C., Chadderton, N., Palfi, A., Batti, L., et al. (2010). AAV-mediated chronic over-expression of SNAP-25 in adult rat dorsal hippocampus impairs memory-associated synaptic plasticity. *J. Neurochem.* 112, 991–1004. doi: 10.1111/j.1471-4159.2009.06516.x

Milanovic, S., Radulovic, J., Laban, O., Stiedl, O., Henn, F., and Spiess, J. (1998). Production of the Fos protein after contextual fear conditioning of C57BL/6N mice. *Brain Res.* 784, 37–47. doi: 10.1016/s0006-8993(97)01266-3

Mill, J., Richards, S., Knight, J., Curran, S., Taylor, E., and Asherson, P. (2004). Haplotype analysis of SNAP-25 suggests a role in the aetiology of ADHD. *Mol. Psychiatry* 9, 801–810. doi: 10.1038/sj.mp.4001482

Miyashita, T., Kikuchi, E., Horiuchi, J., and Saitoe, M. (2018). Long-Term Memory Engram Cells Are Established by c-Fos/CREB transcriptional cycling. *Cell Rep.* 25, 2716.e3–2728.e3. doi: 10.1016/j.celrep.2018.11.022

Mizuno, K., Jeffries, A. R., Abel, T., and Giese, K. P. (2020). Long-lasting transcription in hippocampal area CA1 after contextual fear conditioning. *Neurobiol. Learn. Mem.* 172:107250. doi: 10.1016/j.nlm.2020.107250

Nagy, G., Matti, U., Nehring, R. B., Binz, T., Rettig, J., Neher, E., et al. (2002). Protein kinase C-dependent phosphorylation of synaptosome-associated protein of 25 kDa at Ser187potentiates vesicle recruitment. *J. Neurosci.* 22, 9278–9286. doi: 10.1523/JNEUROSCI.22-21-09278.2002

Okubo, T., Sato, A., Okamoto, H., Sato, T., and Sasaoka, T. (2018). Differential behavioral phenotypes of dopamine D1 receptor knockdown mice at the embryonic, postnatal, and adult stages. *Int. J. Dev. Neurosci.* 66, 1–8. doi: 10.1016/j.ijdevneu.2017.11.004

Ortiz, O., Delgado-Garcia, J. M., Espadas, I., Bahi, A., Trullas, R., Dreyer, J. L., et al. (2010). Associative learning and CA3-CA1 synaptic plasticity are impaired in D1R null, Drd1a-/- mice and in hippocampal siRNA silenced Drd1a mice. *J. Neurosci.* 30, 12288–12300. doi: 10.1523/JNEUROSCI.2655-10.2010

Osen-Sand, A., Catsicas, M., Staple, J. K., Jones, K. A., Ayala, G., Knowles, J., et al. (1993). Inhibition of axonal growth by SNAP-25 antisense oligonucleotides in vitro and in vivo. *Nature* 364, 445–448. doi: 10.1038/364445a0

O'Sullivan, N. C., Mcgettigan, P. A., Sheridan, G. K., Pickering, M., Conboy, L., O'connor, J. J., et al. (2007). Temporal change in gene expression in the rat dentate gyrus following passive avoidance learning. *J. Neurochem.* 101, 1085–1098. doi: 10.1111/j.1471-4159.2006.04418.x

Pare, D., Quirk, G. J., and Ledoux, J. E. (2004). New vistas on amygdala networks in conditioned fear. *J. Neurophysiol.* 92, 1–9. doi: 10.1152/jn.00153.2004

Phillips, R. G., and LeDoux, J. E. (1992). Differential contribution of amygdala and hippocampus to cued and contextual fear conditioning. *Behav. Neurosci.* 106, 274–285. doi: 10.1037//0735-7044.106.2.274

Pittenger, C., Fasano, S., Mazzocchi-Jones, D., Dunnett, S. B., Kandel, E. R., and Brambilla, R. (2006). Impaired bidirectional synaptic plasticity and procedural memory formation in striatum-specific cAMP response element-binding protein-deficient mice. *J. Neurosci.* 26, 2808–2813. doi: 10.1523/JNEUROSCI.5406-05.2006

Pozzi, D., Condliffe, S., Bozzi, Y., Chikhladze, M., Grumelli, C., Proux-Gillardeaux, V., et al. (2008). Activity-dependent phosphorylation of Ser187 is required for SNAP-25-negative modulation of neuronal voltage-gated calcium channels. *Proc. Natl. Acad. Sci. U.S.A.* 105, 323–328. doi: 10.1073/pnas.0706211105

Saito, N., Tainaka, K., Macpherson, T., Hikida, T., Yamaguchi, S., and Sasaoka, T. (2020). Neurotransmission through dopamine D1 receptors is required for aversive memory formation and Arc activation in the cerebral cortex. *Neurosci. Res.* 156, 58–65. doi: 10.1016/j.neures.2020.04.006

Sarinana, J., Kitamura, T., Kunzler, P., Sultzman, L., and Tonegawa, S. (2014). Differential roles of the dopamine 1-class receptors, D1R and D5R, in hippocampal dependent memory. *Proc. Natl. Acad. Sci. U.S.A.* 111, 8245–8250. doi: 10.1073/pnas.1407395111

Schultz, W. (2019). Recent advances in understanding the role of phasic dopamine activity. *F1000Research* 8:F1000FacultyRev-1680. doi: 10.12688/f1000research.19793.1

Shimazaki, Y., Nishiki, T., Omori, A., Sekiguchi, M., Kamata, Y., Kozaki, S., et al. (1996). Phosphorylation of 25-kDa synaptosome-associated protein. Possible involvement in protein kinase C-mediated regulation of neurotransmitter release. *J. Biol. Chem.* 271, 14548–14553. doi: 10.1074/jbc.271.24.14548

Shin, J. H., Kim, D., and Jung, M. W. (2018). Differential coding of reward and movement information in the dorsomedial striatal direct and indirect pathways. *Nat. Commun.* 9:404. doi: 10.1038/s41467-017-02817-1

Soares-Cunha, C., Coimbra, B., Sousa, N., and Rodrigues, A. J. (2016b). Reappraising striatal D1- and D2-neurons in reward and aversion. *Neurosci. Biobehav. Rev.* 68, 370–386. doi: 10.1016/j.neubiorev.2016.05.021

Soares-Cunha, C., Coimbra, B., David-Pereira, A., Borges, S., Pinto, L., Costa, P., et al. (2016a). Activation of D2 dopamine receptor-expressing neurons in the nucleus accumbens increases motivation. *Nat. Commun.* 7:11829. doi: 10.1038/ncomms11829

Stiedl, O., Radulovic, J., Lohmann, R., Birkenfeld, K., Palve, M., Kammermeier, J., et al. (1999). Strain and substrain differences in context- and tone-dependent fear conditioning of inbred mice. *Behav. Brain Res.* 104, 1–12. doi: 10.1016/s0166-4328(99)00047-9

Stubbendorff, C., Hale, E., Cassaday, H. J., Bast, T., and Stevenson, C. W. (2019). Dopamine D1-like receptors in the dorsomedial prefrontal cortex regulate contextual fear conditioning. *Psychopharmacology* 236, 1771–1782. doi: 10.1007/s00213-018-5162-7

Stubbendorff, C., and Stevenson, C. W. (2020). Dopamine regulation of contextual fear and associated neural circuit function. *Eur. J. Neurosci.* 54, 6933–6947. doi: 10.1111/ejn.14772

Tischmeyer, W., and Grimm, R. (1999). Activation of immediate early genes and memory formation. *Cell. Mol. Life Sci.* 55, 564–574. doi: 10.1007/s000180050315

Volman, S. F., Lammel, S., Margolis, E. B., Kim, Y., Richard, J. M., Roitman, M. F., et al. (2013). New insights into the specificity and plasticity of reward and aversion encoding in the mesolimbic system. *J. Neurosci.* 33, 17569–17576. doi: 10.1523/JNEUROSCI.3250-13.2013

Yamaguchi, T., Goto, A., Nakahara, I., Yawata, S., Hikida, T., Matsuda, M., et al. (2015). Role of PKA signaling in D2 receptor-expressing neurons in the core of the nucleus accumbens in aversive learning. *Proc. Natl. Acad. Sci. U.S.A.* 112, 11383–11388. doi: 10.1073/pnas.1514731112

Yamamori, S., Itakura, M., Sugaya, D., Katsumata, O., Sakagami, H., and Takahashi, M. (2011). Differential expression of SNAP-25 family proteins in the mouse brain. *J. Comp. Neurol.* 519, 916–932.

Yamamori, S., Sugaya, D., Iida, Y., Kokubo, H., Itakura, M., Suzuki, E., et al. (2014). Stress-induced phosphorylation of SNAP-25. *Neurosci. Lett.* 561, 182–187. doi: 10.1016/j.neulet.2013.12.044

Yao, R., Nishii, K., Aizu, N., Kito, T., Sakai, K., and Yamada, K. (2021). Maintenance of the amygdala-hippocampal circuit function with safe and feasible shaking exercise therapy in SAMP-10 mice. *Dement. Geriatr. Cogn. Dis. Extra* 11, 114–121. doi: 10.1159/000515957

Conflict of Interest: The authors declare that the research was conducted in the absence of any commercial or financial relationships that could be construed as a potential conflict of interest.

Publisher's Note: All claims expressed in this article are solely those of the authors and do not necessarily represent those of their affiliated organizations, or those of the publisher, the editors and the reviewers. Any product that may be evaluated in this article, or claim that may be made by its manufacturer, is not guaranteed or endorsed by the publisher.

frontiers | Frontiers in Behavioral Neuroscience

ORIGINAL RESEARCH
published: 13 May 2022
doi: 10.3389/fnbeh.2022.750832

Shape and Rule Information Is Reflected in Different Local Field Potential Frequencies and Different Areas of the Primate Lateral Prefrontal Cortex

Kazuhiro Sakamoto[1,2], Norihiko Kawaguchi[2] and Hajime Mushiake[2]*

[1] *Department of Neuroscience, Faculty of Medicine, Tohoku Medical and Pharmaceutical University, Sendai, Japan,*
[2] *Department of Physiology, Tohoku University School of Medicine, Sendai, Japan*

The lateral prefrontal cortex (LFPC) plays a crucial role in executive function by adaptively storing behavior-relevant information as working memory. Neural mechanisms associated with local field potentials (LFPs) may underlie the adaptive properties of the LFPC. Here, we analyzed how LFPs recorded from the monkey LFPC are modulated by the crucial factors of a shape manipulation task. In this task, the test shape is transformed by manipulating a lever to match the size and orientation of the sample shape. The subject is required to temporarily memorize the rules such as the arm-movement-manipulation relationship and the sample shape to generate the sequential behavior of operations. In the present study, we focused on task variables about shape and rules, and examined among which aspects distinguish the ventral and dorsal sides of the LFPC. We found that the transformed shape in the sample period strongly affected the theta and delta waves in the delay period on the ventral side, while the arm-manipulation assignment influenced the gamma components on the dorsal side. These findings suggest that area- and frequency-selective LFP modulations are involved in dynamically recruiting different behavior-relevant information in the LFPC.

Keywords: monkey, lateral prefrontal cortex, shape manipulation task, visual object, behavioral rule, ventral-lateral distinction, theta-delta wave, gamma wave

OPEN ACCESS

Edited by:
Shozo Tobimatsu,
Kyushu University, Japan

Reviewed by:
Heh-In Im,
Korea Institute of Science and Technology, South Korea
Liya Ma,
Radboud University Nijmegen, Netherlands

****Correspondence:***
Kazuhiro Sakamoto
sakamoto@tohoku-mpu.ac.jp

Specialty section:
This article was submitted to Pathological Conditions, a section of the journal Frontiers in Behavioral Neuroscience

Received: *31 July 2021*
Accepted: *25 April 2022*
Published: *13 May 2022*

Citation:
Sakamoto K, Kawaguchi N and Mushiake H (2022) Shape and Rule Information Is Reflected in Different Local Field Potential Frequencies and Different Areas of the Primate Lateral Prefrontal Cortex. Front. Behav. Neurosci. 16:750832. doi: 10.3389/fnbeh.2022.750832

INTRODUCTION

The lateral prefrontal cortex (LFPC) plays a crucial role in executive function, i.e., problem solving and action planning in various environments (Duncan, 2001; Saito et al., 2005; Mushiake et al., 2006; Tanji et al., 2007; Sakamoto et al., 2008, 2013, 2020b; Tanji and Hoshi, 2008; Katori et al., 2011; Passingham and Wise, 2012; Fuster, 2015). The LFPC exists at a nodal point of the hierarchical structure from perception/recognition to behavior/movement (Felleman and Van Essen, 1991), where information from percepts about the external world to internal behavioral norms is integrated (e.g., Petrides et al., 2012) and temporarily stored as working memory (Fuster and Alexander, 1971; Fuster, 1973; Kojima and Goldman-Rakic, 1982, 1984; Funahashi et al., 1989; Wilson et al., 1993; Miller et al., 1996; Rao et al., 1997; Rainer et al., 1998). The coding of information in the LFPC is expected to be flexible depending on the environmental demand (Duncan, 2001), although the neural mechanism underlying flexible recruitment of behaviorally relevant information has not yet been fully elucidated.

Local field potentials (LFPs) are potentials with a relatively low frequency component that are recorded extracellularly in the brain. In recent years, they have received much attention for their roles in flexible and context-dependent information transmission in the brain (Akam and Kullmann, 2014). Such flexibility is also thought to be associated with adaptive information processing in the LFPC. Indeed, specific frequency changes dependent on task event and task content have been reported in the LFPC of macaque monkeys (Buschman et al., 2012; Sakamoto et al., 2015, 2020a; Lundqvist et al., 2016; Wimmer et al., 2016; Ma et al., 2018; Wutz et al., 2018; Dezfouli et al., 2021). All of these suggest that different frequency components make different contributions to different aspects of LFPC function.

The LFPC is anatomically distinguished into ventral and dorsal sides. The ventral side has connections with the orbitofrontal cortex and the temporal lobe known to be involved in object recognition, while the dorsal side has mutual interactions with the parietal lobe involved in spatial perception and the medial frontal lobe involved in internal states (Petrides and Pandya, 1994; Averbeck and Seo, 2008; Yetarian et al., 2012). Consistent with these anatomical backgrounds, neuronal activities reflecting visual objects themselves or the information they contain have been reported from the ventral LFPC of monkeys (Wilson et al., 1993; Ninokura et al., 2004), while the dorsal region is involved in the retrieval of task-related information and its manipulation for action planning and execution (Hoshi and Tanji, 2004; Ninokura et al., 2004). Although there have been reports on LFPs in the LFPC, there are only a few studies of LFPs that distinguished between the ventral and dorsal sides (Wutz et al., 2018; Sakamoto et al., 2020a). It remains to be investigated how the functional differentiation of the LFPC corresponds to the dynamic properties of LFPs.

Here, we analyzed how LFPs recorded from the monkey LFPC are modulated by the important factors of a shape manipulation task. In this task, the test shape is transformed by manipulating a lever to match the size and orientation of the sample shape (**Figure 1A**; Sakamoto et al., 2015, 2020a). The subject is required to temporarily memorize the rules, such as the arm-movement-manipulation relationship and the sample shape, to generate the sequential behavior of the operations. In a previous study that analyzed the overall time-frequency trend, we found that the ventral and dorsal sides could be distinguished based on theta and gamma wave features (Sakamoto et al., 2020a). Hence, in the present study, we focused on these frequency ranges and memories of shape and rules, and examined their changes in different time periods of the task to functionally distinguish the ventral and dorsal sides.

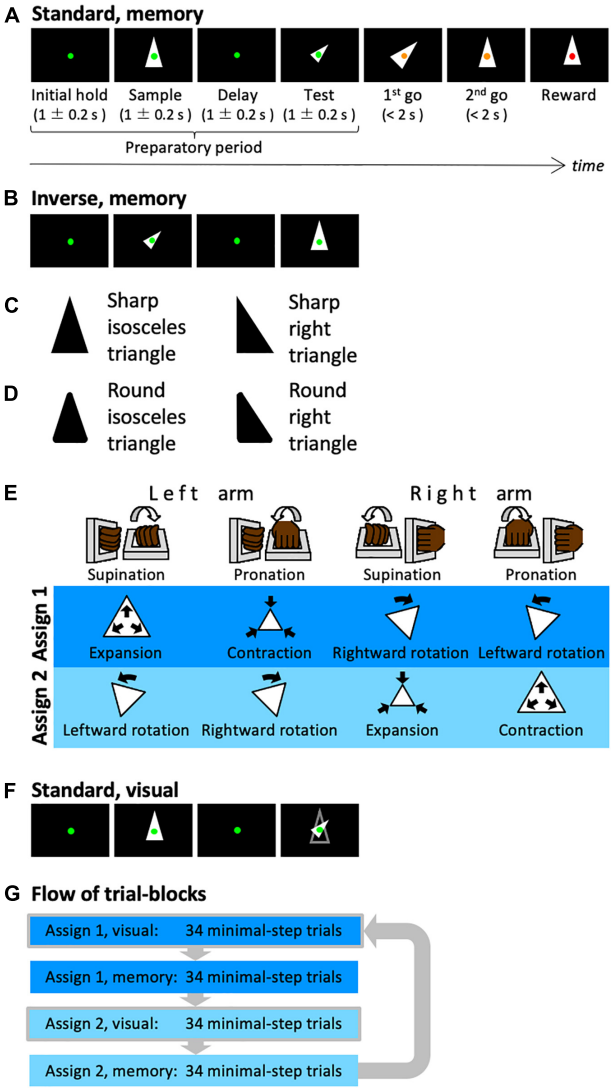

FIGURE 1 | Shape manipulation task. **(A)** The time-course of one trial. In this case, a shape with standard size and upward orientation was presented in the sample period, while the transformed shape was presented in the test period (standard version). **(B)** In this case, the transformed shape was presented in the sample period. **(C)** The types of the presented shapes. An isosceles or right triangle was used. **(D)** The local features of the presented shapes. Sharp or round corners were used. **(E)** Assignments between arm movements and manipulation of the shape. **(F)** In this case, the contour of the sample shape was presented in the test period (visual). The subject can recognize the transformation between the sample cue and the test cue visually, i.e., without memory. **(G)** Illustration of the composition of the trial blocks.

MATERIALS AND METHODS

Subjects

Two male Japanese monkeys (*Macaca fuscata*) weighing 9.0 kg (Monkey 1) and 8.5 kg (Monkey 2) were used in the present experiment. These monkeys had previously participated in published studies (Sakamoto et al., 2015, 2020a). All experimental protocols were approved by the Animal Care and Use Committee of Tohoku University (Permit # 20MeA-2), and all animal protocols conformed with the National Institutes of Health Guidelines for the Care and Use of Laboratory Animals, as well as with the recommendations of the Weatherall Report.

Behavioral Task

The monkeys were trained to perform a shape manipulation task (**Figure 1A**). The goal was to fit the test shape to the sample

shape during a trial. First, a green fixation spot appeared on the screen (initial hold period) before a sample shape was displayed for 1 ± 0.2 s (sample period). Then, after a 1 ± 0.2 s interval (delay period), a test shape that was homothetic to the sample shape but transformed (i.e., expanded/contracted and rotated) was displayed for 1 ± 0.2 s (test period). Subsequently, the color of the fixation point was changed to yellow; this served as a go signal to initiate the first-step movement (first go). Then the monkey was required to execute a movement within the time window of 2 s and wait until the second go signal (second go) appeared. When the monkey completed one movement, the fixation point returned to green and a change in color to yellow was used as a go signal again. At each go signal, the monkeys were allowed to make a single one-arm movement and were also permitted to perform any number of steps if a movement was executed within the time window. When the test shape was successfully transformed to fit the sample shape, the fixation point turned red and the monkeys were rewarded with a drop of an isotonic drink. Each trial was set to require at least two steps to be rewarded.

There are two types of trials: standard trials, in which a shape of standard size and orientation is presented during the sample period, and inverse trials, in which the standard shape is presented during the test period (**Figure 1B**). By presenting the standard and inverse trials in the same proportion randomly, the animals were forced to plan their sequential behavior by comparing the shapes of the sample and test periods. Thereby, the animals had to remember the shape of the sample period. In addition to these two types, trials in which the same arm was used for the first and second steps were conducted (same arm twice trials). For instance, two rotation operations using the same arm were required in the trial where the shapes in the sample and test phases were oriented 90 degrees to one another. By mixing the same arm twice trials from time to time, it is possible to avoid the situation in which the arm to be used for the second step was automatically decided once the first step was decided.

In each trial, a single shape was randomly selected from a set of shapes. We used two types of shapes, isosceles and right triangles (**Figure 1C**), and two types of local features, sharp and rounded corners (**Figure 1D**); i.e., four shape-specific attributes.

The shape manipulations were linked to the movements of two manipulanda installed on the chair and operated with the right or left wrist. To dissociate movements of the arms from manipulative operations of the test shape, the monkeys were trained to perform the task with two different arm-manipulation assignments (**Figure 1E**). For the first cursor assignment (assign 1), left-arm supination and pronation controlled expansion (double the area) and contraction (half the area), respectively, of the test shape and right-arm supination and pronation controlled rightward (–45°) and leftward rotation (45°), respectively, of the test shape. For the second cursor assignment (assign 2), left-arm supination, left-arm pronation, right-arm supination, and right-arm pronation were assigned to leftward rotation, rightward rotation, contraction, and expansion, respectively.

In this task, we used a correction method. The task conditions of incorrect or non-minimal step trials were repeated until the correct answer was obtained in the minimal step trial (two steps). The arm-movement assignment described above was switched for each of the 68 minimal step trials. In the first half of each 68-trial block (34 trials), the contour of the sample cue was displayed during the test cue period (visually guided task: **Figure 1F**), whereas the contour was not displayed in the latter half (memory-guided task, 34 trials). Each block of 34 trials contained 16 standard and inverse trials, and 2 same arm twice trials. Within a block, each condition was presented pseudo-randomly. These trial blocks were executed in the order shown in **Figure 1G**.

Electrophysiological Recordings

The surgical procedure used in the present study has previously been described (Sakamoto et al., 2008, 2015). Following surgery, cortical sulci were identified using a magnetic resonance imaging scanner (OPART 3D-System; Toshiba, Tokyo, Japan) and by mapping single-unit activities that were recorded using conventional metal electrodes. The recording areas in this study is involved in are in the left hemisphere as indicated in **Figure 2A**.

All electrophysiological recordings were performed using linear array multi-contact electrodes (U-Probe; Plexon Inc., Dallas, TX, United States) that contained 15 recording contacts (impedance: 0.3–1.3 MΩ at 1 kHz) with an inter-contact spacing of 150 or 200 μm. The electrode was penetrated with a fixed angle almost perpendicular to the cortical surface except for the regions near the principal sulcus. A guide needle was used to introduce the electrode and once the electrode reached the dura mater, advancement of the guide needle was stopped so the electrode could be inserted into the cortex; each electrode was precisely positioned. The electrodes were lowered until the multi-unit activity that was initially encountered through the bottommost contact (ch. 15) was detected through the top contact (ch. 1). Signals from the electrode were collected using a data acquisition system (Neuralynx, Bozeman, MT, United States) and LFPs and spikes were obtained by band-pass filtering the raw signal from 0.1 to 475 Hz and from 600 Hz to 6 kHz, respectively.

In the following analyses, LFPs recorded from the bottommost contact were used because of the small variability of the spectral patterns compared to those from the upper layers.

Data Analysis

The data from all trials were included in the present analyses. LFPs during the 4 s of the preparatory period were transformed into small time-frequency regions of 0.05-octave and 1/1,240 s using Morlet wavelets with the center frequencies of the kernels ranging from 1 to 256 Hz. The percentages of energy for each transform coefficient were obtained at each moment and averaged across trials to obtain a time-frequency LFP spectrogram for each recording site. In addition, an overall LFP spectrum was obtained by averaging across time and subtracting from the spectrum at each time of the LFP spectrogram. The values were normalized to the standard deviation (SD) at each frequency to yield a normalized LFP spectrogram (**Figure 2B**).

The normalized LFP spectrum was coarse-grained into 100 ms to 0.35 octave time-frequency domains (**Figure 2C**) and divided into six frequency ranges: delta (1–3 Hz), theta (3–7 Hz), alpha (7–14 Hz), beta (14–30 Hz), lower gamma (30–60 Hz), and higher gamma (60–120 Hz). The time intervals for analysis were 1 s

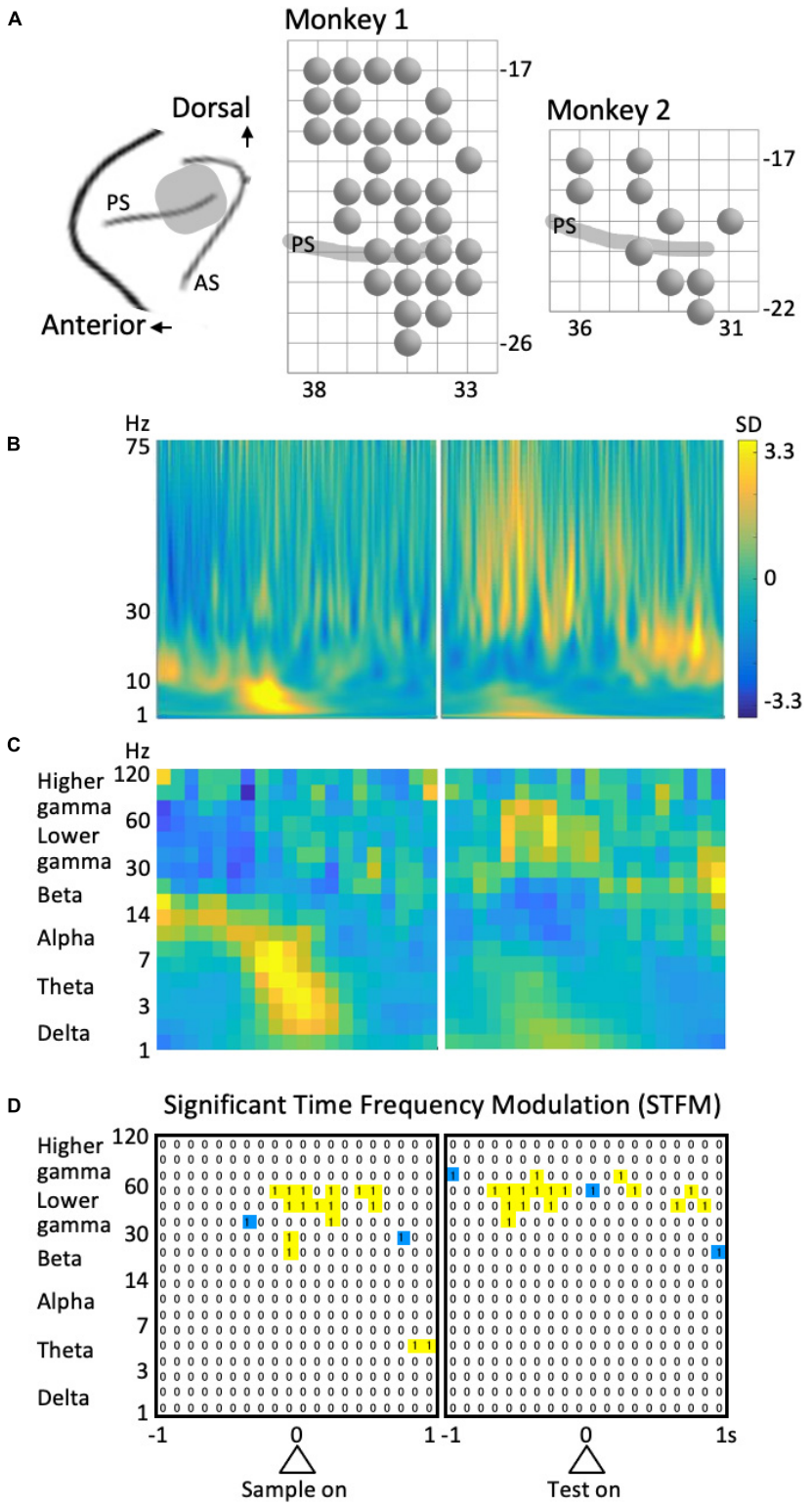

FIGURE 2 | Recording and analysis of LFPs. **(A)** Recording sites. PS, principal sulcus; AS, arcuate sulcus. A circle represents a recording site. The grid interval is 1 mm. **(B)** Example of the time-frequency spectrum averaged across all trials. Same site as in **Figure 3** (left column). **(C)** The coarse-grained time-frequency spectrum obtained from **(B)**. **(D)** An example of the results of stepwise regression analysis for the data shown in **Figure 4** (left column). "1" Represent the time-frequency region that provided a significant model including the predictor variable of interest. To avoid multi-comparison problems, isolated regions (blue) were excluded.

before and after the sample stimulus onset and 1 s before and after the test stimulus onset; i.e., 4 s of the preparatory period (see **Figure 1A**). Therefore, the data from each frequency included 3×40 time-frequency domains (**Figure 2C**).

We executed a stepwise linear-regression analysis of the LFP data for each explanatory factor or predictor variable. The analysis was done for each time-frequency domain mentioned above. We used the "stepwiselm" function of MATLAB, and started from "constant," using the "see" criterion. That is, the criterion to add or remove predictor variables was p-value for an F-test of the change in the sum of squared error by adding or removing the term. We used these options because these provided the strictest results. The p-values used were the defaults: 0.05 for addition and 0.10 for removal. We excluded interaction terms from the analysis for simplicity.

The predictor variables in the stepwise linear regression analysis included the following. For transformed shapes, there were four variables: size of the shape in the sample period (Transformed Shape in Sample Scale), rotation of the shape in the sample period (Transformed Shape in Sample Rotation), size of the shape in the test period (Transformed Shape in Test Scale), and rotation of the shape in the test period (Transformed Shape in Test Rotation). As for shape-specific attributes, we considered the type of shape (i.e., Shape-Specific Attributes Isosceles or Right Angle) (**Figure 1C**) as well as the type of feature (i.e., Shape-Specific Attributes Round or Sharp) (**Figure 1D**). The two variables related to the rules of the task were the assignment between the arm-movements and the operation of shape manipulation (Assignment: **Figure 1E**), and the distinction between memory-guided and visually guided (Visual or Memory: **Figure 1F**). We focus our discussion on these shape- and rule-related variables. The other three variables of animal performance are the distinction between correct and incorrect trials (Correct or Error), the distinction between minimal-step and non-minimal step correct trials (Minimal Steps), and whether the previous trial was an error/non-minimal step trial, i.e., whether the same condition as in the previous trial is repeated (Repeated Trial). For the task structure, there are two variables: whether the standard shape is presented in the sample or test phase (Normal or Inverse, **Figure 2F**), and whether the same arm is required to be used in both the first and second steps (Same Arm Twice Trial). In addition, we used four variables for each of the operations performed on the first and second steps (Manipulation in Step 1 Expansion or Contraction, Manipulation in Step 1 Leftward or Rightward, Manipulation in Step 2 Expansion or Contraction, and Manipulation in Step 2 Leftward or Rightward). Similarly, there were a total of four variables for arm movements in the two steps, including which arm was used and whether the movement was supination or pronation (Arm Movement in Step 1 Left Arm or Right Arm, Arm Movement in Step 1 Pronation or Supination, Arm Movement in Step 2 Left Arm or Right Arm, and Arm Movement in Step 2 Pronation or Supination). Variables were also used for the presence or absence of action at each step (Action in Step 1, and Action in Step 2). In total, 23 factors were used in the stepwise linear regression analysis. **Table 1** lists the correlations among these predictor variables.

To detect the time-frequency domains of significant time-frequency modulation (STFM), we first extracted the domains that provided a model with a significance level of $p = 0.0001$ in the above stepwise regression analysis. However, to avoid multiple comparisons given the number of cases is $6 \times 3 \times 40 \times 23 = 16{,}560$, we did not consider isolated time-frequency regions (blue regions in **Figure 2D**). Namely, time-frequency domains that provided significant models including the identical factor of interest in consecutive time and frequency regions (yellow regions in **Figure 2D**) were considered a domain of STFM. The significance of the time-frequency region taken in this way was $0.0001 \times (1 - 0.9999^8) \times 16{,}560 = 0.0013$, indicating that a predictor variable that is significant in the time-frequency domain is sufficiently reliable.

RESULTS

The two monkeys exhibited high performance in the shape manipulation task (Sakamoto et al., 2012). We analyzed their behavioral performance during the shape manipulation task with minimal steps. In particular, we examined the reaction times (RTs) during 5 days of the training session. On average, Monkeys 1 and 2 performed 2,173 and 1,756 trials per day, respectively. Their success rates were 90% and 99%, and their minimum-step (two-step) success rates were 89% and 89%, respectively. The mean RTs for the first and second steps of the successful minimum-step trials were as follows: Monkey 1: 459 ± 257 ms (1st step), 510 ± 268 ms (2nd step); Monkey 2: 776 ± 264 ms (1st step), 684 ± 213 ms (2nd step).

Local field potentials were recorded from the dorsal and ventral sides of the principal sulcus of the left hemisphere of the LFPC during a shape manipulation task (Monkey 1, 32 locations; Monkey 2, 10 locations; **Figure 2A**), and their time-frequency modulations were analyzed by stepwise regression analysis. Although all task factors were used in the analysis as predictor variables, we focused on the two categories of factors related to presented shape and behavioral rules. In addition, because in a previous study (Sakamoto et al., 2020a) task-phase-dependent modulations of the theta and lower gamma components were well distinguished between the dorsal and ventral sides, we mainly discuss these frequency components below.

Representative examples from the ventral LFPC of the two monkeys are shown in **Figure 3**. In these examples, the predictor variable relevant to action planning, Transformed Shape in Sample (i.e., whether the sample shape is large or small in the sample period) appears to be reflected in the theta modulation during the delay period. **Figures 3A,B** show the differential time-frequency spectra between the cases in which the sample shape was large and small. From these, a large difference in low-frequency components during the delay period are observed in common. To confirm this, the raw LFP waveforms (**Supplementary Figure 1**, top) were filtered in the frequency range of interest to obtain their upper envelopes (**Supplementary Figure 1**, middle and bottom). In the averaged upper envelopes of these examples, persistent significant differences were observed in the theta

TABLE 1 | Correlations between predictor variables during the recording session of the example shown in **Figure 3** left column.

	A	VM	CE	MS	RT	SSAIRA	SSARS	NI	SATT	TSSS	TSSR	TSTS	TSTR	MS1EC	MS1LR	MS2EC	MS2LR	AMS1LR	AMS1PS	AMS2LR	AMS2PS	AS1	AS2
Assignment (A)	1.000	0.056	0.063	0.031	0.003	0.022	–0.034	–0.016	–0.071	0.064	–0.031	0.026	–0.122	–0.430	0.126	0.338	–0.018	–0.055	–0.102	0.047	0.048	–	0.113
Visual or Memory (VM)		1.000	–0.093	–0.077	0.157	–0.028	–0.033	–0.023	–0.126	0.067	0.064	–0.084	–0.107	0.041	–0.090	0.028	0.217	0.046	–0.070	–0.165	0.062	–	–0.100
Correct or Error (CE)			1.000	0.511	0.088	0.010	0.103	–0.027	–0.019	0.101	–0.114	–0.013	0.005	0.075	0.007	0.050	–0.021	–0.141	0.027	0.222	–0.010	–	0.491
Minimal Steps (MS)				1.000	0.172	–0.092	0.033	–0.154	–0.338	0.108	–0.050	0.064	–0.122	0.017	0.042	0.112	0.028	–0.008	0.049	0.241	–0.151	–	0.251
Repeated Trial (RT)					1.000	0.033	–0.072	0.104	0.155	–0.073	0.144	–0.025	0.037	0.025	0.036	–0.042	0.048	0.138	–0.210	–0.120	0.140	–	0.043
Shape-Specific Attribute Isosceles or Right Angle (SSAIRA)						1.000	0.002	0.089	0.122	–0.045	–0.078	–0.086	0.055	0.063	–0.148	–0.039	0.062	0.030	0.057	–0.035	0.064	–	0.005
Shape-Specific Attribute Round or Sharp (SSARS)							1.000	0.040	0.071	0.014	–0.048	–0.107	0.009	0.140	–0.019	–0.024	0.018	0.007	–0.024	0.047	0.125	–	0.105
Normal or Inverse (NI)								1.000	0.293	–0.041	–0.014	–0.017	0.086	–0.014	–0.092	0.032	–0.039	0.077	–0.013	–0.095	0.077	–	0.014
Same Arm Twice Trial (SATT)									1.000	–0.010	–0.177	–0.115	0.180	0.101	–0.111	–0.033	–0.077	–0.055	–0.025	–0.020	0.205	–	0.036
Transformed Shape in Sample Scale (TSSS)										1.000	–0.126	0.008	–0.031	0.309	–0.114	0.367	0.159	–0.417	–0.150	0.329	–0.047	–	0.068
Transformed Shape in Sample Rotation (TSSR)											1.000	0.031	–0.010	0.010	0.364	–0.106	0.334	–0.002	–0.061	–0.047	0.061	–	–0.074
Transformed Shape in Test Scale (TSTS)												1.000	0.012	–0.433	0.089	–0.322	–0.188	0.423	–0.021	–0.346	–0.127	–	0.069
Transformed Shape in Test Rotation (TSTR)													1.000	–0.015	–0.397	–0.013	–0.387	0.060	0.068	–0.072	–0.051	–	–0.072
Manipulation in Step 1 Expansion or Contraction (MS1EC)														1.000	–0.371	–0.199	0.388	–0.331	0.196	0.329	0.314	–	–0.055
Manipulation in Step 1 Leftward or Rightward (MS1LR)															1.000	0.071	–0.246	–0.070	–0.077	0.040	–0.053	–	–0.058
Manipulation in Step 2 Expansion or Contraction (MS2EC)																1.000	–0.273	–0.377	–0.253	0.356	–0.211	–	0.058
Manipulation in Step 2 Leftward or Rightward (MS2LR)																	1.000	–0.078	0.013	0.000	0.160	–	0.057
Arm Movement in Step 1 Left Arm or Right Arm (AMS1LR)																		1.000	–0.038	–0.807	–0.226	–	–0.014
Arm Movement in Step 1 Pronation or Supination (AMS1PS)																			1.000	0.076	0.160	–	0.043
Arm Movement in Step 2 Left Arm or Right Arm (AMS2LR)																				1.000	0.148	–	0.109
Arm Movement in Step 2 Pronation or Supination (AMS2PS)																					1.000	–	0.081
Action in Step 1 (AS1)																						–	–
Action in Step 2 (AS2)																							1.000

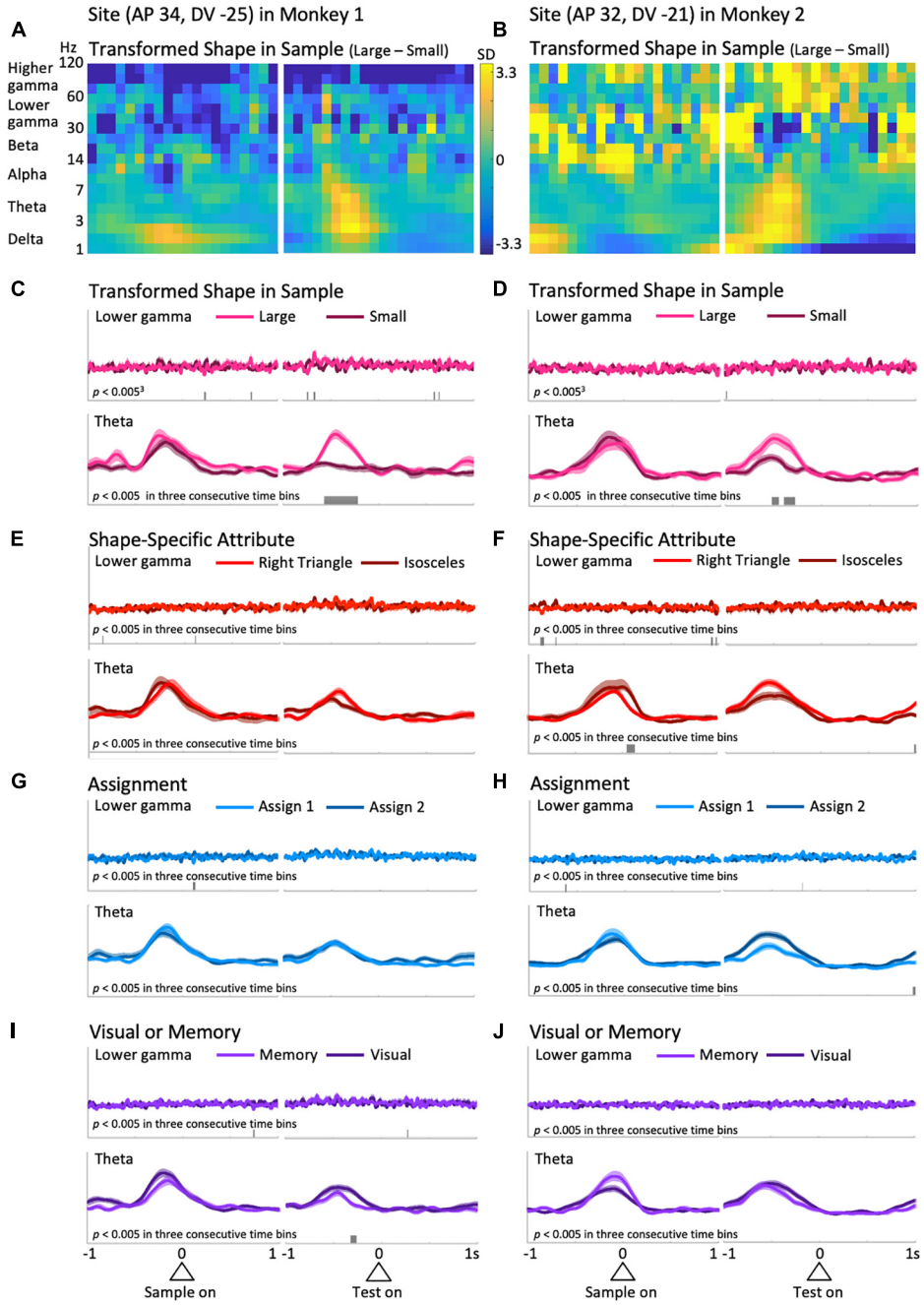

FIGURE 3 | Typical examples from the ventral side of the LFPC in the two monkeys. The left column was obtained from the site with coordinates (AP 34, DV –25); i.e., 34 and –25 mm in the anterior-posterior and dorsal-ventral axes, respectively, while the right column is from (AP 32, DV –21). **(A,B)** The difference in the time-frequency spectra between large and small sizes of the shape presented in the sample period. **(C,D)** The mean upper envelopes of lower-gamma (top) and theta (bottom) waves sorted based on the sample-shape scale factor. **(E–J)** The mean upper envelopes sorted based on variables of shape-specific attributes **(E,F)**, assignment **(G,H)**, and visual or memory **(I,J)**. The scales for the mean upper envelopes were identical in each column. Small bars in each mean upper envelope plot indicate the time regions showing significant differences ($p < 0.005$) in three consecutive time bins.

range during the delay period when the sample shape was large ($p = 1.3 \times 10^{-7}$ at the largest difference, *t*-test: **Figure 3C**, bottom; $p = 0.0020$ at the largest difference, *t*-test: **Figure 3D**, bottom). Similar increases during the delay period were found for the delta range as well, but were not significantly greater in these cases ($p = 0.048$ at the largest difference, *t*-test:

Supplementary Figure 2C, bottom; $p = 0.026$ at the largest difference, *t*-test: **Supplementary Figure 2D**, bottom). Large and clear differences in theta waves during the delay period shown above were not recognized in cases of rule-related predictor variables (Assignment, **Figures 3G,H**, bottom; Visual or Memory, **Figures 3I,J**, bottom) or the other shape-related variable, Shape Specific Attribute, which was not relevant to action planning (**Figures 3E,F**, bottom). In terms of the delta range, consistent modulations between the two examples were not seen, although some predictor variables exhibited significant modulations (**Supplementary Figures 2E–J**, bottom). This observation implies that theta and delta waves do not always show consistent modulations. Similarly, these two examples did not have common predictive variables causing many significant modulations in the lower and higher gamma ranges, although the numbers slightly differ depending on the variables (**Figures 3C–J** top, **Supplementary Figures 2C–J** top).

Typical examples of the dorsal side provide a different impression than the ones above. Differences in higher frequency ranges over the entire preparatory period in the differential spectra for Assignment, the rule the monkeys have to keep in mind during a certain trial block (**Figures 4A,B**), were observed. As in **Figure 3**, to observe this impression in detail, we obtained averaged upper envelopes, and examined the modulations in each predictor variable and frequency range of interest. As can be seen in **Figures 4G,H** (top), the lower gamma range exhibited frequent significant differences due to the predictor variable Assignment. In contrast to the ventral side, we did not recognize striking features common to the two examples in the gamma ranges (**Figures 4C–J** and **Supplementary Figures 3C–J**, top) for other predictor variables including another rule-related variable, Visual or Memory, which seems less burdensome to memorize than Assignment. In the low frequency ranges, the delta range showed slight modulation related to the task event, but not specific to any particular predictor variable. For the theta range, it did not show non-specific modulation in the initial hold and delay periods as seen in the ventral side (**Figures 4C–J**, bottom), except for significant differences that appeared intermittently in the right column examples only (**Figures 4D,F,J**, bottom). The examples shown in **Figures 3**, **4** suggest that task-dependent modulations of LFPs can distinguish the ventral side from the dorsal side. Task-relevant shape information, especially Transformed Shape in Sample Scale, was reflected in LFPs in the theta and lower frequency bands during the delay period on the ventral side while Assignment, the rule to be kept in mind, influenced the overall increase in gamma waves on the dorsal side.

Among the shape- and rule-related predictor variables, Transformed Shape in Sample Scale variable had a prominent number of domains exhibiting STFM, followed by Assignment (**Supplementary Figure 4A**). Each of the other shape- and rule related predictor variables, such as Transformed Shape in Test, which had not been expected to cause LFP modulations during the preparatory period, and Shape-Specific Attribute Round or Sharp, which is not relevant to task execution, had a small number of STFM domains and no characteristic frequency distribution (**Supplementary Figures 4C,D**). Therefore, the following discussion will focus primarily on Transformed Shape in Sample and Assignment.

Local field potentials modulation by Transformed Shape in Sample was common in the lower frequency range (**Figures 5A,B** and **Supplementary Figure 4B**), while STFM by Assignment was seen mainly in higher frequencies (**Figures 5A,C**). The percentages of the counts of the STFM domains exhibiting along the frequency range are shown in **Figure 5A**. In the percentage distribution of STFM domains for all predictor variables ($n = 1{,}923$; **Figure 5A**, dashed gray line), the proportions in the low-frequency (theta and delta) and high-frequency (higher and lower gamma) regions were high, and those in the mid-frequency (beta and alpha) region were low. The Transformed Shape in Sample: Scale trend was significantly emphasized in the low-frequency region compared to the above-mentioned total distribution (theta: $p = 0.043$; delta: $p = 0.00086$, binomial test: **Figure 5A**, red line). By contrast, for Assignment, the distribution in the high-frequency region, particularly in the lower gamma region, was more pronounced ($p = 3.1 \times 10^{-5}$, binomial test: **Figure 5A**, blue line). The frequency distribution of the counts of STFM by Transformed Shape in Sample Scale was higher in the low frequency region than expected from the percentage distribution of Shape-Specific Attributes (theta: $p = 0.013$; delta: $p = 0.00010$, binomial test: **Figure 5B**). On the other hand, the counts of STFM by Transformed Shape in Sample Scale were prominent only in the delta range (**Supplementary Figure 4B**). By contrast, the counts of STFM for Assignment were higher in the high frequency range compared to the expected values from Visual or Memory (higher gamma: $p = 3.4 \times 10^{-8}$; lower gamma: $p = 8.9 \times 10^{-5}$, binomial test: **Figure 5C**).

The time distribution of the counts of STFM, obtained using a sliding time-window of 500 ms to sum, also contrasted between these two predictor variables (**Figures 5D,E** and **Supplementary Figure 5**). As for Transformed Shape in Sample Scale, gamma modulations counts exceeded that of theta-delta modulations in the initial hold ($n = 15$, $p = 0.0012$, binomial test) and test periods ($n = 16$, $p = 1.5 \times 10^{-5}$, binomial test), but the theta-delta modulations increased compared with the gamma modulations in the delay period ($n = 70$, $p = 5.6 \times 10^{-19}$, binomial test: **Figure 5D**). The excess of gamma modulations in the initial hold and test periods appear to be primarily due to the high gamma range (**Supplementary Figure 5A**), while both the theta and delta range exhibited a consistent increase in STFM counts in the delay period (**Supplementary Figure 5B**). On the other hand, the gamma modulations by Assignment were maximal in the early sample presentation period compared with the theta-delta range ($n = 14$, $p = 0.00049$, binomial test), but had other significant peaks in the delay ($n = 13$, $p = 0.00092$, binomial test) and test periods ($n = 8$, $p = 0.0039$, binomial test), and even started to increase from the late initial hold period (**Figure 5E**). This overall increase in STFM counts in the gamma range during the preparatory period cannot be clearly attributed to either higher or lower gamma (**Supplementary Figure 5C**). For the lower frequency range, the STFM counts of delta, but not theta, increased during the test period, although not significantly (**Supplementary Figure 5D**).

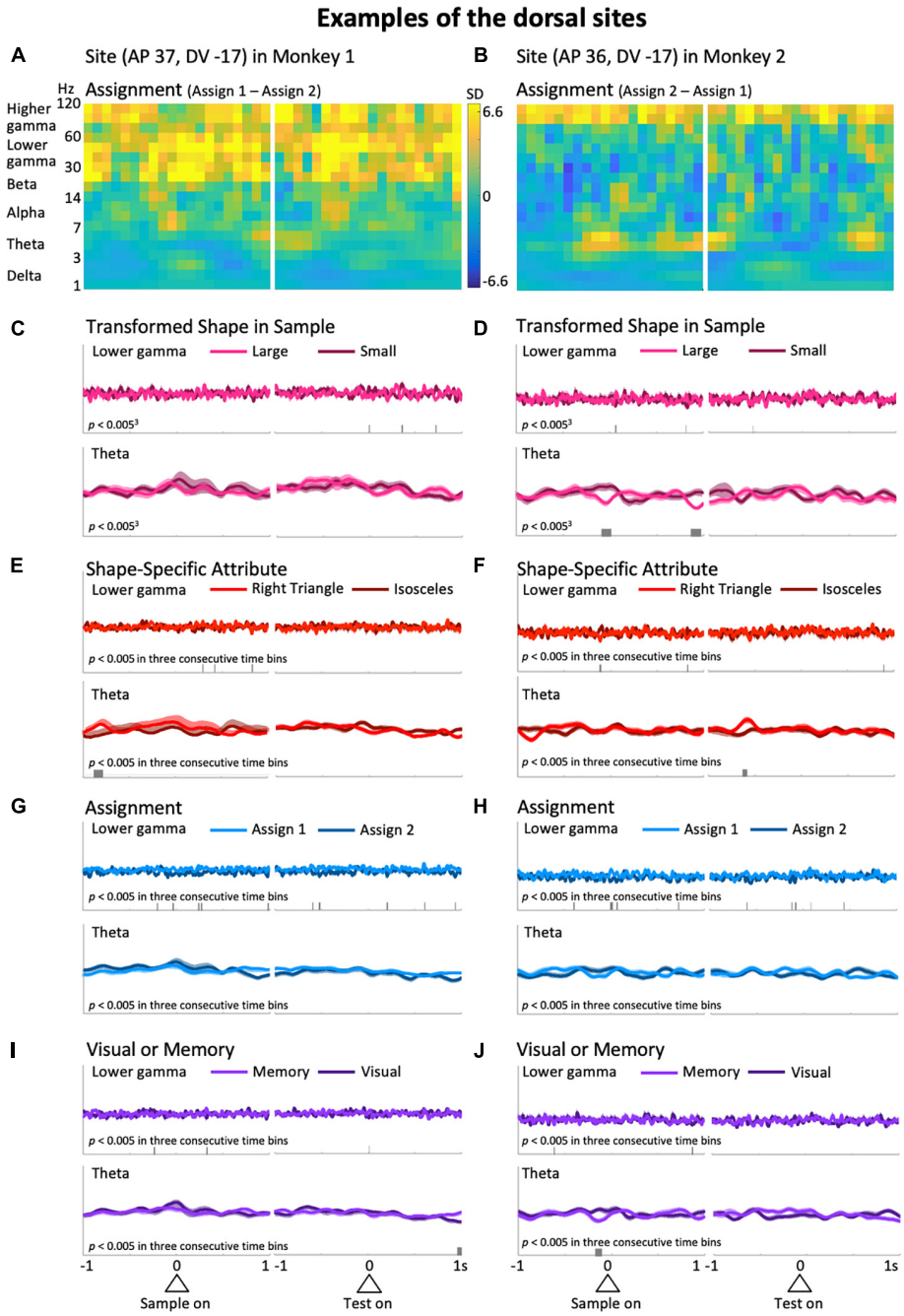

FIGURE 4 | Typical examples from the dorsal side of the LFPC in Monkeys 1 (left column: AP 37, DV -17) and 2 (right column: AP 36, DV -17). **(A,B)** Differences of the time-frequency spectra between assign 1 and assign 2. **(C–J)** Same as the corresponding plots in **Figure 3**. The scales for the mean upper envelopes are identical in each column. Small bars in each mean upper envelope plot indicate the time regions of significant differences ($p < 0.005$) in three consecutive time bins.

Spatial distributions of the STFM counts were also distinguishable between these two predictors. Transformed Shape in Sample Scale had many STFM counts in the theta-delta range on the ventral side of the recorded area (**Figure 5F**) while for Assignment, the STFM counts in the dominant gamma and theta-delta ranges were biased to the dorsal side (**Figure 5G**). The spatial distributions shown in **Figures 5F,G** were tested using the Wilcoxon rank sum test. As shown in **Table 2**, the theta-delta distributions of Transformed Shape in Sample Scale are significantly biased to the ventral side compared to both the theta-delta and gamma distributions of Assignment. The gamma and theta-delta distributions of Transformed Shape in Sample Scale were also distinguished along the anterior-posterior axis. These spatial biases were observed consistently in both monkeys.

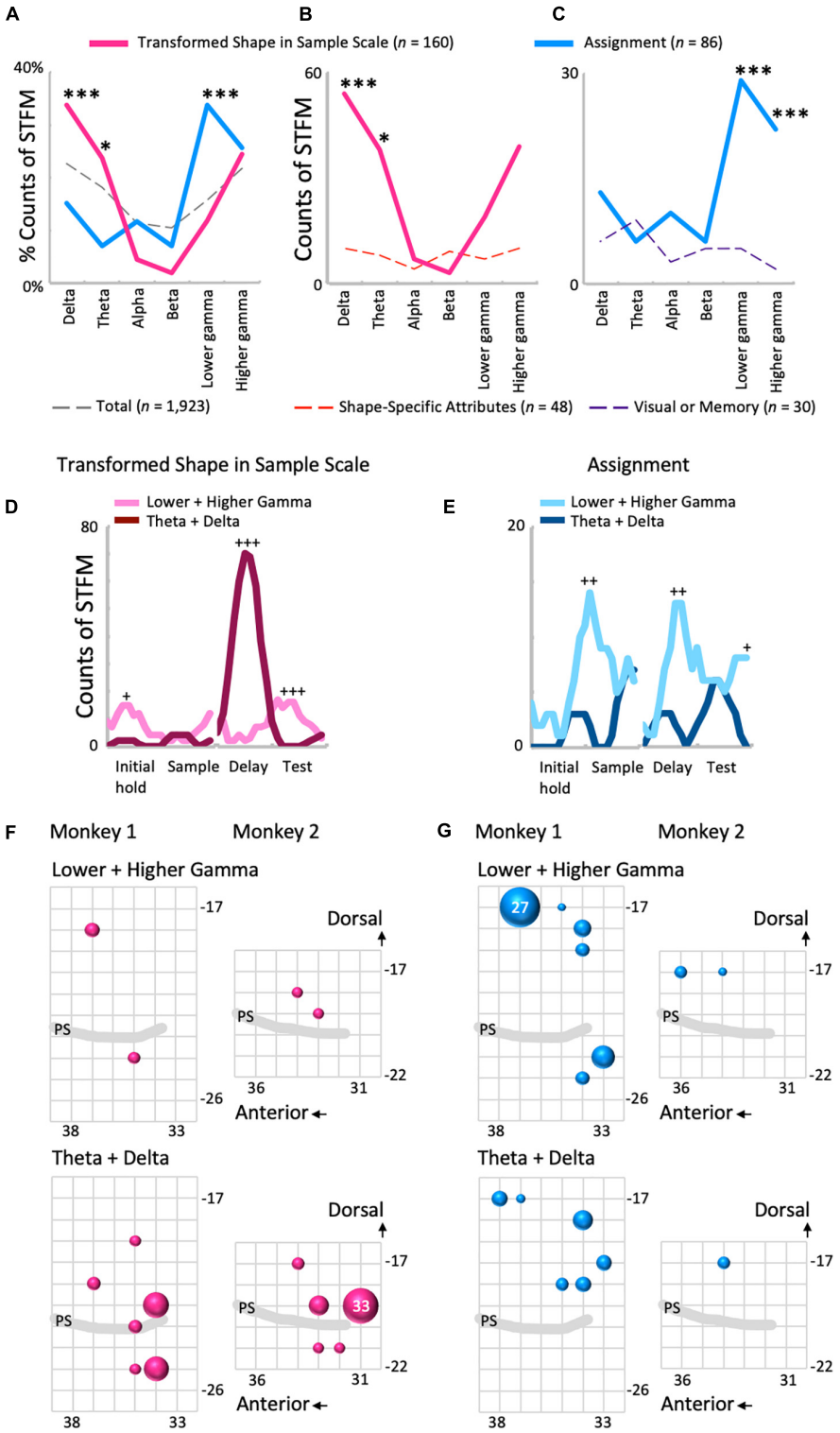

FIGURE 5 | Comparisons between the influence of shape- and rule-related predictor variables on LFP modulations. **(A)** The frequency distributions of the proportions of STFMs for Transformed Shape in Sample Scale **(B)**, Assignment, and all variables (n = 23). **(B,C)** The frequency distributions of the count of STFMs for Transformed Shape in Sample Scale **(B)** and Assignment **(C)** compared to each control. $^{*}p < 0.05$, $^{***}p < 0.001$. **(D,E)** Time-developments of the counts of STFMs for the lower gamma and theta ranges. Transformed Shape in Sample Scale **(D)** and Assignment **(E)**. $+p < 0.005$, $++p < 0.001$, $+++p < 0.0001$. **(F)** Spatial distributions of the STFMs of gamma (top) and theta-delta (bottom) ranges for Transformed Shape in Sample Scale during the delay period. The largest circle represents n = 33. **(G)** Same plots for Assignment. Counts are the summation of the entire preparatory period. The largest circle represents n = 27.

TABLE 2 | Wilcoxon rank-sum test between the STFM distributions shown in **Figures 5F,G**.

Medial vs. Lateral (Monkey1)					
		Transformed shape in sample scale		**Assignment**	
		Lower + higher gamma	**Theta + delta**	**Lower + higher gamma**	**Theta + delta**
Transformed shape in sample-scale	Lower + higher gamma	*p* =	0.065	0.08	0.39
	Theta + delta			0.00000032	0.00000015
Assignment	Lower + higher gamma				0.16
	Theta + delta				
Medial vs. Lateral (Monkey2)					
		Transformed shape in sample scale		**Assignment**	
		Lower + higher gamma	**Theta + delta**	**Lower + higher gamma**	**Theta + delta**
Transformed shape in sample scale	Lower + higher gamma	*p* =	0.0412	0.0571	0.13
	Theta + delta			0.00032	0.0025
Assignment	Lower + higher gamma				1.0
	Theta + delta				
Anterior vs. Posterior (Monkey1)					
		Transformed shape in sample scale		**Assignment**	
		Lower + higher gamma	**Theta + delta**	**Lower + higher gamma**	**Theta + delta**
Transformed shape in sample scale	Lower + higher gamma	*p* =	0.0021	0.42	0.08
	Theta + delta			0.040	0.85
Assignment	Lower + higher gamma				0.35
	Theta + delta				
Anterior vs. Posterior (Monkey2)					
		Transformed shape in Sample Scale		**Assignment**	
		Lower + higher gamma	**Theta + delta**	**Lower + higher gamma**	**Theta + delta**
Transformed shape in Sample Scale	Lower + higher gamma	*p* =	0.0046	0.17	0.80
	Theta + delta			0.0015	0.013
Assignment	Lower + higher gamma				0.6

In the theta-delta map of Transformed Shape in Sample Scale, STFM counts are seen just above the principal sulcus. However, as long as they are not far from the principal sulcus, they are considered to have been obtained from the ventral LFPC. The LFP data analyzed in this study were obtained from the bottom-most contact (ch.15) of a U-probe. When the U-probe penetrated the convex or the cortex almost perpendicularly to its surface, the time-frequency spectra of LFPs was similar across all contacts (**Supplementary Figure 6**). By contrast, when it was inserted into a site dorsal to the principal sulcus, the spectra changed largely along the U-probe shank (**Supplementary Figure 7**). Taking into consideration that the principal sulcus runs in the medial direction (Paxinos et al., 1999; Sakamoto et al., 2015), the LFPs obtained from the lower contacts were expected to be located in the ventral bank of the principal sulcus. This dorsal-ventral distinction was not prominent in other predictive variables in this study (**Supplementary Figure 8**). For Transformed Shape in Sample Rotation, a significant number of STFM can be seen in the ventral side. However, some STFM counts were also seen in the dorsal side (**Supplementary Figure 8A**). The variable Shape-Specific Attribute Isosceles or Right Angle provided scattered distributions in both sides of the principal sulcus (**Supplementary Figure 8B**). Distribution of the rule-related variable Visual or Memory appeared biased to the dorsal side, although this unclear when compared to Assignment.

DISCUSSION

We recorded LFPs from the monkey LFPC during a shape manipulation task and analyzed its task-dependent modulations through wavelet analysis and stepwise regression analysis. Here, we mainly focused on shape- and rule-related task variables (Sakamoto et al., 2020a), and found that the transformed shape in the sample period strongly affected the theta and delta waves in the delay period on the ventral side, and the

arm-manipulation assignment influenced gamma components on the dorsal side.

Our results are sufficiently reliable for the following reasons. First, we analyzed LFPs recorded from the bottommost contacts of multi-contact electrodes, and the characteristic task-related LFP modulations at each recording site were consistent, at least at adjacent sites (**Supplementary Figures 6, 7**). Second, using stepwise regression analysis to generate the best explanatory model from all predictor variables, we were able to avoid spurious models; the difference wavelet spectrum for the Assignment variable shown in **Figure 4A** (left column) shows that differences in the gamma and beta ranges are emphasized. If we had performed a simple regression analysis with each single predictor variable for such data, it would have indicated Assignment as a significant predictor variable for beta waves as well. However, because of the stepwise regression analysis, it was clear that this beta component reflects a trial that repeats the same conditions as the previous trial.

The preponderance of LFP modulations by shape-related information on the ventral side in our results was consistent with previous findings. With respect to visual shape-related processing, the ventral LFPC is anatomically characterized by reciprocal connections with the inferior temporal (IT) cortex (Ungerleider et al., 1989; Webster et al., 1994). Reflecting this, neuronal activities related to visual shape have been reported (Ninokura et al., 2004), including activities in delay period (Wilson et al., 1993; Freedman et al., 2002, 2003). In the delayed matching-to-category task of Freedman et al. (2002, 2003), monkeys were required to forcibly categorize an intermediate sample shape obtained by morphing to one of two test shapes presented after delay. During this task, unit activities influenced by the continuous changes of shape-specific attributes were observed in the IT cortex, while activities reflecting the task requirement, i.e., two-choice categorization during the delay period were seen in the ventral LFPC. These delayed activities may be involved not only in retention of sample information, but also in anticipation or recall of upcoming test stimuli. This aspect of anticipation or recall is also common to the pair-association memory task that has long been used to study the IT cortex (Sakai and Miyashita, 1991). Recently, it has been reported that, during this task, LFP theta waves are generated in the temporal lobe (Koyano et al., 2016; Nakahara et al., 2016). Especially, Koyano et al. (2016) showed that through the processing triggered by a sample stimulus within the cortical six-layer neural circuit, spiking activities reflecting the association of the upcoming test stimulus are generated in the output layer or layer 6, and that these cellular activities are synchronized to the LFP theta rhythm. Considering these findings, the theta waves observed in the ventral LFPC in this study are likely involved in anticipating the upcoming test stimulus as well as retaining the task-relevant shape information of the sample stimulus although interactions with the IT cortex.

As discussed above, predictor variables more relevant to planning and executing the shape manipulation task appear to cause more LFP modulations. In the present study, the shape transformation information during the sample period, which is directly related to behavioral planning, resulted in more STFM domains than the variables of shape-specific attributes. Moreover, among shape-specific attributes, the macroscopic feature isosceles or right triangles (**Figure 2B**) had more STFM domains than the microscopic feature round or sharp corners (**Figure 2C**), which presumably reflects the importance of recognizing macroscopic features as a basis for understanding the transformation between sample and test shapes. These observations suggest that LFPs play an important role in adaptive coding in the prefrontal cortex (Duncan, 2001). Furthermore, the fact that the task-relevant information needed to be retained in working memory in our task and the theta modulation during the delay period was correlated with this behavioral demand is consistent with previous studies suggesting that task-relevant information in the prefrontal short-term memory is stored through theta-range synchronization with other cortical areas (Liebe et al., 2012).

It remains unclear why, among the variables for shape transformation information during the sample period, rotation exhibited fewer STFM domains than scale (**Supplementary Figure 4A**). The scattered spatial distribution of STFM domains for rotation during the sample period (**Supplementary Figure 8A**) may indicate that the working memory for rotation could be stored in a distributed manner, i.e., in both the ventral and dorsal sides. Given the involvement of the dorsal side in spatial working memory, the above observation may imply that the monkeys memorize the rotation information not only as shape transformation but also as the spatial location of particular features of the shape.

The theta-range properties described above were similarly observed in delta waves. While delta waves are widespread in the brain during slow-wave sleep, delta-range synchronization between cortical areas associated with decision making has been reported in awake monkeys (Nácher et al., 2013). Given that information held in working memory is used to make behavioral decisions in our task, the enhanced delta waves seen in the present study may also be involved in decision-making and its associated communication with other brain areas.

More LFPs were modulated by assignment in the dorsal side, which is consistent with the neuronal activity reflecting retrieval of the task-related information in this side (Hoshi and Tanji, 2004). However, in the LFPC during the path-planning task we used in previous studies, which also required switching between motor and operation assignments, the changes in neuronal firing in response to the assignments were less pronounced (Saito et al., 2005). We have not yet analyzed the properties of neuronal firings in this shape manipulation task, but it is possible that the motor-operation assignment affects LFPs and spiking activities differently. The LFP modulation was largest at the beginning of the sample period, but was also large from the beginning of the trial, likely because the task is performed in blocks and it is necessary to keeping the current assignment in mind during the same block. On the other hand, there were few LFP modulations corresponding to the other rule variable, visual or memory. In the visually guided conditions, the contour of the sample period shape was superimposed on the test shape, and thus it was not necessary to remember the transformed shape presented in the sample period and was expected that there would be significant

LFP modulation reflecting this difference in task requirements. However, this was not the case. The observed smaller difference between visual and memory conditions may be because it is advantageous to understand the shape presented in the sample period from the beginning of the trial to perform the task robustly even in the visually guided trials. Alternatively, considering the distinct contributions of the premotor cortex to the generation of visually guided sequential behavior and the supplementary motor cortex to the generation of memory-guided sequential behavior (Mushiake et al., 1991), there may be other areas responsible for the changes in activity associated with the difference in visually and memory-guided trials.

The distinction between ventral and dorsal sides by LFPs shown in this study is consistent with previous studies on neuronal firings, as described above. However, depending on the experimental setup and task factors, it is possible that neither cell firings nor LFP modulations distinguish between ventral and dorsal sides, because dorsal and ventral cells share common inputs (see Tanji and Hoshi, 2008). If the task contains only factors associated with the common inputs, it is natural that the two are not distinguished. As shown in **Supplementary Figure 8**, the LFP modulations by other predictive variables analyzed in this study did not distinguish between ventral and dorsal sides well. It is about the"sharpness" of the task; i.e., the fact that neural activity during a task does not distinguish between two areas does not mean that there are no functional differences between the two areas. It should be recognized that the area called Broadman's 6 was not distinguished until the neural activities during the task requiring visually induced or memory induced generation of sequential actions distinguished premotor and supplementary motor areas within this area (Mushiake et al., 1991). Our results indicate that the gamma and theta waves reflected the information of assignment and transformed shape in Sample, respectively; this is consistent with the view of Roux and Uhlsaas (2014), who proposed that gamma-band waves are generally involved in the maintenance of working memory information, whereas theta-band waves underlie the organization of sequentially ordered working memory items. In our case, the assignment information needed to be firmly maintained during the corresponding block of trials. By contrast, the information of the transformed shape in Sample was temporally stored and used to plan sequential actions.

Wutz et al. (2018) analyzed LFPs in the LFPC during the execution of a dot-pattern categorization task and observed a gamma wave modulation corresponding to less abstract categories in the ventral side and beta wave modulation corresponding to more abstract categories in the dorsal side. The involvement of gamma waves in retaining the dot pattern in working memory for discrimination after a delay period is consistent with the ideas regarding gamma waves discussed above. On the other hand, the interpretation of beta wave modulation as corresponding to complex categories needs to be revisited. Beta waves are often found in cortical motor-related areas (Murthy and Fetz, 1992; Hosaka et al., 2016), and these observations evoke the idea that beta waves are related to the readiness of behavior. In Wutz et al. (2018), animals were to choose between two stimuli that belonged to the same category as the sample stimulus, with free viewing during the choice period. In this task structure, after presentation of the sample, the animals prepare a series of visual search eye-movements to identify the stimulus that belongs to the same category as the sample. The LFPC includes neural activities corresponding to cognitive (Cromer et al., 2010) and behavioral (Shima et al., 2007; Sakamoto et al., 2020b) categories, which are sometimes indistinguishable. Noton and Stark (1971) demonstrated that visual concepts exist in the brain as stylized relationships between features through an experiment in which subjects were shown a large visual image moved their gaze around the features to identify the image. The beta waves reported by Wutz et al. (2018) may reflect such cognitive and behavioral readiness.

Why does functional differentiation exist in the LFPC? Functional differentiation is found in many aspects of the nervous system. For example, organs specialized to detect light provide information essential for survival. However, is it also necessary to have something not specialized in a particular function to cope with various situations? For example, computers can be used for a variety of purposes because they are not specialized for any particular use. Is it important for the LFPC as a center of executive functions to specialize in a particular function? The results of this study refute this notion. Rather, they imply that functionally different parts can work together to create novel ideas when faced with unknown situations; in our society, innovations happen when individuals with different personalities work cooperatively. LFPs and their synchronization may also play an important role in this"cooperation."

DATA AVAILABILITY STATEMENT

The raw data supporting the conclusions of this article will be made available by the authors, without undue reservation.

ETHICS STATEMENT

The animal study was reviewed and approved by the Animal Care and Use Committee of Tohoku University.

AUTHOR CONTRIBUTIONS

KS and HM designed the research. KS and NK performed the research. KS analyzed the data, wrote the first draft of the manuscript, edited and wrote the manuscript. All authors contributed to the article and approved the submitted version.

FUNDING

This work was supported by JSPS KAKENHI Grant Number JP16H06276 (Platform of Advanced Animal Model Support), 17K07060, 20K07726 (Kiban C), MEXT KAKENHI Grant Number 15H05879 (Non-linear Neuro-oscillology), 26120703 (Prediction and Decision Making), 20H05478, 22H04780 (Hyper–Adaptability) and Japan Agency for

Medical Research and Development (AMED) under Grant Number JP18dm0207051.

ACKNOWLEDGMENTS

We thank Midori Takahashi for technical helps.

SUPPLEMENTARY MATERIAL

The Supplementary Material for this article can be found online at: https://www.frontiersin.org/articles/10.3389/fnbeh.2022.750832/full#supplementary-material

Supplementary Figure 1 | A depiction of how upper envelops in **Figures 3**, **4** were obtained. Typical LFP waveforms obtained when a "large" (orange) or "small" (blue) sample shape was presented. Top: raw waveforms. Middle: lower-gamma waves (30–60 Hz) and their upper envelopes. Bottom: theta waves (3–7 Hz) and their upper envelopes.

Supplementary Figure 2 | Waveforms in the delta and high gamma range obtained from the same recording site as in **Figure 3**. **(A–J)** Each panel is identical to the corresponding panel in **Figure 3**.

Supplementary Figure 3 | Waveforms in the delta and high gamma range obtained from the same recording site as in **Figure 4**. **(A–J)** Each panel is identical to the corresponding panel in **Figure 4**.

Supplementary Figure 4 | Distributions of STFM domains across the predictor variables analyzed in this study **(A)** and frequency ranges **(B–D)**. Relations to **Figures 5B,C** are also indicated.

Supplementary Figure 5 | Comparisons between the influence of shape **(A,B)** and rule-related **(C,D)** factors on LFP modulations. Time-developments of the counts of STFMs is shown for the higher and lower gamma **(A,C)**, and theta and delta **(B,D)** ranges. **(A)** Formats are the same as in **Figures 5D,E**. A sliding window of 500 ms was used. $+p < 0.005$.

Supplementary Figure 6 | The differential time-frequency spectra of the transformed shape in sample period (large – small) obtained from the channels along the multi-contact electrode inserted into a site in the convexity of the ventral LPFC of Monkey 1 (AP 34, DV –25). The spectra of ch.15, circled in yellow, are identical to those in **Figure 3A** and **Supplementary Figure 2A**.

Supplementary Figure 7 | Spectra in the same format as **Supplementary Figure 6** obtained from the electrode inserted into a site dorsal to the principal sulcus of Monkey 2 (AP 33, DV -19). Data from ch.15, circled in yellow, are included in the analysis. Note that although these spectra exhibited large changes compared to those in **Supplementary Figure 6**, the lower channels showed spectra similar to that of ch.15, suggesting that the data from the lower channels were obtained from the ventral LPFC.

Supplementary Figure 8 | Spatial distributions of STFM domains for Transformed Shape in Sample Rotation **(A)**, Shape-Specific Attributes Isosceles or Right Rectangle **(B)**, and Visual or Memory **(C)**. The scale of the balls in **(A,B)** of shape-related variables is proportional to that in **Figure 5F**, and that in rule-related **(C)** is proportional to that in **Figure 5G**.

REFERENCES

Akam, T., and Kullmann, D. M. (2014). Oscillatory multiplexing of population codes for selective communication in the mammalian brain. *Nat. Rev. Neurosci.* 15, 111–122. doi: 10.1038/nrn3668

Averbeck, B. B., and Seo, M. (2008). The statistical neuroanatomy of frontal network in the macaque. *PLoS Comput. Biol.* 4:E1000050. doi: 10.1371/journal.pcbi.1000050

Buschman, T. J., Denovellis, E. L., Diogo, C., Bullock, D., and Miller, E. K. (2012). Synchronous oscillatory neural ensembles for rules in the prefrontal cortex. *Neuron* 76, 838–846. doi: 10.1016/j.neuron.2012.09.029

Cromer, J. A., Roy, J. E., and Miller, E. K. (2010). Representation of multiple, independent categories in the primate prefrontal cortex. *Neuron* 66, 796–807. doi: 10.1016/j.neuron.2010.05.005

Dezfouli, M. P., Schwedhelm, P., Wibral, M., Treue, S., Daliri, M. R., and Esghaei, M. (2021). A neural correlate of visual feature binding in primate lateral prefrontal cortex. *NeuroImage* 229:117757. doi: 10.1016/j.neuroimage.2021.117757

Duncan, J. (2001). An adaptive coding model of neural function in prefrontal cortex. *Nat. Rev. Neurosci.* 2, 820–829. doi: 10.1038/35097575

Felleman, D. J., and Van Essen, D. C. (1991). Distributed hierarchical processing in the primate cerebral cortex. *Cereb. Cortex* 1, 1–47. doi: 10.1093/cercor/1.1.1-a

Freedman, D. J., Riesenhuber, M., Poggio, T., and Miller, E. K. (2002). Visual categorization and the primate prefrontal cortex: neurophysiology and behavior. *J. Neurophysiol.* 88, 929–941. doi: 10.1152/jn.2002.88.2.929

Freedman, D. J., Riesenhuber, M., Poggio, T., and Miller, E. K. (2003). A comparison of primate prefrontal and inferior temporal cortices during visual categorization. *J. Neurosci.* 23, 5235–5246. doi: 10.1523/JNEUROSCI.23-12-05235.2003

Funahashi, S., Bruce, C. J., and Goldman-Rakic, P. S. (1989). Mnemonic coding of visual space in the monkey's dorsolateral prefrontal cortex. *J. Neurophysiol.* 61, 331–349. doi: 10.1152/jn.1989.61.2.331

Fuster, J. (2015). *The Prefrontal Cortex*, 5th Edn. Cambridge: Academic Press.

Fuster, J. M. (1973). Unit activity in prefrontal cortex during delayed response performance: neuronal correlates of transient memory. *J. Neurophysiol.* 36, 61–78. doi: 10.1152/jn.1973.36.1.61

Fuster, J. M., and Alexander, G. E. (1971). Neuron activity related to short term memory. *Science* 173, 652–654. doi: 10.1126/science.173.3997.652

Hosaka, R., Nakajima, T., Aihara, K., Yamaguchi, Y., and Mushiake, M. (2016). The suppression of beta oscillations in the primate supplementary motor complex reflects a volatile state during the updating of action sequences. *Cereb. Cortex* 26, 3442–3452. doi: 10.1093/cercor/bhv163

Hoshi, E., and Tanji, J. (2004). Area-selective neuronal activity in the dorsolateral prefrontal cortex for information retrieval and action planning. *J. Neurophysiol.* 91, 2707–2722. doi: 10.1152/jn.00904.2003

Katori, Y., Sakamoto, K., Saito, N., Tanji, J., Mushiake, M., and Aihara, K. (2011). Representa- tional switching by dynamical reorganization of attractor structure in a network model of the prefrontal cortex. *PLoS Comput. Biol.* 7:e1002266. doi: 10.1371/journal.pcbi.1002266

Kojima, S., and Goldman-Rakic, P. S. (1982). Delay-related activity of prefrontal neurons in rhesus monkeys performing delayed response. *Brain Res.* 248, 43–49. doi: 10.1016/0006-8993(82)91145-3

Kojima, S., and Goldman-Rakic, P. S. (1984). Functional analysis of spatially discriminative neurons in prefrontal cortex of rhesus monkey. *Brain Res.* 291, 229–240. doi: 10.1016/0006-8993(84)91255-1

Koyano, K. W., Takeda, M., Matsui, T., Hirabayashi, T., Ohashi, Y., and Miyashita, Y. (2016). Laminar module cascade from layer 5 to 6 implementing cue-to-target conversion for object memory retrieval in the primate temporal cortex. *Neuron* 92, 518–529. doi: 10.1016/j.neuron.2016.09.024

Liebe, S., Hoerzer, G. M., Logothetis, N. K., and Rainer, G. (2012). Theta coupling between V4 and prefrontal cortex predicts visual short-term memory performance. *Nat. Neurosci.* 15, 456–462. doi: 10.1038/nn.3038

Lundqvist, M., Rose, J., Herman, P., Brincat, S. L., Buschman, T. J., and Miller, E. K. (2016). Gamma and beta bursts underlie working memory. *Neuron* 90, 152–164. doi: 10.1016/j.neuron.2016.02.028

Ma, L., Skoblenick, K., Johnston, K., and Stefan Everling, S. (2018). Ketamine alters lateral prefrontal oscillations in a rule-based working memory task. *J. Neurosci.* 38, 2482–2494. doi: 10.1523/JNEUROSCI.2659-17.2018

Miller, E. K., Erickson, C. A., and Desimone, R. (1996). Neural mechanisms of visual working memory in prefrontal cortex of the macaque. *J. Neurosci.* 16, 5154–5167. doi: 10.1523/JNEUROSCI.16-16-05154.1996

Murthy, V. N., and Fetz, E. E. (1992). Coherent 25- to 35-Hz oscillations in the sensorimotor cortex of awake behaving monkeys. *Proc. Natl. Acad. Sci. U.S.A.* 89, 5670–5674. doi: 10.1073/pnas.89.12.5670

Mushiake, H., Inase, M., and Tanji, J. (1991). Neuronal activity in the primate premotor, supplementary, and precentral motor cortex during visually guided and internally determined sequential movements. *J. Neurophysiol.* 66, 705–718. doi: 10.1152/jn.1991.66.3.705

Mushiake, H., Saito, N., Sakamoto, K., Itoyama, Y., and Tanji, J. (2006). Activity in the lateral prefrontal cortex reflects multiple steps of future events in action plans. *Neuron* 50, 631–641. doi: 10.1016/j.neuron.2006.03.045

Nácher, V., Ledberg, A., Deco, D., and Romo, R. (2013). Coherent delta-band oscillations between cortical areas correlate with decision making. *Proc. Natl. Acad. Sci. U.S.A* 110, 15085–15090. doi: 10.1073/pnas.1314681110

Nakahara, K., Adachi, K., Kawasaki, K., Matsuo, T., Sawahata, H., Majima, K., et al. (2016). Associative- memory representations emerge as shared spatial patterns of theta activity spanning the primate temporal cortex. *Nat. Commun.* 7:11827. doi: 10.1038/ncomms11827

Ninokura, Y., Mushiake, H., and Tanji, J. (2004). Integration of temporal order and object information in the monkey lateral prefrontal cortex. *J. Neurophysiol.* 91, 555–560. doi: 10.1152/jn.00694.2003

Noton, D., and Stark, L. (1971). Scanpaths in eye movements during pattern perception. *Science* 171, 308–311. doi: 10.1126/science.171.3968.308

Passingham, R. E., and Wise, S. P. (2012). *The Neurobiology of the Prefrontal Cortex*. Oxford: Oxford University Press.

Paxinos, G., Huang, X.-F., and Toga, A. W. (1999). *The Rhesus Monkey Brain in Stereotaxic Coordinates*. Cambridge: Academic Press.

Petrides, M., and Pandya, D. N. (1994). "Comparative architectonic analysis of the human and the macaque frontal cortex," in *Handbook of Neuropsychology*, eds F. Boller and J. Grafman (Amsterdam: Elsevier Science), 17–58.

Petrides, M., Tomaiuolo, F., Yetarian, E. H., and Pandya, D. N. (2012). The prefrontal cortex: comparative architectonic organization in the human and the macaque monkey brains. *Cortex* 48, 46–57. doi: 10.1016/j.cortex.2011.07.002

Rainer, G., Asaad, W. F., and Miller, E. K. (1998). Memory fields of neurons in the primate prefrontal cortex. *Proc. Natl. Acad. Sci. U.S.A.* 95, 15008–15013. doi: 10.1073/pnas.95.25.15008

Rao, S. C., Rainer, G., and Miller, E. K. (1997). Integration of what and where in the primate prefrontal cortex. *Science* 276, 821–824. doi: 10.1126/science.276.5313.821

Roux, F., and Uhlsaas, P. J. (2014). Working memory and neural oscillations: alpha–gamma versus theta–gamma codes for distinct WM information? *Trends Cogn. Sci.* 18, 16–25. doi: 10.1016/j.tics.2013.10.010

Saito, N., Mushiake, H., Sakamoto, K., Itoyama, Y., and Tanji, J. (2005). Representation of immediate and final behavioral goals in the monkey prefrontal cortex during an instructed delay period. *Cereb. Cortex* 15, 1535–1546. doi: 10.1093/cercor/bhi032

Sakai, K., and Miyashita, Y. (1991). Neural organization for the long-term memory of paired associates. *Nature* 6, 75–81. doi: 10.1038/354152a0

Sakamoto, K., Katori, Y., Saito, N., Yoshida, S., Aihara, K., and Mushiake, H. (2013). Increased firing irregularity as an emergent property of neural-state transition in monkey prefrontal cortex. *PLoS One* 8:e80906. doi: 10.1371/journal.pone.0080906

Sakamoto, K., Kawaguchi, N., and Mushiake, H. (2012). "Is advance planning of sequential movements reflected in the behavior of monkeys?" in *Proceedings of the 22th Annual Conference of Japanese Neural Network Society*, p3–19.

Sakamoto, K., Kawaguchi, N., and Mushiake, H. (2020a). Differences in task-phase-dependent time-frequency patterns of local field potentials in the dorsal and ventral regions of the monkey lateral prefrontal cortex. *Neurosci. Res.* 156, 41–49. doi: 10.1016/j.neures.2019.12.016

Sakamoto, K., Saito, N., Yoshida, S., and Mushiake, H. (2020b). Dynamic axis-tuned cells in the monkey lateral prefrontal cortex during a path-planning task. *J. Neurosci.* 40, 203–219. doi: 10.1523/JNEUROSCI.2526-18.2019

Sakamoto, K., Kawaguchi, N., Yagi, K., and Mushiake, H. (2015). Spatiotemporal patterns of current source density in the prefrontal cortex of a behaving monkey. *Neural. Networks* 62, 67–72. doi: 10.1016/j.neunet.2014.06.009

Sakamoto, K., Mushiake, H., Saito, N., Aihara, K., Yano, M., and Tanji, J. (2008). Discharge synchrony during the transition of behavioral goal representations encoded by discharge rates of prefrontal neurons. *Cereb. Cortex* 18, 2036–2045. doi: 10.1093/cercor/bhm234

Shima, K., Isoda, M., Mushiake, H., and Tanji, J. (2007). Categorization of behavioural sequences in the prefrontal cortex. *Nature* 445, 315–318. doi: 10.1038/nature05470

Tanji, J., and Hoshi, E. (2008). Role of the lateral prefrontal cortex in executive behavioral control. *Physiol. Rev.* 88, 37–57. doi: 10.1152/physrev.00014.2007

Tanji, T., Shima, K., and Mushiake, H. (2007). Concept-based behavioral planning and the lateral prefrontal cortex. *Trends Cogn. Sci.* 11, 528–534. doi: 10.1016/j.tics.2007.09.007

Ungerleider, L. G., Gaffan, D., and Pelak, V. S. (1989). Projections from inferior temporal cortex to prefrontal cortex via the uncinate fascicle in rhesus monkeys. *Exp. Brain Res.* 76, 473–484. doi: 10.1007/BF00248903

Webster, M. J., Bachevalier, J., and Ungerleider, L. G. (1994). Connections of inferior temporal areas TEO and TE with parietal and frontal cortex in macaque monkeys. *Cereb. Cortex* 4, 471–783. doi: 10.1093/cercor/4.5.470

Wilson, F. A., Scalaidhe, S. P., and Goldman-Rakic, P. S. (1993). Dissociation of object and spatial processing domains in primate prefrontal cortex. *Science* 260, 1955–1958. doi: 10.1126/science.8316836

Wimmer, K., Ramon, M., Pasternak, T., and Compte, K. (2016). Transitions between multiband oscillatory patterns characterize memory-guided perceptual decisions in prefrontal circuits *J. Neurosci.* 36, 489–505. doi: 10.1523/JNEUROSCI.3678-15.2016

Wutz, A., Loonis, R., Roy, J. E., Donoghue, J. A., and Miller, E. K. (2018). Different levels of category abstraction by different dynamics in different prefrontal areas. *Neuron* 97, 716–726. doi: 10.1016/j.neuron.2018.01.009

Yetarian, E. H., Pandya, D. N., Tomaiuolo, F., and Petrides, M. (2012). The cortical connectivity of the prefrontal cortex in the monkey brain. *Cortex* 48, 58–81. doi: 10.1016/j.cortex.2011.03.004

Conflict of Interest: The authors declare that the research was conducted in the absence of any commercial or financial relationships that could be construed as a potential conflict of interest.

Publisher's Note: All claims expressed in this article are solely those of the authors and do not necessarily represent those of their affiliated organizations, or those of the publisher, the editors and the reviewers. Any product that may be evaluated in this article, or claim that may be made by its manufacturer, is not guaranteed or endorsed by the publisher.

Advantages of publishing in Frontiers

OPEN ACCESS
Articles are free to read for greatest visibility and readership

FAST PUBLICATION
Around 90 days from submission to decision

HIGH QUALITY PEER-REVIEW
Rigorous, collaborative, and constructive peer-review

TRANSPARENT PEER-REVIEW
Editors and reviewers acknowledged by name on published articles

Frontiers
Avenue du Tribunal-Fédéral 34
1005 Lausanne | Switzerland

Visit us: www.frontiersin.org
Contact us: frontiersin.org/about/contact

REPRODUCIBILITY OF RESEARCH
Support open data and methods to enhance research reproducibility

DIGITAL PUBLISHING
Articles designed for optimal readership across devices

FOLLOW US
@frontiersin

IMPACT METRICS
Advanced article metrics track visibility across digital media

EXTENSIVE PROMOTION
Marketing and promotion of impactful research

LOOP RESEARCH NETWORK
Our network increases your article's readership